Ministry of Education and Science of Ukraine
"Priazovsky State Technical University"
Institute of Materials Research of Slovak Academy of Science

Y. G. Chabak, V. G. Efremenko, V. I. Zurnadzhy,
B. V. Efremenko, I. Petryshynets

IMPROVEMENT OF WEAR RESISTANCE OF STEELS AND CAST IRONS BY PULSED-PLASMA SURFACE MODIFICATION AND COATING DEPOSITION

Monograph

PREMIER Publishing
Premier Publishing s.r.o.

Praha 2024

Authors:
Chabak Yuliia Gennadiivna [1, 2]
Efremenko Vasyl Georgijovych [1, 2]
Zurnadzhy Vadym Ivanovych [1, 2]
Efremenko Bohdan Vasilijovych [1]
Petryshynets Ivan [2]

[1] *Pryazovskyi State Technical University, Dnipro, Ukraine*
[2] *Institute of Materials Research of Slovak Academy of Sciences, Kosice, Slovakia*

Reviewer:
Vlasovets Vitaliy Michailovych (Lviv National Environmental University, Ukraine)

Improvement of wear resistance of steels and cast irons by pulsed-plasma surface modification and coating deposition / Y.G. Chabak, V.G. Efremenko, V.I. Zurnadzhy, B.V. Efremenko, I. Petryshynets – Praha: Premier Publishing s.r.o. 2024. – 172 p.

ISBN 978-80-88612-35-3

DOI: 10.29013/IOW.ChabakY.EfremenkoV.ZurnadzhyV.EfremenkoB.PetryshynetsI.172.2024

The monograph is dedicated to the increasing of exploitation durability of high-alloyed cast irons and ledebutitic steels by means of surface modification and coating deposition. The key technology used is a pulse-plasma generation by high-current discharge which enables the injection of plasma jet with the product of the cathode erosion. The monograph displays the "Microstructure-Properties" correlations regarding the regimes of the treatment and eroded cathode's chemical composition. The book can be useful for the researchers dealing with the Surface Engineering and Tribological Materials Science.

This monograph was published within the frame of:
(a) the project funded by the Ministry of Education and Science of Ukraine (00122U000325);
(b) "EU Next generation EU through the Recovery and Resilience Plan for Slovakia" (No. 09I03-03-V01-00061 and No. 09I03-03-V01-00099).
(c) the project funded by the Slovak Research and Development Agency (APVV-23-0341)

Signed to print 23/05/2024. Format 60×84/16.
Offset Paper. Garniture Minion Pro. Pec. liter. 11.
Typeset in Premier Publishing s.r.o. Praha, Czech Republic.

Printed by Premier Publishing s.r.o.
Praha 8 – Karlín, Lyčkovo nám. 508/7, PSČ 18600, Czech Republic
pub@ppublishing.org, ppublishing.org

ISBN 978-80-88612-35-3

Contents

Prephase

White alloyed cast irons are widely used in various industry sectors (mining and mineral processing, cement production, energy generating plants, agriculture, etc.) for tribotechnical applications due to advanced abrasive, abrasive-corrosive, and erosive wear resistance. These alloys have a high cost due to the significant amount of alloying elements, thus their use must be economically substantiated. To achieve maximum efficiency, the wear performance and service life of white alloyed cast irons should be further improved which is a challenging task. For this purpose, optimizing the chemical composition and employing the technologies of surface engineering are feasible. Among the latter, the most prospective approach is using highly concentrated energy sources (steady plasma jet, high-energy plasma pulses, and laser/electron beams) to modify the structure through phase-structural transformations, protective coatings deposition, and surface alloying. Until now, the mentioned methods of surface engineering have been very limitedly studied and applied regarding the white alloyed cast irons. This resulted in a lack of research data and technological solutions for this topic. Taking into account the above, the present work is aimed at filling this gap by deeply studying the application of pulsed plasma surface treatment for the enhancement of tribological behaviors of white alloyed cast irons.

The monograph presents the results of research projects performed by the authors from 2014 to 2024. The chapters of a book are the articles published during this period in the following research journals: "Problems of Atomic Science and Technology" (Chapters 2 and 3), "Journal of Materials Engineering and Performance" (Chapter 4), "Materials" (Chapter 5), "Surface and Coating Technology" (Chapter 6), "Vacuum" (Chapter 7) and "Metals" (Chapter 8).

In Chapter 1, the common information about the applied equipment and research methods used in this work (in different chapters) is presented. Specifically, the design and operating principles of the electro-thermal axial plasma accelerator (EAPA) used in all chapters as a pulsed plasma source are described. Chapters 2 and 3 are dedicated to the physical basis and mathematical modeling of the processes of surface heating (structure modification) and coating deposition through high-current pulsed discharge using EAPA. Chapters 4 and 5 describe the pulsed-plasma-induced formation of

thing layers (coatings) with the chemical composition of high Cr cast iron; also, the structure and properties of the coating are characterized. Chapter 6 presents the structural peculiarities and properties of layered Cr-W carbide coating obtained by pulsed plasma. In Chapters 7 and 8 the fabrication of coatings (metallic matrix+carbides (WC, TiC)) by using the eroded composite cathodes and the evaluation of their structure and tribological behaviors are elucidated.

The book's authors express their gratitude to the reviewer Doctor of Science in Engineering, Professor Vitaliy Vlasovets (Head of Department of Mechanical Engineering, Lviv National Environmental University, Ukraine) for valuable comments on the book's content. The authors are grateful to colleagues and co-authors (Victor Fedun, Angeliki Lekatou, Kazumichi Shimizu, Alexandros Karantzalis, Alexander Azarkhov, etc.) for their help in conducting research and discussions on the results.

The authors hope that the results of the research presented in this monograph may be of interest to researchers and engineering workers specializing in the field of tribological Materials Science and Surface Engineering, and it can also be useful for the students of the related specialties.

Chapter 1. EXPERIMENTAL PROCEDURE

The pulsed-plasma modification and coating deposition were performed using the electro-thermal axial plasma accelerator (EAPA) the design and electric installation thereof are detailed described in [1–3]. EAPA was designed and installed at the Department of Physics of Pryazovskyi State Technical University by Kolyada Yu. and Fedun V. The sketch of EAPA is shown in (Fig. 1.1). EAPA consists of the plasma accelerator chamber and the electric circuit. The accelerator chamber is a standard tubular discharger РТФ-6-0.5/10У1 which is a dielectric tube of 430 mm length, with a coaxial hole of 8 mm diameter and 17 mm wall thickness made of paper reinforced fibrobakelite and compressed at both ends by steel shells (1) and (6). The electric circuit is composed of an impulse voltage generator (IVG) unit and an impulse current generator (ICG) unit. The shell (6) serves as an anode while axially positioned inside the tube expendable rod (2) serves as a cathode. The distance between the cathode edge and the tube exit (6) is 50–60 mm. The ICG unit consists of capacitive energy storage (C_1) and a nonlinear inductance (L). The IVG unit includes capacitive energy storage (C_3), a triggered spark gap (G), a pulse transformer, and a decoupling capacitor (C_2). A central electrode (cathode) was a rod 5 mm with diameter made of conductive material. The voltage of the charge in capacitive energy storage device (1.5 mF) was up to 4 kV; the distance from the EAPA edge to the specimen surface is 50 mm.

The discharge current and the voltage were recorded using the Rogowski coil, the ohmic voltage divider and digital oscilloscope INSTRUSTAR ISDS205A. The plasma flux flowing was registered using a "Nikon 1 s 1" camera with an interval between frames of 1/1200. The increment of specimen temperature induced by PPT was determined by a thermocouple attached to opposite (relatively plasma action) surface of the specimen.

For microstructural characterizations, transversely cross-sectioned specimens were prepared by a multi-stage polishing for mirror state using SiC sandpapers (600 to 1200 grit) and alumina aqueous solutions (3 to 1 μm) to get a mirror state and etched in 4% nital solution. The optical microscopes Axiovert 200 M (Ziiess) and Eclipse M200 (Nikon) and the scanning electron microscopes JSM-6510 (JEOL) and Ultra-55 (Ziiess) were used for microstructural observations.

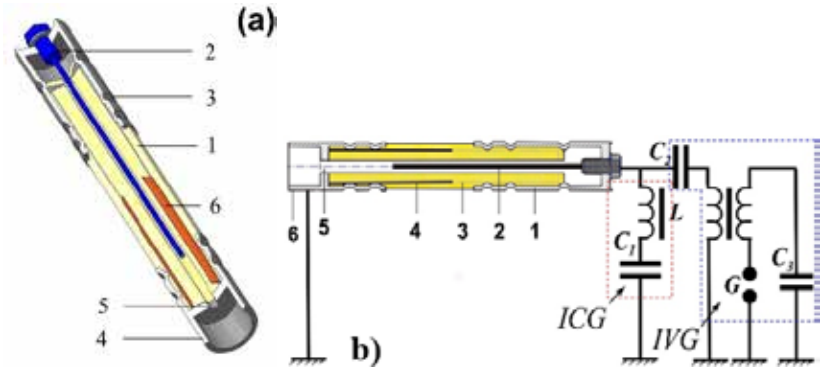

Figure 1.1 – The principal (a) and electrical (b) schemes of EAPA ((a) 1 – paper reinforced bakelite tube, 2 – cathode, 3 and 4 – steel shells, 5 – exit edge, 6 – sheet copper cylinder; (b) 1, 6 – steel shells, 2 – cathode, 3 – Bakelite tube, 4 – sheet copper shield, 5 – tube exit)

The volume fraction of the carbide phases was calculated by the lineal Rozival method [4]. The secondary dendrite arm spacing (SDAS) was determined by measuring the distance between the dendrite centers of adjacent secondary dendrites. Five fields of view were used for the measurement of the mean SDAS. Each field included approximately 60 secondary dendrite arms.

Phase chemical composition and chemical element distribution were investigated by energy dispersive X-ray spectrometry (EDS) using the JED-2300 detector (JEOL). Each reported value is the mean of values received from at least 4 fields of view (3–5 values per each field).

Phase identification was carried out by X-Ray Diffraction (XRD) using the following diffractometers X'Pert PRO(PANalytical) and IV Pro (Rigaku) under Cu-K_α radiation and following parameters: generator voltage is 40 kV, tube current is 50 mA, scan step is 0.03342 degree, and scan speed is 0.0689 degree/s. The volume fraction of retained austenite (f_{RA}) was calculated as [5]:

$$f_{RA} = \frac{100\%}{1 + G(I_\alpha / I_\gamma)}, \qquad (1.1)$$

where I_α and I_γ are the intensities of diffraction lines of αFe (200), (211) and γFe(200),(220),(311); G is the fitting parameter for different peaks combinations [6].

The retained austenite (RA) volume fraction was averaged for f_{RA} values calculated for different pairs of lines. The content of carbon in retained austenite (C_{RA}) was derived from the equation:

$$\alpha_\gamma = 0.3556 + 0.0453 \cdot C_{RA} + 0.000095 \cdot Mn, \quad (1.2)$$

where α_γ and Mn are a lattice parameter (angstrom) and manganese content (wt %) in RA, accordingly.

The lattice parameter was found as [7]:

$$a_\gamma = (h^2 + k^2 + l^2)^{0.5} \frac{\lambda}{2\sin\theta}, \quad (1.3)$$

where *h, k, l* are the indices of crystallographic plane of diffraction; λ is the X-ray wave length; θ is a Bregg angle derived from XRD pattern.

The Rockwell C hardness was measured in cross-section (150 kg load, diamond cone indenter). Microhardness tests were performed by an FM-300 microhardness tester (Future-Tech Corp., Japan) under a load of 20–50 g. The microhardness profile (coating cross-actions) was obtained by averaging the results of measurements along 7 lines perpendicular to the coating surface in different coating points.

The tribological characteristics of the coating were evaluated by "three-body abrasion" tests and "ball-on-plate" dry-sliding tests at room temperature under a relative humidity of 60–70% controlled by humidity sensor head Testo 625. Before abrasive wear testing the surface of grey cast iron was ground by sandpaper to Ra = 0.638 μm and Rz = 2.387 μm; the coating surface had as-coated condition. During "three-body abrasion" tests, the specimen was pressed to a rubber roller of 40 mm diameter under a load of 20 N at a rotating speed of 10.8 s^{-1}. Abrasive particles (Al_2O_3 of 0.5–0.6 mm diameter) were fed to the gap between the specimen and the roller at a feed rate of 0.75 kg·min^{-1}. After each one-minute cycle, the specimen was cleaned by alcohol and weighed on an electronic balance of 0.1 mg accuracy to measure its weight loss. The total cycle number was ten. An average value of three tests was considered as the final result.

The dry-sliding behaviour was studied under the testing according to the "Ball-on-Plate" reciprocating sliding scheme using the "Micron-tribo" tribometer (Micron-System). The test was performed at ambient temperature and at a relative humidity of 60–70 %. Before testing the surface of the specimen was polished to mirror state for better wear track observation (the averaged values of Ra = 0.08 μm and Ra = 0.22 μm for the substrate and the

coating accordingly). The coating served as a plate while a counter body was a 3 mm diameter ball made of hardened 100Cr6 steel AISI 52100 (63 HRC) or SiC (2600 HV) as well as the diamond cones with an apex angle of 120 °. A normal load on a ball/plate contact was 5 N. The ball moved forth and back with a stroke length of 3.5 mm to make 2500 strokes to run the total sliding distance of 8.75 m. The sliding speed was 7.0 mm/s^{-1}. The recording rate was 10 readings per second, and then the data on the coefficient of friction (CoF) were averaged for each sliding cycle [8]. These cycle-averaged values were then used to calculate the mean CoF value for the entire test (without a running-in period). The dry-sliding wear resistance of the coating was assessed by the volumetric wear value derived from the wear track characterization using the profilometer "Micron-beta" (Micron-System, Kyiv, Ukraine). The volumetric wear (ΔV) value was calculated as $\Delta V = VL - VI$, where VL is a volume loss (wear-track-deepening volume) and VI is a volume increase (wear-track-protrusions volume). VI and VL values were derived by analyzing the wear-track profile relative to the profile baseline (as shown in Figure 1.2). The volumetric wear of the wear track was measured in three different intervals of 785 μm length lying within the track's middle part. The same measurements were performed for three tracks obtained on each of three different specimens. The volume loss is the average value of all measurements. The worn profile of the coating was characterized using a "Micron-beta" profilometer to evaluate the wear resistance.

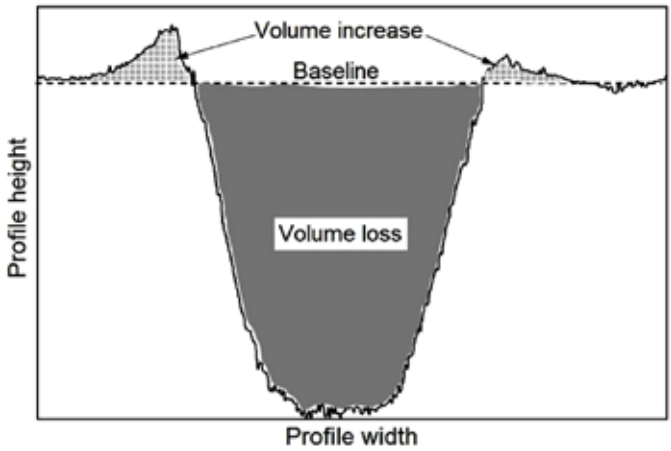

Figure 1.2 – The scheme of the volumetric wear calculation using the wear track's profile

Chapter 2. MODIFICATION OF STEEL SURFACE BY PULSED PLASMA HEATING

Plasma technologies are among the most promising are-as of surface engineering. The pulse-plasma treatment (PPT) is used for surface strengthening by means of modifying effects and coating deposition [9–11]. Surface modification is the result of fast quenching during plasma exposure. The result is a surface modified layer having a fine-grained martensitic structure with increased density of defects and distorted crystal lattice, which has improved hardness and brittle fracture resistance [12]. In addition, the dynamic impact of plasma pulse leads to strain hardening and to radiation-stimulated diffusion of surface atoms into the substrate [13]. Pulse plasma treatment is carried out using various sources of plasma beam, including the electrothermal axial plasma accelerator (EAPA) [1, 2]. EAPA operates under hydrodynamic regime; its ad-vantage is the operation in air under atmospheric pressure. During PPT using EAPA the coating is being formed out of the vapor and droplets of the central electrode material and out of vapor of the dielectric chamber walls. In [3, 14] the features of the microstructure and microhardness of complex coatings de-posited using EAPA are described. The works [15, 16] are fo-cused on study of modified layers obtained on structural steels by means of PPT/EAPA technology. However, the theoretical background of surface modification associated with nature of plasma generation inside EAPA and with its interaction with the surface, remains poorly understood. This applies particularly to time-temperature parameters of surface heating/cooling which crucially predetermines the possibility of quenching the steel surface. The object of this work is to study the dynamics of heat fields in near-surface layers of steel specimen under PPT using electrothermal axial plasma accelerator.

PPT was carried out using the electrothermal axial plasma accelerator as follows: the voltage of the charge in capacitive energy storage device (1.5 mF) is up to 4 kV; the distance between the electrodes is about 50 mm; the distance from the EAPU edge to the specimen surface is 50 mm; number of pulses is six; duty cycle is 30-40 s. A central electrode (cathode) was a rod 5 mm with diameter made of cast iron of the chemical composition 2.34 % C; 27.39 % Cr; 3.13 % Mn; 1.26 % Si; 0.20 % Ti, Fe – balance. The target specimens of 10 ×

× 10 × 20 mm were made of hot-rolled steel grade 75 Mn1 (0.75 % C, 0.91 % Mn, 0.28 % Si).

The oscillograms of time dependences of the discharge current and voltage on the EAPA electrodes are shown in (Fig. 2.1). As it follows from (Fig. 1), under the voltage of pre-charge accumulator of 4 kV, the current reaches its maximum (~ 18.5 kA) in 0.2 ms after initiation of the discharge, while the total discharge duration is approximately 0.6 ms. Numerical integration of the oscillograms (Fig. 2.1) showed that the high-current pulsed discharge in EAPA chamber of volume ~ 10 cm^3 in a time of ~ 0.6 ms results in releasing an energy of about 10 kJ. This leads to: a) sublimation of the dielectric dis-charge chamber walls, b) melting and vaporization of the electrodes, c) heating and ionization of gaseous erosion products forming the plasma flux. The flux flows from the discharge chamber and reaches the steel surface of the specimen. As demonstrated by the high-speed shooting in ultraviolet, produced using the filter ФС8, an intense exposure of plasma flux on the specimen lasts no longer than 1 ms (Fig. 2.2).

After the falling the plasma flux on the specimen its temperature increase in 10-20 K was registered. Thus, under the above-mentioned EAPA operation regime with one plasma pulse the temperature increase (ΔT) was found as 16 °C. This allowed to estimate the energy transferred to the specimen by plasma flux. Considering known values of the geometry and physical values of the specimen material the received energy was estimated as ~ 110 J.

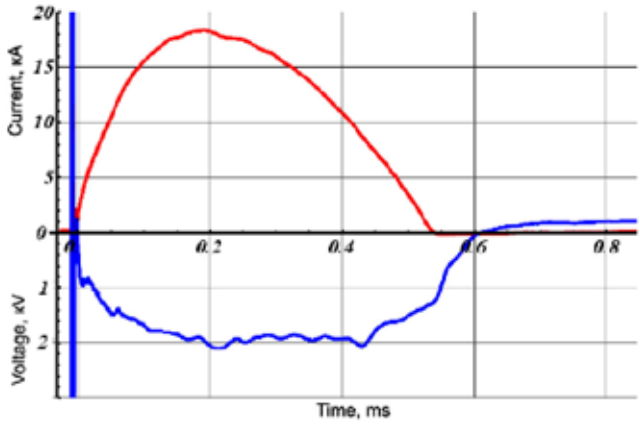

Figure 2.1 – The oscillograms of the discharge in EAPA

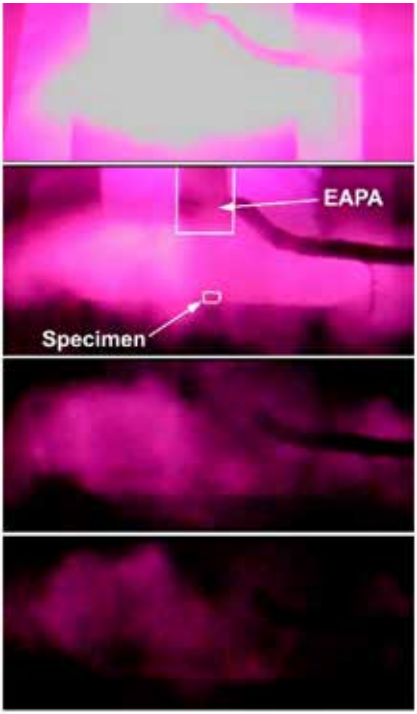

Figure 2.2 – Photoregistration of the specimen irradiation by the plasma flux in the ultraviolet part of the spectrum. The interval between shots is 1/1250 s

For the analysis of laboratory experiment results, one should understand the evolution of temperature fields in the specimen under PPT. For this purpose, the numerical method to solve the heat conduction task was used, basing on the approach of short-term heat sources distributed over the surface:

$$\rho c \frac{\partial T}{\partial t} = -\frac{\partial}{\partial x}\left(\lambda \frac{\partial T}{\partial x}\right), \tag{2.1}$$

where ρ is density; c is specific heat capacity; λ is thermal conductivity.

The speed V_f of movement of interface "liquid-solid" was defined based on:

$$\rho \Lambda V_f = \lambda_l \left[\frac{\partial T}{\partial x}\right] - \lambda_c \left[\frac{\partial T}{\partial x}\right], \tag{2.2}$$

where Λ is specific melting heat; λ_c and λ_l are thermal conductivity of solid phase and liquid phase, respectively.

The boundary conditions were defined by the surface density of heat sources $q(t, x)$:

$$(\lambda \frac{\partial T}{\partial x})\Big|_{x=0} = \mathrm{q(t,x)} = \begin{cases} q_0 \sin(\pi t / \tau), 0 < t \le \tau, \\ 0, \quad t > \tau, \end{cases}, \tag{2.3}$$

while the initial conditions were defined by the temperature distribution over the specimen depth:

$$T(x, 0) = T_0 = 300\ K \tag{2.4}$$

The q_o value in (2.3) can be found from the heat balance equation:

$$\rho_p c_p S_p h_p \Delta T = S_p \int_0^{\tau} [q_0 \sin(\frac{\pi t}{\tau})] dt \tag{2.5}$$

The left side of equation (2.5) represents the change of specimen internal energy ($\rho_\rho, c_\rho, S_\rho, h_\rho$ – density, specific heat capacity, base area and height of the specimen, ΔT – specimen temperature change), and the right one is the amount of heat received by the specimen from plasma flux during the discharge (τ). It should be noted that this model does not take into account the environmental cooling of the specimen.

Integrating the expression (2.5) we get:

$$q_0 = \frac{\pi \rho_p c_p h_p \Delta T}{2\tau} \tag{2.6}$$

For steel specimen ($\rho_\rho = 7830$ kg/m^3, c_p = 420 J/(kg · K), h_p = 10 mm, $\Delta T \sim 16K$) q_0 value was calculated as $1.4 \cdot 10^9$ W/m^2. When calculating the physical values were taken from the literature [17]. The task of temperature field development was solved by the explicit finite-difference scheme [18]. The results of numerical experiments for different values of the heat flux q_o, provided by various PPT modes, are presented below.

In the mode *I*, where the value q_o is $1.4 \cdot 10^9$ W/m^2, the surface temperature reaches its maximum (1400 °C) in 440 μs (Fig. 2.3). Since the temperature does not exceed the solidus temperature of 75 Mn1 steel (1410 °C), then the surface melting is unlikely. Maximum speed of the surface heating is close to $4.5 \cdot 10^6$ K/s, and the cooling rate is close to $3.7 \cdot 10^6$ K/s (Fig. 2.4). In deeper layers these speeds are also quite high: at the depth of 40 μm a heating speed is ~$1.7 \cdot 10^6$ K/s and a cooling speed is ~ $0.3 \cdot 10^6$ K/s.

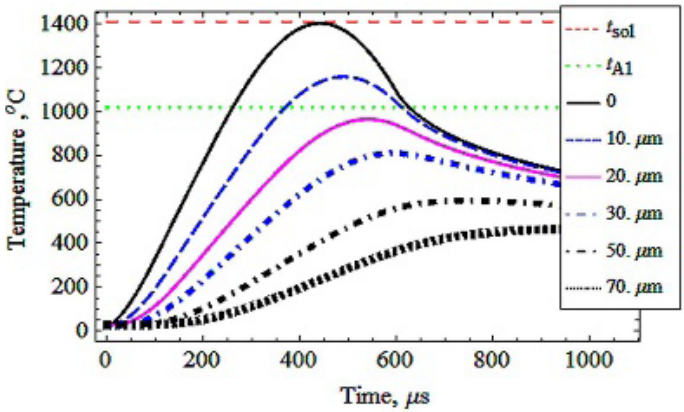

Figure 2.3 – Layerwise temperature distribution in the specimen under PPT in the mode I

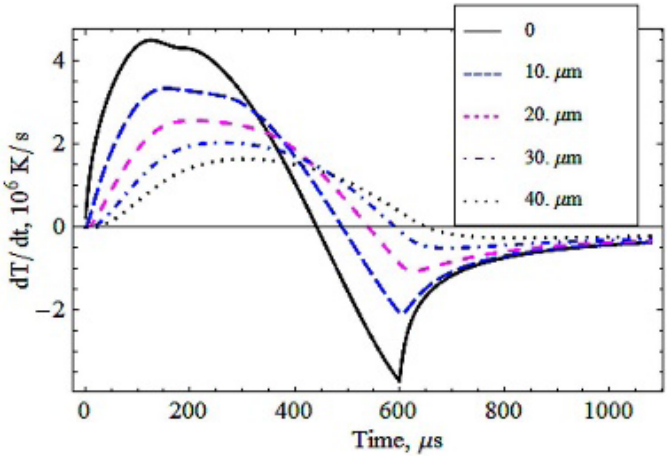

Figure 2.4 – The speed of layerwise temperature change in the specimen under PPT in the mode I

The calculations showed the possibility of ultra-fast heating/cooling of the surface layers as a result of interaction "specimen/plasma flux". It is known that by increasing the heating rate the growth of Ac_1 critical point (the temperature of the appearance of the austenite) occurs in steels, due to the delay of $\alpha \rightarrow \gamma$ polymorphic transformation and carbon redistribution [19]. As shown in [20] point Ac_1 of annealed plane steel with 0.8% C (close to 75 Mn1) is shifted from the equilibrium value of 727 °C to 1021 °C during the heating

at a rate of ~ 10^6 K/s. The latter value was taken as the critical point for steel grade 75 Mn1 in the case of plasma heating. Since the temperature on the specimen surface is higher than 1000 °C, and its cooling rate exceeds the critical quenching speed for steel grade 75 Mn1 (35 K/s [21]), then the heated surface layers must undergo a shear phase transformation with a change (modification) of the structure and properties of the metal. The depth of the surface modification can be determined from (Fig. 2.5), which shows the temperature distribution over the cross-section of the specimen at different time intervals. As seen from (Fig. 1.7) the specimen may be heated above Ac_1 to a depth of not more than ~ 15 μm, which is the predictable thickness of the modified layer. The maximum depth of specimen heating under PPT does not exceed ~ 230 μm.

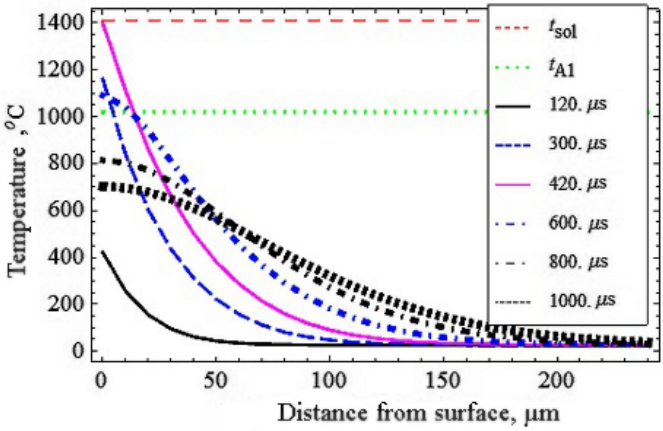

Figure 2.5 – The temperature distribution over the cross section of the specimen under PPT in the mode I

In the mode *II* (q_o = 1.75 · 10^9 W/m^2) the heat input into the specimen surface increases, causing surface temperature rising. The surface temperature reaches 1680 °C, exceeding the melting point of steel, and the specimen is melted to a depth of about 10 μm (Fig. 2.6). The stay time in the liquid state is about 300 μs, while the melting starts approximately at the moment of maximum heat flux in 250–300 μs after the heating start (Fig. 2.7). At this point, the heating speed of the surface reaches ~ 5.5 · 10^6 K/s, and at a depth of 40 μm the heating speed is ~ 2.0 · 10^6 K/s. The depth of the layers heated to a temperature above Ac_1 increases as compared with the regime *I*,

reaching ~ 27 μm (including molten layer) (Fig. 2.8). The heating is followed by cooling with the speed of: at the surface – $5 \cdot 10^6$ K/s, at a depth of 40 μm – $0.5 \cdot 10^6$ K/s, which are much higher than critical quenching speed for steel grade 75 Mn1. Thus, the modified (quenched) layer depth under PPT mode *II* may be of about 27 μm. Within modified layer the very surface layers up to a depth of 10 μm will be quenched from the liquid state, and the below layers will be quenched from the solid state.

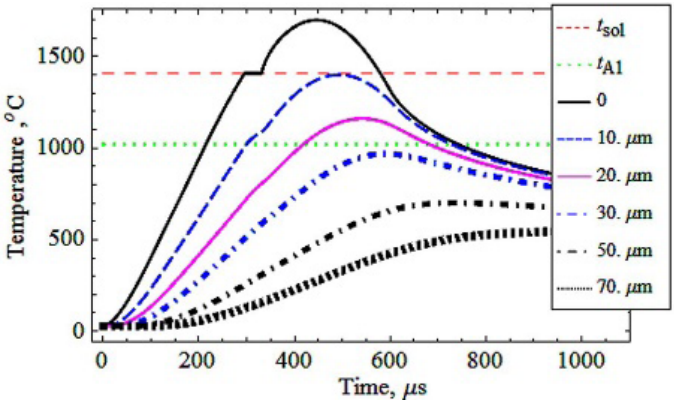

Figure 2.6 – Layerwise temperature distribution in the specimen under PPT in the mode II

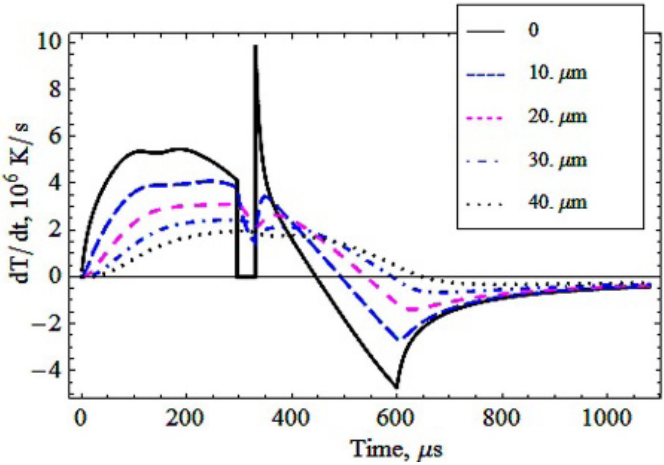

Figure 2.7 – The speed of layerwise temperature change in the specimen under PPT in the mode II

The findings of numerical experiment were confirmed by the laboratory experiment in which the steel specimen was subjected to PPT under the mode *I* (up to six pulses). (Fig. 2.9) shows the microstructure of the specimen surface area. The basic structure of the specimen is mainly pearlite with a broken ferrite network along the grain boundaries. As a result of the PPT with one pulse a "white" modified layer appeared on the surface being very different from pearlite structure of substrate (Fig. 2.9, a). On the top of modified layer the thin coating of cathode material (high-Cr cast iron) was formed.

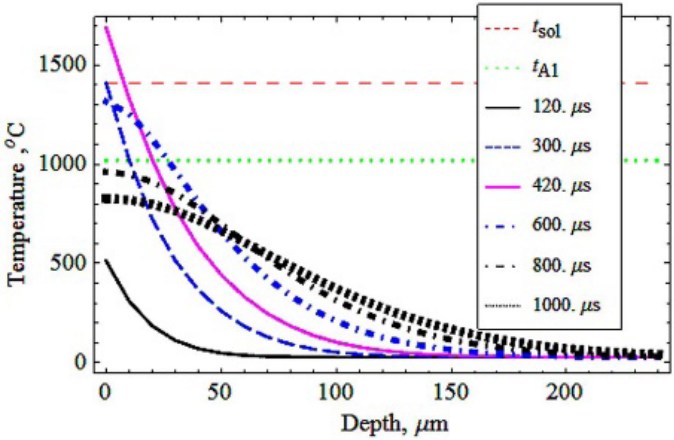

Figure 2.8 – The temperature distribution over the cross section of the specimen under PPT in the mode II

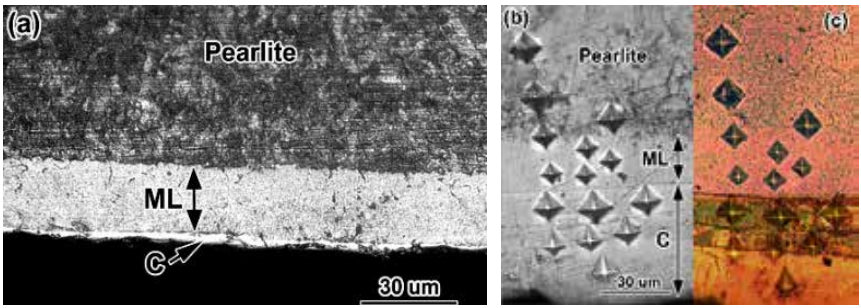

Figure 2.9 – The microstructure of steel 75 Mn1 subjected to PPT under the mode I: ML – modified layer, C – coating (a) one pulse, (b) six pulses (after chemical etching (a, b) and thermal etching (c))

After six pulses, the thickness of the modified layer practically did not change, but the thickness of the coating increased sharply (Fig. 2.9, b, c). The boundary between modified layer and the coating was clearly revealed due to thermal etching. The border "modified layer/coating" is flat, indicating no melting during the layer formation. The thickness of the modified layer varies from 20 to 23 μm, which is slightly higher than the results of a numerical experiment (15 μm). One of possible reasons for the discrepancy between the calculated and experimental results is the inappropriate temperature selected as the Ac_1 point in this case. Presumably, this temperature (1021 °C) has been somewhat overstated, resulting in reduced thickness of the layer, heated to the austenitic state. Taking into account the corrections the actual value of Ac_1 for the steel 75 Mn1 under heating rate used could be considered as ~ 950 °C.

Figure 2.10 shows the profile of microhardness in cross section of surface layers (without coating). According to (Fig. 2.10), PPT resulted in sharp strengthening of specimen surface. It was found that one-pulsed modified layer possesses higher microhardness (900–1000 HV) indicating its martensitic nature. Beyond the modified layer the microhardness drops dramatically: starting at a depth of ~ 40 μm it reaches the level of substrate – 220–300 HV. Ii is known that an acicular martensite is formed in steel with 0.7–0.8% C during conventional quenching [21]. In the case of plasma quenching the acicular morphology of modified layer was not detected. This is because of high dispersity of martensite originated from fine-grained austenite. According to the theory of homogeneous nucleation the critical radius of nucleus $(r*)$ and the energy barrier of nucleation (ΔG^*) are inversely proportional to the degree of superheating at the phase transformation [22]:

$$r^* = \left[\frac{2\gamma T_0}{\Delta H}\right] \cdot \frac{1}{\Delta T_o} \tag{2.7}$$

$$\Delta G^* = \left[\frac{16\pi(\gamma)^3 T_0^2}{3(\Delta H)^2}\right] \cdot \frac{1}{(\Delta T_o)^2} \tag{2.8}$$

where γ – surface energy, ΔH – enthalpy change, T_o – the critical temperature, ΔT_0 – the superheating degree.

In its turn, the superheating degree increases with increasing heating rate. Due higher plasma heating rate, the critical radius of austenite nuclei should decrease, resulting in a greater number of grains with a corresponding

decrease in their size. Fine-grained austenite transforms into fine-crystalline martensite, the structure of which is not detected by optical microscopy.

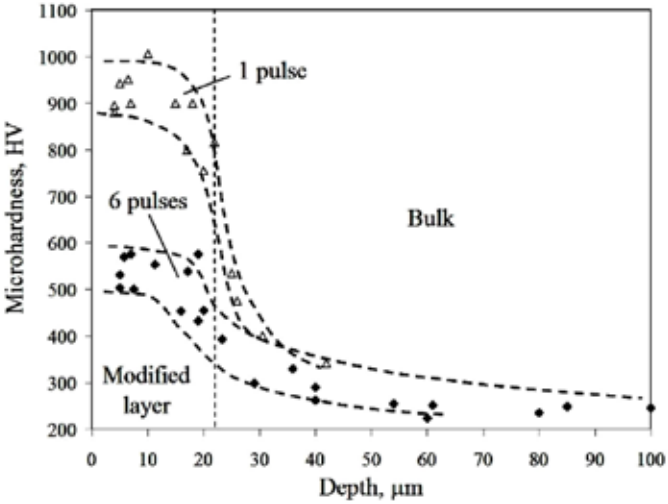

Figure 2.10 – The microhardness distribution over the cross section the modified layer

PPT with six pulses led to decrease of modified layer microhardness to 500–575 HV, while at the depth of 15–23 μm the scatter in the microhardness value increased to 400–575 HV. The reason of softening is the subsequent plasma pulses causing repeated "heating/cooling" cycles in previously formed modified layer. These cycles may cause re-quenching or tempering; the latter leads to martensite softening. With increasing coating thick the maximum cycle temperature in modified layer decreases; thus the tempering starts to prevail over the re-quenching, resulting the microhardness decrease.

A comparison of calculations results for two PPT modes shows that increase of heat flux density leads mostly to increase of surface temperature and surface heating/cooling rates. In the same time, the depth of layer heated above Ac_1 increases to a lesser extent. This is because of limited thermal conductivity of steel, due to which the heat accumulation in the surface layers is substantially ahead of heat conductivity inside the specimen body. This may cause the specimen overheating and melting (with an undesirable change of the surface microgeometry) without a significant increase in modified layer depth. Thus, the increasing the heat flux density

at PPT has rational limits, which depends on the chemical composition of the alloy being processed.

After the performing the above research, the following conclusion were drawn:

The numerical model of temperature field in the steel specimens in contact with a plasma flux induced by high-current pulsed discharge in EAPA chamber is proposed and verified. It is shown that under PPT by the mode, providing the heat flux density (1.4–1.75) · 10^9 W/m^2, the surface temperature can reach 1400–1680 °C, approaching or exceeding the steel melting point. The maximum depth of heating above Ac_1 may be of 15–27 μm, while surface "heating/cooling" may proceed with the speed of about (3.7–5.5) · 10^6 K/s. Single-pulsed PPT at q_o = 1.4 · 10^9 W/m^2 without melting results in modified layer of 20…23 μm formed on the surface of steel grade 75 Mn1. The modified layer has the microhardness of 900–1000 HV which is by three times higher than that of the substrate. The recorded thickness of the modified layer is close to the calculated value.

Content of the chapter is adopted from Modification of steel surface by pulsed plasma heating / Yu. G. Chabak, V. I. Fedun, T. V. Pastukhova, V. I. Zurnadzhy, S. P. Berezhnyy, V. G. Efremenko // Problems of Atomic Science and Technology. – 2017. – Vol. 110, no 4. – P. 97–102.

Chapter 3. PLASMA COATING FORMATION BY THE DEPOSITION OF CATHODE MATERIAL ERODED THROUGH HIGH-CURRENT PULSED DISCHARGE

Plasma-assisted technologies are widely used in the surface engineering practice for the renovation and surface modification of metal parts through deposition of protective coatings [3, 23, 24]. These technologies include pulsed-plasma treatment (PPT) based on the generation of plasma pulses directed to the surface [25–27]. High energy density transferred to the surface by plasma pulse leads to ultra-high-speed heating followed by very fast cooling due to heat evacuation inward the bulk of substrate [28]. The result is a modification of the near-surface layer, i.e. changing its structure and properties [10, 28, 29]. Different devices are used for PPT as plasma source [30–32]. One of them is electro-thermal axial plasma accelerator (EAPA) intended for both modification and protective coating deposition [1, 3, 14, 33]. The coating is formed by the vapors of EAPA inner chamber material as well as by the vapor and micro-droplets of cathode material which are the result of high-current discharge inside the chamber. It is obvious that in this conditions the chemical composition and the structure of the coating are greatly influenced by the material of cathode which is the electrode axially positioned inside EAPA chamber. As a rule, refractory materials (mostly tungsten) are used for cathode in plasma accelerators [30, 34]. In contrast, in [3, 14] it is shown that cathode should be made of material with low melting temperature. This facilitates the cathode surface melting which leads to increase in mass transfer by micro-droplets fraction. Subsequently the velocity of coating formation increases. These cathode materials may include the alloys containing eutectic structural constituents like white cast irons [3] and ledeburitic tool steel [14]. The chemical composition of these alloys allows to obtain the coating with high volume fraction of hard carbides which are necessary to improve the resistance to abrasive and abrasive-erosive wear [35–37].

It is found that PPT may lead to metastable structure in coating resulted from rapid crystallization of plasma transferred material (i.e. "solute trapping" effect [38, 39]). Depending on PPT regime different plasma-chemical reaction may occur leading to specific phase state of the coating. It is

important to understand the mechanisms and time-temperature conditions of micro-droplets formation during the discharge in EAPA chamber. It would help the PPT prognosing and choosing optimal technological parameters. In this connection, the object of present work is a study of formation of cathode micro-droplets in EAPA chamber and further coating formation on the metallic substrate.

The phenomenology of processes. During high-current pulsed discharge in EAPA an energy equal to ~ 10 kJ is released during ~ 10^{-3} s in a volume of ~ 10 cm^3 [28]. This leads to evaporation of the dielectric walls of the discharge chamber, to evaporation and melting of the electrodes (mainly the cathode) leading to plasma jet forming.

The molten cathode material is carried away by the gas stream and, possibly, partially enters the inner surface of the discharge chamber, which leads to its intense heating at the points of contact with the liquid metal. Due to the intense evaporation of fibrobakelite, the melt particles are discarded from the wall and removed from the EAPA chamber by plasma flux along the axis of the tube. When conducting experiments metallization of the inner surface of the tube was not observed. As high-speed shooting shows, when a gas outflows from the chamber within a few milliseconds, ejection of liquid metal drops occurs. This process was previously documented by high-speed (1250 s^{-1}) photo-shooting to visualise the ejection of the liquid droplets (Fig. 3.1). As seen in (Fig. 3.1, a), an intensive flash under the arc discharge made the first photos very light so disabling the plasma flux observation. The first picture in which the details can be discerned corresponds to 5 ms after discharge (Fig. 3.1, b). In this picture, the droplets moving away from the EAPA are clearly seen, shown by the arrows. The subsequent photos (Figs. 3.1, c-f) enabled the observation of a significant number of liquid droplets emitted from EAPA. This process lasted for at least 25 ms wherein the droplets' velocity was approximately 5 $m \cdot s^{-1}$ [28].

To assess the degree of plasma mass transfer, the central electrode was made of both drop-forming materials (Al, Ti, bronze, cast iron, steel, Ni-Cr), as well as of slightly eroding refractory tungsten. Table 3.1 shows the values of specific erosion of cathode depending on the material. The specific erosion was found as cathode mass loss divided by the electric charge transferred during the discharge.

From (Table 3.1) it follows that specific erosion is directly proportional to cathode material's melting temperature. From this dependence falls titanium, having an erosion value close to low-melting aluminium. This is

probably due to the in-creased ability of titanium oxide to adsorb atmospheric gases upon heating [40].

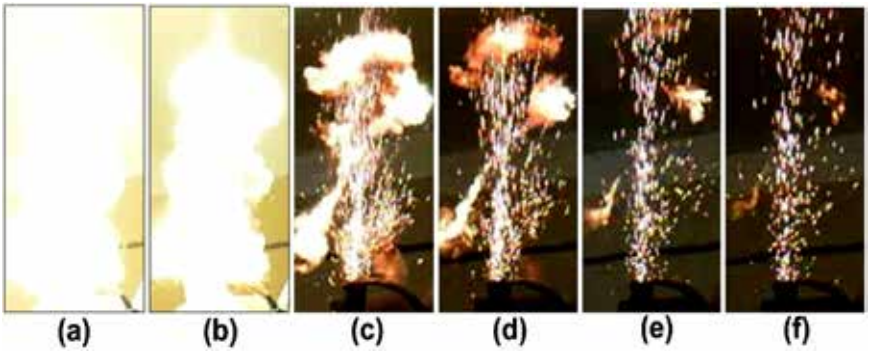

Figure 3.1 – The ejection of the liquid metallic drops out of EAPA after arc discharge (Uo = 4 kV) (discharge voltage of 4 kV, AISI 1020 steel cathode; (a) 5 ms, (b) 7.5 ms, (c) 11.7 ms, (d) 15 ms, (e) 20.8 ms, (f) 25 ms)

Table 3.1 – Specific erosion of materials of EAPA cathode

Cathode material	**Specific erosion, mg/C**	**Melting temperature, °C**
Steel 1020	4.37	1440
Cu	6.35	1083
Al	24.7	660
Ti	20.7	1668
Ni-Cr	6.93	1390
Bronze	7.64	950

Metallographic studies show that after 10 plasma pulses using refractory tungsten cathode a thin coating with uneven thickness occurred on the surface of cast iron specimen (Fig. 3.2, a). For comparison, in (Fig. 3.2), b shows the microstructure of the coating obtained using a cathode made of steel ASTM 1020. It can be seen that in the second case the thickness of the coating is about three times as high as in the first case with a greater uniformity of coating's thickness.

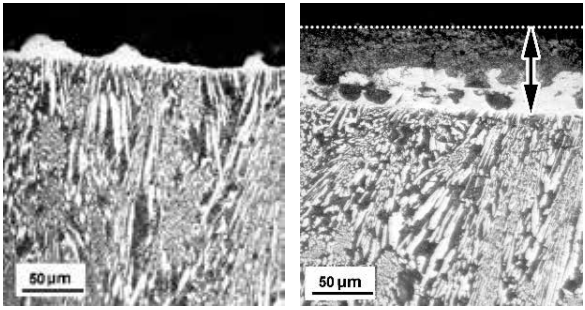

a) b)

Figure 3.2 – The microstructure of the surface of high-chromium cast iron treated with tungsten cathode (a) and cathode of steel ASTM 1020 (b) (U_o = 4 kV)

To analyze the obtained experimental results, the following problems should be resolved, specifically: (a) the intensity of erosion of the central electrode (cathode); (b) the formation and acceleration of erosion drops; (c) thermal impact of plasma flow on the substrate surface; (g) forming of the coating of cathode material on substrate surface.

Erosion of the central electrode (cathode). Let us estimate the consumption of the material of the cathode in a single discharge realization. For low-melting materials the noticeable erosion is observed on an area of about 1 cm^2 (Fig. 3.3). It is obvious that through this area the main charge transfer takes place, accompanied by intensive ion bombardment. In this case, the energy is transferred to cathode surface both due to the ions kinetic energy and due to their recharge [41].

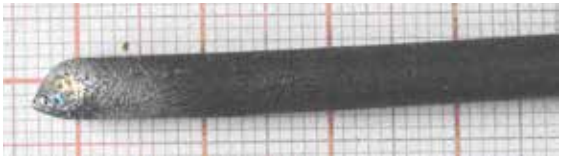

Figure 3.3 – The working part of the cathode made of steel ASTM 1020

Then, in a unit of time, the entire current-receiving region receives energy due to the kinetic energy of the ions:

$$g_k = I + U_c \alpha_k \tag{3.1}$$

and due to ions recharge:

$$g_n = I + (U_i - \varphi)\alpha_n, \tag{3.2}$$

where I_+ is the ion current which is about 10% of the total current; $U_c \cong 100 \quad V$ is cathode potential drop; $U_c \cong 14\ V$ is ionization potential of gases-vapours of the material of the dielectric chamber (N_2, H_2, CO_2, etc.); φ is the electron work function of the cathode material ($\varphi \cong 5-10\ V$); $\alpha_k \cong 1$ and $\alpha_n \cong 0.5$ are the corresponding accommodation coefficients [41].

Therefore, the considered section of the cathode surface during the discharge time $t_p \approx (0.5-1)$ ms will receive the energy equal to:

$$E = \int_0^{t_p} (g_n + g_n)dt = \int_0^{t_p} I_+ (U_C\, a_k + (U_i - \varphi)a_k)dl \tag{3.1}$$

Assuming that during the whole discharge the values of U_c, U_i, φ, α_k and α_n remain unchanged, then:

$$E = 0{,}1(U_C a_k + (U_i - \varphi)a_k)q, \tag{3.2}$$

where q is the charge that passed through the circuit during the discharge.

If we assume that the energy E is released instantly and locally on the metal surface, then according to [26] the mass (M) of the molten cathode material can be estimated as:

$$M = 0.31\frac{F}{cT_L}, \tag{3.3}$$

where c and T_L are the specific heat capacity and the melting point of the cathode material, accordingly.

Then the maximum possible value of specific erosion is:

$$\left[\frac{M}{q}\right]_{\max} = 0.031\frac{U_C a_k + (Ui - \varphi)a_k)}{cT_L}. \tag{3.4}$$

The calculation by expression (6) for a steel (ASTM 1020) cathode (c = =462 J/(kg · K), T_L = 1663 K) gives the value of the maximum possible specific erosion equal to $6.1 \cdot 10^{-6}$ kg/C, which is close to the value of erosion determined empirically (Table 3.1). These results show that the molten cathode material is almost completely carried away by the plasma from the central electrode. Some difference may be due to the peculiarities of the processes of formation of droplets and their evacuation by gas flow.

The following facts indicate the possibility of droplet formation in a pulsed discharge. First, the thin molten layer has a thickness h, which can be estimated from the melting area (Sliq):

$$h = \frac{M}{\rho_M S_{liq}} \approx \frac{\left[\frac{M}{q}\right]_{\max}}{\rho_M S_{liq}} q, \tag{3.5}$$

where ρ_M is the melt density.

For example, for typical operation modes of EAPA (C_{SE} = 1.5 mF, U_o = =4 kV, q = 6 C) using a steel cathode (ρ_M = 7850 kg/m^3) with a melting area characteristic for EAPU, equal to about 10^{-4} m^2, we have h ≈ 5 · 10–5 m.

The formation of a drop begins with the formation of a protrusion on the liquid surface (the radius of which, for simplicity, will be considered equal to the thickness of the molten layer). Then it is necessary that the pressure drop of the gas at the free end of the cathode and the melt boundary farthest from it should be comparable with the Laplace pressure:

$$\Delta p_1 \geq \frac{\sigma}{h}, \tag{3.6}$$

where σ is the surface tension coefficient of liquid metal (for steel $\sigma \approx 1.8\ N/m$).

Then, for steel cathode:

$$\Delta p_1 \geq \frac{\sigma}{h} = \frac{1.8}{5 \cdot 10^{-5}} = 3.6 \cdot 10^4 \text{ (Pa)}. \tag{3.7}$$

Assume that the pressure drop along the cathode is uniform, i.e.:

$$\frac{\Delta p_1}{\Delta p_K} = \frac{\Delta l_1}{\Delta l_K}, \tag{3.8}$$

where Δp_1 and Δp_K are pressure drop along the melt and along the entire cathode, respectively; Δl_1 and Δl_K are the length of the molten area (~ 10 mm) and the length of the entire central electrode (~ 300 mm), respectively.

When condition (3.8) is fulfilled, the pressure inside the chamber during the formation of droplets may differ from the atmospheric one by a value of about 10 atm. This value does not contradict the data given in [40].

As shown in [42], droplets with a diameter of d_D= 1.89 h are formed from a flux of a diameter h. Consequently, the diameter of the droplets ejected from the EAPU can reach 100 μm.

Drop movement in the chamber of the accelerator. The ejection of droplets from the EAPA chamber (Fig. 3.1) is provided by the outflowing gas flow. It is obvious that the gas flow is directed along the axis of the accelerator chamber. The movement of the liquid drop is provided by the gas pressure on its surface and gravity. It is easy to show that in this case the drop acceleration is much greater than the gravity acceleration. Consequently, gravity can be neglected. Then, not paying attention to the cause of pressure on the drop surface, its movement can be described by the Euler equation:

$$\rho_D \frac{dv}{dt} = -grad\ p\,, \tag{3.9}$$

where ρ_D is material density; v is the drop velocity.

The results of high-speed photography (see Fig. 3.1) show that the time Δt_{exit} of flight of a drop inside the accelerator chamber is almost an order of magnitude shorter than the time of ejection of all drops. Indeed, when the distance between the electrodes is l_{KA} = 60 mm, the value $\Delta t_{exit} \approx 2\,l_{KA}/v \approx$ $\approx 2 \cdot 10^{-2}$ s, which is an order of magnitude longer than the time of a high-current discharge, but significantly less than the duration of the ejection of all droplets. Then the out-flow of gas from EAPU during the evacuating one drop can be considered as quasistationary. Since the droplets trajectories coincide with the gas flow direction inside the chamber, the previous equation can be integrated along the trajectory. As a result, the Bernoulli equation is obtained:

$$\rho_D \frac{v^2}{2} = p_K - p_0\,, \tag{3.10}$$

where p_K is the gas pressure near the cathode tip; p_o is the atmospheric pressure at the edge of the chamber (the value of which is close to atmospheric).

Assuming that the velocity of steel drops ejecting from EAPU is approximately 5 m/s, taking into account (3.10), the pressure drop will be estimated as $\approx 8 \cdot 10^4$Pa. Note that the values of pressure drops Δp_1 and $(p_K - p_o)$, according to expressions (3.7) and (3.10), are comparable in magnitude.

Thus, the erosion of the central electrode (cathode) is due to an instantaneous (within less than 1 ms) energy release on the surface area of the electrode near its end. The amount of erosion is determined by the physical properties of the cathode material, by the properties of the plasma-forming gas and the amount of charge passing through the discharge gap. The main role is played by the cathode surface melting. Due to the presence of a

pressure gradient in EAPA chamber, the erosion droplets are formed, are torn away from cathode surface and are accelerated.

Collision of the drops with the substrate surface. Fig. 3.4 presents an image of steel droplets on a glass substrate obtained at U_o = 2 kV. The reduced charge voltage was chosen to obtain the solitary drops. As can be seen from (Fig. 3.4), when colliding with a substrate, the drop acquires near-disk shape. Let us estimate the geometrical dimensions of such disks, taking into account the transformation of drop energy.

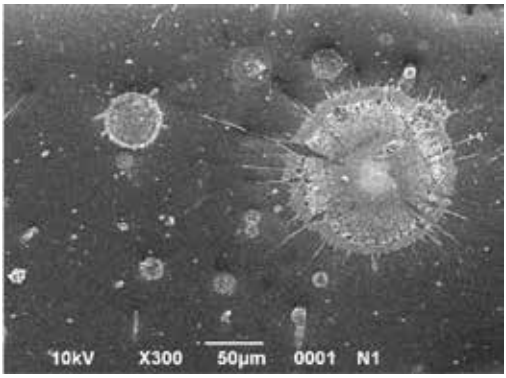

Figure 3.4 – Drops of ASTM 1020 steel on a glass substrate

The drop ejected from EAPA when approaching the substrate has kinetic energy (Ek) and surface potential energy (E_{surf}):

$$E_\kappa = \frac{\rho_D V_D v^2}{2} = \frac{\rho_D \pi d_D^3 v^2}{12},\ E_{surf} = \sigma S_D = \pi d_D^2 \sigma \qquad (3.11)$$

where V_D and S_D are the volume and surface area of the drop.

When colliding with an obstacle, the drop transformes into a stationary thin liquid disk of radius R_{DH} and thickness of $h_{DH} << R_{DH}$, whose surface energy is equal to $\pi R_{DH}^2 \sigma$. Eliminating viscosity from consideration, according to energy conservation law, we have:

$$\frac{1}{12}\rho_D \pi d_D^3 v^2 + \pi d_D^2 \sigma = \pi R_{DH}^2 \sigma, \qquad (3.12)$$

or

$$\frac{1}{2}\rho_D \frac{1}{6}\pi d_D^3 v^2 + 6\frac{1}{6}\pi d_D^3 \frac{\sigma}{d_D} = \pi R_{DH}^2 h_{DH} \frac{\sigma}{h_{DH}}. \qquad (3.13)$$

When dividing expression (15) by the drop volume $\left(V_D = \pi d_D^3 / 6 = \pi R_{DH}^2 h_{DH}\right)$ we obtain:

$$\frac{\rho_D v^2}{2} + 6\frac{\sigma}{d_D} = \frac{\sigma}{h_{DH}}, \tag{3.14}$$

from where the disk thickness is found as:

$$h_{DH} \approx \frac{d_D}{6 + \frac{d_D}{\sigma}\frac{\rho_D v}{2}} \tag{3.15}$$

It follows from (3.15) the thickness of the disk formed from a drop does not exceed 1/6 of the drop's diameter. So, taking into account the estimates (3.4), (3.7) and (3.11), the disk thickness is equal to:

$$h_{DH} \approx \frac{1.89 \cdot 5 \cdot 10^{-5}}{6 + \frac{5 \cdot 10^{-5}}{1.8} 8 \cdot 10^4} \approx 10^{-5}, (\text{m}). \tag{3.16}$$

and its radius:

$$R_{DH} = \sqrt{\frac{d_D^3}{6 h_{DH}}} \cdot 10^{-4}, \text{ (m)}. \tag{3.17}$$

The calculation according to (3.17) gives the values of the radius (≈ 100 μm) which was confirmed experimentally. As follows from the analysis of (Fig. 3.4), the radius of droplets frozen on a glass surface varies from 10 μm to 145 μm, which is close to calculated value.

Drop cooling on the substrate. For further consideration, the value of time interval Δt_{exit} between drop separation and its exit from the EAPA chamber is of interest. When the distance between the electrodes (l_{KA}) is 60 mm, the Δt_{exit} value is an order of magnitude longer than the time of a high-current discharge. Consequently, the effect of the plasma flow on the substrate and the processes occurring during the deposition of droplets on the substrate are separated in time. At the initial moment, the plasma flow expires from the EAPA, encountering an obstacle (substrate); at the second stage microdroplets are injected from the EAPA, falling on the substrate surface.

When a plasma flux collides with an obstacle (sample), the high-temperature gas causes ultra-fast heating of the surface. In a previously published paper [28], a method for calculating the thermal field in a steel sample

heated by EAPA plasma pulse was presented. According to the calculations, with a heat flux density (q_o) equal to 1.75 · 109 W/m^2, the metallic sample can melt to a depth of 10 μm. In addition to melting, the surface of the sample is also subjected to a force due to the dynamic pressure p_D, which is comparable in magnitude to the pressure in EAPA chamber (i.e., $p_D \sim 10^6$ Pa). Then, taking into account the justification of the formula (3.8), we conclude that the sample surface can be covered with a molten layer of thickness.

$$h_{kp} \approx \frac{\sigma}{p_D} = \frac{1.8}{10^6} \approx 2 \cdot 10^{-6} \text{ (m)}. \qquad (3.18)$$

The remaining amount of molten steel will be removed by the gas flow from the sample surface. Therefore, for determination of the temperature field at the moment of drops collision with the sample surface, comparable to Δt_{exit} (~ 2 · 10^{-2} s), the most interesting is the mode of EAPA with q_o = 1.75 · 10^9 W/m^2. At this mode the melting point is reached only in near-surface layer of the sample. The results of such calculations (according to [28]) are shown in (Fig. 3.5). It can be seen that 10 ms after the discharge, the temperature of the surface layers of the sample to a depth of ~ 100 μm can be considered constant. Thus, when a flying drop meets the sample surface, the temperature gradient is practically absent in the latter. This sets the initial conditions for calculating the velocity of erosion drop which are cooled on the substrate surface.

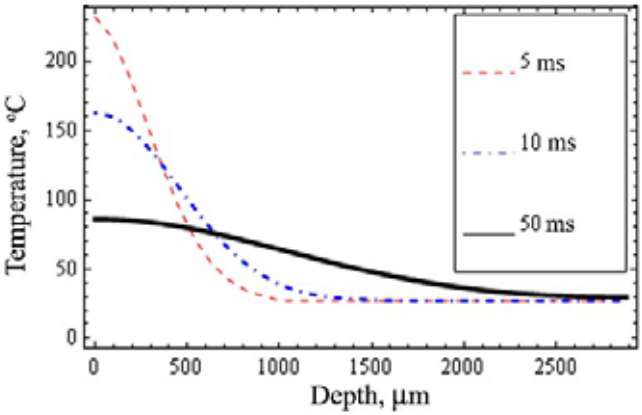

Figure 3.5 – Temperature fields in the sample bulk at time moment of 5, 10, and 50 ms after exposure to plasma flux at q_o = 1.75 · 10^9 W/m^2

As was shown above, the thickness of a disk formed from a drop is much smaller than its radius. Then the task of drop cooling is one-dimensional task of cooling a thin layer on a substrate, which is solved using the equations (3.15–3.17). The initial conditions are given by the temperature distribution over the sample depth:

$$T(x,0)=\begin{cases}T_1, & 0<x<h_{DH},\\ T_2, & x>h_{DH},\end{cases} \tag{3.19}$$

where T_1 is the drop temperature, which exceeds the material melting point ($T_1 > T_{liq}$); T_2 is the temperature of the substrate, previously heated by the plasma flux.

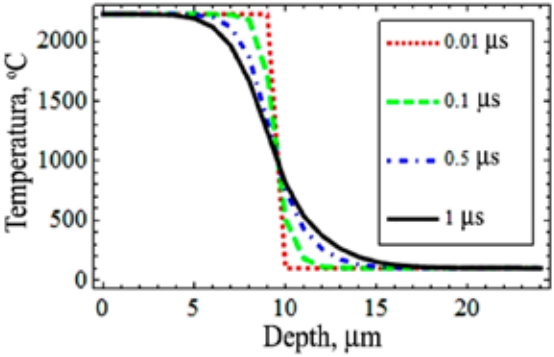

Figure 3.6 – Temperature field in sample bulk and inside the cooling drop after its deposition

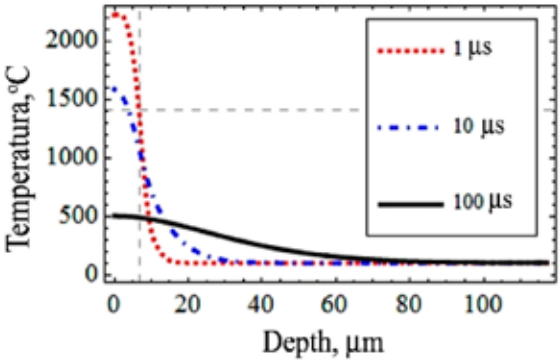

Figure 3.7 – Temperature fields in the sample bulk and inside the cooling drop at time moment of 1, 10 and 100 (μs)

The solution of this task by the finite differences method according to an explicit scheme is presented in (Fig. 3.6) and (Fig. 3.7). The calculations were carried out at the following values: T_1 = 2500 K, T_2 = 373 K, h_{DH} = =10 μm. The cathode and sample material was steel 75 Mn, for which ρ = =7830 kg/m^3, c = 420 J/(kg·K), Λ = 140 J/kg, $\lambda_L = 24\ W \cdot m^{-1} \cdot K^{-1}$ and λ_S = $=48\ W \cdot m^{-1} \cdot K^{-1}$ [43].

As can be seen from these figures, the cooling rate of the droplet material reaches value of 10^8 K/s, which is an order of magnitude greater than the rate of temperature change in the sample surface when exposed to a plasma flux. This creates the condition for the "freezing" the drop, when the crystalliza-tion of the coating proceeds by a non-equilibrium mechanism with the formation of a solid solution supersaturated with al-loying and impurity elements [44, 45]. Such a single-phase (austenitic) coating structure is formed when using the cathode of heterogeneous materials as T1 tool steel [14] or high-chromium cast iron [44]. These materials both contain large amount of carbide particles in the initial state (before PPT).

The evaporation of fibrobakelite from the inner wall of the tube increases the concentration of carbon in the plasma flux, Carbon is transferred to the substrate and enriches the crystallizing coating material. This significantly affects the microstructure of the coating, in particular, high-carbon acicu-lar martensite is formed, the amount of carbides and the frac-tion of retained austenite increase, the stoichiometry of car-bide inclusions changes, etc. [3, 14, 44]. Atmospheric nitro-gen, which is similar to carbon in its influence on structure, can also affect it. As for the oxidation of the coating in contact with atmospheric oxygen, than the previous EDS studies of the high-chromium (28% Cr) coating did not reveal any signifi-cant enrichment of it with oxygen [3, 44]. As an example, (Fig. 3.8), a presents the microstructure of the coating obtained using the EAPA on substrate of 75Mn steel using a cathode made of high-chromium (28% Cr) cast iron. After 10 pulses, a coating of 150–170 μm thick formed on the surface. It consists of aus-tenite oversaturated with carbon and chromium with the mi-crohardness not exceeding 650 HV. The increasing coating microhardness and tribological characteristics requires an ad-ditional heat treatment to decompose the supersaturated solid solution with hardening phases precipitations and shear $\gamma Fe \rightarrow \alpha Fe$ phase transformation [46, 47]. In this case, the post-plasma holding at 950 °C for 2 hours led to the precipitation of a large number of carbides

$(Cr, Fe)_7C_3$ in the coating with sub-sequent doubled increase in coating microhardness.

The conclusions on the Chapter were drawn as follows:

During high-current discharge a two-stage expiration of the plasma products from EAPA occurs. In the first stage, a high-temperature gas expires within 1 ms, in the second stage microdroplets formed due to erosion of electrodes are injected at a speed of 5 m/s. The specific erosion of the EAPA cathode increases with a decrease in material melting temperature, reaching 25 mg/C for aluminum. Erosive transfer of the cathode material ensures the formation of a coating on the substrate. Upon collision with the substrate surface, the erosion drops acquire near-disks shape with a radius of up to 100 microns. The rate of drops cooling on a metal substrate reaches 10^8 K/s, which forms a coating with the structure of a supersaturated solid solution.

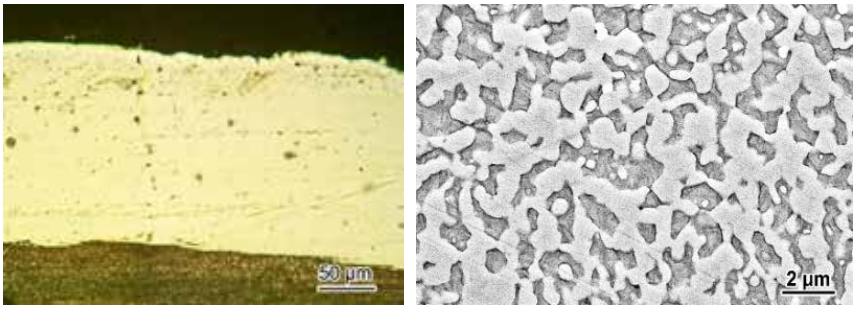

a) b)

Figure 3.8 – Microstructure of the coating obtained on 75Mn steel using a cast iron (28% Cr) cathode: (a) after PPT; (b) after PPT and holding at 950 °C

The content of the Chapter is adopted from Plasma coating formation by the deposition of cathode material eroded through high-current pulsed discharge / Yu. G. Chabak, V. I. Fedun, V. G. Efremenko T. V. Pastukhova, B. V. Efremenko // Problems of Atomic Science and Technology: Series Plasma Physics.– 2019.– Vol. 123.– P. 167–174. https://doi.org/10.46813/2019–123–167

Chapter 4. COMPARATIVE ANALYSIS OF THE MICROSTRUCTURAL FEATURES OF 28 wt% Cr-CAST IRON FABRICATED BY PULSED PLASMA DEPOSITION AND CONVENTIONAL CASTING

High chromium cast irons (HCCIs) are commonly used for parts and components requiring excellent abrasion resistance [48]. However, HCCIs possess poor fracture toughness, which considerably limits their application potential under repetitive impacts or cyclic loading. HCCIs are complex microcomposite systems comprising hard carbide phases and a soft metallic matrix. The eutectic carbide (EC) morphology is considered to play a key role in the wear resistance and mechanical properties of HCCIs. Conventional foundry technologies lead to the formation of coarse microstructural constituents (eutectic carbides and matrix dendrites) that negatively affect the toughness and impact resistance of HCCIs. Numerous methods of morphological modification by Ti, V, Nb, Al, B, Rare Earth inoculation have been employed with the aim to improve the fracture resistance of HCCIs [49–53]. Furthermore, melt treatment techniques, such as vibration, ultrasonic waves and electric current impulses are reported [51, 53] to be effective ways of reducing the eutectic carbide particle size.

A considerable structural refinement of HCCIs could be obtained by means of accelerated crystallization by a spray-forming technology [54, 55]. Matsuo et al [56] showed that spray-formed 14–20 wt.% Cr-HCCI comprises eutectic carbide particles of substantially reduced size (by 10 times) in comparison with conventionally cast HCCIs; as a result, increased bulk hardness and pin-on-disc wear resistance were attained. Hanlon et al. [57] found that spray-formed 18 wt.% Cr cast iron has better forging property than its conventionally cast counterpart one due to the presence of fine discrete M_7C_3 particles that allowed matrix flow around them during forging. The same authors [58] reported that the high temperature wear performance of spray-cast HCCIs is considerably better than that of conventionally fabricated castings. According to Guo et al. [59], spray-formed HCCI has higher fracture resistance as compared to sand-cast materials.

A high crystallization rate (10^7–10^{10} K/s) [60] can be achieved by pulsed plasma deposition (PPD), which ensures significant microstructure refine-

ment with low segregation and supersaturated metastable phase formation [61]. Different PPD techniques are described in [3, 11, 60, 61]. In recently published works [2, 14, 62], a PPD technique employing an electrothermal axial plasma accelerator (EAPA) for surface modification and coating deposition has been described. EAPA allows to deposit the cathode material, which evaporates and melts under arc discharge inside the accelerator. The cathode constituents (ions, atoms, microdroplets) are transferred by plasma flux followed by superfast crystallization on the surface. Information about microstructural features of PPD-fabricated alloys (including HCCIs) is still limited. The objective of the present study is a comparative analysis of the microstructure, as well as evaluation of microhardness and abrasive wear resistance, of a 28 wt.% Cr-cast iron prepared in a conventional foundry manner and using EAPA pulsed plasma deposition.

Experimental procedure. The studied material was a 28 wt.%-Cr cast iron containing (wt.%): 2.34 C; 27.39 Cr; 3.13 Mn; 1.26 Si; 0.20 Ti, Fe – balance. An appropriate mixture of pig cast iron, steel scrap, and Fe-Mn, Fe-Cr, Fe-Si, and Fe-Ti master alloys were melted in an induction furnace (holding temperature: 1400 °C). The melt was cast into CO_2-treated sand molds having the shape of: a) rods of 25 × 25 mm cross-section and 250 mm length and b) rods of 5 mm diameter and 150 mm length.

Square cross-section rods were used for the microstructural evaluation of conventionally cast HCCI. The specimens were cut from the rod and subjected to the following heat treatment (HT): a) isothermal holding (950 °C, 2 h, oil quenching), b) tempering (200 °C, 2 h). Circle cross-section rods were used in as-cast state as EAPA cathodes for pulsed plasma deposition. PPD was carried by an axial electro-thermal plasma accelerator. The construction details and operational principles of EAPA have analytically been described in [2, 3, 14, 62]. The operation parameters employed were: Cathode material: 28 wt.% Cr HCCI, voltage: 4.0 kV, arc discharge current: 10 kA, atmospheric pressure, working gas: air, working distance (EAPA edge to substrate): 50 mm, time interval between pulses: 15 s, coating deposition in ten plasma pulses.

As a substrate to the PPD HCCI coating, a 15 wt.% Cr-cast iron was employed. Its nominal chemical composition was (wt.%): 2.60 C; 14.50 Cr; 3.96 Mn; 1.38 Si; 0.10 Ti; 0.10 V; 0.21 Ni, Fe – balance. The substrate was sand-cast, as described in the first paragraph. Specimens of dimensions of 10 × 10 × 25 mm were cut from the square cross-section rods and annealed at 650 °C for 20 h to attain a stabilized pearlitic matrix [47]. Subsequently, grinding (Ra = 0.2 μm) was conducted, in order to remove the oxidized

outer layer (~ 0.5 mm). The pulsed plasma deposited area was 10 × 25 mm. The PPD specimens were subjected to post-plasma HT at 950 °C for 2 h with subsequent oil quenching.

As-deposited coating was subjected to post-heat treatment that was a holding in dry air atmosphere at 950 °C with consequential cooling in oil (20 °C). The holding temperature was selected according to [44, 63] as optimal for destabilization processes in high-Cr cast irons. The holding duration was 5 min, 15 min, 30 min, 60 min and 120 min. To compare bulk microstructure with coating microstructure, as-cast iron was subjected to correspondent heat treatment: holding at 950 °C for 120 mm with cooling in oil.

Characterization of conventionally cast 28 wt.%-Cr iron. Fig. 4.1 shows the microstructure of the conventionally cast 28 wt.%-Cr iron (HHCI-1). As can be seen, HCCI-1 is a hypoeutectic alloy comprising matrix pre-eutectic dendrites and eutectic carbide (EC)/Fe-rich solid solution microconstituent. The secondary dendrite arm spacing was measured as 14.7 ± 0.9 μm. The volume fraction of the eutectic carbide phase was calculated as 29.9 ± 0.9 vol.%.

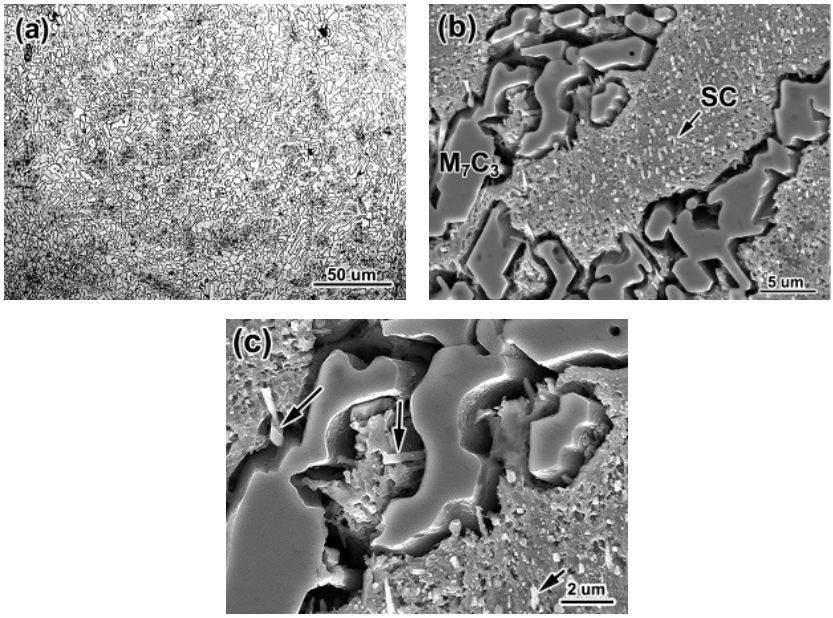

Figure 4.1 – The microstructure of HCCI-1 ((a) OM-image; (b, c) SEM-images. SC: secondary carbide particles; the arrows point at SC particles)

SEM observation at higher magnification (Fig. 4.1, b, c) revealed that eutectic carbides have the morphological features of Cr-based carbide M_7C_3, i.e. coalesced hexagonal-shaped rods with center protrusion parallel to the {0110} crystal plane [64]. The width of the carbide particles-agglomerates varies in the range of 2.0–3.0 μm. Apart from eutectic carbides, numerous grainy and rod-shaped secondary carbides (SC) (shown by arrows in Fig. 4.1, b and c) are seen to uniformly be distributed inside the dendrites, as well inside the matrix of the eutectic carbide colonies. The SC particles are much smaller than the EC particles (agglomerates); their cross-section size was estimated as 0.17 ± 0.02 μm. The average bulk hardness of HCCI-1 was measured as 57.5 ± 0.7 HRC.

The X-ray diffractogram of HCCI-1 is given in (Fig. 4.2). The XRD-pattern shows that HCCI-1 comprises martensite, austenite and carbide phase. According to the peak intensities martensite is the main matrix phase. The martensitic nature is revealed by the shift of the (110) Fe_α peak to smaller diffraction angles relatively to the α-ferrite peak; this shift indicates lattice distortion induced by displacive transformation.

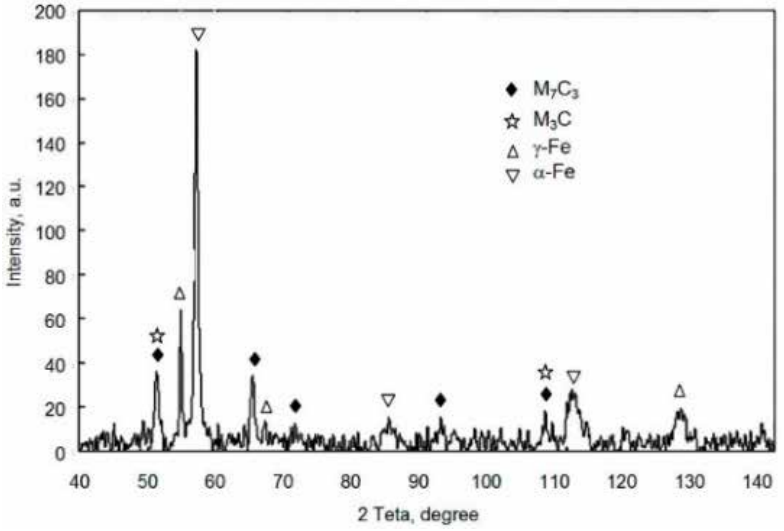

Figure 4.2 – XRD-pattern of HCCI-1; α-Fe (6–0696), γ-Fe (4–0829), $(Cr, Fe)_7C_3$ (5–0720), Fe_3C (35–0772)

The predominantly martensitic nature of the matrix of HCCI-1 is the outcome of the heat treatment, namely: secondary carbide precipitation

at 950 °C followed by "austenite → martensite" transformation upon oil quenching [33]. Several reflections correspond to M_7C_3 confirming the SEM observations. Two peaks at $2\theta = 51°$ and $2\theta = 107°$ may be assigned to both M_7C_3 and M_3C carbides. Since there is no reflection uniquely assigned to carbide M_3C, its presence could not be confirmed.

Table 4.1 – Chemical composition (wt.%) of the dendrites and eutectic carbides in conventionally cast 28 wt.%-Cr iron, as determined by EDX quantitative analysis

Phase	C	O	Si	Cr	Mn	Fe
Dendrite	3.2±1.3	1.1±0.3	1.5±0.2	20.5±1.2	3.1±0.2	70.6±2.4
Eutectic carbide	9.8±0.2	–	–	64.6±1.0	2.3±0.1	23.4±1.2

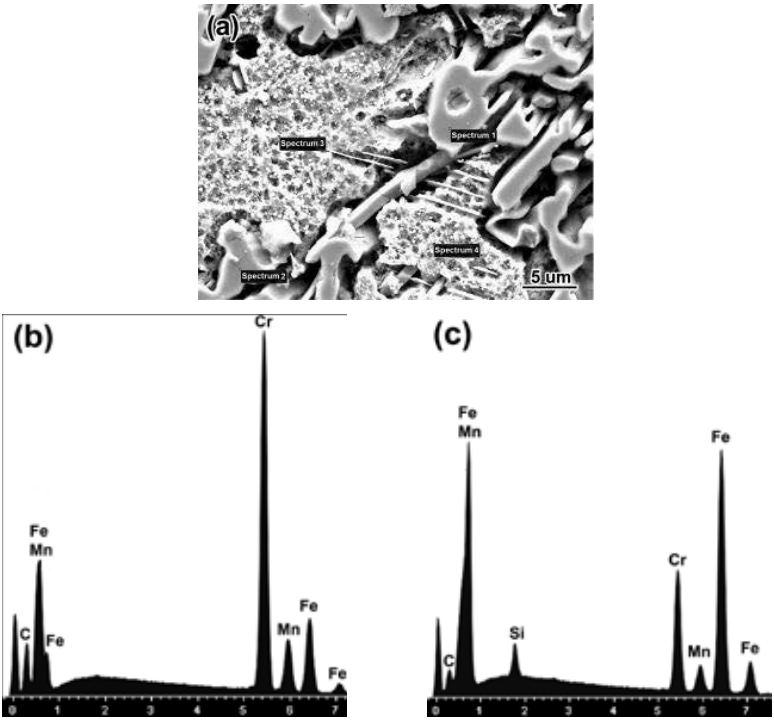

Figure 4.3 – (a) SEM micrograph of HCCI-1 and representative EDX point spectra from (b) eutectic carbide M_7C_3 and (c) the dendrite

The phase chemical composition of HCCI-1 is given in (Table 4.1). The main alloying element of the eutectic carbides is chromium (about 65 wt.%), also shown in the EDX-spectrum of (Fig. 4.3, b). Additionally, ECs are alloyed with smaller amounts of carbide forming elements, such as iron and manganese. Unlike the ECs, Fe is the main alloying metal of the dendrites, whereas silicon and manganese are present as well (Fig. 4.3, c).

The chromium content in the dendrites is three times lower compared with that of the E, as Cs. Here it should be noted that the EDX analyses of the dendrites include both the matrix (martensite/austenite) and the secondary carbides. Since the secondary carbide particles are very fine and uniformly distributed in the metallic matrix, the distances between the SC particles are less than the spatial resolution of the EDX analysis. Therefore, the secondary carbide particles were inevitably involved in the point EDX-area significantly affecting the measured values. Hence, the real Cr content in the matrix is expected to be lower and the Si content higher than those presented in (Table 4.1).

Characterization of pulsed plasma deposited 28 wt.%-Cr iron.
28 wt.%-Cr cast iron was used as a working electrode (cathode) for the pulsed plasma deposition. PPD resulted in the formation of a high-chromium coating of thickness of about 100 μm which significantly differs from bulk cast iron with its microstructure (no eutectic carbides characteristic for bulk 28 wt.% Cr cast iron were found in it). As demonstrated in (Fig. 4.), a, as-deposited coating performs "frozen" homogeneous structure bieing smoothly bonded with the substrate. After prolonged nital etching (about 5 min) the coating gained the layered "dark contrast-light contrast" pattern, illustrated in (Fig. 4 b). No eutectic carbides were discerned in the as-deposited coating. The SEM observation revealed that the dark bands contain a fine carbide network surrounding small grains of 0.5–2 μm in diameter (Fig. 4.4, c). It is assumed that the dark bands are heat affected zones which underwent intergranular carbide precipitation induced by the plasma heat pulses [3]. The microhardness of as-deposited HCCI-2 had an unchanged character throughout the entire section of the coating within the range of 630–750 $HV_{0.05}$ with a mean value of 650 $HV_{0.05}$ (Fig. 4.5). Based on the microstructural examination and the microhardness level, it is suggested that the as-deposited microstructure of HCCI-2 is that of.

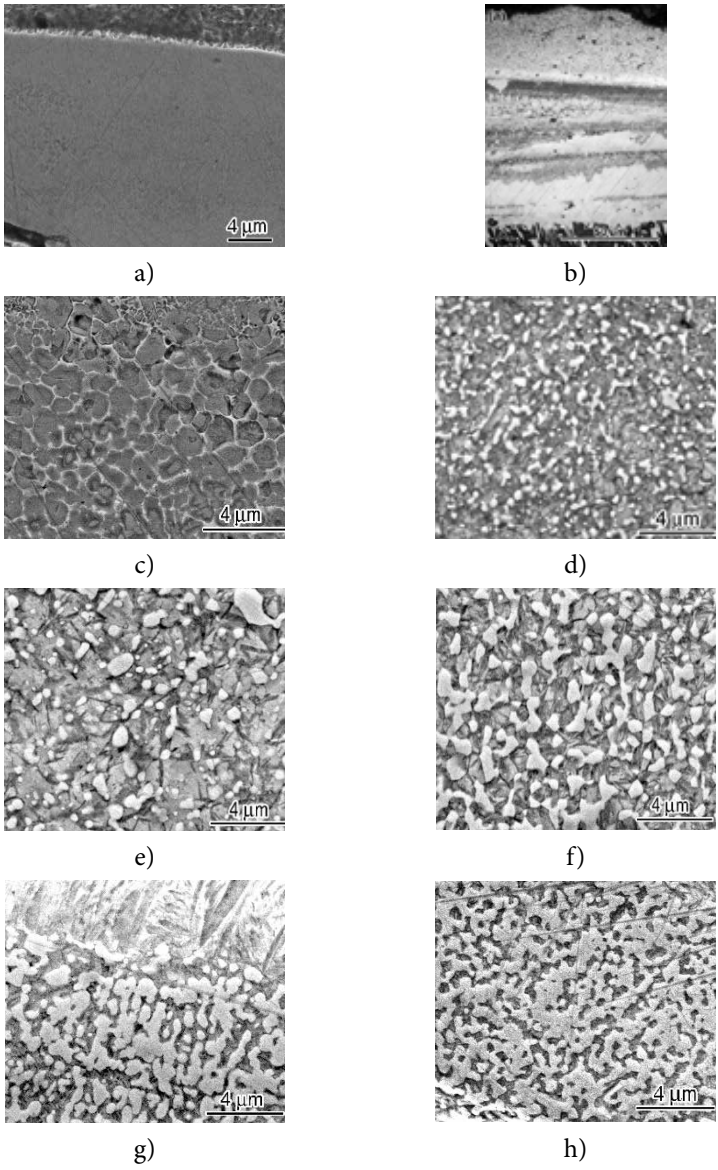

Figure 4.4 – (a, b) Microstructure of as-deposited coating, and after heat treatment with holding duration of (d) 5 min, (e) 15 min, (f) 30 min, (g) 60 min and (h) 120 min austenite/martensite mixture with a fine carbide network in heat affected layers

The post-heat treatment expectedly changed the coating microstructure. Even after initial holding (5 min) at 950 °C the precipitates of grainy fine carbides of 0.05–0.07 μm diameter were revealed in the coating to be associated with grain boundaries (Fig. 4.4, d). Borderline carbide agglomerations of 0.15–0.40 μm width were found as well. Holding for 15 min led to continuation of carbide precipitation with simultaneous coagulation resulted in carbide coarsening (up to 1.3 μm). As seen from Fig. 4e, carbide coarsening allowed to reveal the matrix structure which is acicular martensite with ultrafine needles (less than 2 μm in length). The holding for 30 min caused the formation of coarse blocky-shaped carbides (tending to merge in the network) with very few fine carbides (Fig. 4.4, f); the martensite needles are clearly distinguished in the matrix grains as well. Increasing the holding duration to 60 min resulted in progressive increase in carbide volume fraction, manifesting in thickening of carbide network (Fig. 4.4, g). This process lasted for 120 min leading to formation of bulky continuous carbide network enclosing the matrix grains (Fig. 4.4, h).

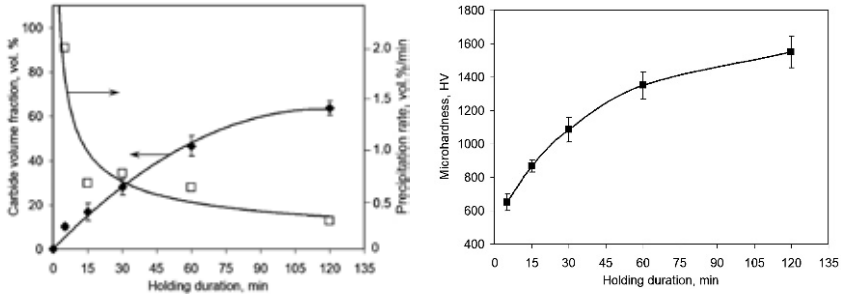

a) b)

Figure 4.5 – Effect of holding duration: (a) carbide volume fraction and precipitation rate; (b) coating microhardness

The mean precipitate size was estimated as 0.64 ± 0.06 μm. Apart from the blocky carbides, a small amount of fine roundish precipitates of mean diameter of 0.14 ± 0.02 μm were found inside the Fe-alloy grains. The total volume fraction of bulky and roundish precipitates was measured as 57.2 ± 4 vol%. It is noteworthy that the HCCI-2 microstructure had no signs of dendrite pattern, thus SDAS could not be measured according to routine procedure. As an analogue of SDAS, the mean distance between the centers of adjoined Fe-alloy grains (i.e. separated by carbide particles) was measured. It was estimated as

1.29 ± 0.13 μm, which is more than 10 times lower as compared to the SDAS of HCCI-1 (14.7 ±. 0.9 μm).

As follows from (Fig. 4.5, a), with holding duration increase the carbide volume fraction gradually increases while precipitation rate decreases. After holding for 5–15 mm the amount of carbide was 11.1–16.7 vol.% which corresponds to the highest precipitation rate. This carbide amount was almost doubled after 30 min holding (up to 28.1 vol.%). After 60 min holding the volume fraction of carbide increased to an greater extent – to 46.6 vol.%. With further holding the precipitation rate significantly decreases while carbide volume fraction reached 63.7 vol.%. The kinetics of carbide precipitation and the precipitation rate (PR) were precisely approximated by the following equations:

$$\text{CVF (vol.\%)} = -0.004 \cdot \tau^2 + 1.06 \cdot \tau \qquad R^2 = 0.99 \qquad (4.1)$$

$$\text{PR (vol.\%/min)} = 165.66 \cdot \tau^{-0.49} \qquad R^2 = 0.85 \qquad (4.2)$$

where τ is the holding duration (min).

As carbide amount increased, coating microhardness gradually increased with holding duration from 650 ± 47 HV (as-deposited state) to 1553 ± 92 HV after holding for 120 min (Fig. 4.5, b). The microhardness profile closely fits to CVF profile reflecting the tight connection with carbide precipitation and coating properties.

XRD method was employed to determine the phase constituents of the coating (Fig. 4.6). In as-deposited state the coating microstructure consists of alpha-phase (BCC) and gamma-phase (FCC) with a predominance of the latter (71.6 vol.%) (Table 4.2). Negligible amount cementite carbide (M_3C) existed in the structure as well according to weak line (130) M_3C. HT with holding for 30 min almost had no effect on XRD pattern shape. XRD pattern for 60 min reflects the significant phase transformation manifesting in appearance of strong diffraction peaks for carbide M_7C_3. After 120 min holding M_7C_3 peaks were supplemented with weak peaks of carbide $M_{23}C_6$. As assumed by the intensity of the respective peaks, the carbide phase in heat-treated coating is a mixture of hexagonal M_7C_3 carbide and cubic $M_{23}C_6$ carbide with prevalence of M_7C_3.

Table 4.2 – Variation of austenite volume fraction in matrix depending heat treatment duration

Heat treatment duration, min	as-deposited	30	60	120
Austenite volume fraction, vol.%	71.6	70.3	26.9	11.5

Apart of carbide precipitation, HT drastically changed the phase status of metallic matrix. The transformation of matrix can be tracked by Fig. 4.6, b showing the variation of intensity for the strongest peaks gamma-phase (111) and alpha-phase (110). It can be concluded that with holding duration increase "gamma-phase/alpha-phase" ratio changed in favour of the alpha-phase. Thus, austenite volume fraction was decreased to 26.9 vol.% and 11.5 vol.% after holding for 60 min and 120 min accordingly.

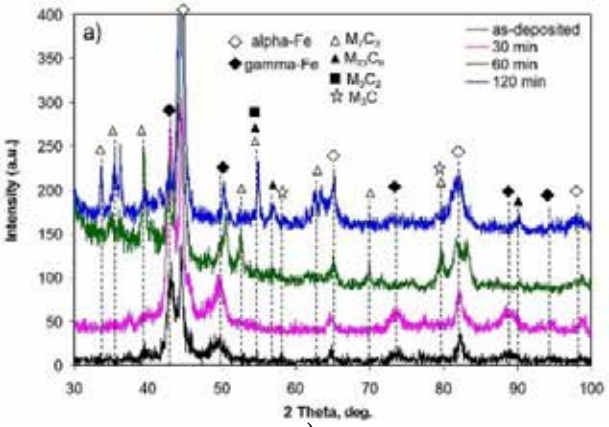

a)

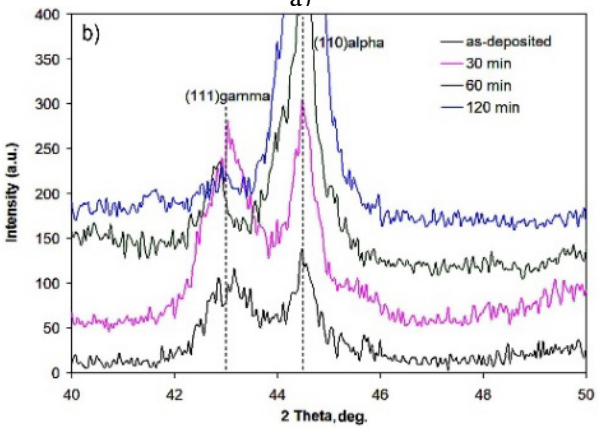

b)

Figure 4.6 – XRD patterns of as-deposited and heat treated coatings (using the data-bases: alpha-phase (6–0696), gamma-phase (4–0829), $(Cr, Fe)_7C_3$ (5–0720), Cr_3C_2 (5–0677), Fe_3C (35–0772), $Cr_{23}C_6$ (35–0783)) (a) total studied range of 2 Theta angle; (b) 2 Theta angle range for (111) gamma-phase and (110) alpha-phase

The XRD study was supplemented by EDX quantitative chemical analysis of the main observed phases. The results are listed in (Table 4.3).

Table 4.3 – Phase chemical composition (wt.%) of pulsed-plasma deposited 28 wt.%-Cr iron, determined by EDX

Phase	C	O	Si	Cr	Mn	Fe
As-deposited metal grains	5.4±0.6	0.5±0.2	1.7±0.2	27.3±0.2	1.6±0.1	63.5±1.1
Blocky carbide (HT)	9.5±0.4	0.6±0.2	1.2±0.1	27.5±1.4	2.0±0.3	59.3±1.8
Fe-alloy grains (HT)	6.8±0.5	0.8±0.2	1.8±0.2	16.9±1.5	1.1±0.1	72.6±0.9

According to the data obtained, the chromium and silicon concentrations in the as-deposited metal phase of the coating are close to the total chromium content of the cathode material, while the manganese content is almost half the Mn content of the HCCI-1 dendrites (A typical field of view and representative point EDX spectrum are presented in (Fig. 4.7, a and 4.7, b). In the HT coating, where blocky carbides have formed occupying a large volume fraction, Mn is distributed in both the Fe-alloy phase and carbides, whilst prevailing in the latter. The chromium concentration in the blocky carbides is notably lower than that of the eutectic carbide phase in HCCI-1 (Tables 4.2, 4.3) (A typical field of view and representative point EDX spectrum are given in Fig. 4.7, a, c). The HT-matrix conversely was found to be Cr-impoverished containing about 17 wt % Cr (compare the spectra of Figs. 4.7, d and 4.7, e). The above result is considered an artefact of the EDX quantitative analysis of the matrix of the as-deposited coating. Fig. 4.4, a and Fig. 4.7, a show that the majority of the (as-deposited) metal grains have diameters less or close to 1 μm. As such, (since the EDX spatial resolution for high atomic number elements is 0.2 to 1 μm^3 for voltage in the range of 15 to 25 kV [65]), there is a high probability that the analysis of Cr in the fine metal grains of the as-deposited coating is exaggerated as it is affected by the surrounding Cr-rich carbide network.

Similarly, the unexpectedly low Cr content of the blocky carbides (the minimum Cr content in M_7C_3 is reported as 45 wt.% [66]) is likely to be affected by the adjacent Fe-alloy grains. The latter is confirmed by the detection of 1.2 wt. % Si in the blocky carbide phase, while silicon is known to be negligibly dissolved in the carbide phases, specifically in M_7C_3 [67].

The obtained results were compared with the data of thermodynamic modelling (Fig. 4.8). Equilibrium crystallization of carbides in 28 wt% Cr cast starts from eutectic transformation "Liquid → Austenite + M_7C_3" at 1280 °C. At further cooling to 870 °C carbide M_7C_3 precipitates from austenite. In a temperature range below 870 °C carbide transition M_7C_3 → → $M_{23}C_6$ takes place.

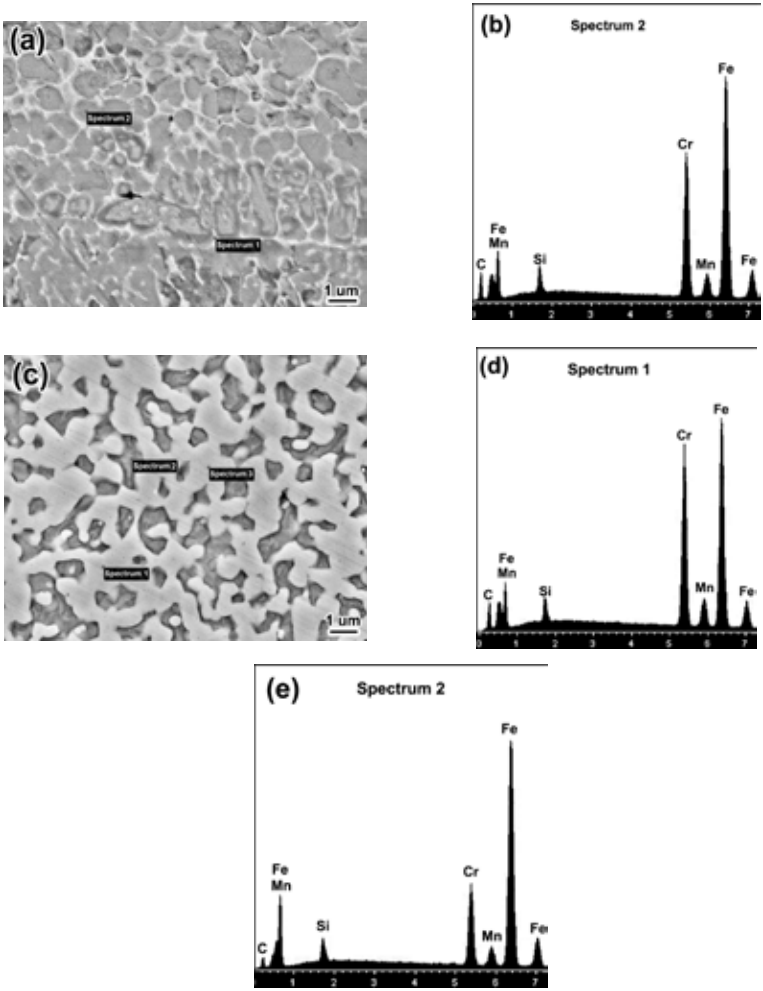

Figure 4.7 – Indicative points and corresponding EDX point spectra (a, b) as-deposited HCCI-2; (c, d, e) heat-treated HCCI-2; (d) blocky carbide; (e) Fe-alloy grain

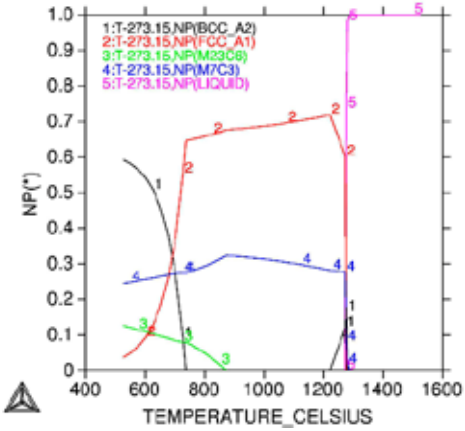

Figure 4.8 – Mass fractions for alloy 28 wt% Cr cast iron as a function of temperature ("Thermo-Calc Sofware" modelling)

In a temperature range below 600 °C the equilibrium microstructure consists of alpha-phase (BCC), carbides M_7C_3, $M_{23}C_6$ and a minor (less than 5 mass.%) amount of austenite. Because of superfast crystallization, the "solute trapping" effect occurs, thus almost all carbon and carbide-forming elements (Cr, Mn) are retained in austenite without eutectic reaction. The "frozen" coating gained a non-equilibrium microstructure consisting of oversaturated austenite and alpha-based solid solution (with a minor amount of transition carbide M_3C as well). Further formation of carbide M_7C_3 proceeds under HT through the solid-state reaction "Austenite (enriched) → M_7C_3 + Austenite (depleted)". It is worth noting that the carbide was nucleated along the grain boundaries with further growth as bulky network. This manifests that M_7C_3 precipitation was controlled by grain boundary diffusion of Cr atoms. Carbide M_7C_3 was nucleated on the interface of the cementite network appeared after deposition (Fig. 4.1, c) therefore in-situ transformation $M_3C \rightarrow M_7C_3$ occurred at earlier stage of heat treatment.

After holding for 30 min neither M_7C_3 nor M_3C were identified on XRD pattern, apparently because of carbides minor amount and due to the proximity of the strong line of carbide M_7C_3 to austenite line (111). Only after holding for 60 min carbide M_7C_3 was definitely revealed on XRD pattern due to the appearance of carbide M_7C_3 authentic lines. Holding for 120 min resulted the in appearance of the lines of carbide $M_{23}C_6$ meaning that formation of $M_{23}C_6$ requires prolonged holding since according to stoichiometry

this carbide has higher Cr content as compared with M_7C_3. As reported in [28, 68] the nucleation of $M_{23}C_6$ may process via in-situ transition $M_7C_3 \rightarrow$ $\rightarrow M_{23}C_6$ occurring on austenite/M_7C_3 interface.

After holding for 30 min neither M_7C_3 nor M_3C were indentified on XRD pattern, apparently because of carbides minor amount and due to the proximity of the strong line of carbide M_7C_3 to austenite line (111). Only after holding for 60 min carbide M_7C_3 was definitely revealed on XRD pattern due to appearance of carbide M_7C_3 authentic lines. Holding for 120 min resulted in appearance of the lines of carbide $M_{23}C_6$ meaning that formation of $M_{23}C_6$ requires prolonged holding since according to stoichiometry this carbide has higher Cr content as compared with M_7C_3. As reported in [28, 68] the nucleation of $M_{23}C_6$ may process via in-situ transition $M_7C_3 \rightarrow M_{23}C_6$ occurring on austenite/M_7C_3 interface.

The driven force of carbide precipitation is caused by the distortion of austenite lattice due to oversaturation with interstitial (C) and alloying (Cr, Mn) atoms. The highest precipitation rate corresponds to the beginning of holding when austenite saturation is maximal. It can be presumed that at this stage cementite carbides are formed first as more kinetically preferred process which does not require Cr atoms fluctuation. With holding duration increase Cr atoms diffusion promotes the formation of Cr atoms fluctuations necessary for nucleation of carbide M_7C_3 and further – carbide $M_{23}C_6$. Thus, the carbide precipitation in the coating may presumably include sequential carbide transformations $M_3C \rightarrow M_7C_3 \rightarrow M_{23}C_6$.

Kinetics of carbide precipitation is found to be gradually decelerating as austenite depletes with carbon and chromium [69]. This stimulates austenite to displacive phase $\gamma \rightarrow \alpha$ transformation which manifests in increase in Ms temperature [70]. Destabilized austenite transforms into martensite under cooling in oil, leading to predominantly martensitic matrix which is proven by acicular morphology of microstructure and intensive diffraction peaks of alpha-phase on XRD pattern. Appearance of hard martensite follows carbide precipitation leading to almost 2.5-fold increase in coating microhardness. It is noteworthy that microhardness profile coincides with CVF profile meaning the strong correlation between these two parameters.

Comparing the experimental results with "Thermo-Calc" modelling shows that heat-treated coating has almost the same phase constituents as predicted by thermodynamic calculations, i.e.: (a) alpha-phase (BCC) + M_7C_3 + $M_{23}C_6$ (equilibrium state); (b) alpha-phase (martensite, BCT) + + M_7C_3 + $M_{23}C_6$ + minor amount of retained austenite (post-heat treated

state). This means that post-heat treatment closely approached the coating microstructure to thermodynamically stable state. However, the real chromium content in carbide M_7C_3 considerably differs from equilibrium value. According to "Thermo-Calc" calculations carbide M_7C_3 should contain 62.1 wt.% Cr while EDX analyzing detected by 1.6 time less value (30.05 wt.% Cr). This discrepancy can be explained based on carbide volume fraction. Heat-treated coating posses 63.7 vol.% carbides in its structure which is almost two-folds as compared with bulk 28 wt.% Cr cast iron (29.9 vol.% [71]). This phenomenon is associated with erosion of inner wall of EAPA during the generation of plasma pulse [72, 73]. The material of the wall is a paper-reinforced bakelite $(C_6H_6O \cdot CH_2O)_n$ which is easily burnt and evaporated under high-current discharge. The released carbon atoms get into plasma flux being transferred to the coating. The increase in carbon content in melt results in formation of extra carbides. These extra carbides are not equilibrium for 28 wt.% Cr cast therefore they are depleted with chromium in favour of iron. Increase in carbide volume fraction due to plasma-induced carbon enrichment can be beneficial for the coating wear resistance [74]. It should be noted that surface oxidation on the coating surface was not pronounced during post-heat treatment. In fact, not any signs of surface oxidation were observed by SEM (Fig. 4.9). Such a good oxidation behavior is attributed to the high amount of chromium in the deposited layer, resulting in the formation of a thin protective Cr_2O_3 scale [75].

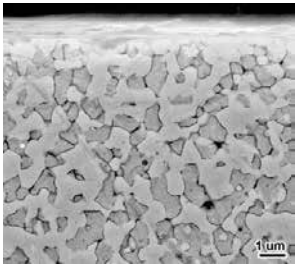

Figure 4.9 – The microstructure of the coating by the free surface after post heat treatment

Figure 4.10 illustrates the microstructure of the substrate to HCCI-2 coating transition zone. As seen in (Fig. 4.9, a (secondary electron (SE) mode), there is no clear boundary line implying strong metallurgical bonding between the coating and the substrate. The back scattered electron (BSE) micrograph of Fig. 4.9, b revealed that the eutectic carbides in the substrate

are darker than the matrix, mostly due to the high carbon content. In addition, the concentration of Cr (Z = 24) in the carbides is much higher than the concentration of Cr the HT-matrix (see Table 4.3), whereas the concentration of Fe (Z = 28) in the carbides is much lower than that in the HT-matrix.

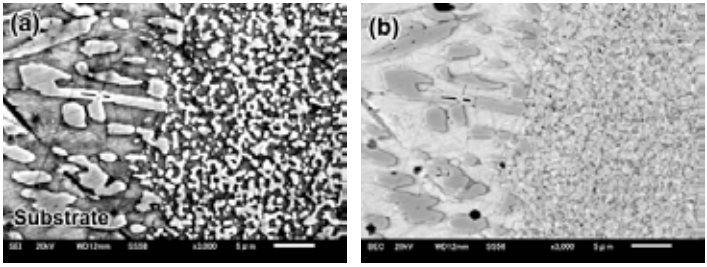

Figure 4.10 – Substrate to coating transition zone (post heat treated): (a) SEI-image and (b) BSE-image

EDX mapping revealed that there is a gradient of Cr concentration within the transition zone. Figure 4.11 clearly shows that the chromium content is reducing from the coating toward the substrate (according to the scale bar, the level of chromium concentration increases from black to white color). The layer of 6–11 μm width adjacent to the substrate has an intermediate Cr content (i.e. lower than that of the substrate and higher than that of the coating). This narrow layer can be identified as the diffusion layer presumably formed owing to plasma-induced melting of the substrate surface with further mixing with the cathode microdroplets. In the melted pool, the cathode material was partially diluted resulting in a gradient of the Cr concentration from the coating to the substrate.

Wear tests results. The tribological behaviors of PPD cast irons (deposited and heat treated) in comparison with conventional cast iron were evaluated by three-body abrasion wear testing. The results of the wear tests are presented in (Fig. 4.12). As seen in (Fig. 4.12, a), the maximum mass losses for both PPD and "PPD+post HT" specimens were recorded at the beginning of the testing; during the first three test cycles, the mass loss decreases considerably. The specific profile of the mass loss curve is explained by the surface roughness caused by plasma deposition owing to an uneven distribution of the microdroplets over the specimen surface. During the first test cycles, surface running-in takes place by protrusion cutting and relief smoothening, which is accompanied by a rapidly increasing mass loss.

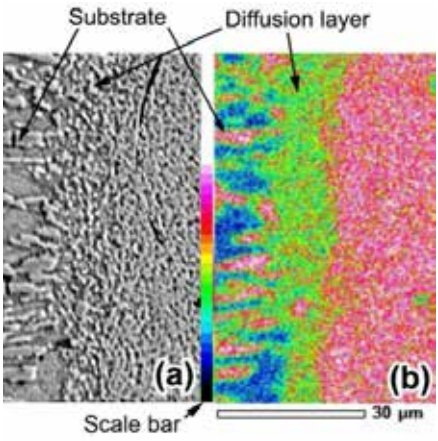

Figure 4.11 – Chromium distribution within the transition zone (post-heat treated cast iron): (a) SEI-image; (b) corresponding EDX mapping of chromium distribution

After the completion of the run-in stage and attainment of working relief, the wear process is stabilized being dependent only on the structure and properties of the coating material. After the test completion the coatings had not been completely removed, thus the substrate did not affect the test results. It should be noted that conventional cast iron (HCCI-1) exhibits a different wear curve profile characterized by almost stable mass losses through all the test cycles.

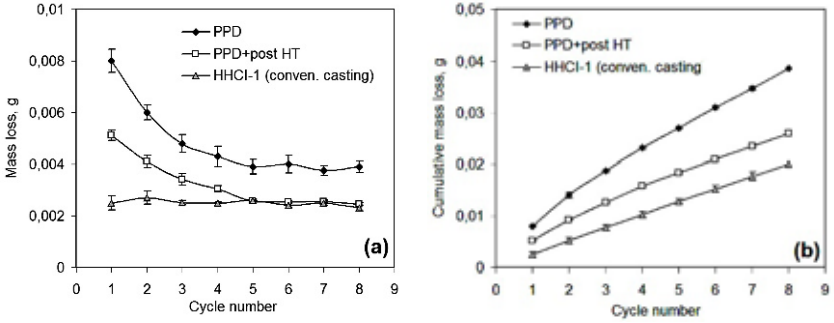

Figure 4.12 – The results of the abrasive wear test: (a) mass loss as a function of cycle number; (b) cumulative mass loss as a function of time

Fig. 4.12, a shows that the PPD (as deposited) coating presents higher mass loss values as compared with the "PPD+post HT" coating, which is consistent with the microstructure and microhardness evolution during post plasma HT (i.e. a high volume fraction of carbides (blocky and some fine) and a predominantly martensitic matrix for the "PPD+post HT" specimen leading to a higher hardness as compared to that of as deposited specimen). According to the curves of cumulative mass loss in (Fig. 4.12, b), the total cumulative mass loss was calculated as 0.0387 ± 0.0006 g (PPD), 0.0259 ± 0.0004 g ("PPD+post HT") and 0.0198 ± 0.0004 g (HHCI-1) showing an advantage for conventionally cast iron. However, the higher total cumulative mass loss of the "PPD + post HT" specimen (as compared to that of HCCI-1) has been affected by the running-in process. Therefore, it is considered more appropriate to compare the wear behavior after completing the running-in period, i.e. from the 5th cycle onward. Indeed, the curve sections from the fifth to the eighth cycle for "PPD+post HT" and HHCI-1 coincide (Fig. 4.12, a). According to this approach, the cumulative mass losses from the fifth to the eighth cycle are 0.0156 ± 0.0005 g (PPD), 0.0101 ± 0.0001 g ("PPD+post HT") and 0.0098 ± 0.0002 g (HHCI-1). In this way, the post PPD heat treated cast iron exhibits almost the same abrasive wear resistance as the conventional cast iron.

Comparison of HCCI-1 and HCCI-2 microstructures. A comparison of the microstructures of the 28 wt.%-Cr cast irons fabricated by conventional casting and pulsed plasma deposition manifested a significant refinement of the microstructure induced by pulsed plasma deposition combined with post-plasma HT. The experimental results indicate that PPD followed by HT led to a 3–5-fold decrease in the carbide cross-section size, as compared to the conventionally cast alloy. Besides, the micro-segregation in the plasma-deposited cast iron was reduced significantly, which is from the 10 times decrease in the SDAS values.

As shown in [54–57], as-spray-formed high-Cr cast irons contain refined eutectic carbides, which indicates their formation via the "Liquid → → Austenite + M_7C_3" eutectic reaction. By contrast, under PPD, ultra-fast solidification of the coating inhibits the liquid/solid diffusion reactions resulting in the formation of a supersaturated matrix. The matrix absorbs all the chemical elements of cathode material ("solute trapping" effect [38, 55, 76]). Since the supersaturated matrix is thermodynamically unstable, during high temperature holding, it is expected to return to the equilibrium state through solid state diffusion-driven precipitation of carbides primarily

rich in Cr (strong carbide forming element) and secondarily rich in Fe and Mn. Hence, post-plasma HT results in the solid-state reaction of "enriched austenite → depleted austenite + secondary carbides" and subsequent (upon oil quenching) martensite transformation. Thus it can be assumed that coating microhardness increase is affected by an increase in the volume fraction of carbides and by the appearance of hard martensite in Fe-alloy grains.

The comparison of XRD and EDX results for HCCI-1 and HCCI-2 (Figs. 4.2, 4.6 and Tables 4.1, 4.2, respectively) showed the differences in the chemical compositions of the carbide phases. Despite the limitations of the EDX analysis, the qualitative trends and rough differences in phase chemical compositions are revealed. Conventionally fabricated cast iron HCCI-1 comprises eutectic M_7C_3 carbides, which are highly enriched with chromium (about 65 wt.%, Table 4.1). Rapidly solidified and post-HT cast iron HCCI-2 contains carbides of three stoichiometries: M_7C_3, M_3C and M_3C_2. The Cr content in the HCCI-2 blocky carbides was found less than 30 wt.% (Table 4.2). Even if it is considered that the EDX measurements are not quite accurate because of the adjacent matrix "effect", this value seems too low as compared to that of the eutectic carbides in HCCI-1 (Table 4.1). Eventually, the chromium contribution to the formation of carbides in HCCI-2 was not as clearly pronounced as in HCCI-1. Table 4.3 shows that, as compensation, much more iron atoms were involved in the HCCI-2 carbide formation resulting in an average iron content of 59.3 wt.% Fe. The above observations indicate the appearance of carbides M_3C and M_3C_2, having lower stoichiometric Cr content which can accommodate less Cr than M_7C_3 [66].

In the above context, a question arises regarding the cause of HCCI-2 carbide depletion of chromium relative to HCCI-1. The answer could be associated with the notably increased carbide volume fraction in HCCI-2 (~ 57%) as compared to that in HCCI-1 (~ 30%). Since the carbide formation requires first and foremost carbon atoms, it can be presumed that during pulsed plasma deposition using EAPA, an unexpected increase in the carbon content of the deposited material occurred due to erosion of the inner channel walls of the plasma accelerator under high-current arc discharge and pulsed plasma [3]. The inner channel walls are composed of bakelite (a paper-reinforced polymer); thus, carbon atoms can be released during polymer decomposition and paper burning. The released carbon atoms were transferred with the plasma flow to the substrate, where they doped the liquid cathode microdroplets. Increasing the carbide amount

due to the increased carbon content resulted in lowering the chromium content in the carbides and, eventually, in changing the carbide nature from M_7C_3 to M_3C and M_3C_2. The latter explains the fact that, despite the higher content of carbides, the coating has similar abrasive wear resistance to that of its conventional counterpart (HCCI-1). Probably this is due to the fact that carbides with lower chromium content have less wear resistance, which does not allow to realize the advantage of an increased amount of carbides in the coating. Another reason of that is porosity in the coating caused by incomplete fusion of microdroplets on the substrate surface. The pores are actively eroding by abrasive particles promoting mass loss. This levels the advantage of the coating after PPD+HT in carbides volume fractions.

The wear tests showed that PPD+HT coating had the same wear resistance as conventionally fabricated HHC-1. Since high-Cr cast irons are well recognized to have much higher abrasive/erosive wear resistance as compared with structural and tool steels [77], PPD+HT coating (HHC-2) can be considered as a metallic material with advanced tribological behavior as well.

Thus, the present effort claims that plasma deposited HCCI can be applied for strengthening machine parts, the working life of which is limited by wear of micron scale. Some potential applications could be: parts of engine fuel equipment operating under conditions of friction and high-temperature oxidation; guide details of machine-tools; cylinder liners etc. An HCCI coating up to 100 micron thick can also be used for renovation of worn precision details with allowance for the fine finish machining. Hence, due to the PPD technique, the high-Cr cast irons can be used in thin surface layer applications, where other technologies (conventional casting, arc weld deposition) are not appropriate.

The results presented in this chapter can be concluded as follows:

The microstructure of a conventionally sand-cast 28 wt.%-Cr iron comprises about 30 vol.% of eutectic carbides M_7C_3 within an austenite/martensite matrix reinforced with secondary carbides. Pulsed plasma deposition of 28 wt.% Cr cast iron on steel surface using EAPA technique results in formation of the coating with non-equilibrium microstructure, obtained due to the extremely high rate of thermalization and heat transfer. This microstructure consists of oversaturated gamma-phase and alpha-phase solid solutions with minor amount of M_3C carbide whilst not any eutectic carbides were detected. The microhardness of as-deposited coating is about 650 HV.

Subsequent post-plasma heat treatment (holding at 950 °C) leads to austenite decomposition manifesting in precipita-tion of net-shaped carbides M7C3 (major) and M23C6 followed by transformation of depleted austenite into acicular marten-site. This provides 2.5-fold increase in coating microhardness (up to ~ 1550 HV) as compared with as-deposited state.

The carbide precipitation proceeds according to decelerating kinetics with the highest rate at the initial holding. The first precipitates appear just after 5 min holding as fine grainy particles or thin elongated carbide agglomerations. With duration increase the carbides tend to coarsen making bulky net-work enclosing matrix grains. The volume fraction of carbide gradually increases reaching 63.7 vol. % after 120 min hold-ing. Carbide formation presumably process via transition $M_3C \rightarrow M_7C_3 \rightarrow M_{23}C_6$ *which corresponds to reaching the equilibrium state.*

The PPD technique leads to a significant refinement of the high-chromium cast iron microstructure. This is manifested in the 3-5-fold decrease in the carbide size and the 10 times decrease in the SDAS value, as compared to the conventionally cast alloy. The carbides in the heat treated PPD HHCI are found significantly depleted of Cr in favor of Fe (in comparison with the conventional counterpart). This depletion is caused by the increase in the carbide volume fraction due to coating enrichment with carbon during PPD. The plasma de-posited 28 wt. %-Cr cast iron subjected to post-heat treatment exhibits similar three-body abrasive resistance as the conventionally cast one.

The content of the Chapter is adopted from Comparative analysis of the microstructural features of 28 wt.% Cr cast iron fabricated by pulsed plasma deposition and conven-tional casting / Yu.G. Chabak, V.G. Efremenko, K. Shimizu, A. Lekatou, T.V. Pastukhova, A.Yu. Azarkhov, V.I. Zurnadzhy // Journal of Materials Engineering and Performance. – 2018. – Vol. 27, no. 2. – P. 379-388. https://doi.org/10.1007/s11665-017-3102-z

Chapter 5. EVALUATION OF THE MICROSTRUCTURE, TRIBOLOGICAL CHARACTERISTIC, AND CRACK BEHAVIOR OF A CHROMIUM CARBIDE COATING FABRICATED ON GREY CAST IRON BY PULSED-PLASMA DEPOSITION

Grey cast iron (GCI) is a traditional structural material which is widely used in mechanical engineering due to its good manufacturability, low production cost, improved vibro-damping properties, and better dry-sliding wear resistance [78]. However, GCI is characterized by its low abrasive wear resistance because of the presence of the graphite phase, which easily degrades under abrasion [79]. This common problem can be solved by surface modification or protective coating deposition. Laser beam scanning is an effective approach to structurally modify GCI and increase its abrasive wear resistance [80]. Pang et al. [81], Sui et al. [82, 83] and Yang et al. [84] applied a laser Nd:YAG treatment to form biomemically located modified areas on the GCI surface. The modification was achieved without changing the chemical composition of GCI and by forming chilled areas with a hard ledeburite structure under rapid crystallization after laser melting. The matrix of the chilled areas consisted of martensite and retained metastable austenite, which contributed to an improved wear resistance [85]. Different techniques, such as surface doping in the mold [86], laser carburizing [87], direct surface alloying through the deep laser beam melting of preliminary deposited carbides (Cr_3C_2, WC), [88, 89], have been adopted to create the composite structure on GCI surface. Zhong et al. [90] revealed the improvement of corrosion and wear characteristics of grey iron liner resulted from laser alloying by Ni-Cr powder. The similar result was obtained in [91] where Cr laser alloying was used to enhance GCI thermal fatigue resistance. Laser cladding of Fe-based alloy [92] and Ni-based alloy [93] was applied to chemically modified grey cast aiming at voids elimination and further interfacial behaviors regulation.

The other direction of GCI properties improvement is a protective coating deposition. Different techniques were repeatedly applied to deposit the coating on GCI's surface. They are powder thermal spraying [94], arc spraying/sintering [95], physical vapor deposition [96–98], laser cladding [99, 100],

plasma surfacing [101–103], plasma spraying [104, 105], electric contact deposition [106], etc. which were previously reported to improve GCI's resistance to abrasive wear, corrosion, thermal fatigue, and cavitation damage.

Among the variety of surface treatment techniques the plasma-related methods are stand out due to their advantages for surface modification and coating deposition. Sokolov et al. [107] and Park et al. [108] applied plasma ionic nitriding to enhance the corrosion resistance and cavitation resistance of GCI. Agarwal et al. [109] employed plasma nitrocarburization to improve the tribological properties of stamping dies made of GCI. Moreover, plasma electrolyte oxidation and ceramic coating deposition have also been used for GCI surface modification [110, 111]. Cheng et al. [112] improved the wear characteristics of grey nodular cast iron by steady plasma beam surface melting. Detonation-based pulsed-plasma treatment proposed by Tyurin et al. [113, 114] was also used to modify ductile cast iron [115]. Cherenda et al. [116] reported the application of a compression plasma flow to form a coating of the GCI surface. Kolyada et al. [2, 63] highlighted the applicability of high-dynamic pulsed plasma flow generated in an electrothermal axial plasma accelerator (EAPA) for metallic surface modification. The design and operational principles of EAPA, which operates under atmospheric conditions, are outlined in detail in earlier studies [2, 3, 63]. Further, EAPA was used for the surface structure modification (case hardening) of steel [28] and GCI [117]. Moreover, EAPA was employed for the deposition of coatings due to the erosion of the axial electrode (cathode) under high-current discharge [118, 14]. However, EAPA was not previously attempted to deposit the protective coating on GCI surface. Assuming the graphite presence in GCI, the coating/substrate interaction with carbon diffusion to the coating was expected to affect the coating performance. Considering the novelty of this approach, the present work was aimed at studying microstructural and tribological properties of a high-chromium (28 wt. %) coating deposited on the surface of GCI by EAPA pulsed-plasma deposition.

Experimental procedure. The substrate for the coating was made of grey cast iron with a chemical composition of 2.95 wt. % C, 1.45 wt. % Si, 0.95 wt. % Mn, 0.11 wt. % P, 0.08 wt. % S. Specimens of 6 mm × 12 mm × × 25 mm size were cut from a casting of 30 mm diameter and 300 mm length. The source material for coating deposition was high-Cr white cast iron with a chemical composition of 2.34 wt. % C, 27.39 wt. % Cr, 3.13 wt. % Mn, 1.26 wt. % Si, 0.20 wt. % Ti. A high-chromium cast iron rod of 5 mm diameter served as the cathode of a plasma accelerator.

Pulsed-plasma deposition was performed using EAPA under following [arametres: envirpment is open air, voltage stored in the capacitor is 4.0 kV, distance between EAPA electrodes is 50 mm, distance from the EAPA edge to the target surface is 50 mm, pulse number = 10. The as-deposited specimens were subjected to a post-plasma heat treatment (two hours of holding at 950 °C) followed by oil cooling [3, 14]. During heating, the coating was covered by coal to prevent surface oxidation and decarburization.

Microstructure and phase constituents. The initial microstructures of the substrate and the cathode are displayed in (Fig. 5.1). The microstructure of the substrate (grey cast iron) consisted of ferrite grains with an average microhardness of 223 ± 25 HV and graphite lamellae of 0.5–3.0 μm thickness (Figure 1 a). The microstructure of the cathode (hypoeutectic cast iron) was composed of solid-solution pre-eutectic dendrites surrounded by eutectic Cr-rich M7C3 carbides (Fig. 5.1, b) [3].

Hexagonal rod-shaped eutectic carbides with a volume fraction of 34–35 vol.% coalesced into agglomerates of 1–4 μm size. A coating of 210–250 μm thickness was formed after pulsed-plasma deposition. The as-deposited coating possessed a laminar structure consisting of alternating bright and relatively dark bands (Fig. 5.1, c). High-magnification observation allowed to reveal that these dark bands contained metal grains surrounded by a thin (0.03–0.12 μm) carbide network (insert of Fig. 5.1, c).

Coarse eutectic carbides were not detected in the as-deposited coating structure. Moreover, cracks were seen in the coating to be oriented perpendicularly to the coating surface. These cracks grew from the "coating/substrate" interface, and some of them went through the entire coating width. The coating contained pores with a volume fraction of 2.5 vol.%. The microhardness of the coating varied in the range of 620–670 HV (Fig. 5.2).

After post-plasma heat treatment a gradient pattern consisting of three clearly distinguished sub-surface zones (A (the coating), B, C) appeared in near-surface layer (Fig. 5.1, d). Zone C was a bulk of the specimen with a microstructure consisting of graphite lamellae and needle-shaped martensite matrix having the microhardness of 553–710 HV (Fig. 5.1, e). Closer to the surface, martensite was gradually replaced by ferrite, forming a ferrite/martensite zone B of a variable thickness (190–290 μm) between the martensitic bulk and the coating. Ferrite was predominantly found in zone B, and martensite areas existed adjacent to graphite lamellae (Fig. 5.1, f).

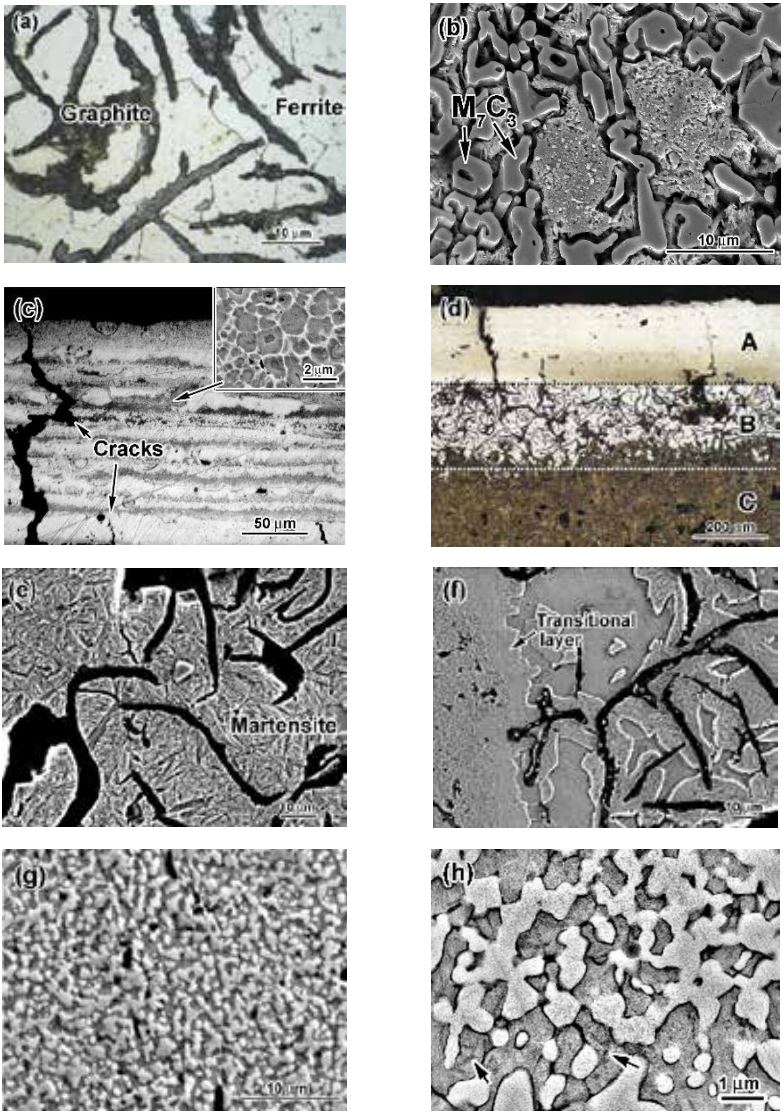

Figure 5.1 – (a, b) Initial microstructures of grey cast iron and the 28 wt.% Cr cathode, respectively. (c) Microstructure of the as-deposited coating. (d) Near-surface structural zones in the heat-treated specimen. (e) Needle-shaped martensite and graphite lamellae in zone C. (f) Ferrite/martensite zone adjacent to the transitional layer. (g, h) Carbides in the coating

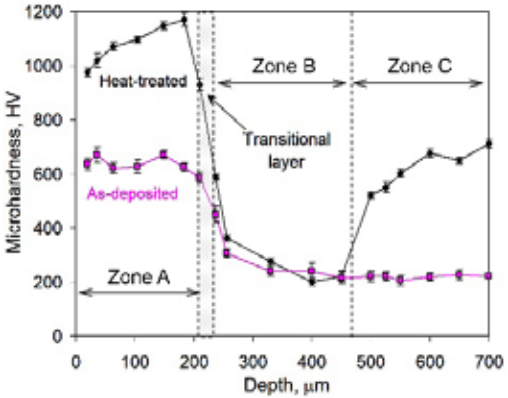

Figure 5.2 – Cross-sectional microhardness profiles of the coated specimens (as-deposited and heat-treated)

Numerous irregularly-shaped carbide precipitates of 1 μm size coalesced into a broken network engulfing matrix grains (Fig. 5.1, g). Moreover, smaller roundish carbide precipitates (0.1–0.6 μm) were observed inside matrix grains (Fig. 5.1, h). A needle pattern was observed between carbide precipitates (shown by arrows in Fig. 5.1, h), revealing the formation of a high-carbon martensite matrix. The carbide volume fraction in the coating was calculated as 48.2 vol.%. Post-heat treatments increased the coating microhardness from 980 HV (near the top) to 1180 HV (close to the coating/substrate interface) (Fig. 5.2). The microhardness profile had a recess from the ferrite-martensite matrix (zone B) to the martensite matrix (zone C). Zones A and B were separated by an 8–25 μm wide graphite-free transition layer containing a small amount of carbides (Fig. 5.1, f). The microhardness of the transition layer decreased from 930 HV at the coating boundary to 580 HV at the ferrite-martensite zone boundary.

The phase constituents of the coating were investigated by X-ray diffraction (Fig. 5.3). The XRD pattern for the as-deposited coating contained peaks of matrix phases $(\gamma\text{Fe} \quad \text{and} \quad \alpha\text{Fe})$ and carbide phases (Cr_7C_3 and Fe_3C). γFe (austenite) was found as the major phase, and its volume fraction in the matrix was 84 vol.%. Carbides were found in the matrix in a small amount according to their weak peaks. The XRD pattern of the post-heat-treated specimen contained the same set of peaks; however, a significant change in peak intensities was detected. The intensity of γFe drastically decreased, whereas the αFe peak had an increased intensity. The

$\gamma Fe \rightarrow \alpha Fe$ phase transformation during post-heat treatment resulted in a retained austenite volume fraction (in the matrix) of 8.1 vol.%. Moreover, heat treatments led to an increase in the M_7C_3 carbide amount, as followed from numerous carbide peaks appeared in the XRD pattern. Taking into account the total carbide volume fraction of 48.2 vol.%, the volume fractions of martensite and retained austenite in the heat-treated coating were recalculated as 47.6 vol.% and 4.2 vol.%, respectively.

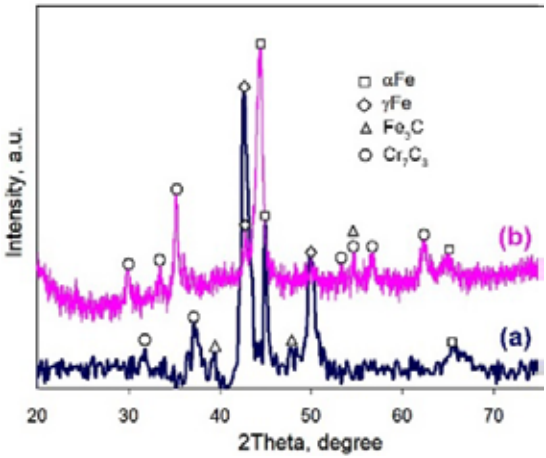

Figure 5.3 – XRD patterns of the coating (αFe (6–0696), γFe (4–0829), $(Cr, Fe)_7C_3$ (5–0720), Fe_3C (35–0772)) (a) as-deposited state; (b) after post-heat treatment

The EDS analysis was performed in a "mapping" mode to qualitatively assess the distribution of chemical elements in near-surface layers. The color of the "map" refers to elemental concentrations corresponding to the scale located on the left side of the "map" (from 0 wt.% (black) to 100 wt.% (white)). A gradient in elemental distribution with a gradual decrease in Cr, Mn, C contents and an increase in the Fe content was noticed from the top of the coating to the substrate (Fig. 5.4, a).

The $Cr_{K\alpha}$ "mapping" more closely shown in (Fig. 5.4), e reveals a smooth chromium gradient at the coating/substrate interface. Pores in the coating were enriched with manganese and chromium, reflecting the presence of oxides (MnO_2, Cr_2O_3) in these pores. The transitional layer (area II) had slightly higher chromium content as compared to the base (area I). In the transitional layer, chromium was mainly accumulated in carbides, whereas matrix was depleted in chromium.

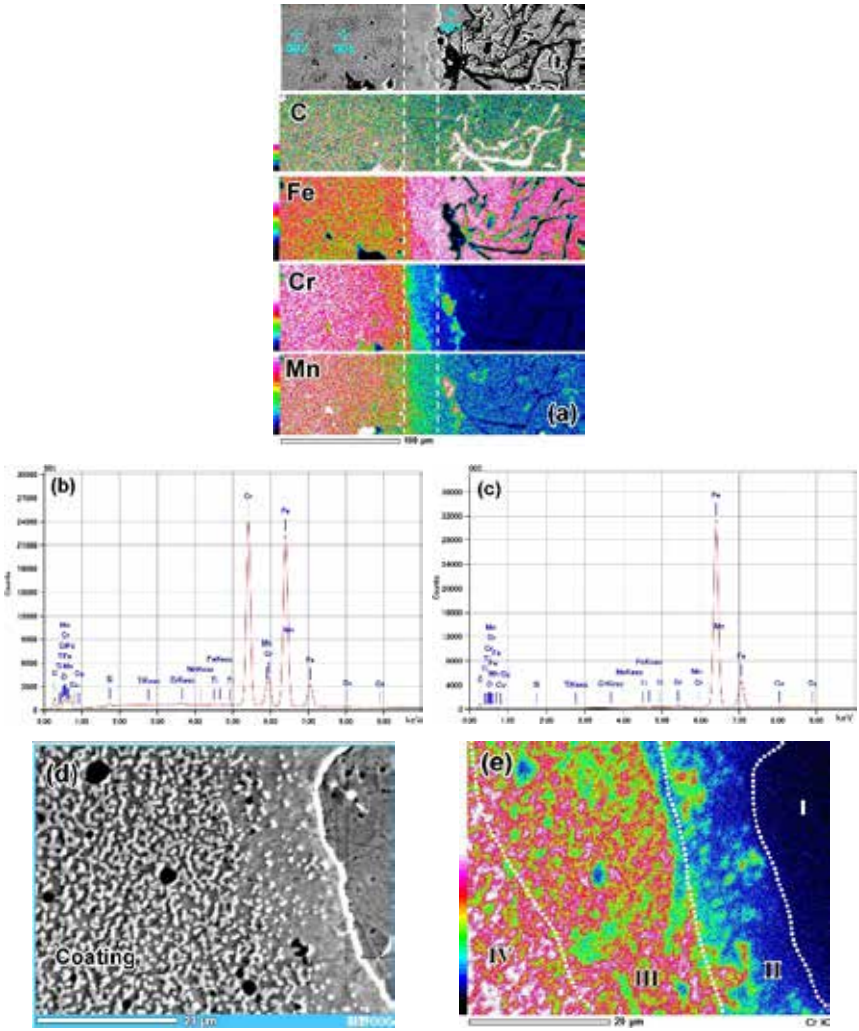

Figure 5.4 – EDS analysis results: (a) elemental mapping of C, Fe, Cr, Mn; (b, c) EDS spectra of the local chemical analysis at points 001 and 003, respectively; (d) SEI image; (e) Cr mapping of the transition layer

The coating had a much higher chromium concentration than the transitional layer; however, the distribution of chromium was uneven. The chromium concentration was low in area III and high in area IV, and it could be tracked by the color of carbides in areas III (pink) and IV (white-pink).

The color of the matrix also changed from green in area III to pink-green in area IV. Different chromium contents in carbides of areas II, III, IV reflected a variation of the carbide type from the transitional layer to the top of the coating. The "mapping" observation is supported by elemental profiles presented in Figure 5.5. The contents of chromium and manganese increased from the coating/substrate boundary to the top of the coating and became stabilized at a distance of 55–60 μm from the boundary.

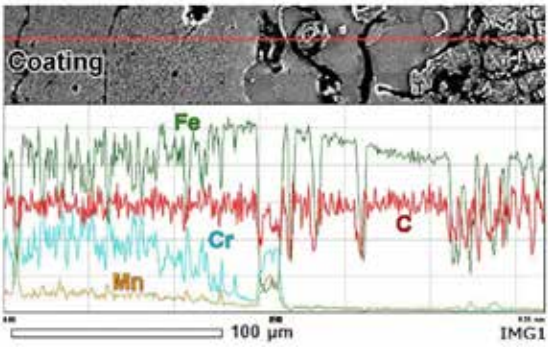

Figure 5.5 – Cross-sectional EDS profile of Fe, Cr, Mn, C from the coating to the substrate

The local EDS analysis of the coating at points 001 and 002 in Figure 5.4, a reveals that the coating had a chemical composition of 29.43 wt.% Cr, 1.96 wt.% Mn, 0.62 wt.% Si, 0.68 wt.% Cu, 0.03 wt.% Ti, iron – balance (Fig. 5.4, b). As the carbide size was less than the EDS spatial resolution [65], carbides and matrix areas both contributed to the EDS response. Therefore, the presented chemical composition could be considered as the average composition of the coating, and it corresponds to the composition of the cathode material (~ 28 wt. % Cr cast iron). The ferritic matrix existing next to the transitional layer (point 003 in Fig. 5.4, a) contained 0.27 wt. % Cr, 0.88 wt. % Mn, 1.78 wt. % Si, 0.09 wt. % Cu, iron - balance (Fig. 5.4, c). The presented EDS results should be considered as semi-quantitative because of a high EDS sensitivity for carbon contamination.

Tribological characteristics. Figure 6 presents the results of "Three-body abrasion" tests. Upon completion of the tests, the total weight loss of the heat-treated coating (16.0 mg) was 2.7 times and 2.3 times lower than that of the substrate (43.7 mg) and the substrate-HT (37.4 mg) accordingly. During abrasive tests, all the specimens maintained close behavior only during the first test cycle

when the coating roughness caused by plasma deposition was removed (Fig. 5.6, a), and afterward, the coating had a much lower wear rate (1.3 mg/min) than the substrate (4.2 mg/min) and the substrate-HT (3.7 mg/min). Evaluation under the stable wear process (from the second cycle to the 10th cycle) showed that the coating performed much better tribological behavior under abrasive conditions which was 3.2 times and 3.0 times higher as compared with the substrate and the substrate-HT. The worn surface of the coating featured a closed crack network with a "cell" of 0.5–1.0 mm diameter. Inside the "cell", the surface was smoothly abraded (Figure 6 b) with the average roughness parameters of R_a = = 0.635 μm and R_z = 2.184 μm (Fig. 5.6, d). The worn surface of the sub-strate had deep parallel grooves (Fig. 5.6, c), exhibiting a rougher profile with the average roughness parameters of R_a = 4.585 μm (increased by 7.3 times) and R_z = = 9.033 μm (in-creased by 4.1 times). The worn surface of the substrate-HT had slightly lesser roughness with R_a = 3.436 μm and R_z = 8.573 μm which was consistent with its lesser weight loss compared with the substrate.

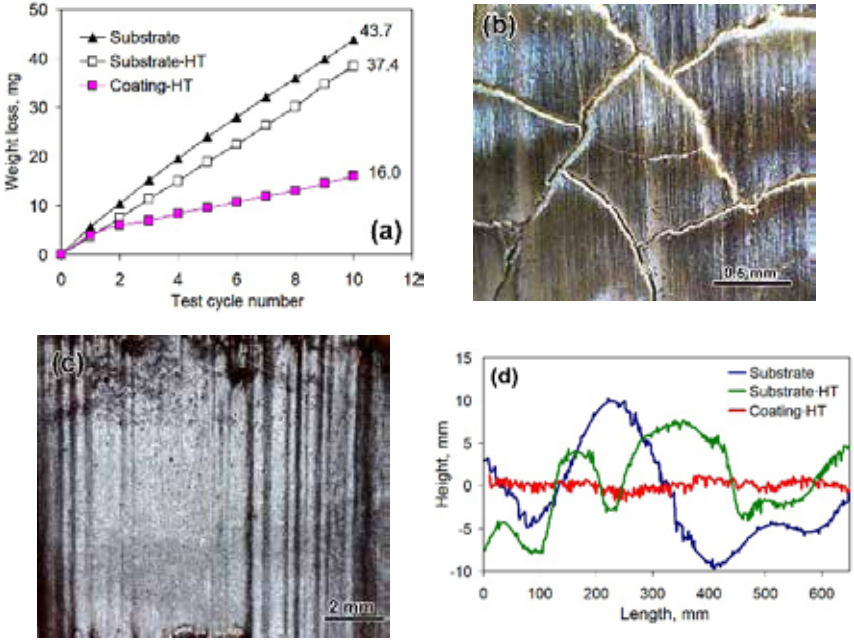

Figure 5.6 – Abrasive wear characteristics of grey cast iron and the coating: (a) cumulative weight loss curves. (b) crack network on the abraded heat-treated coating surface; (c) abraded substrate surface; (d) worn surface profiles

The dry-sliding characteristics of the coating are presented in (Fig. 5.7 and 5.8. Figure 5.7), a presents the volume loss related to 1 μm of wear track. It is evident from (Figure 5.7), a that the volume loss of the substrate was in a direct pro-portion to the counter-body microhardness. The volume loss value slightly increased from 87.1×10^{-3} μm^3 (against the steel ball) to $98.7 \times \times 10^{-3}$ μm^3 against the SiC ball and drastically increased to 592.3×10^{-3} μm^3 against the diamond cone (Figs. 5.7, (b-d)).

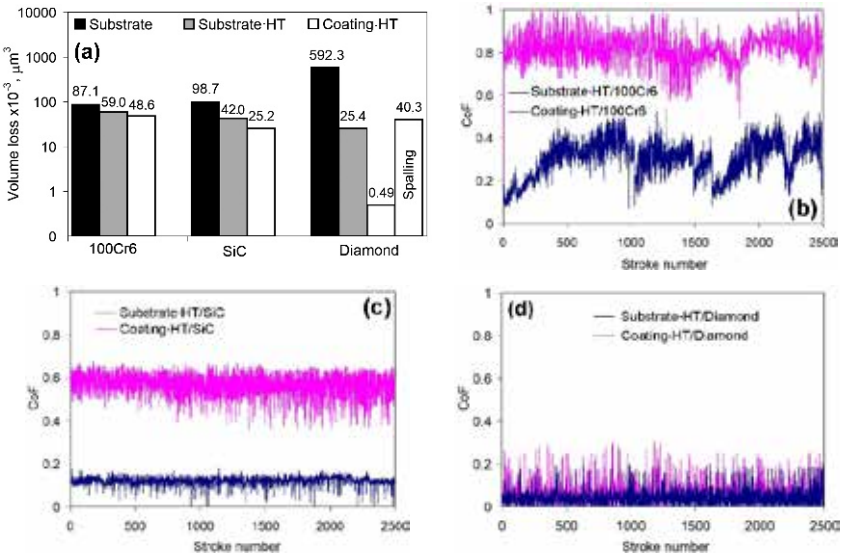

Figure 5.7 – Dry-sliding wear characteristics of the substrate, the substrate-HT and the heat-treated coating: (a) consolidated data on specimens' volume losses; (b) CoF variation for testing against 100Cr6 steel ball; (c) CoF variation for testing against SiC ball; (d) CoF variation for testing against diamond cone

For the coating, the opposite tendency was found when its volume decreased from 48.6×10^{-3} μm^3 (steel ball) to 0.49×10^{-3} μm^3 (diamond cone) as the counter-body microhardness increased. The substrate-HT performed an intermediate volume loss values. The coating had a lower volume loss as compared to grey cast iron with any counter-body. The volume loss of the coating was 1.8 times, 3.9 times, and 1208.8 times lower than the substrate when it tested against the steel ball, the SiC ball, and the diamond cone, respectively. When compared to the substrate-HT the advantage of the coating decreased: its volume losses were 1.2 times (the steel ball), 1.7 times

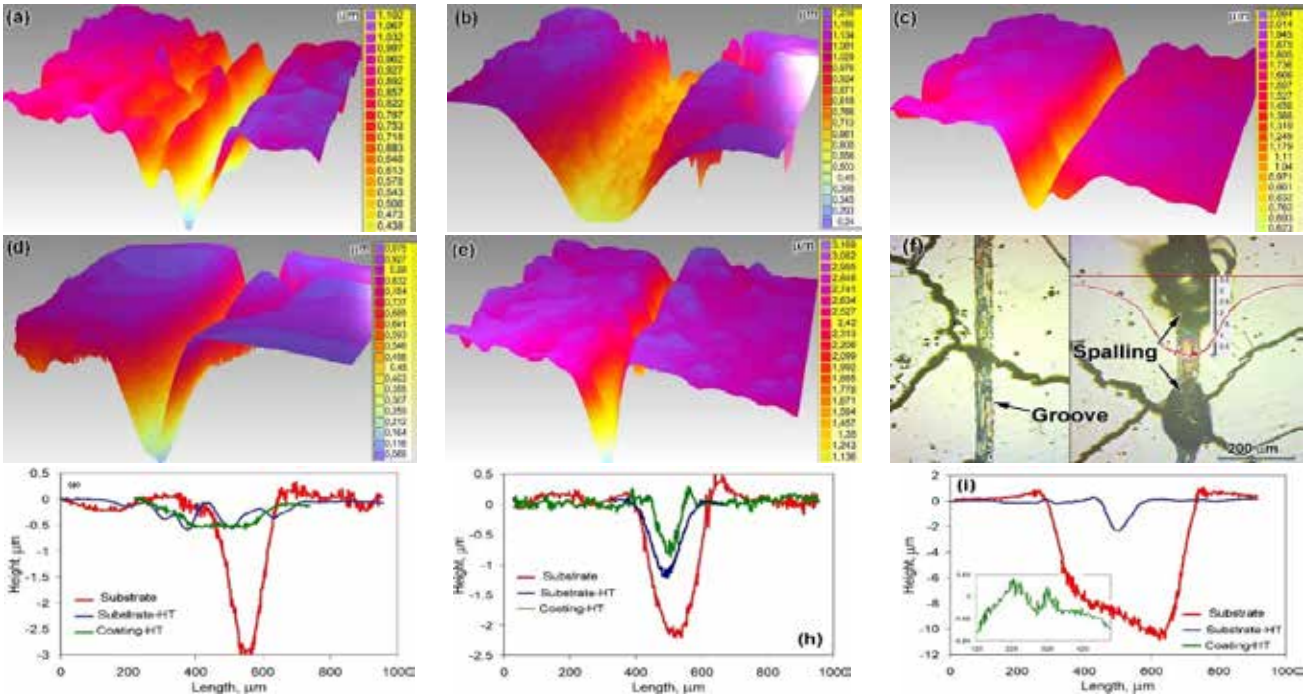

Figure 5.8 – Dry-sliding worn surface characterization: (a, c, e) 3D images of wear tracks on the substrate-HT; (b, d) the heat-treated coating after testing against; (a, b) the 100Cr6 steel ball; (c, d) SiC ball; (e) the diamond cone; (f) different fragments of a "diamond cone" wear track on the heat treated coating (depth scale bar is given in micrometers); wear track profiles for testing against; (g) the 100Cr6 steel ball, (h) SiC ball; (i) the diamond cone

(SiC ball), and 51.8 times (the diamond cone) lower than that of heat-treated GCI. The CoF of the "Substrate-HT/100Cr6 ball" pair was characterized by pronounce instability with areas of increase up to 0.50–0.55 and a sharp decrease to 0.07–0.10 (Fig. 5.7, b).

The CoF of the "Coating/100 C 6 ball" pair was more stable as compared to the previous one with a higher mean level (about 0.81) and a rather big scatter (0.62–1.00). Under sliding against SiC ball the CoF level decreased while the difference in CoF remained approximately in the same proportion (Fig. 5.7, c). CoF values were rather stable with a decreased scatter: CoF smoothly fluctuated within 0.07–0.16 (mean value – 0.12) for the substrate-HT and 0.35–0.67 (mean value – 0.56) for the coating. Sliding against the diamond cone resulted in the lowest CoF level for both specimens. The "Substrate-HT/Diamond cone" pair performed CoF mean value of about 0.04 with a scatter of 0–0.20 while the "Coating/Diamond cone" showed a slightly higher CoF mean value (0.06) and a scatter (0–0.30) (Fig. 5.7, d).

Wear tracks observed on the worn surfaces were of different geometry depending on specimen state and counter-body type as seen from their 3D reconstruction (Figs. 5.8, a-e). The wear track profiles for testing against the steel ball are illustrated in (Figure 5.8, g). It is seen that wear tracks were wide and shallow (up to 0.5 μm) for the coating and the substrate-HT (the track for the latter was 1.5 times wider). In contrast, the substrate showed a deep (3 μm) and more narrow (300 μm) wear track. When testing against SiC ball (Fig. 5.8, h), all specimens performed the rather narrow wear grooves with a different depth: the width/depth of the groove were minimal for the coating (~ 100 μm / ~ 1 μm accordingly) and maximal for the subtrate. The most pronounced difference on the wear track profile was noted for testing against the diamond cone. As follows from (Figure 5.8), i, the wear track for the substrate was very wide and deep (up to 11 μm). The substrate-HT exhibited a narrow groove with moderate depth (2.1 μm). On the coating, the very shallow wear track of a negligible depth (0.015 μm) was formed (enlarged cross-sectional profile is shown in the insert of Figure 5.8, i). The distinctive feature of a "diamond cone" wear track was the occasional spalling observed mostly at the intersections of the groove and crack (Fig. 5.8, f right). The volume loss in spallingfree sections of a "diamond cone" wear track (Fig. 5.8, f left) was very low (0.49×10^{-3} μm^3). However, the volume loss in spalling sections increased by two orders of magnitude (up to 40.3×10^{-3} μm^3) due to the formation of deep (2–3 μm) holes by spalling.

As shown above, pulsed-plasma deposition followed by post-plasma heat treatment significantly improved grey cast iron wear characteristics. GCI's abrasion wear resistance increased by 3.0–3.2 times while dry-sliding wear resistance increased by 1.2–1208.8 times depending on the counter-body material. This happened due to the formation of a composite coating containing about 50 vol. % Cr-rich carbides in the structure [119].

The coating smoothly connected with the substrate through the transitional layer, indicating a strong metallurgical bonding between them. This phenomenon can be attributed to the melting of a GCI's near-surface layer under the plasma flow. The possibility of plasma-induced surface melting could be evaluated by analyzing the temperature field of near-surface layers in contact with the a plasma flow. The numerical modeling of substrate surface heating was executed based on the solution of a heat conduction task according to the approach of a short-term heat source (q_o) evenly distributed over the target surface. The modeling approach was previously described in detail in [120]. Calculations were conducted using grey cast iron parameters: density = 7200 $kg \cdot m^{-3}$, specific melting heat = 140 $kJ \cdot kg^{-1}$. The temperature-dependent heat capacity and thermal conductivity values were adapted from the literature [121]. The value of specific power density ($q_o = 1.75 \times 10^9$ $W \cdot m^{-2}$) corresponded to the EAPA working regime [28].

Numerical modeling results of the temperature distribution over the cross-section of the grey cast iron specimen are displayed in (Fig. 5.9, a). It is noticeable that the plasma flow rapidly heated the substrate surface. After 200 μs of collision with the plasma flow, the substrate surface reached the solidus temperature (shown by the dashed line in Fig. 5.9, a) and melted to a depth of about 1.5 μm. Further heating resulted in an alteration of the melting depth according to the curve presented in (Fig. 5.9, b). The surface temperature reached the maximum value of 2350 °C after 440 μs of the collision, whereas the melting depth reached the maximum value of 15 μm after 570 μs (the surface heating rate maximally reached 12.3×10^6 $K \cdot s^{-1}$ [120]). During the next 100 μs of the collision, the substrate surface cooled below the melting temperature with the maximum cooling rate of 9.0×10^6 $K \cdot s^{-1}$. The calculations showed the possibility of plasma-induced melting of the substrate which is in accordance with a microstructure observation. The calculated melting depth (15 μm) complied with the transitional layer width (7–25 μm), confirming that the latter originated from surface melting. The molten layer of cast iron was mixed with the plasma liquid/gaseous material, forming a strong metallurgical coating/substrate bonding.

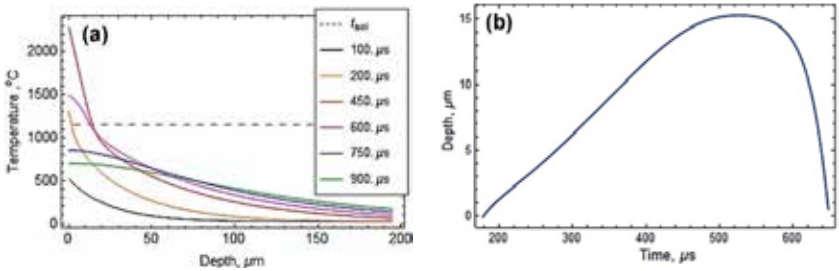

Figure 5.9 – Numerical simulation results of the temperature field of the specimen under plasma heating (time is given from the contact with the plasma flow) (a) time-wise cross-sectional temperature distribution; (b) time dependency of the melting depth

XRD analysis and microscopic observation results revealed that the as-deposited pulsed-plasma coating consisted mostly of austenite matrix (84.0 vol.%) with a small amount of M_7C_3 and M_3C carbides. This observation confirms the previous findings for EAPA pulsed-plasma coatings deposited by a cathode made of eutectic Fe-based alloys (high-Cr cast iron and 18 wt% W high-speed steel) [3, 14]. The high-current discharge inside the EAPA chamber led to the evaporation and melting of the cathode [118, 120]. Thus, the coating consisted of cathode erosion products, mostly microdroplets, that were transferred by the plasma flow to the target surface. These microdroplets, being deposited, underwent superfast cooling, resulted in the inhibition of eutectic reactions [122]; thus, oversaturated (thermodynamically unstable) austenite grains were formed in the as-deposited coating. Austenite was partially decomposed through carbide precipitation under the heating induced by subsequent plasma pulses. M_7C_3 and M_3C carbides precipitated in the form of a thin network around matrix grains (see insert of Fig. 5.1, c). The formation of Cr-depleted cementite carbide was kinetically preferential at this stage [123].

The as-deposited structure is not suitable for abrasion applications because of its lower hardness. In order to improve the hardness and tribological behavior of the coating, post-plasma heat treatment was carried out [3, 14]. During heat treatment, austenite grains turn into their thermodynamically stable state through the precipitation of Cr-rich carbides. The heat treatment at 950 °C for two hours allowed the diffusion of Cr atoms to form M_7C_3 carbide in the coating [47]. The precipitation of Cr-rich carbides led to austenite depletion by carbon and chromium enabling austenite →

→ martensite transformation during oil cooling. The formation of hard phases (M_7C_3 carbides, martensite) increased the coating's hardness up to 1180 HV. M_7C_3 carbides mainly precipitated as a network along grain boundaries. M_7C_3 carbides appeared on the cementite network, proving the transition of metastable M_3C carbides into stable M_7C_3 ones. M_7C_3 carbides in the coating were four-fold smaller as compared to eutectic carbides in the cathode, confirming the refinement of the carbide phase under the plasma-assisted treatment [124].

During the prolonged holding at 950 °C, carbide precipitation was accompanied by the elemental partitioning in the coating and the substrate. Hence, the saturation of the substrate matrix with carbon occurred due to graphite dissolution, and carbon-rich austenite was then transformed into high-carbon martensite, causing a significant increase of the matrix microhardness. Moreover, a counter element partitioning occurred: carbon was partitioned from the substrate to the coating, whereas chromium and manganese were partitioned from the coating to the substrate. Carbon diffused from the matrix toward the coating to be bond with chromium to form carbides, thus making the matrix C-depleted, resulting in the formation of a ferrite-martensite zone (zone B) below the coating. On the contrary, Cr and Mn atoms diffused from the coating to the transitional layer in order to level their concentrations at the "coating/substrate" interface; hence, Cr distribution had a descending profile toward the substrate (Fig. 5.5). The counter-flow of carbon and chromium atoms led to a structural gradient in the coating. Specifically, Cr-depletion and C-enrichment caused the appearance of layer III (Fig. 5.4, e), which contained Cr-depleted carbides (presumably, cementite $(Fe, Cr, Mn)_3C$)). The matrix in layer III was also Cr-depleted, causing an increase of the Ms point and leading to a low austenite volume fraction (high martensite amount). Hence, layer III had the maximum microhardness (Fig. 5.2), which reduced toward the surface due to an increase in the chromium content in the coating. These processes caused a smooth structural transition, contributing to the strong adhesion between the coating and the substrate.

The pulsed-plasma high-Cr coating showed an increased abrasive wear resistance due to the synergetic interaction of M_7C_3 carbides with martensite-austenite matrix, in which austenite grains might perform TRIP-effect under abrasion [84, 125]. The volume fraction of carbides (about 50 vol.%) was notably higher than that of the EAPA cathode (28 wt.% Cr cast iron). The increase in the carbide volume fraction relative to the cathode was

influenced by carbon enrichment of the coating. The sources of carbon enrichment could be (a) carbon atoms released due to the evaporation of bakelite walls of the EAPA channel under arc discharge [3] and (b) carbon atoms diffused to the coating from the substrate. Closely-located carbides in the coating effectively resisted abrasion and led to shallow scratches with low surface roughness. On the contrary, the ferrite/graphite structure (substrate) had an increased wear rate with 4–7 times higher roughness.

Dry-sliding wear tests have confirmed the enhanced tribological properties of the carbide coating. GCI had a lower CoF when it tested against steel and SiC balls due to the presence of a solid lubricant (graphite) in the structure [126]. As the coating did not contain graphite inclusions, its CoF increased by 2.7 times against the steel ball and by 2.0 times against the SiC ball as compared to the substrate. Despite this fact, the coating had much higher dry-sliding wear resistance, and its volume loss decreased by 1.8 times against the steel ball and by 3.9 times against the SiC ball as compared to the substrate. This phenomenon was caused by higher coating hardness (decreasing a depth of counter-body penetration) and by a low adhesion between coating carbides and the counter-body material (decreasing a galling manifesting). Notably, the coating had 1.9 times higher wear resistance against the hard SiC ball as compared to testing against softer steel balls. This fact can be explained by much lower adhesion between the coating matrix (BCC/FCC lattices) and SiC (HCP lattice) related to the high hardness of counter surfaces and to a mismatch in their unit cell configuration. This assumption is also confirmed by the lower CoF (mean value of about 0.56) of the "coating/SiC" pair than that of the "coating/steel" pair (CoF = 0.81). Unexpectedly, the "coating/diamond cone" pair had a very low CoF (0.06) and negligible volume loss (0.49×10^{-3} μm^3). Such CoF value indicates the minimal adhesion which eliminated the galling-induced wear loss. High hardness of the coating allowed mainly elastic strains in contact with the diamond cone, causing a small penetration to the coating surface and very shallow wear tracks. The wear process presumably proceeded through tribo-chemical interactions with oxide microchips spalling-off [127], accompanied by a negligible wear rate.

The high-Cr coating demonstrated a high tendency of crack formation during pulsed-plasma deposition. The merging of cracks led to a closed crack network, which covered the entire coating surface (Fig. 5.6, b). The most probable reason for cracking are the tensile stress generated in the coating [128] under its deformation (ε) upon cooling from the solidus temperature (T_{sol}) to room temperature (RT):

$$\sigma = \frac{\varepsilon \cdot E}{(1-\nu)}, \tag{5.1}$$

where E is Young's modulus and ν is Poisson's ratio.

The total deformation can be considered as a sum of thermal contraction (ε_T) and the linear effect of phase transformation (ε_{PT}).

$$\varepsilon = \varepsilon_T + \varepsilon_{PT}. \tag{5.2}$$

The constituents of Equation (5.2) can be roughly found as:

$$\varepsilon_T = \alpha_A (T_{sol} - Ms) + \alpha_A f_A (Ms - RT) + \alpha_M f_M (Ms - RT), \tag{5.3}$$

$$\varepsilon_{PT} = \frac{f_M \cdot \Delta V_{A \to M}}{3}, \tag{5.4}$$

where α_A and α_M are the linear thermal expansion coefficients of austenite and martensite, respectively; f_A and f_M are the volume fractions of austenite and martensite, respectively; M_s is the starting temperature of martensitic transformation; ΔV is the volumetric effect of austenite → martensite transformation.

According to XRD analysis results, the as-deposited coating matrix contained 84 vol.% and 16 vol.% of the αFe phase. It can be assumed that αFe appeared from martensitic transformation; hence, the M_s temperature could be derived from the Koistinen-Marburger equation.

$$f_M = 1 - \exp(-a_m \cdot (M_s - TQ)), \tag{5.5}$$

where α_m is a fitting coefficient (0.008 for Fe-1.86 vol% C alloy [129]); TQ is the quenching temperature (20 °C).

Now, taking f_M = 16 vol%, the M_s temperature was calculated as 42 °C. The tensile stress was calculated according to Equations (5.1)–(5.5) using the following parameters: T_{sol} = 1320 °C [49], E = 200 G Pa [130], ν = 0.22 [131], $\alpha_A = 18.6 \times 10^{-6}\ K^{-1}$, and $\alpha_M = 13.9 \times 10^{-6}\ K^{-1}$ [132]. The volumetric effect of austenite → martensite transformation was derived from the equation: $\Delta V_{A \to M} = 2.5–1.08 \cdot (C_\gamma\ \%)$ [133] assuming a carbon content in austenite (C_γ %) of 1.50 wt. %. Eventually, the stress in the as-deposited coating was calculated as 5832 M Pa, which is almost an order of magnitude higher than the ultimate tensile strength (UTS) of austenite. This stress was not relieved through plastic deformation because of superfast cooling after plasma heating, thus it was relieved through the crack formation.

A similar cracking phenomenon was previously observed in pulsed-plasma coating deposited using the cathode made of a high-speed steel of

T1 AISI grade. The chemical composition of this steel (about 0.8 wt. % C, 18 wt. % W, 4 wt. % Cr, 1 wt. % V) was appropriate for the formation of a coating with fully austenitic matrix [14]. Completely different cracking behavior was demonstrated by pulsed-plasma coating having a martensitic matrix [134]. The martensitic coating was deposited in an EAPA chamber using a cathode of AISI 1020 low-carbon steel. Due to plasma-induced carbon enrichment [3], the coating possessed a high-carbon martensite structure (750 HV) with no cracks. Assuming f_M = 90 vol. % and f_A = = 10 vol. %, the Ms temperature was estimated as 310 °C (Eq. 5.5). Based on the above calculations, the stress value for martensitic coating was found as 2524 MPa which is two-fold lower than that for austenitic matrix. The decrease in the stress was due to the compensation of thermal contraction (tensile stress) by the expansion caused by austenite → martensite transformation (compressive stress). The stress level was compared with the martensitic UTS which was derived from the correla-tion proposed in [135]:

$$\text{UTS (MPa)} = 3.734 \cdot \text{HV} - 99.8. \tag{5.6}$$

Equation (5.6) was valid for the hardness range of 129–592 HV, and its extrapolation to 750 HV yielded a UTS value of 2701 MPa. Therefore, the stress calculated for the martensitic coating (2524 MPa) was lower than its UTS preventing crack formation. Concluding, the austenitic matrix is not appropriate for the pulsed-plasma coating since it promotes crack formation due to its lower specific volume. By contrast, martensite has a much bigger specific volume (tetragonal lattice), contributing to crack prohibition. This issue should be considered when selecting a cathode material for coating deposition.

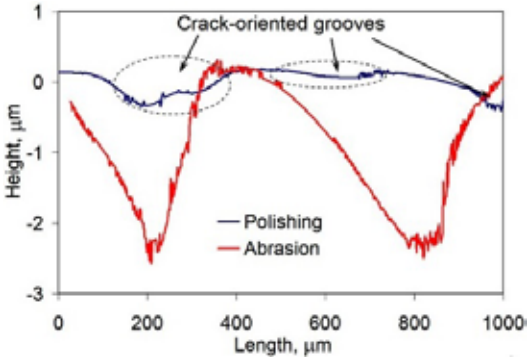

Figure 5.10 – Surface profile of the coating after polishing and abrasive wear testing

Cracking is a drawback of the studied high-Cr coating [136] since cracks accelerate abrasion at the crack edges. This resulted in a specific convex-shaped relief with the formation of grooves along crack edges and bulges between cracks. It is noticeable from (Figure 5.10) that even after a smooth polishing the grooves of about 0.5 μm depth appeared. During abrasive tests, localized wear led to increase in the grooves depth to about 2.5 μm. However, the surface roughness between cracks in convex-shaped areas was very low, reflecting an improved wear behavior of the coating. Thus, the coating abrasive response could be much higher if cracks are absent.

Moreover, the convex-shaped relief caused a "jumping" of the diamond cone resulted in the surface impacting. Due to an increased coating hardness, the diamond cone penetrated slightly and caused high stress in the contact spot. Under the impact, the stress increased very fast and led to local brittleness and spalling the coating. In contrast, dry-sliding against steel and SiC balls did not cause surface spalling, and it can be ascribed to lower stress in the contact spot of the "ball/plane" contact scheme.

The research showed the advantages and drawbacks of the plasma-deposited high-Cr coating. The coating has advanced wear behaviour and it is promising for the abrasive and dry-sliding applications when the local high-stress contacting is limited. An additional improvement of tribological abilities of the coating could be achieved by preventing cracking by means of obtaining the as-deposited martensitic matrix or by forming a composite structure in which the precipitates would decrease the thermal contraction of an austenite matrix. These approaches imply further intensive research. After overcoming the above shortcoming, the pulsed-plasma chromium carbide coating can be used to strengthen wear-loaded tool steels for cold stamping and forming of hybrid car bodies', components of rolling equipment, die forms, etc.

The following conclusions from this chapter can be drawn:

A high-chromium coating of 210–250 mm width was fabricated on the surface of grey cast iron by atmospheric pulsed-plasma treatment using an eroded cathode made of high-Cr cast iron (2.3 wt.% C-27.4 wt.% Cr-3.1 wt.% Mn). The as-deposited coating had a γFe (84 vol.%)/αFe (16 vol.%) matrix with a low amount of carbides. Post-plasma heat treatment resulted in the precipitation of M_7C_3 carbides leading to the coating microhardness of 990–1180 HV and a microstructure consisting of 48 vol.% carbides (M_7C_3, M_3C), 48 vol.% martensite, and 4 vol.% retained austenite.

Under pulsed-plasma deposition the plasma-induced melting of the substrate took place leading to a transitional layer of 8–25 μm width. The formation of the coating microstructure under post-plasma heat treatment occurred under counter-diffusion flow of Cr, Mn atoms from the coating to the substrate and the movement of C atoms toward them. This phenomenon led to a smooth elemental/structural gradient through low-carbide transition layer/ ferrite/ martensite zones, providing a good metallurgical bonding between the coating and the substrate.

The heat-treated coating performed the improved wear characteristics comparing with grey cast iron (non-heat-treated and heat-treated conditions):

- *by 3.0–3.2 times higher abrasive wear resistance;*
- *by 1.8–3.9 times lower volume loss (sliding against 100 Cr 6 steel ball);*
- *by 1.2–1.7 times lower volume loss (sliding against SiC ball);*
- *by 51.8–1208.8 times lower volume loss (sliding against a diamond cone).*

The coating manifested a tendency of solidification cracking caused by tensile stress due to the formation of a mostly austenitic structure with a lower specific volume. Cracks locally facilitated abrasion wear and caused occasional spalling under sliding against the diamond cone. Under sliding against 100Cr6 steel ball and SiC ball cracks negligibly affected the coating wear mechanism.

The content of the Chapter is adopted from Evaluation of the microstructure, tribological characteristics, and crack behavior of a chromium carbide coating fabricated on gray cast iron by pulsed-plasma deposition / Y. Chabak, V. Efremenko, M. Džupon, K. Shimizu, V. Fedun, K. Wu, B. Efremenko, I. Petryshynets, T. Pastukhova // Materials. 2021. Vol. 14, no. 12. P. 3400. https://doi.org/10.3390/ma14123400

Chapter 6. PULSED PLASMA DEPOSITION OF Fe-C-Cr-W COATING ON HIGH-Cr-CAST IRON

Plasma-assisted treatments belong to the most promising technologies of surface engineering. They can perform synchronous surface modification, strengthening and protective coating deposition on a variety of metallic materials [12, 137, 138]. Among these methods, the pulsed plasma techniques (PPTs) stand out due to the expanded capabilities of surface property improving arising from additional beneficial factors, such as shock-wave-induced strengthening and radiation stimulated diffusion [11, 13, 139, 140]. PPTs may employ various devices based on different working principles of plasma flux generation [13, 140]. One of them is the electrothermal axial plasma accelerator (EAPA) with gas-dynamic working regime [1, 33]. EAPA generates a pulsed high voltage discharge in air with subsequent formation of plasma flux. Upon contact with the plasma, substrate subsurface modification takes place. As reported in [12], surface heating of tool steels with high velocity plasma is followed by surface quenching, which results in the formation of a modified layer of super-hard martensite [12, 139]. Furthermore, EAPA cathode material may be transferred by the plasma flux (atoms, ions, microdroplets) and deposited as a coating on a modified surface. EAPA has successfully been adopted for [1, 2, 33, 63]: a) excitation of elastic pulses in the fluid, b) surface modification of steels, c) metallic nanostructure formation and d) protective coating deposition.

The composition and structure of the deposited coating largely depend on the EAPA cathode and inner channel materials, which are subjected to evaporation and/or melting under the electric discharge [2]. The amount of substance to be transferred by plasma flux, as well as the coating thickness, are strongly affected by the physical properties of the cathode material (thermal capacity and conductivity, melting temperature, evaporation temperature, vapor pressure, etc.) [63]. When the cathode consists of a refractory material (graphite, W, Mo etc.), then evaporation is mostly responsible for the substance transfer [141]; as a result, thin and non-uniform coatings are formed. If the cathode material melting point is lower than that of a common refractory material, evaporation could be accompanied by cathode melting, which results in micro-droplet transportation via plasma

flux; thus, thicker and more uniform coatings are formed. By combining different cathode materials in an alternating mode of deposition, it is possible to deposit multi-layered coatings with gradient microstructure and properties. The formation of gradient structures is reported as a most promising approach to improve the tribological behavior of many materials, such as ceramic composites [142, 143], alloys [144], coatings [145]. A post-deposition heat treatment can also be considered as a complementary stage for improving coating properties [38, 146]. Investigations focused on the selection of a proper EAPA cathode material for multi-component coatings with desired properties, as well as on the effect of post-deposition heat treatment are so far in initial stages.

High-chromium cast irons (HCCI) are well-known materials for tribotechnical applications. They are characterized by high wear resistance due to the presence, in their structure, of significant volume fractions (VF) of hard phases – carbides, nitrides, borides etc. [35, 147, 148]. As a rule, these alloys are subjected to bulk heat treatment (HT) in order to increase their hardness and wear performance [149, 150]. However, the HT HCCIs do not always meet the growing demands for operational durability. The improvement of HCCI tribological properties could be based on surface engineering approaches, in particular, on the use of plasma-assisted technologies. Plasma treatment has been shown to be highly effective for surface hardening of a casting made of gray or ductile cast iron [151, 152]. Nevertheless, adopting plasma-assisted treatments for HCCI strengthening still remains essentially unstudied. Taking into account the above considerations, a multi-layer coating resulting from the combination/alternation of two cathode materials (T1 high speed steel and super-high Cr cast iron) was deposited on an HCCL by EAPA aiming to investigate: a) the relationship between cathode material and coating layer microstructure/hardness and b) the effect of post-deposition heat treatment on the coating features.

Experimental procedure. HCCL was used as a substrate; its nominal composition is presented in Table 1. As cast HCCL in the form of plates of dimensions of 10 × 10 × 25 mm was subjected to annealing at 650 °C for a period of 20 h [153]. After heat treatment (HT), the specimens were polished (R_a = 0.2 μm) to remove 0.5 mm of decarburized upper layer.

Coating deposition was carried out by EAPA. Two alloys were used as cathode materials alternately deposited in the coating: T1 high speed steel (W 18) and super-high Cr cast iron (Cr 28). Their chemical compositions are given in Table 6.1. Regarding the W 18 cathode, the tail portion of com-

mercial T1 high speed steel (HSS) drill of 5 mm diameter was used in the as-manufactured state. Regarding the Cr 28 cathode, a cast rod of 5 mm diameter was used in the as-cast state. The carbide volume fractions (CVF) of the cathode alloys are also included in (Table 6.1). The cathode materials were selected on the following grounds:

(a) The coatings to be formed should have a higher content of strong carbide-forming elements in relation to their substrate, so that, higher carbide volume fractions (chromium rich carbides (M_7C_3, $M_{23}C_6$) or tungsten rich carbides (M_6C, M_2C)) and, consequently, a higher wear resistance could be attained.

(b) The coatings to be formed should have an appreciable thickness due to the relatively low cathode melting point (in comparison with the melting point of a cathode consisting of a refractory material). As aforementioned in the Introduction, the lower the solidus temperature the easier cathode melting, thus enhancing micro-drop transfer and, consequently, coating thickness.

Table 6.1 – Chemical compositions (wt.%) and CVFs (vol.%) of substrate and cathode materials

Materials		C	Cr	W	Mn	V	Si	Ti	Ni	CVF
Substrate	HCCL	2.60	14.50	–	3.96	0.10	1.38	0.10	0.21	–
Cathode	W18	0.75	3.85	17.92	0.34	1.07	0.30	–	–	16.0
Cathode	Cr28	2.34	27.39	–	3.13	–	1.26	0.20	–	34.5

The solidus temperature of T1 steel was determined as the temperature of "L → austenite + M 6 C" eutectic reaction [154], which had been estimated by Halfa [155] to take place at 1342 °C. This also follows from Fig. 6.1 which presents the equilibrium temperature-concentration phase diagrams of the systems Fe-18%W-4%Cr-1%V–C and Fe-28wt%Cr-2wt%Mn-1.3wt%Si-C, calculated using the Thermo-Calc software. As shown in Fig. 6.1, b, eutectic reaction "L → (austenite + M_7C_3)" occurs at 1293 °C. Hence, solidus temperature values for W18 and Cr 28 are found to be much lower as compared to that of the refractory materials (graphite (~ 3700 °C), W (3422 °C), Mo (2623 °C)), which usually serve as cathode in plasma-generating devices. Therefore, it is expected that employing W18 and Cr28 in the PPT process would result in enhanced microdroplet-mass transferring.

The final coating was obtained after eight impulses. In order to achieve a laminated gradient coating, the cathodes were alternately substituted after every two impulses as follows: 1st and 2d impulses were carried out with

W18; 3d and 4th impulses – with Cr 28; 5th and 6th impulses – with W18; 7th and 8th impulses – with Cr 28 (2 pulses per coating layer). Coating deposition was followed by bulk HT: the specimens were heated up to 950 °C, retained at this temperature for 2 h and, then, oil quenched. HT was conducted in dry air while the specimens were covered by charcoal carburizing material in order to prevent surface oxidation. The PPT-treated specimens were investigated both in the as-deposited and HT states.

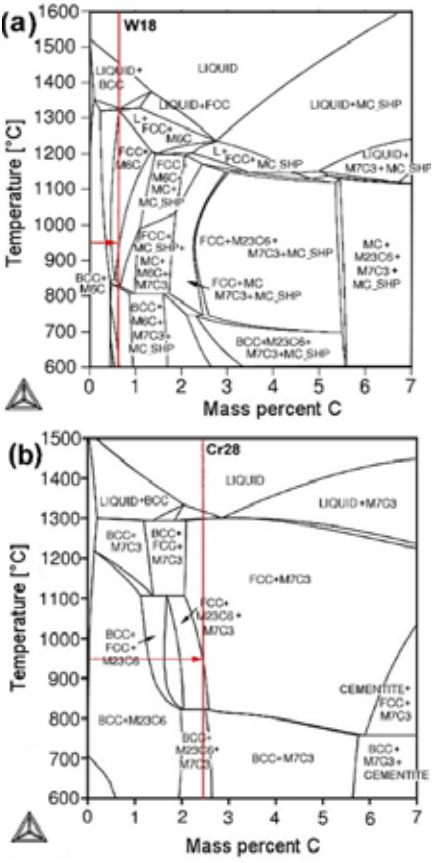

Figure 6.1 – Phase diagrams: (a) Fe-18%W-4%Cr-1%V–C; (b) Fe-28%Cr-2%Mn-1.3%Si-C

Microstructure of the substrate and cathode materials. The initial microstructure (i.e. before plasma treatment) of the HCCL substrate was that of "pearlite + M_7C_3" eutectic and dendrites consisted of pearlite (Fig. 6.2, a).

The presence of the just mentioned structural components is in agreement with the result of an earlier study [75] concerning HCCL of approximately the same chemical composition (2.7 wt.% C; 14.55 wt.% Cr; 2.2 wt.% Mn, 0.93 wt.% Ni) also annealed at 650 °C. The matrix microhardness was measured as 450 ± 31 HV.

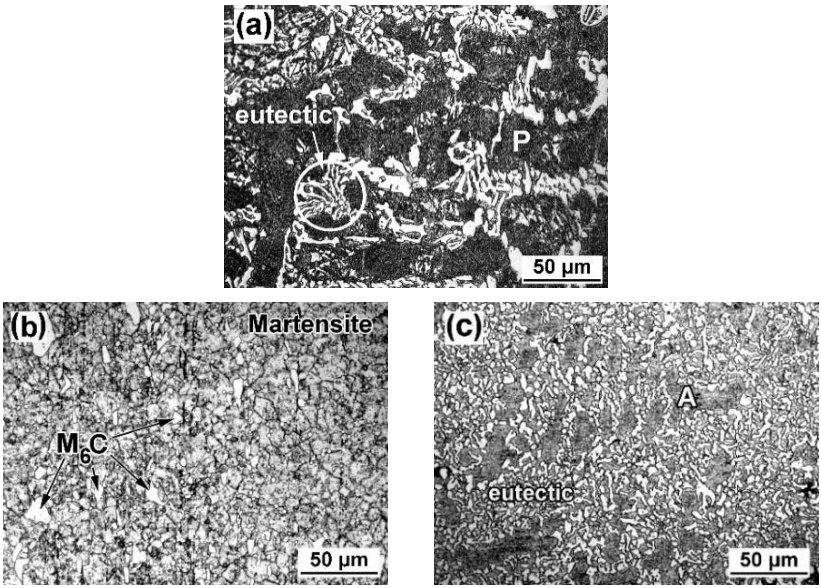

Figure 6.2 – The initial microstructure of (a) substrate (HCCI), (b) cathode W 18, and (c) cathode Cr 28 (P, A: pearlite, austenite accordingly)

The microstructure of the W18 cathode consisted of bulky and fine carbides distributed in a metallic matrix (Fig. 6.2, b). According to [156], the microconstituents of heat treated T1 HSS are martensite and M_6C (predominant amount), MC, $M_{23}C_6$ carbide phases. The CVF was measured as 16 vol.%. The microhardness of the W18 cathode material was measured as 945 ± 25 HV.

The microstructure of the Cr 28 cathode is shown in (Fig. 6.2, c). As can be seen, Cr28 is a hypoeutectic cast iron consisting of eutectic carbide and pre-eutectic dendrites of solid solution. XRD analysis revealed the presence of austenitic matrix, M_7C_3 and M_3C_2 carbides with the latter being of minor amount (Fig. 6.3, Table 6.2). The eutectic carbide VF was 34.5 vol.%. The matrix microhardness was measured as 335 ± 21 HV.

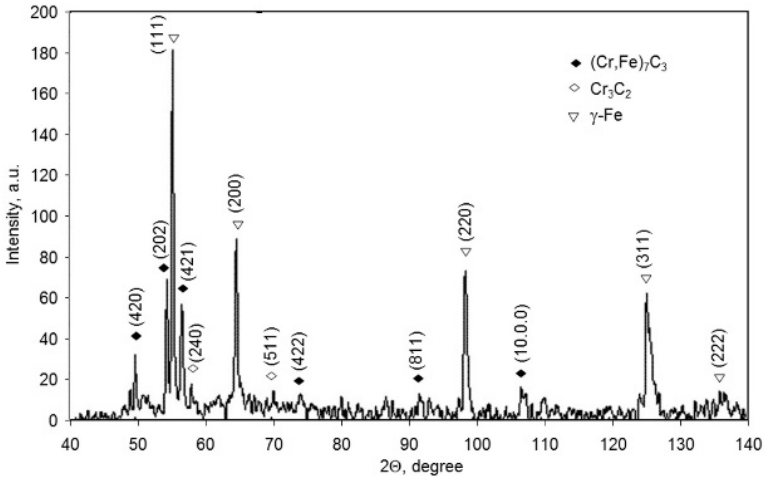

Figure 6.3 – XRD-pattern of Cr28 material; γ-Fe (4–0829), (Cr, Fe)$_7$C$_3$ (5–0720), Cr$_3$C$_2$ (5–0677)

Table 6.2 – The average precipitate volume fractions (vol.%) in the HT coating layers

Layers	A	B	C	D	E
CVF	61.3±3.0 / 15.2±1.1*	51.7±4.0	55.4±3.2	43.9±4.3	21.7±3.5

* *as-deposited state*

Fig. 6.4, a shows the microstructure of the as-deposited coating (optical, cross-section). As can be seen, the PPT resulted in the emergence of a light contrast layer ("white layer") of 80–120 μm thickness on the top of substrate. The white layer has a laminated texture, composed of alternating bright contrast ("white") and relatively dark ("gray") bands. Gray color is due to more intensive etching in areas of very fine structure of dark contrast (Fig. 6.4, b). A distinguished feature of this structure is a fine network of precipitates surrounding the grain boundaries (Fig. 6.4, c). Occasionally, roundish shrinkages are revealed inside the coating (Fig. 6.4, a). The free surface of the coating is wave-shaped. A clear boundary line between coating and substrate cannot be seen: the layer, which lies closest to the substrate, smoothly adjusts to the substrate structure.

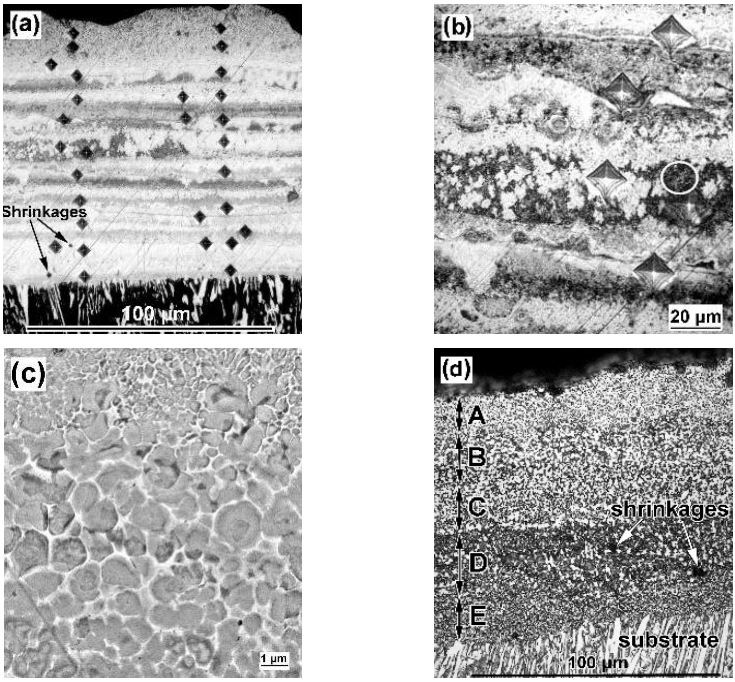

Figure 6.4 – The microstructure of coating and substrate (optical, cross-section) (a, b, c) as-deposited; (d) heat-treated (4 vol.% Nital); (c) presents the microstructure within the circle shown in (b)

Fig. 6.4, d shows that the post-deposition HT resulted in a drastic alteration of the coating microstructure. Nital-etching revealed that the coating consists of five heterogeneous layers obviously differing from each other. The top layer, presenting the brightest contrast, is layer A; its thickness is 15–25 μm. Similar morphological features are observed in layer C, which is lying in a distance of 30–50 μm from the coating surface. These two layers are separated by layer B of 15–25 μm thickness with coarser structure / bulkier "white" phase. Below layer C, a relatively dark layer (of darker contrast than layers A, B and C), layer D, is observed consisting of quite large light microareas against a darker background; the thickness of layer D is 14–30 μm. Below layer D, the light contrast dispersion becomes fine, dense and uniform, defining a layer adjacent to the substrate, layer E; layer E has a homogeneous appearance and a thickness of 11–18 μm. The absence of clearly defined boundaries between all the layers should be highlighted.

The microhardness profile of the as-deposited coating is presented in Fig. 6.5 (the black solid lines correspond to the plots of the mean values). Fig. 6.5, a shows that the measured microhardness values are widely dispersed within the range of 500–655 HV with an average value of 560 HV through the bulk of the coating. The large scatter of microhardness values is mostly owing to the laminating structure of the coating: generally the microhardness of the "white" bands is about 50 HV higher than that of the "gray" bands. Along the narrow layer delimiting the coating and the substrate, microhardness increases up to 700–750 HV; after that, it drops to 420–480 HV stabilizing at this level in the bulk of substrate.

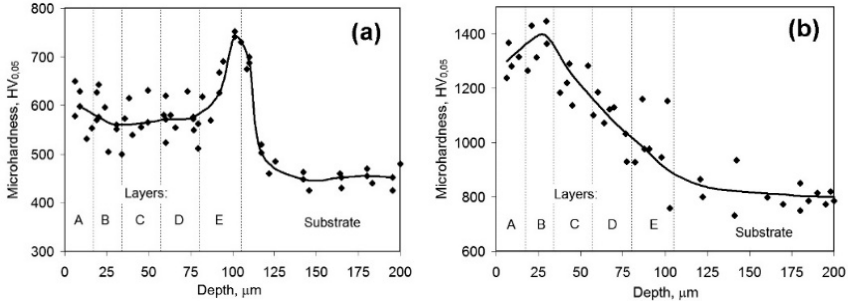

Figure 6.5 – The microhardness profile of coating and substrate (in cross-section): (a) as-deposited; (b) heat-treated

Fig. 6.5, b manifests significant strengthening of the coating caused by the HT-due microstructural changes. Layer A possesses microhardness of 1240–1360 HV with a mean value of 1300 HV The highest microhardness values were measured in layer B (1265–1445 HV with a mean value of 1400 HV). Microhardness through layers C, D and E decreases monotonically with depth, reaching 950–1050 HV in layer E. The substrate has a microhardness of 730–930 HV with a mean value of 800 HV, which is much lower than that of the coating but almost double the hardness of the substrate before HT.

A more detailed characterization of the HT coating microstructure can be accomplished using SEM observation (Fig. 6.6). Figs. 6.6, a and 6.6, c reveal great amounts of light contrast precipitates in layers A and C, respectively.

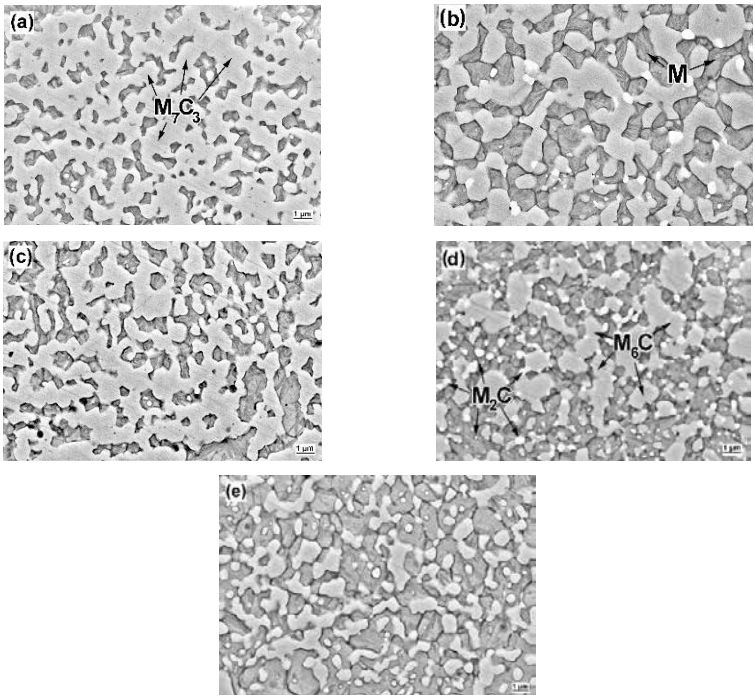

Figure 6.6 – The microstructure of coating (SEM, cross section, HT state): (a) layer A, (b) layer B, (c) layer C, (d) layer D, (e) layer E

In layer A, the precipitates form a massive net engulfing dark matrix grains; small roundish precipitates are seen inside matrix grains too. Layers B and D contain bulky light-colored contrast precipitates (1–4 μm in cross-section), which are surrounded by the matrix areas (Fig. 6.6, b, 6.6, d). A distinguished feature of the microstructure of layer B and D is the presence of numerous very fine (0.03–0.5 μm in cross-section) precipitates of bright-white contrast uniformly distributed within the matrix; some of them (mostly larger ones) are situated along the contour of the bulky precipitates. The needles of martensite are also discerned in the matrix of layers B and D (Fig. 6.6, b). The volume fraction of precipitates in the HT coating varies with the layer depth. As shown in (Table 6.2), the highest precipitate VF is found in layer A – 61.3 vol.%; the precipitate VF in layer C is somewhat lower (55.4 vol.%), whilst the lowest precipitate VF is found in layer E (21.7 vol.%).

Leyer-wize chemical element distribution. EDS mapping of the coating cross-section (after HT) showed that the observed laminated structure has been caused by an uneven chemical element distribution. (Fig. 6.7) illustrates the distribution of chromium, tungsten and iron within the coating. A comparison of these Figures with (Fig. 6.4, d) reveals that the "layer-to-layer" transition is owing to the alteration of chromium and tungsten concentrations.

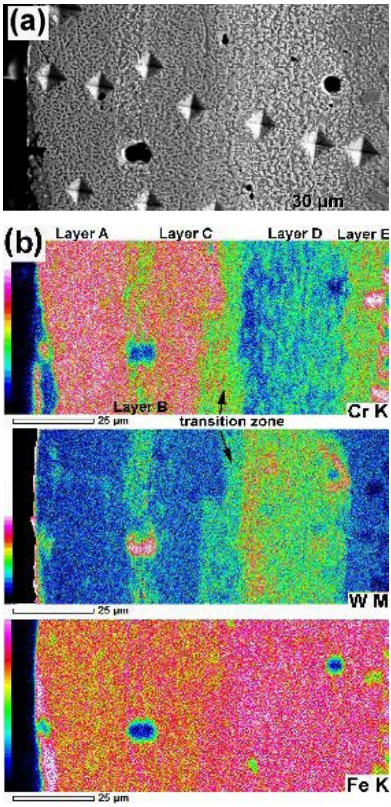

Figure 6.7 – (a) SEI-image of the coating cross-section (after HT) and (b) corresponding EDX mapping of Cr, W and Fe

Thus, layers A and C are enriched with chromium; they are separated by layer B which contains higher tungsten at the expense of chromium. Between layers C and D, a narrow diffusion zone is discerned with intermediate Cr and W contents. Layer D is enriched with tungsten, whilst impov-

erished in chromium. In contrast, adjoining (substrate and coating) layer E is poor in tungsten, while its chromium content is much lower comparing to layers A and C. Therefore, layer E can be identified as the transition zone between the coating and the substrate. Iron mapping shows that the concentration of Fe from the middle of the transition zone to the substrate surface is notably higher than that from the top of the coating to the middle of the transition zone. The gradient of the Fe concentration constitutes a strong evidence of the good coating/substrate adhesion.

The described distribution of Cr and W is the outcome of deposition with alternating cathode material; namely, layers A and C were deposited using Cr28 cathode, whereas layers B and D were obtained using W18 cathode. This is a major reason for the higher CVF contents in layers A and C as compared to layers B and D (Table 6.2). Cr28 cathode has higher content of carbon than W18 cathode (Table 6.1), allowing for higher CVFs in the resulting layers A and C.

Layer E origination was of special interest to be studied and discussed. The interlayer area between layers D and E is shown in (Fig. 6.8) in higher magnification. As it can be seen from the secondary electron (SE) image (Fig. 6.8, a), layer E includes net-shaped precipitates, which are similar to the precipitates of layers A and C. Additionally, massive eutectic carbide particles are observed within layer E. The distribution of elements with regard to their atomic number Z was evaluated by back scattered electron (BSE) imaging. According to (Fig. 6.8, b), carbide particles in layer D are brighter than their matrix, thus they are bound to be enriched with heavier element (presumably, W with Z = 74); the very bright contrast of the fine carbide particles indicates their higher content of tungsten. In contrast, layer E has a darker contrast throughout its volume, reflecting its relatively high content in lighter elements (Cr and/or Fe). (Indeed, Fig. 6.7 shows that layer E is richer in Cr than layer D.) Massive eutectic carbide particles and matrix appear dark, i.e. they are enriched with chromium (Z = 24), while the net-shaped precipitates appear slightly brighter, i.e. they are enriched with iron (Z = 26). So, layer E contains very few massive eutectic carbide particles; besides, it is poor in tungsten. Based on this observation, it is indicated that layer E is a modified substrate sub-surface layer, which was formed as a result of surface melting induced by the first plasma impulse using W18 cathode. Surface melting led to a eutectic carbide dissolution followed by smaller carbide precipitation during heat treatment. The above indication is in agreement with the low microhardness of layer E as compared to that of

the other coating layers (approaching the microhardness of the substrate). To conclude, the presence of transition layer E (manifested by gradients in microstructural features (Table 6.2), microhardness (Fig. 6.5, b) and chemical composition (Fig. 6.7) strongly suggest the high adhesion of the coating to the substrate. Moreover, the coating interlayer transition zones noted in (Fig. 6.7) are considered to reduce interlayer stresses and increase interlayer adhesion as well.

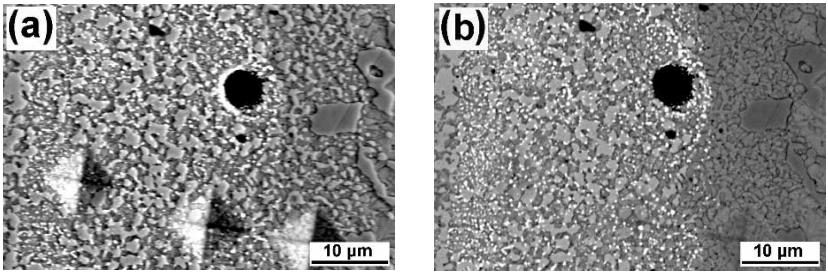

Figure 6.8 – D/E interlayer area: (a) SEI-image; (b) BSE-image illustrating layer D (lighter contrast) and layer E (darker contrast)

XRD- and point EDS-analysis. The XRD diffractograms of the coatings in the as-deposited and HT states are given in (Fig. 6.9). The XRD-pattern of the as-deposited coating surface (Fig. 6.9, a) shows that the top of coating consists of matrix phases γ-Fe (austenite) and α-Fe (ferrite) and carbide phases – M_3C, $M_{23}C_6$. Peak intensities indicate that γ-Fe and cementite are the main matrix and carbide phases, respectively. Austenite peak (111) is shifted to diffraction angles smaller those observed for the PDF cards. This behavior could be attributed to a supersaturated state of austenite as a result of its fast solidification upon deposition. Analogous XRD features were reported by Totten et al. [157] regarding austenite supersaturated with nitrogen after plasma nitriding. It is most likely that α-Fe is martensite (i.e. distorted ferrite), as suggested by the diffraction angles, which are slightly displaced from the ones corresponding to α-Fe, according to the PDF cards and the increased microhardness of the as-deposited coating. The microhardness values achieved are 600–655 HV, which are almost three times higher than those of highly-alloyed austenite in non deformed Hadfield steel (215–230 HV) [158].

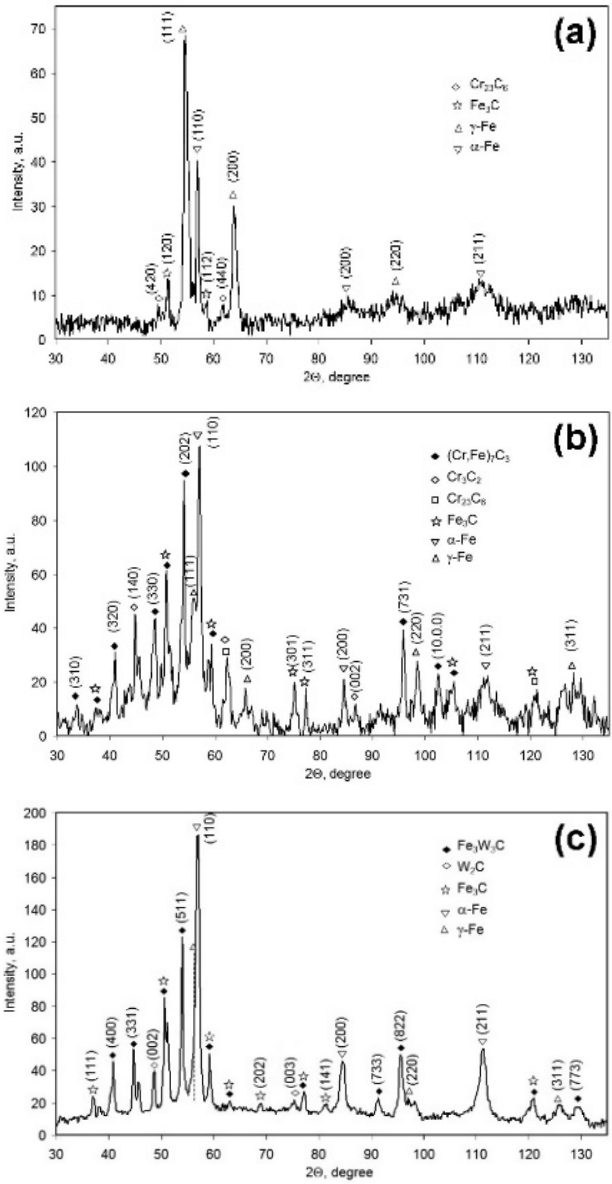

Figure 6.9 – XRD-patterns: α-Fe (6–0696), γ-Fe (4–0829), $(Cr, Fe)_7C_3$ (5–0720), Cr_3C_2 (5–0677), Fe_3C (35–0772), $Cr_{23}C_6$ (35–0783), Fe_3W_3C (3–0980), W_2C (2–1134). (a) as-deposited layer A, (b) HT layer A and (c) HT layer D

The XRD pattern of heat treated top layer A (deposited with Cr28 cathode) manifests that martensite has become the main matrix phase and M_7C_3 the main carbide phase. The carbide presence is more abundant in comparison with as-deposited layer A, as deduced from the higher intensities and occurrence of the respective peaks, most likely due to diffusion of C and Cr from the supersaturated austenitic lattice to the carbide phases during HT. Cr diffusion has led to the precipitation of carbides that can accommodate higher amounts of Cr in their structure (Cr_3C_2, $M_{23}C_6$ and M_7C_3) [66] than M_3C (predominating carbide stoichiometry in as deposited layer A). Therefore, the XRD patterns are compatible with the microhardness data (compare Figs. 6 a and 6 b). More analytically, the peaks of carbides M_7C_3, Cr_3C_2, $M_{23}C_6$ and M_3C are revealed (Fig. 10 b). Some of these peaks may be assigned to more than one carbide types, making, thus, carbide identification difficult. Anyway, four strong peaks can uniquely be assigned to (320), (330), (202), (731) peaks of M_7C_3. Similarly, some peaks can uniquely be assigned to (301), (311) peaks of M_3C and (140), (002) peaks of Cr_3C_2. Based on the XRD results, it is indicated that the net-shaped carbides shown in (Fig. 7 a) are mostly hexagonal Cr-rich M_7C_3 carbides. The predominance of M_7C_3 over $M_{23}C_6$ and Cr_3C_2 is attributed to the fact that the free energy of formation of chromium carbides follows the order: $\Delta G_f^o(Cr_7C_3) < \Delta G_f^o(Cr_{23}C_6) < < \Delta G_f^o(Cr_3C_2)$ [159]. The metallic matrix in HT layer A consists of austenite and α-Fe (martensite); according to the relative intensities of α-Fe and γ-Fe reflections, martensite is the predominant phase in the matrix.

The diffractogram of coating layer D was received after smooth polishing to remove layers A, B and C. Layer D, deposited with W18 cathode, contains carbides M_6C (Fe_3W_3C), M_2C (W_2C) and M_3C (Fig. 6.9, c). The highest carbide peak intensity (511) corresponds to M_6C, whereas the lowest one (141) corresponds to M_3C. The metallic matrix is mostly martensitic. Minor peaks (002) and (003) are assigned to M_2C. Based on these results, it is strongly suggested that the bulky precipitates in (Fig. 7 d) are M_6C-type, while the fine sized bright W-rich precipitates are M_2C-type. XRD analysis was supplemented by EDS point analysis. Here, it should be noted that the analyzed phases (especially the matrix) were dimensionally less than the spatial resolution of EDS quantitative analysis, as shown in (Fig. 6.10). So, it is acknowledged that the quantitative EDS results do not exactly characterize the chemical composition of the phases because their composition is likely affected by the surrounding areas; however, they can reveal qualitative trends and rough differences. Furthermore, carbon analysis is not included,

because EDS quantitative analysis of carbon in an electron microscope is difficult, owing to the low energy of the Carbon x-ray K line and its consequent easy absorption, as well as hydrocarbon contamination [160].

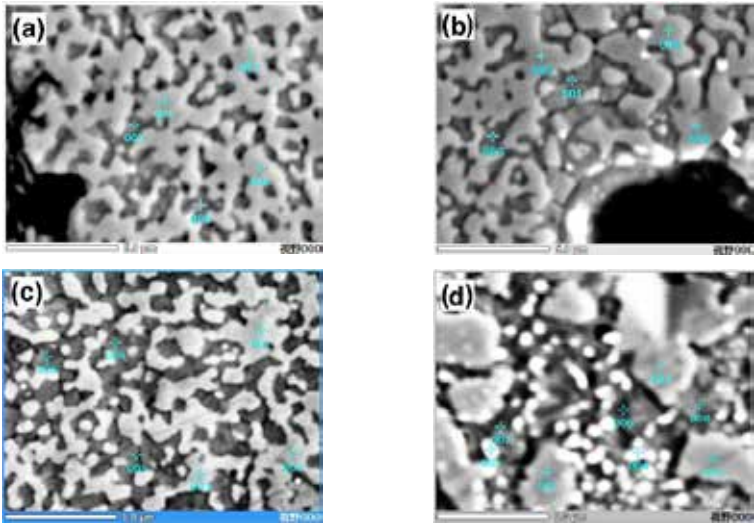

Figure 6.10 – Indicative points of EDS analysis in coating:
(a) layer A, (b) layer B, (c) layers C and (d) D

The phases of layer A are enriched with chromium: its concentrations in carbides and matrix have been measured as 30.2 wt.% and 25.6 wt.%, respectively. The latter value is probably excessive because of the effect of the carbide net that surrounds the small matrix areas (0.1–1 μm in diameter). It is noted that 3.0 wt.% W was found in the carbides despite layer A having been deposited with Cr 28 cathode. Manganese is partitioned between matrix and carbides with a slight prevalence in the carbide phase. Approximately the same alloying element distribution was observed for layer C, as well.

The matrix of layer B was found slightly alloyed with tungsten (0.9 wt.%) while the chromium content (13.9 wt.%) was lower as compared to layer A. The carbides in layer B are alloyed with tungsten and chromium: bulky carbides contain 26.9 wt.% Cr and 15.4% W, whereas fine carbides contain 12.4% Cr and 40.3 wt.% W. Thus, fine carbides are enriched with tungsten, which proves the BSE observation (Fig. 6.8, b). The qualitative diferences of the W concentration in the matrix, bulky carbide particles and fine carbide

particles are demonstrated in the EDS spectra of (Fig. 6.11). Although layer B was deposited using W18 cathode, relatively high chromium contents in its phases are noted, supposedly due to Cr diffusion from adjacent layers A and C. Enrichment of bulky M_6C particles with chromium lowered iron content (as compared with layer D) which presumably provided the increased carbide hardness. This sequence of diffusion events can explain the maximum on microhardness profile assigned to layer B (Fig. 5.6, b). More specifically, the highest hardness of layer B (despite the CVF that is lower than that of layers A and B) is mostly attributed to: a) the high contents of W and Cr in both bulky and fine carbide precipitates, and b) the fine dispersion of W-rich carbides in the matrix.

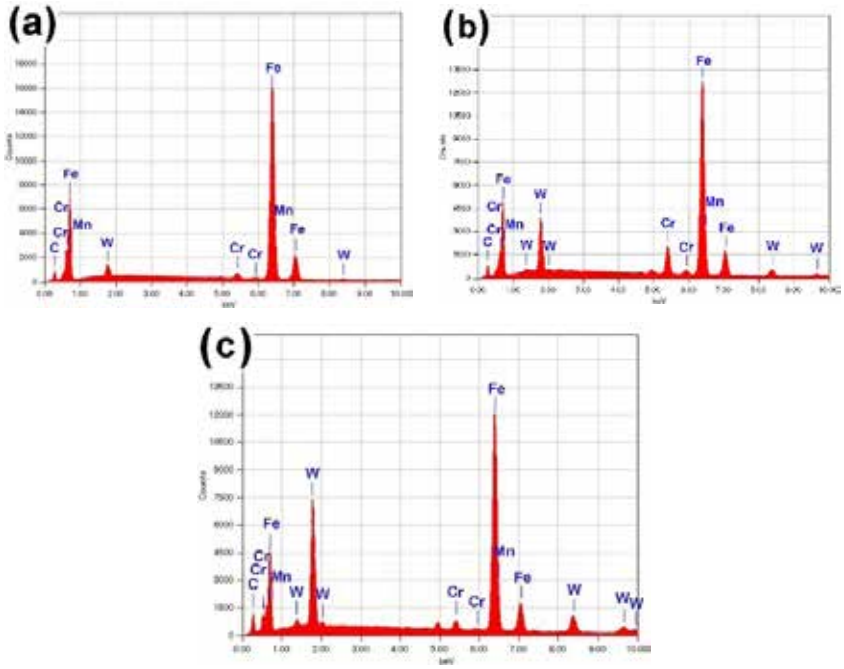

Figure 6.11 – EDS spectra showing qualitative chemical composition of distinct constituents in layer D: (a) matrix, (b) bulky carbide, (c) fine carbide

In comparison with layer B, the matrix in layer D presents higher tungsten and lower chromium concentration. The carbide particles in layer D were found to be enriched with iron and depleted of carbide-forming elements: the bulky carbides were found depleted of Cr by more than 50%;

the fine carbides were found depleted of W by nearly 10 wt.%. The latter is assumed as underestimating: due to the small size of the fine carbide particles, EDS analysis results have (most likely) greatly been affected by the surrounding matrix. In general, layer D presents the lowest hardness amongst layers A, B and C mostly because of the lowest CVF.

Discussion on as-deposited coating. The data presented above show that pulse plasma treatment has led to a modified (by melting) sub-surface zone of HCCL. This modified zone has acted as an underlayer for the PPT coating providing a smoother transition from the substrate to the coating microstructure. Due to the high temperature of the plasma flux, each deposited layer melts down the previously deposited layer, thereby forming a multilayer coating, where interlayer boundaries are fused together, as follows from the microstructure observations.

According to evaluation by Kolyada et al. [2], the temperature of plasma in EAPA reaches 10000 K that is higher than the melting point of carbides (2730 °C – for W_2C and 1755 °C – for Cr_7C_3 [161]). Thus, the electric discharge inside EAPA could cause complete melting (dissolution) of carbides in a thin layer of the cathode surface subjected to plasma heating. This assumption has been proved by microscopic examination of the as-deposited coating, which showed the absence of any coarse carbide that pre-existed in the raw materials (compare Figs. 6.2, b, c with Fig. 6.4, a).

Melted-evaporated cathode substance was transferred to the substrate surface to be rapidly solidified. In equilibrium conditions, alloys W18 and Cr28 solidify according to eutectic reactions "L → austenite + M_6C" (W18) and "L → austenite + M_7C_3" (Cr 28) that result in eutectic carbide crystallization (Fig. 6.1). During PPT-deposition, this mechanism changed because of ultra-fast ion condensation and microdroplet crystallization on the substrate surface. In the condition of suppressing of atom movement, the appearance of eutectic carbides became kinetically unfavorable, thus carbon and carbide-forming elements were retained in liquid state until the end of solidification. This resulted in a coating with a structure consisting of supersaturated austenite and α-Fe-based solid solution (Fig. 6.9, a).

A similar "solute trapping" effect has been observed by Fenech et al. [38], Hemmati et al. [39], Vamsi Krishna and Bandyopadhyay [45] in coatings deposited by different laser deposition techniques. These authors have noted the necessity of post-deposition HT to decompose supersaturated matrix in order to improve coating properties. Alternatively, Michaiski and Olszyna [162] found dispersed M_6C particles in an as-deposited tungsten

high speed steel (T1)-coating obtained by PPT. They explained this finding by heat accumulation in the coating induced by repeated plasma impulses. In the present work, the combination of "solute trapping" and cumulative heat-induced transformations was detected.

In the course of deposition of each layer, the previously deposited layer undergoes heating and deformation induced by plasma flux. This causes phase transformations in the heat-affected zone (HAZ), such as: (a) martensite tempering; (b) carbide precipitation from the austenite followed by (c) the transformation of the depleted austenite to ferrite. Owing to fast "heating-cooling", carbides precipitate as a fine cementite carbide network, as suggested by (Fig. 5 c) and the XRD pattern in (Fig. 6.9, a). (This carbide phase is kinetically more favorable because its formation does not require any substantial fluctuations of W and/or Cr atoms). Thus, a sandwich-like structure composed of alternating carbide-poor martensite/austenite (M/A) layers and HAZ layers forms (Fig. 6.12). The microhardness of carbide-poor (light contrast) bands is higher, which is attributed to the "austenite/martensite" structure. Darker HAZ-bands are somewhat softer (as aforementioned in 3.2), most likely because of partial martensite tempering and austenite → ferrite transformation. Hence, the above explanation accounts for the alternating grey-white bands observed in (Fig. 6.4, a).

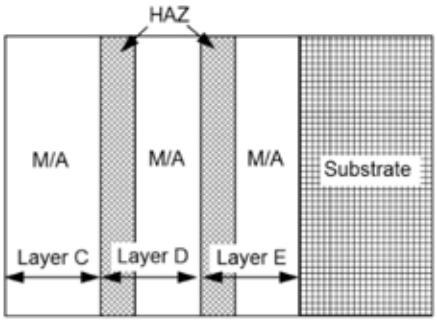

Figure 6.12 – The as-deposited coating structure

Discussion on heat treated coating. The as-deposited coating is thermodynamically unstable due to the supersaturated solid solutions. It can turn to the stable state through carbide precipitation at temperatures of elevated Cr and/or W atoms diffusivity. In this work, stable state was attained by post-deposition heat treatment. Based on the calculated using Thermo-Calc the phase diagrams of (Fig. 6.1), heating at 950 °C would lead

to "austenite + M_7C_3" and "austenite + M_6C" for Cr28 and W18, respectively. The isothermal treatment in this area promoted the depletion of austenite by carbon and carbide-forming elements (W, Cr, Mn), leading to the formation of large number of carbides in the coating (compare Fig. 6.4, a with Fig. 6.4, c). The high temperature and prolonged isothermal treatment allowed the formation of thermodynamically stable carbides in accordance with the equilibrium phase diagrams (Fig. 6.1). Carbide precipitation led to a sharp increase in the coating microhardness: the microhardness of layers A and B (1250–1450 $HV_{0.05}$) is close to that of pure carbides M_7C_3 and M_6C (1600–1800 HV [163]). Thus, the post-deposition heat treatment is proved to be an important stage for coating property improving.

Isothermal HTs of as-cast HCCIs at 900–1000 °C usually aim at the precipitation of fine secondary carbides of M_7C_3 and $M_{23}C_6$ stoichiometries [147, 149, 150, 164]. These have most likely nucleated as nanosized particles [47] mostly on defects inside austenite grains due to Cr atoms volume diffusion [150]. In contrast, in Cr 28-deposited layers, precipitation has led to the formation of relatively coarse carbide particles in the form of a carbide network, as illustrated in (Fig. 6.6, a, b and Fig. 6.11, a and c). Presumably, they nucleated at grain boundaries and their growth was controlled by a mechanism of grain boundary diffusion. Owing to a lower activation energy, this mechanism can provide the intensive diffusion flux of Cr atoms required for the formation of bulky carbides. Since austenite has variable carbon solubility, some dissolution of carbides could occur at 950 °C. Regarding the HT W18-deposited layers, similar arguments can be raised bearing in mind that W18-steels in practice are subjected to hardening HT at 1200–1300 °C, where carbides are dissolved in austenite, which, by quenching, is then transformed to a stable and hard martensite; tempering is applied at 550–600 °C leading to precipitation of fine M_2C coexisting with remaining coarse primary M_6C carbides [165]. Based on: (a) the above facts, (b) the minimal content of W dissolved in the matrix of layer B and (c) the extensive presence of bulky M_6C in the microstructure of layer B, it is obvious that the microstructure of the HT W18-deposited layers is neither a case of carbide dissolution in matrix nor a case of tempering. Therefore, the kinetics of isothermal carbide precipitation in the coating should further be studied. Such an approach will allow the selection of the optimal post-deposition heat treatment mode in order to obtain the maximum coating hardness.

The amount of carbides in the HT coating should also be discussed in further detail. As shown in (Table 6.2), the carbide volume fractions in the

coating layers are much higher (by 2–3 times) in comparison with those of W18 and Cr28 alloys (Table 6.1). This suggests that during PPT, a by-process has occurred leading to carbon enrichment of the coating in relation to the cathode materials. This process is most likely erosion of the inner channel walls of the EAPA by the pulsed plasma. Since the channel is made of paper-reinforced bakelite $(C_6H_6O \cdot CH_2O)_n$, carbon atoms can easily be released as a result of paper burning and polymer decomposition under high-current discharge. Released carbon atoms are transferred by the plasma flux to the substrate surface, where they saturate the liquid microdroplets of the cathode material. This extra-carbon causes the formation of extra carbide particles as compared to the carbide VF of the cathode materials which could improve the coating wear resistance (besides hardness). However, plasma-induced carbon enrichment may decrease ductility, a matter that may be faced with proper heat treatments. These issues are the subject of on-going research by the authors. It should be noted that even after ten depositions, the microstructure and the microhardness values were reproducible. Every ten depositions, the material of the tube walls was replaced in order to keep the microstructure and the related properties under close control.

It was also of interest to evaluate the carbon enrichment of the coating layers with respect to the cathode materials. For this purpose, Thermo-Calc calculations for Fe-28wt%Cr-2wt%Mn-1.3wt%Si-C alloys were carried out. The results of calculations are demonstrated in (Fig. 6.13), in terms of mass fractions (MF) of carbide phases versus temperature in alloys with different carbon contents. As follows from (Fig. 6.13), Thermo-Calc predicts the MF of $M_{23}C_6$ and M_7C_3 – at 2.2 wt. % C (that corresponds to Cr28), and M7C3 – at 4.0 and 5.5 wt. % C; total carbide mass fractions varied within the range of 35–67 wt. %. In order to be able to compare the data with the carbide VFs in the coating layers, MF was converted to VF according to the following relation:

$$VF = \frac{\dfrac{MF_{M_7C_3}}{\rho_{M_7C_3}} + \dfrac{MF_{M_{23}C_6}}{\rho_{M_{23}C_6}}}{\dfrac{MF_{M_7C_3}}{\rho_{M_7C_3}} + \dfrac{MF_{M_{23}C_6}}{\rho_{M_{23}C_6}} + \dfrac{MF_{\gamma}}{\rho_{\gamma}}} \times 100\% \qquad (6.1)$$

where, $MF\gamma$, MFM_7C_3, $MFM_{23}C_6$: mass fractions of austenite, carbides M7C3 and $M_{23}C_6$, accordingly; $\rho\gamma$, ρM_7C_3, $\rho M_{23}C_6$: density of austenite (7.85 g·cm^{-3}) and carbides (ρM_7C_3 = 6.97 g · cm^{-3}, $\rho M_{23}C_6$ = 7.20 g · cm^{-3}

[161]). For the calculations of (Fig. 6.13), it has been assumed that MF_{γ}, MF_{M7C3}, and MF_{M23C6}, are the values corresponding to the temperature of the eutectoid transformation initiation

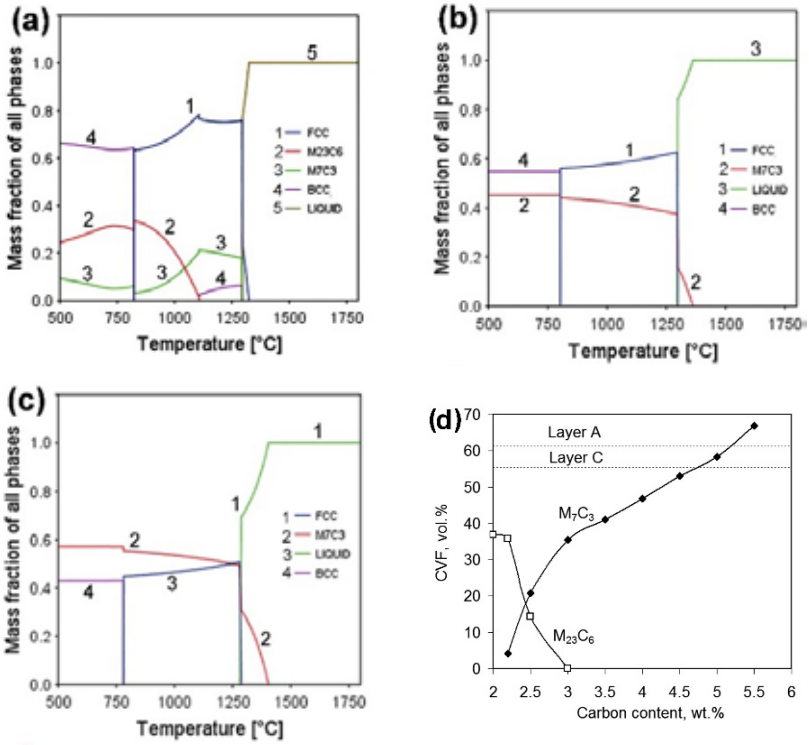

Figure 6.13 – Phase mass fractions for Fe-28%Cr-C system for different carbon contents: (a) 2.2 wt%C, (b) 4 wt% C, (c) 5.5 wt% C. (d) CVF as a function of the carbon content

As seen in (Fig. 6.13, d), the calculated VF of the eutectic carbides in Cr28 (2.24 wt.% C) is 35.8 vol.%, which is close to that of the VF value experimentally found in Cr28 (Table 6.1). According to the Thermo-Calc calculations (Fig. 6.13), the carbide VF values in Cr-based layers A and C (61.3 and 55.4 vol.%, respectively, Table 6.2) can be obtained when carbon contents are about 4.7 and 5.2 wt.% respectively, which are quite higher than that of Cr28 material. Although the "austenite + M_7C_3" area at 950 °C covers a wide range of carbon content including 4.7–5.2 wt% (see phase diagram in Fig. 6.1, b), these results are unexpected because they mean doubling of

the carbon content during the PP treatment. The same doubts arise for W-based layers B and D since, according to the Fe-18%W-4%Cr-1%V–C phase diagram (Fig. 6.1, a), M_6C at 950 °C appears only at carbon concentrations lower than 1.8 wt.% C.

Considering the short time of the plasma jet action, the actual enrichment of coating with carbon should be much lower than the calculated values. It allows to assume that the carbide precipitation in the coating during HT resulted in the formation of larger amounts of carbides depleted of carbide-forming elements. Indeed, significant Cr deficiency of M_7C_3 confirming the aforementioned assumption. The Cr content of M_7C_3 in layers A and C has been estimated as 30.2 and 31.5, respectively, which is much lower than that reported in previous works. More specifically, according to Laird II [166], the Cr-content of M_7C_3 in 3.2C-29Cr-HCCI is 60.9 wt.%. Moreover, Filipovic et. al [167] found chromium concentration in M_7C_3 (2.9C-19Cr-HCCI) is in the range 39.8–53.36 wt.%. Similar values (43.70––44.22 wt.% Cr) have been reported for eutectic M_7C_3 in 2.7C-14.6Cr-HCCI [75]. Even if one considers that EDS measurements are erroneous due to matrix "effect", these values seem to be excessively low as compared with the just mentioned published values. (Here it should be noted that bulky carbide particle dimensions are higher or marginally within the limits of EDS spatial resolution; the EDS spatial resolution for high atomic number elements is reported as (0.2–1) μm^3 for high atomic number elements, for usual high voltage conditions (15–25 kV) [65]). The formation of M_7C_3 carbides in the coating involved much more iron atoms resulting in an iron content of 63.8–64.8 wt.% (layers A and C). According to the carbide chemical composition, the formula of M_7C_3 in the coating can be claimed as $(Fe_{4.8}Cr_{2.2})\ C_3$. Since iron largely replaced chromium in the carbides, more chromium was available to form new carbides increasing their VF in the coating. Similar arguments can be made for carbides M_6C in layers B and D: these carbides also seem depleted of tungsten, with respect to previous work [168]. In particular, the W content of M_6C in M2 tool steel, which has been reported as 37.81 wt.% [168], is much higher than the one reported in the present effort. M_6C formulas can be presented as $(Fe_{3.8}W_{1.4}Cr_{0.8})$ C for layer B and $(Fe_{4.4}WCr_{0.6})$ C for layer D. Thus, it can also be postulated that W was largely replaced by Fe in the M_6C lattice. Tungsten liberated to the matrix formed new carbide particles.

This work showed that pulse plasma technique using an electrothermal axial plasma accelerator can successfully be employed for the surface

modification of and coating deposition on HCCIs. Using cathode with relatively low melting points allowed the formation of a coating of about 100 θm thickness by relatively few plasma pulses. In the above context, the employment of eutectic phase containing alloys (high-Cr cast irons, high speed steels, multi-component cast alloys, etc.) as cathode materials seems promising in view of their relatively low solidus temperature and the ability to obtain wear resistant coatings with notably high amount of hard phases (carbides, borides, etc).

A comparison with results obtained earlier [169–171] using the EAPA device shows that the new approach for PPT proposed in the present work (low-melting cathode plus post-deposition HT) has some apparent advantages. For instance, Cheiliakh et al. [169] describe the coating obtained by EAPA using a titanium cathode without post-deposition HT. Due to a higher melting point (1668 °C), the titanium cathode led to the formation of a thinner coating (50–60 μm after 6 pulses), that is almost 1.5 times thinner than that of the present work. Secondly, the hardness of the Ti-based coating was 870–1000 HV, while in this study, the coating hardness has reached 1240–1445 HV.

The combination of cathode materials makes possible the production of a laminated coating structure with improved properties as compared to a single cathode material. Such coatings allow to conjoin the barrier layers of different functionalities depending on the application. In particular, in the conditions of impact loadings, the presence of a ductile layer under the wear-resistant brittle layer may inhibit the crack nucleation and prevent coating cracking. In the conditions of high-temperature application or severe sliding wear, the Cr-rich layer can protect coating from high-temperature oxidation and so on. The deposition of layers with different chemical compositions may induce mutual diffusion processes. A combination of functionalities is realized in this work by alternating Cr-rich and W-rich layers throughout the coating: layers A and C (Cr-rich) can act as corrosion protectors in oxidizing environments, while layer B (W-rich) has the highest microhardness owing to the presence of M_6C carbides with decreased iron content. Here it should be noted that although the substrate/coating interface is quite smooth, the following layer microstructure is more chaotic. A question is arising, whether this microstructure can negatively affect the mechanical properties of the coating. The "substrate–coating" interface is formed under the first plasma impulse. The smoothness of its interface could be the outcome of substrate surface melting under plasma, followed

by very fast solidification due to the low temperature of the substrate. This has led to the formation of a thin layer with a very fine crystalline structure where the substrate smoothly "transits" into the coating. At subsequent pulses, the previously deposited layers are in a higher temperature than the initial substrate temperature, which increases the rate of crystallization of deposited microdroplets. This promotes more pronounced mechanical mixing of droplets which leads to coarsening of microstructure. Despite this coarsening, the coating also includes fine dispersions of roundish precipitates (Fig. 6.6) that provide dispersion strengthening. Furthermore, the heat affected interlayers and transition layer E can provide strong metallurgical bonding. Also, the gradient composition smoothly adjusting to the composition of the substrate, provides strong evidence of the good coating/substrate adhesion, as noted in section 3.3, end of first paragraph and two last sentences. Finally, alloying of the metallic part of the carbides with W provides solid solution strengthening of the carbides. The above strengthening factors are surpassing the negative contribution of structure coarsening, as shown in (Fig. 6.5, b).

It should be emphasized that, not only is the heat treated coating much harder than its substrate but its hardness decreases with coating depth in a functionally gradient pattern; the latter allows for a more uniform stress distribution and good adhesion at the coating/substrate adhesion. Additional improvement of functional abilities of layered coating could be achieved by post-deposition HT which implies further intensive research.

The conclusions for the chapter results are:

An Fe-C-Cr-W coating of thickness 80–120 μm was deposited on 14.5 wt% Cr-cast iron by pulsed plasma treatment employing an electrothermal axial plasma accelerator. The coating process was carried out by alternately depositing cathodes made of 18 wt%W-high speed steel and 28 wt%Cr-cast iron. PPT has led to modification of substrate sub-surface layer with formation of a zone that provided a smooth transition from the substrate to coating. Transition zones are noted between the upper coating layers as well, contributing to a smooth interlayer transition. The as-deposited coating has a layered microstructure, consisting of intermittent "martensite/austenite" and heat-affected layers. The cross-sectional microhardness of the as-deposited coating varies in the range of 500–655 $HV_{0.05}$ to be being higher in the "martensite/austenite" layers.

Post-deposited HT has led to the precipitation of numerous carbide particles within the coating. In the layers deposited using W18 cathode, the carbides are of M_6C and M_2C types; in the layers deposited using Cr28 cathode, the carbides are of M_7C_3 (predominant amount) and $M_{23}C_6$ types. The layered alternation in the nature of the carbides resulted in a sharp increase in the coating microhardness up to 1240–1445 $HV_{0.05}$. During PPT, plasma-due erosion of the inner channel walls of the EAPA under high-current discharge resulted in significant enrichment of the coating with carbon. This likely occurs due to discharge-induced erosion of the inner EAPA channel walls which promotes the release carbon atoms to be captured by the plasma flux. The carbon enrichment is responsible for the notable increase in the carbide volume fraction as compared to that of the cathode materials. As a result the carbides in coating are found to be Cr/W depleted in favor of Fe.

The content of the Chapter is adopted from Pulsed plasma deposition of Fe-C-Cr-W coating on high-Cr-cast iron: Effect of layered morphology and heat treatment on the microstructure and hardness / V. G. Efremenko, Yu. G. Chabak, A. Lekatou, A. E. Karantzalis, K. Shimizu, V. I. Fedun, A. Yu. Azarkhov, A. V. Efremenko // Surface and Coatings Technology. – 2016. – Vol. 304. – P. 293–305. https://doi.org/10.1016/j.surfcoat.2016.07.016

Chapter 7. FORMATION MECHANISM, MICROSTRUCTURAL FEATURES AND DRY-SLIDING BEHAVIOR OF "BRONZE/WC CARBIDE" COMPOSITE SYNTHESISED BY ATMOSPHERIC PULSED-PLASMA DEPOSITION

Composites are widely used in different engineering applications to address the challenges where specific combinations of the properties are required [172, 173]. Numerous works have been dedicated to the study of Cu-containing composites where the copper (or Cu-based alloy) is a matrix providing high plasticity/impact toughness and preferable physical and chemical properties (low electrical resistivity, high heat conductivity, enhanced corrosion resistance) [174, 175]. The hard phases (carbides, borides, etc.) are employed as strengthening agents to increase the mechanical and wear behaviours of the Cu-based composite [176, 177]. Silvain et al. [178] proposed copper-carbon composites as thermal-management materials in power electronic packages. Dias et al. [179] designed a WC–Cu cermet with 50–75 vol.% of copper to be used as a thermal barrier in a nuclear reactor. Li et al. [180] found that TiB_2/Cu composites with single-scale and dual-scale TiB_2 particles are prospective materials with improved arc erosion behaviour which is a necessary property for electrical contacts. Banthia et al. [181] applied electro-deposition to synthesise the Cu/Cu-SiC functionally graded coatings with a low coefficient of sliding friction preferable for electrical contacts. Cui et al. [182] used the excellent wettability between Al and the carbon matrix to develop a C/C–Al–Cu composite reinforced with 2.5D-polyacrylonitrile-based carbon fibre for use as railway current collectors for locomotives.

The composites are fabricated as a bulk material by powder metallurgical processes [178–180,122,183], casting [184], epoxy/fillers hardening [185], infiltration technique [186], or as a coating by surface deposition [96, 103, 118, 173,185–187]. Plasma transferred arc hardfacing was used to create a Fe-35 wt.% WC–Co composite to modify the surface of a low carbon AISI 1020 steel [188]. Pulsed-plasma deposition (PPD) is amongst the most promising methods for surface layering [34, 189, 190]. A repeated plasma

flux allows the modification of the structure [28, 141, 191] and chemical composition [191] of metallic surface, or the deposition of protective layers of different functionality [14, 34, 141]. Detonation-based pulsed-plasma treatment is comprehensively described in [34]. This method utilises the products of a gaseous mixture (C_3H_8, O_2, N_2) burning in a special detonation chamber to short the electrical circuit for activating the arc discharge inside the plasmatron. This method has been frequently used for surface hardening and surface dopping of different steels (such as structural steel 40Kh [141], AISI 4140 steel [192], T8 steel [193], etc.).

An alternative approach for PPD is using the repeated arc discharges initialised inside the closed chamber. Fujii et al. [194] fabricated diamond-like-carbon thin films using the technique, where the plasma flux irradiates a graphite target through the discharges with further deposition of the ablated particles on the substrate as a thin film. A device for PPD with concentrically arranged electrodes is described in [195] which allows the activation of short (μs range) plasma pulses of high intensity ($5–6 \times 10^4$ J/m^2) sufficient for nitrogen and argon atoms implantation into the steel surface. The same principle of switching the high-voltage discharge is used in an electro-thermal axial plasma accelerator (EAPA) described in [2, 14, 28]. EAPA produces the plasma flux of 10–15 thousand K degrees temperature that provides gas-dynamic impact on the treated surface resulting in its quenching and thermo-mechanical strengthening [28].

PPD enables a composite coating formation due to high plasma temperature and plasma velocity. Tyurin et al. applied detonation-based technology for pulsed-plasma deposition of a WC–Co-Cr composite on the surface of corrosion-resistant steel [196] and a ZrB_2–$MoSi_2$ coating on a carbon/carbon composite [197]. Rosinski et al. [198] produced W/Cu composites using low-temperature pulsed-plasma sintering. The composite layers "Carbides M_7C_3(M_6C, M_2C, $M_x(C, B)_y$)/High-C Martensite" were in-situ consolidated on steel and cast iron surfaces by EAPA using expandable cathodes made of high-Cr cast iron [3, 119], T1 high-speed steels [14] and 1.7wt.% C-14wt.%Cr-0.6wt.%V-1.2wt.%B steel [199]. The plasma-induced melting of an expandable cathode surface provides the flux of the cathode material to form the coating on the target surface [14]. As shown in [3, 14, 119, 199] after the pulsed-plasma deposition the coatings mostly consisted of soft austenite oversaturated with carbide-forming elements. Thus, post-plasma heat treatment (HT) was needed to precipitate the carbide phases from the austenite and to ensure the austenite-martensite transformation. However,

the post-plasma HT is not always applicable since it may negatively affect the bulk structure and the properties. Therefore, new approaches for the PPD technique should be found to eliminate post-plasma HT when fabricating the composite coating. As was suggested in [200], PPD/EAPA can be used for the direct formation of a composite "carbide/matrix" layer by using a composite cathode made of the components (carbides and a metallic binder) with a big difference in melting point. In this case, the easy melting of the binder may enable the direct plasma-transfer of non-melted carbides to the target substrate without the need of post-heat HT to precipitate them. This concept was assayed in the present work through the fabrication of "Cu-based matrix/carbides" composite coating using PPD/EAPA technology. The expandable cathode made by the sintering of aluminium bronze (as a low-melting matrix) and hard-to-melt WC carbides (as reinforced particles) taken in equal proportion was used for pulsed-plasma direct fabrication of a "matrix/carbide" composite coating.

Experimental procedure. The new concept of PPD cathode material was to create a composite combining the hard-to-melt components (carbides/borides) and easy-to-melt metallic matrix. Easy melting of the matrix may facilitate the erosion of the EAPA cathode so intensifying the plasma transfer of the cathode material to the treated surface. In this case, the direct plasma-transfer of non-melted carbides to the target can be enabled. Thus, the carbides may be deposited on the surface without the need of the post-heat HT which is usually used to precipitate the carbides from the matrix. The main precondition to implementing this approach is a big difference in the melting point of the components of the composite cathode. Accordingly, the components were selected as tungsten carbide WC and 5 wt% Al-bronze. WC is a refractory compound with a melting point of 2776 °C [201]. Aluminium bronze nominally contains 4–6 wt.% Al with the copper as a balance. According to the pseudo-binary phase diagram of Cu-Al alloys (Fig. 7.1) 5 wt.% Al-bronze belongs to single-phase alloys with an FCC lattice. The melting of 5wt.% Al-bronze occurs in a temperature interval of 1067–1072 °C which is 2.6 times lower than that of tungsten carbide. The powders of WC and aluminium bronze with a particle size less than 30 μm were used to get 50 vol.% WC – – 50 vol.% Al-bronze mixture prepared in a Turbula for 4 hours of rotation. The expendable electrode (cathode) was fabricated as a rod of 5 mm diameter and 60 mm length by sintering the powder mixture at 1050 °C.

PPD was fulfilled employing the EAPA in the air under atmospheric pressure with a energy of 12 kJ accumulated in capacitor C1 (a voltage of

4.0 kV). The discharge pulses were repeated with the time interval of 15 s to charge the capacitor. The total number of pulses was ten. The target was the specimens of 6 × 12 × 25 mm in size made of grey cast iron (GCI) with a chemical composition of 2.95 wt.% C, 1.45 wt.% Si, 0.95 wt.% Mn, 0.11 wt.% P, and 0.08 wt.% S. The microstructure of the GCI consisted of ferrite grains and graphite flakes (Fig. 7.1, b). The target was positioned at a distance of 50 mm from the accelerator edge.

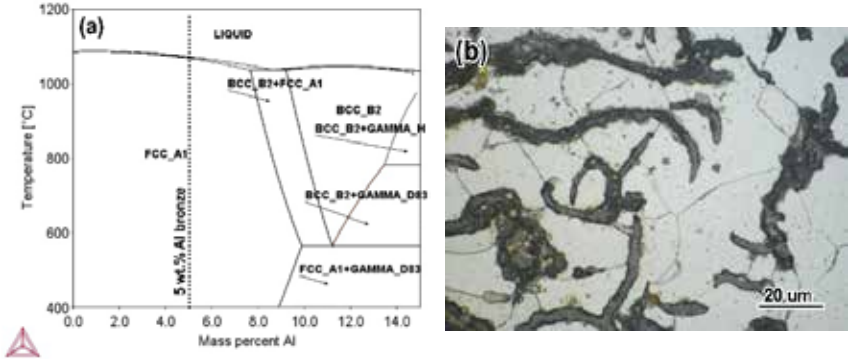

Figure 7.1 – (a) Pseudo-binary phase diagram of Cu-Al alloys (Thermo-Calc) and (b) the microstructure of grey cast iron (the substrate)

Coating microstructure characterisation and phase elemental composition. The microstructural observation of the PPD-treated specimen revealed a pulse-plasma deposited layer with the thickness varying from 85 to 135 θm (Figs. 7.2). The layer had a specific heterogeneous structure consisting of tungsten carbide precipitates (white colour) unevenly distributed in a metallic matrix. WC carbide size varied in the range of 0.1–9.3 μm with a mean value of 2.45 ± 0.19 μm where most of the carbide precipitates (64 vol.%) had the size of 1.0–4.0 μm (Fig. 6.3, a). Carbide inclusions were present throughout the thickness of the coating, but they were mostly concentrated in the outer layer of the coating with a volume fraction varying within 30–50 vol.%. Between the outer layer and the substrate, a transitional zone of about 50 μm width was observed containing much less (up to 5 vol.%) WC carbides. WC carbides lying in the transitional zone had a near spheroidal shape (shown by the arrows in Fig. 7.2, b) while the carbides in the outer layer had a preferentially irregular shape (shown by double arrows). The carbide microhardness was measured as 1556–2383 HV with an average value of 2025 ± 480 HV, which is consistent with the literature data for WC [202].

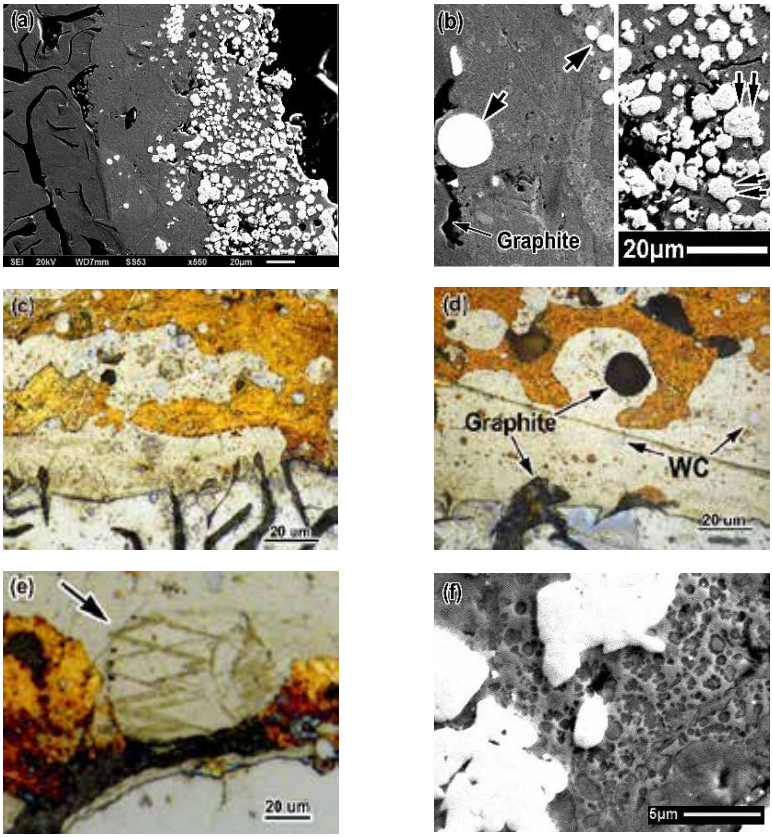

Figure 7.2 – Microstructural features of pulsed-plasma composite coating: (a) general view, (b) WC carbides of different shape, (c) dual matrix of transitional layer, (d) globular graphite in transitional layer, (e) acicular martensite next to graphite flake, (f) cellular structure in light-yellow area. (a, b, f) – SEM images, (c, d, e) – OM images

OM observation revealed the hybrid-matrix structure of the transitional zone which consisted of alternating jumbled areas of light-yellow colour and orange colour (Figs. 7.2, c, d). The light-yellow areas were positioned mostly near the substrate/coating interface; they contained the roundish carbide precipitates and small orange spheres (Fig. 7.2, d). The light-yellow areas were predominantly free of graphite, however, some graphite flakes penetrated into these areas from the substrate to be associated with the

acicular pattern characteristic for high-carbon martensite (Fig. 7.2, e). Besides the occasional graphite globules were revealed to be embedded in light-yellow areas (Fig. 7.2, d). The microhardness of the light-yellow areas varied in the range of 533–807 HV with an average value of 659 ± 22 HV. SEM observation with higher magnification allowed the observation of a cellular structure inside the light-yellow areas as shown in (Fig. 7.2, f). The cellular pattern was presumably caused by the coarse carbide net surrounding the matrix islands of approximately 1 μm and less in diameter. The orange-contrast matrix areas had a fairly low microhardness of 144–172 HV with an average value of 150 ± 17 HV. For comparison, the microhardness of ferrite in the substrate was slightly higher at 163–223 HV, with a mean value of 201 ± 41 HV.

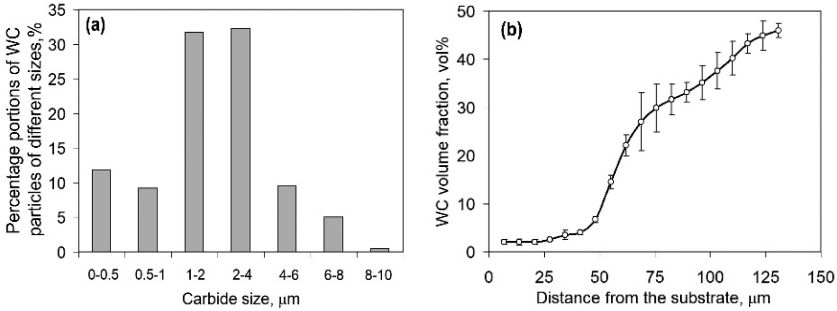

Figure 7.3 – The data on WC carbide in the coating:
(a) carbide size distribution, (b) carbide volume fraction
distribution in the cross section of the coating

The phase composition of the coating was studied by X-ray diffraction. The XRD pattern of the coating is presented in (Fig. 7.4). The diffraction peaks were identified as specific for tungsten carbide WC and the matrix phases of Cu (FCC) and α-Fe (BCC). A weak peak (200) belonging to cementite carbide M_3C was also revealed at 2 ϑ = 39.9 grad. Based on the ratio of diffraction peaks intensities, it was calculated that 80.5 vol. % of the matrix was attributed to the FCC-phase associated with copper (bronze). Accordingly, about 20 vol. % of the matrix was associated with iron (as the substrate). Thus, the phase constituents revealed by XRD analysis were consistent with the material of a substrate (α-Fe-based grey cast iron) and a composite cathode (Cu(FCC)-based bronze and WC carbide).

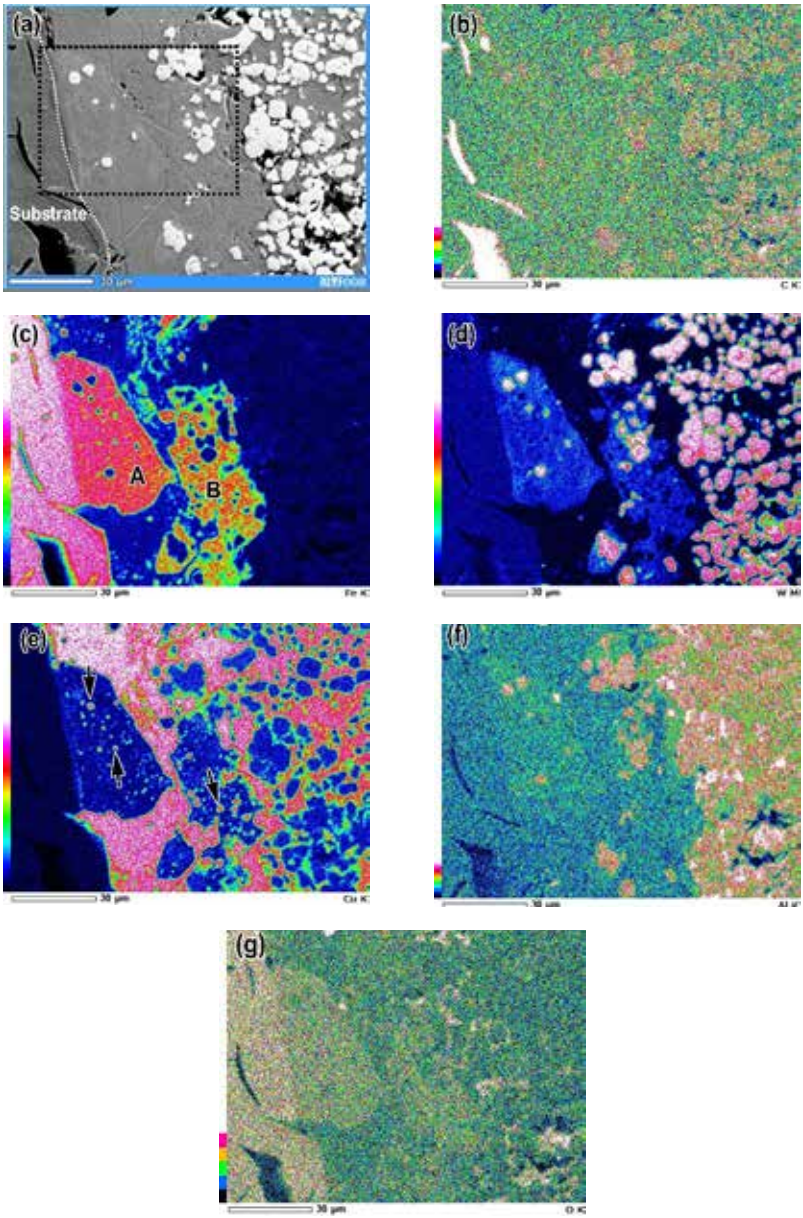

Figure 7.5 – Elemental mapping of the transitional zone and the coating: (a) SEI-image; (b) C; (c) Fe; (d) Cu; (e) W; (f) Al; (g) O

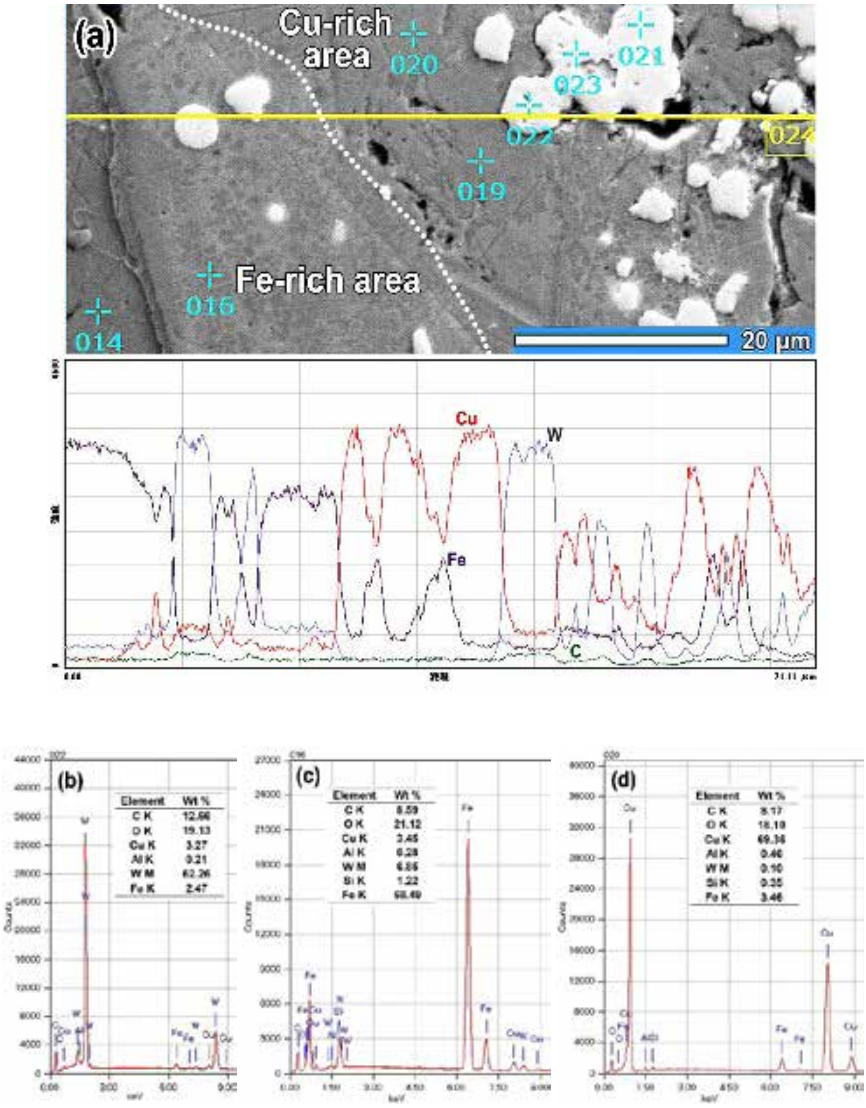

Figure 7.6 – (a) The profiles of C, W, Cu and Fe from the substrate to the coating, (b) WC carbide (point 22), (c) Fe-rich area (point 16), (d) Cu-rich area (point 20)

Table 7.1 – Phase chemical composition of the coating

Phase	Content of the elements (wt.%)						
	C	O	Cu	W	Al	Fe	Si
WC carbide	12.65 ± 0.08	19.17± 0.68	2.57 ± 0.60	63.52 ± 1.20	0.22 ± 0.05	1.87 ± 0.11	–
Fe-rich matrix	8.02 ± 1.22	20.94 ± 0.41	4.34 ± 1.00	8.02 ± 2.05	0.17 ± 0.06	57.33 ± 3.50	1.18 ± 0.14
Cu-rich matrix	7.51 ± 1.50	18.10 ± 0.11	68.73 ± 4.30	0.09 ± 0.03	0.38 ± 0.15	4.80 ± 2.71	0.39 ± 0.58
Substrate (GCI)	6.49 ± 0.27	22.13 ± 0.25	0.06 ± 0.01	–	0.23 ± 0.04	69.02 ± 0.25	2.07 ± 0.20

Apart from carbon, oxygen, and tungsten, the presence of copper (2.6 wt.%), aluminium (0.2 wt.%), and iron (1.9 wt.%) were detected in the WC carbides as well (see EDS-spectrum for the indicated point 22 in (Fig. 6.6, b). Fe-rich matrix areas contained 57.3 wt.% Fe with the addition of tungsten (8.0 wt.%), copper (4.3 wt.%), silicon (1.2 wt.%), and aluminium (0.2 wt.%). A characteristic EDS-spectrum for the Fe-rich areas is shown in (Fig. 7.6, c) for the indicated point 16 situated within area A (Fig. 7.5, c). In their turn, Cu-rich matrix areas of the coating basically consisted of copper (68.7 wt.%) and iron (4.8 wt.%) with the minor addition of silicon (0.4 wt.%), aluminium (0.4 wt.%), and tungsten (0.1 wt.%), as proved by EDS-spectra from the point 20 presented in Fig. 6.6, d. The EDS elemental profiles from the substrate to the coating top (Fig. 7.5, a) allowed the observation of the intensive chemical heterogeneity of the Fe-rich and Cu-rich matrix areas manifested in the occurrence of micro-zones enriched in copper (within Fe-rich areas) or enriched in iron (within Cu-rich areas).

Tribological behaviour. The "Bronze/WC carbide" composite coating was subjected to dry-sliding testing according to the above-described procedure. Two more sets of specimens (grey cast iron as a substrate and technically pure copper) were tested for comparison.

Figures 7.7 and 7.8 present the wear tracks of all three sets of specimens. The tracks are the grooves the cross-sectional profile of which depends on the tested materials and the counter body type. As seen from (Figs. 7.7, a, 7.7, c), after sliding against the steel ball the wear tracks on the "Bronze/WC carbide" coating and copper were characterised by large protrusions on both sides of the track due to the material being pressed out from the track by the counter body during the friction. An additional peculiarity of the copper

wear track was rather deep (~ 3 μm) rifts lying between the protrusion and non-worn surface (shown by the arrows in Fig. 7.7, c).

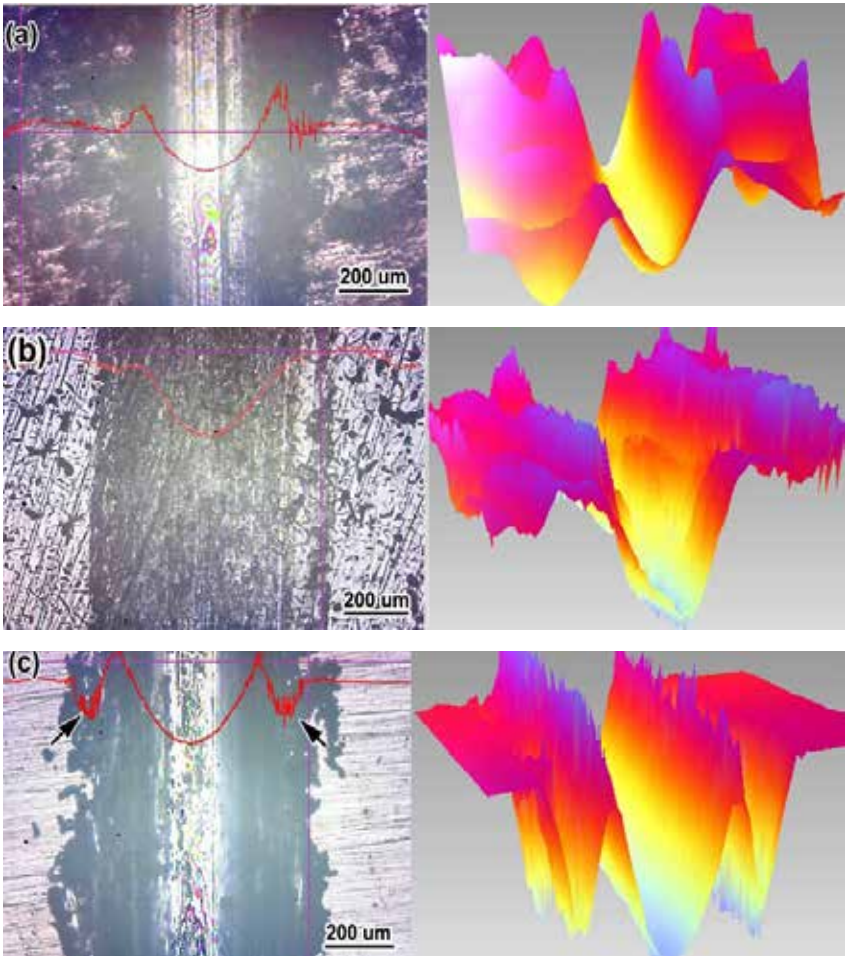

Figure 7.7 – OM micrographs and 3D images of wear tracks after testing against the steel ball: (a) "Bronze/WC carbide" coating; (b) grey cast iron, and (c) copper

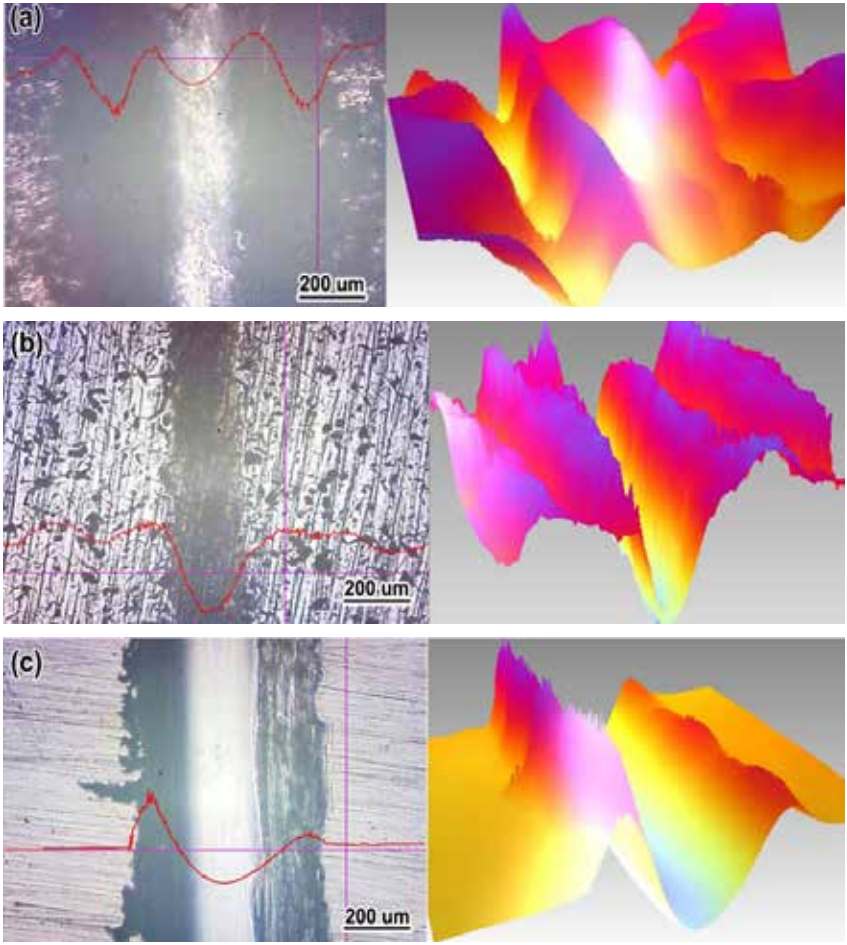

Figure 7.8 – OM micrographs and 3D images of wear tracks after testing against the SiC ball: (a) "Bronze/WC carbide" coating; (b) grey cast iron, and (c) copper

The wear track for GCI was rather wide but shallow with very low protrusions (Fig. 7.7, b). After sliding against the SiC ball, the wear track on the "Bronze/WC carbide" coating was characterised by both the protrusions and the rifts (Fig. 7.8, a), while the track for copper only had the protrusions (Fig. 7.8, c). The wear profile for GCI was close to that for steel balls except for the track width which became narrower (Fig. 7.8, b).

Figure 7.9 collects the cross-sectional wear track profiles for different samples enabling the comparison of the wear behaviour of the tested materials. The wear behaviour was evaluated using the parameters derived from the wear track profiles namely: (a) width of wear track (W), (b) the maximum total height of a track profile (R_{max}), (c) the volume loss (VL) which is the deepening's volume, (d) the volume increase (VI) which is the protrusions volume, and (e) the volume difference (VL–VI). VI and VL values were found relative to the baseline as shown in (Fig. 7.9, b). The volume difference was considered as material removal from the surface during the test (material loss).

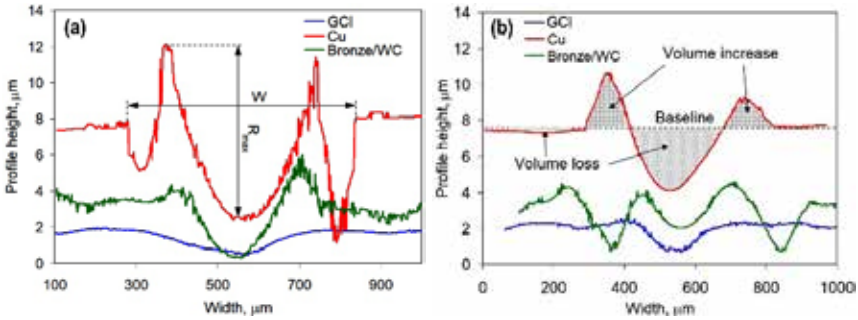

Figure 7.9 – Cross-sectional profiles of wear tracks after sliding against (a) steel ball and (b) SiC ball

All the wear parameters are collected in (Fig. 7.10). As can be seen from (Fig. 7.10, a), after sliding against the steel ball the "Bronze/WC carbide" composite produced the lowest width of wear track (377 μm) while the copper specimen had the largest W value (567 μm). The maximum total height of the track profile was also attributed to the copper specimen (9.6 μm), while the shallowest wear track was noted for grey cast iron (1.1 μm) (Fig. 7.10, b). The R_{max} value for the "Bronze/WC carbide" composite (3.7 μm) was rather closer to GCI than to copper. Accordingly, grey cast iron showed the lowest volume loss of $5.2 \cdot 10^{-4}$ μm^3, being two and seven times lower than the "Bronze/WC carbide" and copper, respectively (Fig. 7.10, c). Notably, the "Bronze/WC carbide" had 3.5 times lower VL as compared to copper ($VL_{Cu} = 35.1 \cdot 10^{-4}$ μm^3).

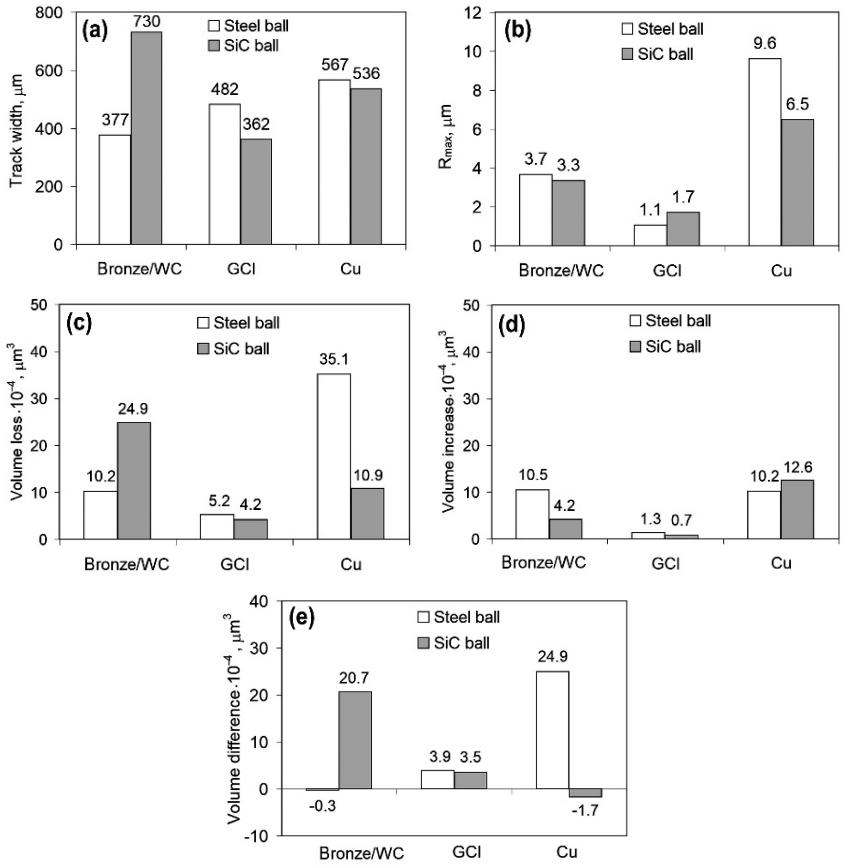

Figure 7.10 – Wear profile characteristics: (a) wear track width, (b) the maximum relief height difference, (c) the volume loss, (d) the volume increase, (e) the volume difference

The VI values for the "Bronze/WC carbide" and copper were almost the same ($10.5 \cdot 10^{-4}$ μm³ and $10.2 \cdot 10^{-4}$ μm³ respectively), much higher than that for GCI ($1.3 \cdot 10^{-4}$ μm³) (Fig. 7.10, d). The volume difference was close to zero for the "Bronze/WC carbide" (Fig. 7.10, e) meaning that the sliding wear was mostly accompanied by metal extrusion from the groove to the protrusions without significant material loss. In contrast, GCI and copper had positive volume difference val-ues reflecting the metal loss during wear. For copper, the vol-ume difference reached $24.9 \cdot 10^{-4}$ μm³ which is 71 % of

volume loss, i.e. the most part of the metal extruded from the groove was lost as wear debris.

The sliding against the SiC ball changed the wear response of the "Bronze/WC carbide" composite. The track width increased significantly, almost twice that of the steel ball sliding. This happened due to the formation of two wide (of 200–220 μm) rifts on both sides of the main wear track. It is worth noting, that the copper specimen had no such rifts, and its track width value was close to that of sliding against the steel ball. An increase in W value for the "Bronze/WC carbide" doubled its volume loss as compared to sliding against the steel ball. In contrast, VL_{Cu} value decreased three times resulting in a change in volume loss ranking: under test-ing in contact with the SiC ball the "Bronze/WC carbide" composite demonstrated the highest volume loss ($24.9 \cdot 10^{-4}$ μm^3) amongst all tested materials.

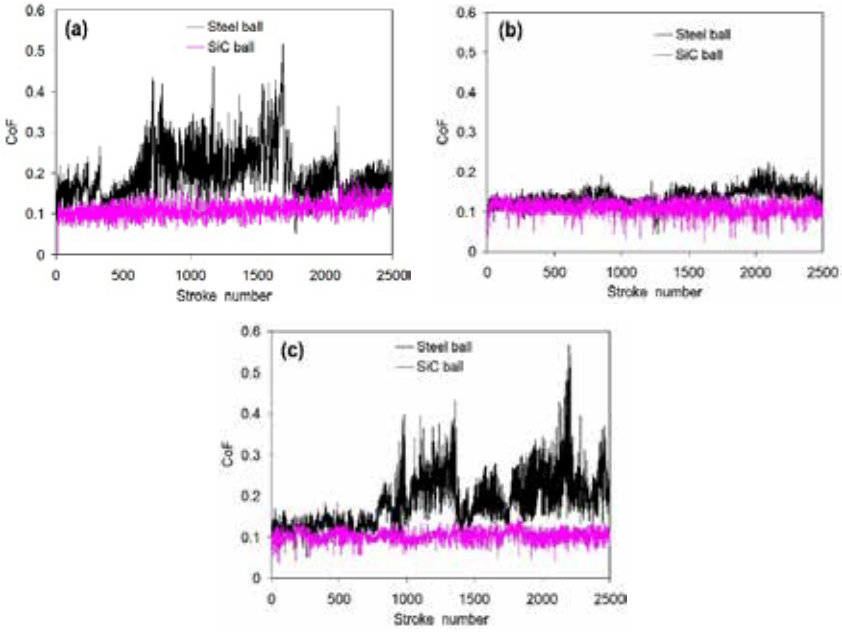

Figure 7.11 – Alteration of CoF value during the wear test: (a) "Bronze/WC carbide" composite, (b) grey cast iron, (c) copper

In these test conditions, the lowest volume loss was manifested by grey cast iron ($VL_{GCI} = 4.2 \cdot 10^{-4}$ μm^3). As seen from (Fig. 7.10), e, the volume

difference value was the highest for the "Bronze/WC carbide" composite reflecting an intensive material loss under wear. In contrast, the volume difference value for copper was negligible meaning minimal material loss. The (VL–VI) value for GCI was the same as for sliding against the steel ball showing the stability of the wear behaviour of the grey cast iron against both counter body types.

The coefficient of friction (CoF) value changes under the sliding test are presented in (Fig. 7.11). As can be seen, the CoF variation character significantly depends on the counter body material. When sliding against the SiC ball all three materials demonstrated a near-constant CoF value of about 0.1 with a small deviation of ± 0.05. When the counter body was the steel ball, the situation then changed. The "Bronze/WC carbide" composite and copper produced a wavy CoF profile featuring a periodical increase in CoF up to 0.5–0.55, followed by a sharp decrease to 0.1–0.15. At the same time, grey cast iron demonstrated stable frictional behavior close to that of sliding against the SiC ball, though a slight increase in CoF to 0.15–0.20 was revealed by the end of the test.

The mechanism of the coating formation. Since the composite coating was composed of EAPA cathode components, the mechanism of their plasma-transportation to the target surface is a key factor to understand the features of the coating formation. The results of the microstructural observation and EDS characterisation were used to assess the PPD process affecting the coating structure and properties. As suggested in [118], the arc discharge inside the EAPA results in the two-stage flowing of a plasma flux out of the accelerator. In the first stage, a high-current (up to 19 kA) short-lived (approximately 0.6 ms) pulsed arc discharge is initiated inside the EAPA. According to the working parameters of EAPA, the energy released due to discharge can be estimated as about 10 kJ [118]. The release of this energy for a short time can enable the following processes: (a) sublimation (erosion) of the dielectric channel walls, (b) the erosion of the electrodes through melting and evaporation in the electrode spots, and (c) heating and ionisation of gaseous erosion products with a subsequent formation of plasma flux [28] containing the atoms/ions of the electrodes/channel walls elements (Cu, W, Al, Fe, C) (Fig. 7.12, a). At this stage, the pressure inside the channel rises to 10^6–10^7 Pa causing the ionized vapours expansion inside the EAPA and their ejection out of the EAPA channel.

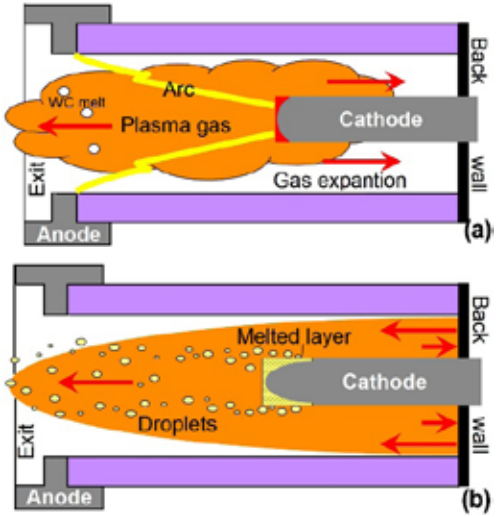

Figure 7.12 – The stages of cathode materials ejection from EAPA channel: (a) cathode evaporation and plasma flux formation, (b) cathode melting and micro-droplets evacuation

In the cathode spots, the erosion proceeds through the evaporation and the emission of the micro-droplets. In [204, 205], based on the model of hydrodynamic pressure on the surface of the molten metal, an analytical dependence of the micro-droplet velocity in the arc channel on the cathode material was obtained. Within the framework of this model, the velocity of copper micro-droplets emitted from the cathode spots was evaluated as 150–400 $m \cdot s^{-1}$ [205]. This result agrees with the conclusions of the works [206, 207] where the micro-droplet velocity in the flow of the evaporated substance was estimated to be in the range of 3–1000 $m \cdot s^{-1}$. These estimations were confirmed by the authors of [207, 208] who experimentally showed that the micro-droplet velocity value is directly proportional to the cathode melting temperature, being about 150 $m \cdot s^{-1}$ for the copper cathode.

In the present work, the distance from the EAPA cathode edge to the target was 0.1 m. Assuming a velocity of bronze droplets emitted from the cathode spots of 150–400 $m \cdot s^{-1}$, the droplets should reach the target in 250–670 μs. When passing through the discharge gap, an intense heat and mass exchange of erosion products with the surrounding plasma occurs. Presuming that the heat fluxes at both the interface of the erosion products

and at the target surface were comparable (~ 109 W · m^{-2}), an intense evaporation of micron-sized bronze drop-lets and melting of tungsten carbides could occur during the plasma transportation. The concentration of WC micro-droplets in the plasma flux was expected to be low due to high refractory property of WC [202] and its low erosion rate in the cathode spots [200].

Expanding inside the EAPA channel, the gas reflected from the back wall and directed towards the open exit, performing the second stage of plasma flux ejection (Fig. 7.12, b). During the time lag between the discharge initiation and the ejection of the reflected flux, the cathode surface remains molten due to the low melting temperature of the bronze matrix (1067–1072 °C), while the refractory tungsten carbides remain unmolten. (The assumption on the non-melted status of WC carbides is confirmed by their angular shape, characteristic for the initial WC powder (see Fig. 7.2, b)). When the reflected gas moves back it tears off the liquid droplets from the molten cathode surface so ejecting them out of the EAPA channel.

The droplet diameter can be evaluated according to the approach suggested in Chapter 2. For the used PPD regime the values of E and S_{Liq} from the equations (2.6–2.8) were previously estimated [118] as 300 J and 10^{-4} m^2 respectively. Assuming that only the bronze matrix is melted in the cathode material, the parameters of Eqs. (6.1) and (6.2) for Al-bronze were taken as ρ_{Bronze} = 8200 kg · m^{-3}, T_{Bronze} = 1070 °C, and c_{Bronze} = 380 J · kg^{-1} · K^{-1}. Thus, the thickness of the molten layer on the cathode surface was calculated as 300 μm, while the mass of the molten bronze was assessed as 0.1 g and the WC mass was assessed as 0.2 g. According to [209], a breakup of a liquid jet of a diameter h into droplets may result in the formation of droplets of about 1.89h in diameter. Consequently, the droplets of a diameter up to 550 μm can be ejected from the EAPA channel. A droplet of such size can accommodate dozens of unmolten WC carbides, carrying them to the target surface.

When the plasma flux contacts the target surface it may cause surface heating exceeding the substrate melting temperature. The depth of the plasma-affected layer was evaluated numerically using the approach presented in the Chapter 1 (equations 1.1–1.3). The temperature distribution in the sample under the plasma heating was calculated assuming $q_o = 1.75 \cdot 10^9$ W · · m^{-2}, ρ_S = 7200 kg · m^{-3}, and Λ = 140 kJ · kg^{-1} while the values of c_S and λ_S were taken from the temperature dependences (Figs. 7.13, a,b) adapted from [121] for grey cast iron. The results are shown in (Figs. 7.13, c,d). The contact of the substrate with the plasma flux triggers the fast surface heating

with a velocity up to $12.3 \cdot 10^6$ K · s^{-1} causing a sharp surface temperature rise. In 440 μs the surface temperature reaches 2350 °C then decreases. This temperature exceeds the Liquidus temperature and Solidus temperature of the grey cast iron (1310 °C and 1147 °C respectively), thus the sample melts to a depth of about 15 μm. In this layer, the temperature reaches the Solidus in 570 μs after heating onset while the heating velocity reaches the maximum ($4.5 \cdot 10^6$ K · s^{-1}) in 120μs.

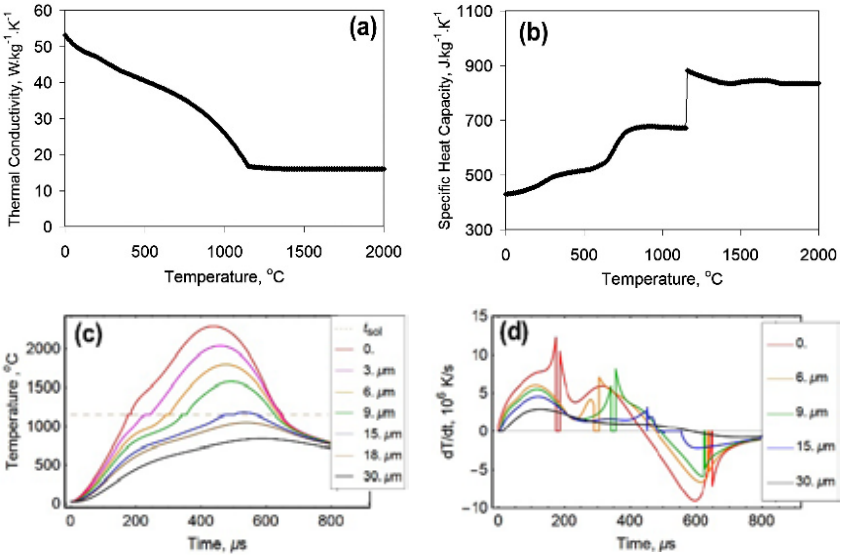

Figure 7.13 – The temperature dependences for (a) thermal conductivity and (c) specific heat capacity for grey cast iron. The calculated cross-sectional (c) temperature and (d) heating/cooling velocity distribution inside the target specimen under PPT

The results of the numerical study and EDS investigation allows the suggestion of the following mechanism of the coating formation. The plasma flux bearing rare liquid W/C-rich drops reaches the grey cast iron surface in 0.25–0.67 ms after the arc discharge causing its heating and melting up to a depth of 15 μm (Fig. 7.14, a). The graphite flakes mostly dissolve so saturating the melt with carbon, however, some of the flakes do not dissolve completely remaining in the structure as graphite globules (Fig. 7.2, d). Due to the high kinetic energy, the plasma flux provides the hydro-dynamic stirring and fragmentation of the molten substrate layer (Fig. 7.14, b).

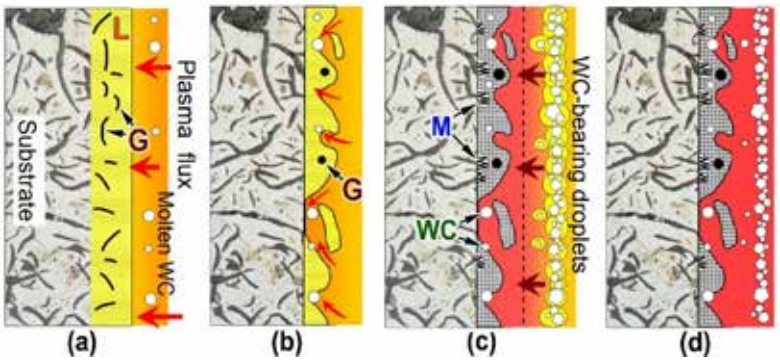

Figure 7.14 – The stages of the coating formation: (a) plasma-induced target surface melting in contact with the plasma flux, (b) hydro-dynamic stirring of the molten layer, (c) the WC-bearing droplets deposition, (d) coating solidification (L – liquid, G – graphite, M – martensite, WC – tungsten carbide)

Plasma-induced heating is quickly turns to cooling caused by heat removal inside the specimen. According to (Fig. 7.13, d), the cooling velocity of the molten layers varies from $9.0 \cdot 10^6$ K· s^{-1} (the surface top) to $2.2 \cdot 10^6$ K · s^{-1} (15 mm depth). Therefore, super-fast crystallisation of the molten substrate layer occurs accompanied by the condensation of the electrode's vapours. The vapours condense in the gaps in the molten layer leading to a heterogeneous dual structure next to the unmolten substrate interface. The fragments of molten substrate crystallise as light-yellow contrast areas (Figs. 7.2, c, d) rich in iron (areas A and B in Fig. 7.5, c). The silicon content in these areas (1.5 wt.%) is close to that of the substrate (2.6 wt.%) confirming their "substrate-parent" origin. Fe-rich areas also contain an increased amount of tungsten (10.5 wt.%) and copper (5.5 wt.%) as a result of the interaction of the melt with (Cu/W)-rich plasma flux. Some small spalls of plasma flux directly penetrated into the substrate melt resulting in solidification of spheroidal Cu-rich inclusions and globular WC carbides, as shown in (Figs. 7.2, b, d). The spherical shape of the WC carbides confirms that they crystallised from the liquid W/C-rich drops transferred by the plasma flux.

The dissolution of graphite flakes results in the over-saturation of the Fe-rich melt by carbon. As a result, under crystallisation, a network of cementite carbide is precipitated around the BCC-Fe matrix grains, developing the

cellular structure shown in (Fig. 7.2, f the presence of cementite carbide and BCC-Fe in the coating was confirmed by XRD study). In Fe-rich areas adjusted to non-dissolved flakes, the carbon saturation is not enough to form the cementite network, thus only high-carbon martensite appears here, as seen from the characteristic "zigzag"-acicular pattern shown in (Fig. 7.2, e). The presence of cementite carbide and high-carbon martensite results in a rather high microhardness of the Fe-rich areas (533–807 HV). In the gaps between the Fe-rich melt areas, the Cu-rich matrix areas solidified from the plasma flux show an orange contrast in LOM. Actually, these areas are the bronze matrix (83.6 wt.% Cu) alloyed with Fe, Al, Si and W (see Table 7.1). The presence of 6 wt.% Fe and 0.5 wt.% Si in the Cu-rich matrix is explained by interfusion of the plasma flux with the substrate melt. It is worth noting, that the content of aluminium in the Cu-rich matrix is much lower than that of Al-bronze. This might be caused by intensive aluminium high-temperature oxidation/dissipation occurring in the plasma flux. All the above processes lead to the transition zone formation being the essence of the first stage of the coating formation.

The second stage starts about 5–25 ms thereafter when the numerous liquid bronze droplets bearing unmolten WC carbides reach the target surface (Fig. 7.4, c). At this moment the surface temperature drops to less than 700 ^{o}C (Fig. 7.13, c) thus the droplets fall on a solid surface where they crystallise fusing with the transitional zone and forming strong metallurgical bonds with the substrate (note the absence of visible interface between the single droplets in Fig. 7.2, a). Transferred WC carbides are fixed inside the Cu-rich matrix due to the crystallisation of the surrounding liquid droplet (Fig. 7.14, d). The above described two-stage mechanism is repeated during each consequent plasma pulse going through ~ 15 μm-melting of the previously deposited layer. The latter provides further compression and bonding between the coating layers, causing some rounding of the angular WC carbides edges.

From the dry-sliding test the "Bronze/WC carbide" composite fabricated by pulsed-plasma deposition showed much better wear behaviour as compared to copper when sliding against the steel ball. Notably, the wear of the "Bronze/WC carbide" composite proceeded mostly through the lateral extrusion of the material from the groove to form the side protrusions without measurable material loss. This can be ascribed to the effect of hard carbide particles which provide a strengthening effect and decrease the adhesion between the sliding surfaces [35]. In contrast, copper exhibited significant metal loss with the highest wear track roughness (R_{max}) and the

formation of additional rifts lying on either side of the groove. A possible explanation for this is an intensive galling on the contact copper/steel interface which was confirmed by the notable variation of coefficient of friction with the sharp CoF spikes up to 0.5–0.55 (Fig. 7.11, c). A similar wavy CoF behaviour was observed for the "Bronze/WC carbide" composite, although in this case the CoF spikes were caused by the abrasive interaction between WC carbides (on the composite surface) and the steel ball surface rather than by galling manifestation. Moreover, the hard WC precipitates took the external load thus protecting the softer Cu-rich matrix in contact with the counter steel ball surface.

The sliding against the SiC ball was characterised by the same low CoF level for all tested materials. This was due to low adhesion of SiC to Cu (Fe) caused by the difference in crystal structure. In this wear condition the "Bronze/WC carbide" composite was inferior to copper in wear performance. A possible explanation is a high level of Young's modulus (388–417 GPa [210] and hardness (2200–3000 HV [211]) of the SiC carbide resulting in a high stress concentration in the friction contact. The soft copper responds to this stress by the plastic redistribution of the metal from the groove to the protrusions without noticeable metal loss due to the low SiC/Cu adhesion. In contrast, the "Bronze/WC carbide" composite exhibits a lower ductility resulting in stress-induced ruptures on both sides of the central groove. The stress concentration facilitates the fracture along the WC/matrix interface leading to spalling off of WC carbides and to an inevitable mass loss.

Grey cast iron showed the best tribological behaviour as compared with the "Bronze/WC carbide" composite and copper. Notably, all the wear parameters (Fig. 7.10) for GCI were about the same for both the steel ball and silicon carbide ball testing. Such performance of GCI is reasoned by the higher microhardness of the matrix (201 ± 41 HV for GCI and 150 ± ± 17 HV for the "Bronze/WC carbide") and the presence of graphite flakes in the structure. It is known that graphite is a self-lubricating agent [212, 213] which effectively protects against adhesion/galling due to its layered structure with weak van der Waals forces between the atomic layers [126].

This work shows that the PPD/EAPA technique enables the direct production of a "Carbide/Metallic matrix" composite without performing an additional post-plasma heat treatment. The advantage of this method is the possibility of obtaining a composite layer of decades-micron thickness for thin surface layer applications. The wear test showed that the "Bronze/WC carbide" composite synthesised by pulsed-plasma deposition can suc-

cessfully compete with the Cu-based alloys considering the material of the counter body. In particular, such composite coatings can be prospective for electrical contact surfaces, a topic which requires additional research.

The conclusions presented based on this Chapter results are:

A "Bronze/WC carbide" composite coating of 85–135 μm width was synthesised on the surface of grey cast iron by pulsed-plasma deposition using an electro-thermal axial plasma accelerator. The deposited material was eroded from the cathode under high-current (up to 19 kA) discharge and transferred by plasma flux to the target through a two-stage plasma ejection out of the EAPA channel. The big difference in melting point of the cathode components (50 wt.% of Al-bronze and 50 wt.% of WC carbide) facilitated the cathode surface melting to intensify the mass transfer via liquid bronze droplets bearing unmolten WC carbides to the target surface.

The numerical assessment and OM/SEM/EDS observation showed that the plasma flux resulted in substrate melting to the depth of 15 μm with its hydrodynamic stirring by plasma flux. This resulted in the formation of a transition zone, of up to 50 μm width, composed of Fe-rich high-carbon areas and Cu-rich areas. The transition zone ensured good bonding with the target serving as a substrate for the subsequent deposition of 30–50 vol.% WC carbides embedded into the bronze matrix.

The composite coating comprised the tungsten carbides of 0.1-–9.3 μm diameter of two different shapes. The near-spherical WC carbides crystallised from the liquid micro-droplets in the transitional zone in the first stage of the coating formation. The largest portion of WC carbides had an angular shape and were transferred in unmolten state in the second stage of a plasma flow.

The "Bronze/WC carbide" pulsed-plasma composite showed a promising wear response under dry-sliding against a steel ball having a significant advantage over bulk copper. In the friction conditions against a SiC ball, the "Bronze/WC carbide" composite was inferior in wear resistance to the copper specimen.

The content of the Chapter is adopted from Formation mechanism, microstructural features and dry-sliding behaviour of "Bronze/WC carbide" composite synthesised by atmospheric pulsed-plasma deposition / V. G. Efremenko, Yu. G. Chabak, V. I. Fedun, K. Shimizu, T. V. Pastukhova, I. Petryshynets, A. M. Zusin, E. V. Kudinova, B. V. Efremenko // Vacuum. – 2021. – Vol. 185. – P. 110031. https://doi.org/10.1016/j.vacuum.2020.110031

Chapter 8. STRUCTURAL AND TRIBOLOGICAL STUDIES OF "(TiC+WC)/HARDENED STEEL" PMMC COATING DEPOSITED BY AIR PULSED PLASMA

The composites are specific materials for different engineering applications which are consisted of dissimilar materials with different physical and mechanical properties. Due to increased strength the metal matrix composites are frequently used in automotive and aviation industries, cutting tools manufacturing, electronics, etc. [214]. Particle reinforced metal matrix composites (PMMCs) present the ceramic particles spread in metallic (Al-based, Ti-based, Fe-based etc.) matrix [215–217]. PMMCs are among the first options for using against erosion and wear [218] due to the synergetic interaction of hard wear-resistant particulates and a tough matrix that tightly holds the particles in a conglomerate [219, 220]. Liquid metallurgy and powder consolidation are the common methods for PMMCs fabrication however different deposition technologies are also employed to form PMMC as a protecting coating on a surface [221]. Electrodeposition [222], cold spraying with plasma gas atomization [223–225], resistance seam welding [226], spark plasma sintering [227], direct constrained sintering on a surface [228, 229], self-propagating high-temperature synthesis [230], high-velocity oxygen fuel deposition [231], severe plastic deformation with simultaneous addition of the reinforcing alumina powder and the air-oxidation treatment [232] were successfully used for the deposition PMMC coating with improved tribological properties.

Highly-concentrated energy sources (laser beam, ion beam, plasma flow) are frequently reported as effective ways for PMMC coating synthesizing [233–235]. Kotarska et al. used laser cladding [236] to produce Inconel/(10–40 vol.% TiC) composite with improved resistance to solid particle erosion. Li et al. [237] described the significant increase in the wear/corrosion resistance of Ni-Al-bronze due to laser surface cladding of Co-based alloy composite reinforced by carbides (TaC, Cr_3C_2) and intermetallic (Co_3Ta) particulates with optimal properties at 20 wt.% of Ta C. Tan et al. [239] attempted to in-situ synthesize Al_2O_3 ceramic and M_7C_3 carbide in the iron matrix by laser cladding to improve microhardness and dry-sliding wear properties due to complex effects of the grain refinement, precipitation hardening, and solid solution strengthening.

The plasma-related surface deposition was also applied for PMMCs coating fabrication as reported in [187, 240]. Powder plasma transferred arc welding was used to consolidate a "TiC/synthetic diamond/Co-based alloy" composite featuring 140 times higher abrasive wear resistance as compared with 400 HB-heat treated steel [241]. Zhang et al. [242] applied plasma cladding for in-situ fabrication of (TiB_2+TiC)-reinforced Ni-based alloy to decrease the friction coefficient and to prevent severe abrasive/adhesive wear under high load (up to 60 N). Rokanopoulouet al. [243] showed the effectiveness of adding TiS_2 to (Al_2O_3+Fe) powder mixture to create a self-lubricating wear-resistant PMMC coating on duplex stainless steel 2205 surface. Huang et al. [244] utilized a plasma transferred arc process to protect Q235-carbon steel by PMMC coating consisting of 30 wt.% Cr_3C_2 particles embedded to γ(Ni, Fe)-matrix; besides it was found that Cr_3C_2 carbide was partially melted to form a hyper-eutectic structure. Sivkov et al. [245] reported that a coaxial magneto-plasma accelerator generates a high-speed ($\sim 3\ km \cdot s^{-1}$) plasma flow enabling the formation of a PMMC TiC/Ti coating with strong adhesion to the copper substrate due to deep penetration of titanium particles into the substrate structure. Tyurin with the colleagues applied the detonation-based pulse-plasma deposition to produce a WC/Co-Cr coating on corrosion-resistant steel [246] and a ZrB_2–$MoSi_2$ coating on a carbon/carbon conglomerates [247]. A low-temperature pulsed-plasma sintering was used in [248] to fabricate WC/Cu composites.

Among PMMCs coatings, the Fe-based compositions are stand out for their low cost, good manufacturability, and high abrasive wear resistance [249, 250]. They are mostly obtained using the mixture of Fe powder with strengthening particulates or precursors. According to Salloom et al. [251], a laser cladding of a (B_4C+ 4 wt.% Fe) precursor resulted in a nanocomposite with a multi-phase structure comprising B_4C, Fe_2B and Fe_3C phases precipitated from liquid under the laser melting. Iron-based (VC, TiC, WC)-containing coating was produced by diode laser to perform an improved abrasive water-jet erosion resistance [252]. PMMCs coatings with the alloyed steel matrix perform an improved tribological behaviour due to increased matrix microhardness: hard (martensitic) matrix successfully withstands the abrasion thus preventing an easy spalling of reinforcing particles. According to this approach, Chen et al. [253] produced a H13 steel/TiC laser cladded composite with an austenite-martensite matrix and integrated microhardness of 1365 HV. A similar H13/TiC composite of increased erosion resistance was fabricated by Jiang and Kovacevic [254] via

laser deposition. Gordo et al. [255] used a powder metallurgy technique to produce the NbC/TaC-reinforced PMMC with the matrix of M3/2 high-speed steel which effectively withstands wear under the sliding against alumina pin. Concluding, the alloyed steel matrix broadens the functionality of the PCCM coatings through the enhancement of the matrix properties.

The steel-based PMMC coatings can be fabricated by pulsed-plasma deposition (PPD) using an electro-thermal axial plasma accelerator (EAPA) described in [2, 3, 63]. This installation enables the generating high-energy plasma pulses just in the air under atmospheric pressure. EAPA is equipped with a consumable electrode (cathode) which intensively erodes under high-current discharge inside EAPA internal chamber. The eroded material (ions, atoms, micro-droplets) is transferred by plasma flux to form a coating on the substrate surface. The EAPA cathodes made of high-Cr cast iron and high-W speed steel were previously used to synthesize the carbide/matrix composite coatings [14, 120]. Since these cathode materials contained the eutectic carbides (M_7C_3 or Me_6C, respectively) their plasma transfer was expected to form the PMMC coating on the substrate surface. However, as-deposited coatings had a soft austenitic microstructure without carbide reinforcement since all eutectic carbides were completely melted under high-current discharge. Owing to fast solidification the alloying elements (Cr, Mn, W, V) were trapped in the matrix resulting in its stabilization. In order to stimulate in-situ carbide precipitation (with further austenite → martensite transformation) the destabilizing post-heat treatment was performed at 950 °C leading to the "Carbide/Martensite" composite structure [14, 120]. However, the high-temperature post-heat treatment may deteriorate the bulk structure/properties; therefore the PPD technique should provide the direct PMMC coating formation without additional heat treatment. This requirement can be met by using a composite electrode comprising the hard-to-melt particulates and easy-to-melt binder. An easy-melting binder allows adjusting EAPA parameters in order to decrease the energy released under arc discharge. This could prevent carbides melting enabling their plasma transfer in a non-molten state. Such PPD-EAPA approach was previously utilized in [120] to fabricate the pulsed-plasma composite "WC/Al-bronze" coating with improved dry-sliding properties. However, it was not attempted yet to synthesize a pulsed-plasma wear-resistant PMMC with a matrix of hardened (martensitic) steel. This task was resolved in the present work by developing a novel design of a consumable EAPA cathode.

Experimental procedure. Pulsed plasma deposition was performed in this work using an electro-thermal axial plasma accelerator. EAPA cathode has a multipart design consisting of a consumable ending part (6) (intended for the coating deposition) and a permanent steel rod connected with an electrical circuit. The consumable part is attached to the steel rod by a copper tube mount (4). EAPA-PPD technique implies the selection of the composition of consumable part, since the coating formation proceeds through the transfer of the cathode material eroding under arc discharge inside the EAPA. Earlier [3, 14, 44] a consumable part was a rod-shaped bulk metallic material. Alternatively, a composite structure of the cathode ending part was proposed in [120] to consist of the refractory ceramics particles and a low-melting metallic binder. The lower melting point of a binder enables the coating deposition under low discharge voltage (meaning lower energy released inside the EAPA), ensuring that the particles will remain non-molten during plasma-transferring to the substrate surface. In this case, post-heat treatment to precipitate the carbides from a supersaturated solution is not required. When pursuing the formation of wear-resistant PMMC coatings, it is necessary to focus on direct obtaining (without heat treatment) a hard metal matrix of a plate martensite characteristic for quenched high-carbon steel [4]. Also, the EAPA cathode should have a high electrical conductivity to ensure the arc switching between an anode and the tip of a cathode ending part. This allows an intensive erosion of the latter to form a coating of the desired composition. In the case of low electrical conductivity, the arc cathode spot moves from the consumable tip to more electrically conductive cathode parts, in particular, to the copper mount, leading to rather the erosion of the latter instead of the carbide-containing cathode part.

Based on the above considerations, a novel approach to fabricate a consumable part of the EAPA cathode was proposed in the present work. A consumable part was designed as a tube made of plain low carbon steel filled with epoxy resin-bonded ceramics particles. The steel tube as a cathode body has the following advantages: (a) high electrical conductivity of a steel tube enables a discharge between the anode and the consumable part tip, ensuring an intensive erosion of the latter; (b) the erosion of the steel tube will supply a plasma jet with iron (as atoms and micro-droplets), which is necessary to form a steel matrix of a composite; (c) the tube can be used as a container to bear ceramics particles needed for PMMC coating formation.

The second original approach was to fill a tube by reinforcing particles bonded with epoxy resin. The use of epoxy resin instead of a metal to

bind the particles has a number of advantages [256, 257]: (a) an easy filler preparation (mixing instead of sintering or casting), (b) the epoxy binder easily burns out (evaporates) under the arc discharge, releasing the ceramics particles to be directly plasma-transferred to the target.

The acquiring hard (plate martensite) matrix of PMMC coating presumes the following conditions: (a) the saturation of matrix with carbon, (b) preventing formation of excessive amount of retained austenite (RA). The sources of carbon which can be plasma-transferred in EAPA/PPD process are: (a) carbon of steel tube, (b) carbon released during EAPA walls erosion (evaporation), (c) carbon released during epoxy resin burning (evaporation). The carbon saturation of the coating due to EAPA wall erosion was previously described in [3], where the volume fraction of carbide in the coating was two times as compared to cathode material. In this regard, it is important that the tube material must be precisely low-carbon plain steel to prevent a reduce the Ms temperature due to excessive carbon saturation and/or effect of alloying elements. Otherwise it may lead to increased amount of retained austenite affecting coating hardness/wear resistance. The formation of martensite matrix will occur on the surface directly under PPD: mixing with iron carbon atoms forms a high-carbon liquid which solidifies to plate martensite due to ultrafast coating crystallization [28].

The burnout of the carbide/epoxy mixture ensures the release of carbide particles. The epoxy binder burns in contact with arc (in cathode spot) and in contact with plasma moving inside EAPA channel before the ejecting. In order to increase the surface of contacting plasma flow with "carbide/epoxy" filler, it was proposed to make through holes in the tube wall, thus allowing the filler come to the tube surface. In this work, the consumable cathode part was a 60 mm long steel tube of 6 mm outer diameter and 0.8 mm a wall thickness. The rows of through holes were drilled along the tube circumference with the distance between the rows of 4 mm. Each row consisted of four 2.5 mm diameter holes drilled with a step of 90 degrees. Each subsequent row of holes was offset by 45 degrees from the previous one, as shown in (Figure 8.1).

Figure 8.1 – The solid model of the consumable part of the EAPA cathode

The tube was made of low-carbon plain steel of ASTM 1020 grade (0.15 wt.% C; 0.28 wt.% Si; 0.65 wt.% Mn; 0.010 wt.% S; 0.017 wt.% P) with "Ferrite + Pearlite" structure (Fig. 8.2, a).

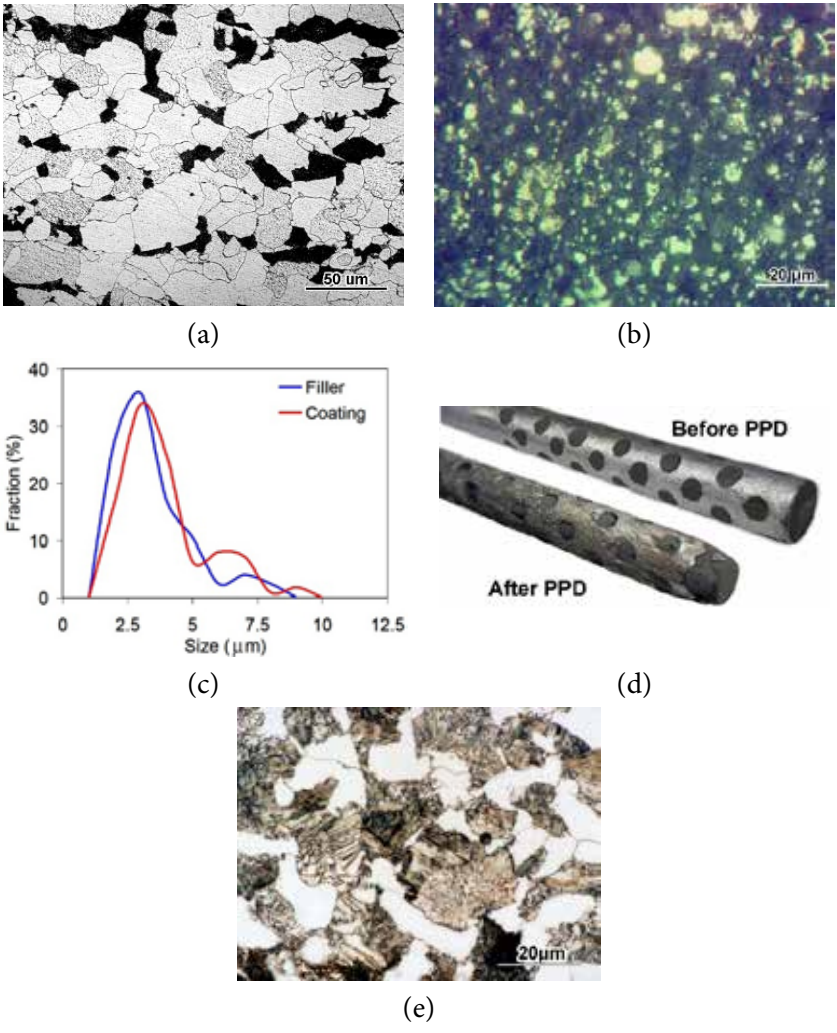

Figure 8.2 – The consumable part of the EAPA cathode: the microstructure of (a) a steel tube and (b) a filler, (c) carbide size distributions for the filler and the coating, (d) general view of the ready cathode before PPD and the eroded cathode after deposition of five coatings (50 pulses). (e) The microstructure of a substrate (steel of AISI 4145H grade)

The mixture of WC carbide and TiC carbide powders taken in equal proportions was prepared by mixing for 4 hours in a turbula type 3D-mixer (homemade, volume of 0.34l, rotation speed is 30 min^{-1}). The carbide powder was thoroughly mixed by liquid epoxy resin in a volume ratio of 2:1. Immediately after preparation, the carbide/epoxy mixture was used to fill the tubes. After filler solidification the consumable cathode part was ready for PPD. The microstructure of the indurate filler (carbides (white) + epoxy resin (dark)) is shown in (Fig. 8.2, b). Carbide volume fraction was 24.9 ± 2.0 vol.%; carbide size varied in a range of 0.3–8.5 μm with the most part falling to the interval of 1–4 μm (Fig. 8.2, c). A general view of the ready consumable part of the EAPA cathode is demonstrated in (Fig. 8.2, d). The working parameters of a pulsed-plasma deposition were as follows: discharge voltage – 4.0 kV; discharge duration – 1 ms; distance between EAPA electrodes – 50 mm; distance between EAPA edge and the target surface – 50 mm; the number of pulses – 10; pressure – atmospheric. The eroded surface of the cathode is depicted in (Fig. 8.2, d). A target material was commercial steel of AISI 4145H grade. The specimens of 6 × 12 × 25 (mm) in size were cut from an as-rolled plate of 25 mm thick of chemical composition of 0.48 wt.% C; 0.26 wt.% Si; 0.74 wt.% Mn; 0.013 wt.% S; 0.015 wt.% P. The substrate (steel of AISI 4145H grade) had a "Ferrite + Pearlite" structure typical for middle carbon steel with a hardness of 220 HV (Fig. 8.2, e).

Coatings microstructure and phase composition characterization. Pulsed plasma deposition resulted in a coating of 24–31 μm thickness shown in cross-section in Fig. 8.3, a. The coating had a typical PMMC structure consisting of compact equiaxial carbide particulates with a volume fraction of 24.1 ± 3.0 vol.% distributed within the metallic matrix (Fig. 8.3, b). The particulates were of different shapes (roundish and angular), their size varied in a rather wide range of 0.6–12.0 μm. Most of the particles had a size of 1–3 μm; their size distribution was close to that of carbide size in the cathode filler (Fig. 8.2, c). Some particles were not tightly adjusted to the matrix: the oxide shell was seen at the carbide/matrix interface (Fig. 8.3, b). Besides, the extended thick oxide films were found in the structure not to be closely associated with carbides that revealed the matrix oxidation in a plasma flow (Fig. 8.3, c). The total oxide volume fraction was estimated as 2.25 ± 0.98 vol.%. The matrix featured in optical microscope a homogeneous smooth pattern although in the carbide-free areas a needle-like pattern was revealed attributed to plate martensite [4] (Fig. 8.3, d). Under SEM observation, some matrix areas were characterized by a thin carbide network engulfing fine matrix grains (Fig. 8.3, e).

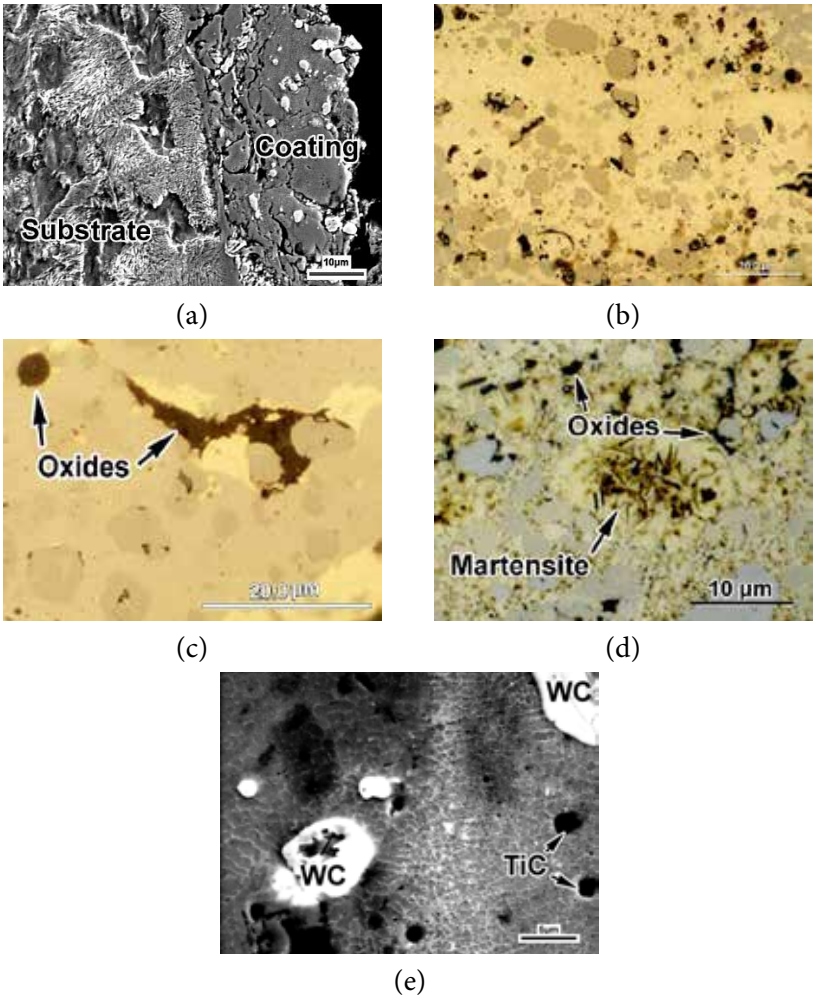

Figure 8.3 – The coating microstructure: (a) SEM (secondary electron image – SEI); (b-d) – OM, e – SEM (back-scattered electron image – BSEI) (a, d) cross-sectional direction; (b, c) a view from above

Figure 8.4 depicts the results of the coating microhardness measurements. The matrix was rather hard, its microhardness varied from 500 to 1044 HV. According to the diagram (Fig. 8.4) almost half on the measurements (41%) fell into the interval of 700–800 HV, furthermore, the 67% of values exceeded 700 HV which corresponds to the structure

of plate-martensite. The values higher 1000 HV can be attributed to the matrix areas reinforced by thin carbide net or fine carbide precipitations. Occasional enlarged particles were used to define carbide microhardness. It was measured as 1516–2029 HV with the most values fractions (55%) lying in the range of 1700–2000 HV (average value of 1857±151 HV) which is consistent with the data reported for tungsten carbide [202].

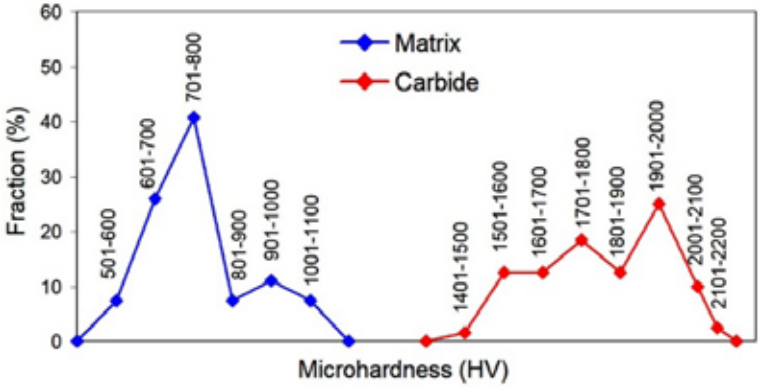

Figure 8.4 – The coating microhardness: distribution of the values for the matrix and carbide particles

The phase composition of the coating was identified by X-ray diffraction. The XRD pattern of the coating (Figure 8.5) presents the diffraction peaks belonging to the Fe-based dual-phase (αFe + γFe) matrix as well as reinforcing carbide phases. Both αFe and γFe were characterized by intensive and multiply peaks reflecting the predominant share of Fe-based matrix in a composite structure. According to the αFe and γFe peaks intensities ratio, austenite slightly prevailed in the matrix with 57 vol.%. Calculation gave a carbon content in austenite of 1.43 wt.%. Also, the multiply peaks attributed to WC and TiC carbides were identified on the XRD pattern proving that both carbides were plasma-transferred from the cathode to the coating. Also, the weak peaks lying at $2\theta = 54–59$ deg were uniquely associated with cementite (M_3C) carbide peaks (023) and (130). Moreover, the specific peaks at $2\theta = 38.1$ deg, $2\theta = 39.9$ deg and $2\theta = 70.8$ deg can be assigned to M_3C and W_2C both. Thus, the carbide phase composition of the coating only partly corresponded to the cathode filler carbides (WC, TiC) while M_3C and W_2C phases were obviously newly formed during deposition. In low angles interval, some peaks are positioned that can be assigned to the oxide phases (TiO_2, WO_2, WO_3).

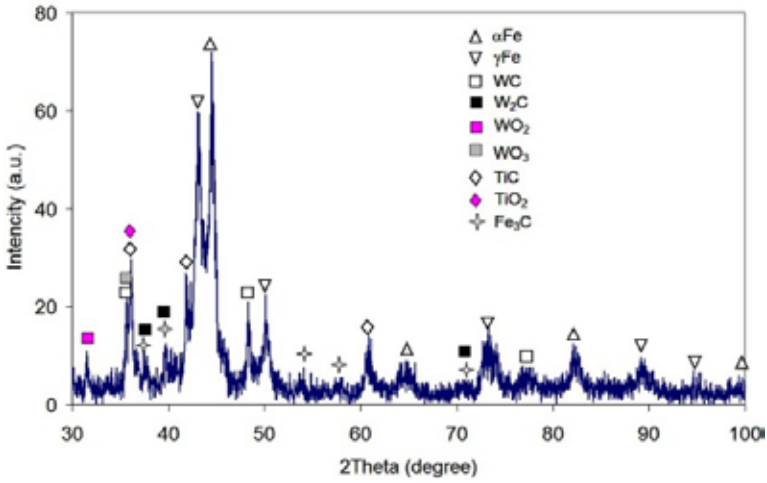

Figure 8.5 – XRD pattern of the coating

EDX-spectrometry was employed to assess the phase elemental distribution within the coating area shown in (Fig. 8.6, a). EDX-mappings for W, Ti, Fe and C coating are presented in (Figures 8.6, b-e). An element concentration is qualitatively depicted on the map by a specific colour according to the colour scale (left side of the map) to vary from 0 wt.% (black colour) to 100 wt.% (white colour). Coarse WC and TiC carbides are clearly distinguished in (Figs. 8.6, b and 8.6) accordingly as the white spots meaning high concentrations of tungsten/titanium. As seen, the location of white spots does not match, which indicates that titanium and tungsten were not mutually fused under their plasma transfer to the substrate. It is noteworthy that carbides were enveloped by the colourized halo revealing the partial dilution of these elements in the surrounding matrix. Iron was concentrated in a matrix with no visual trace in coarse carbides (Fig. 8.6, d). As follows from Figure 6e, the distribution of carbon was mostly associated with carbide particles. The oxygen distribution was associated with the oxide conglomerates (Fig. 8.6, f).

The mapping results were supported by elemental EDX-profiling. The results are shown in (Figure 8.7) which presents the back-scattered electron images of two coating's areas. Figure 9 a illustrates the profiles of W, Ti, Fe and C across the different carbides. Coarse carbides WC (point 004) and TiC (point 009) responded by sharp spikes in W and Ti concentration

accompanied by the sharp drop in iron content. In contrast, the dotted conglomeration of smaller carbides had lower W/Ti profiles and higher Fe profile. This behaviour was presumably due to (a) smaller carbide size and (b) presence of M_3C carbides having lower amount of W and Ti.

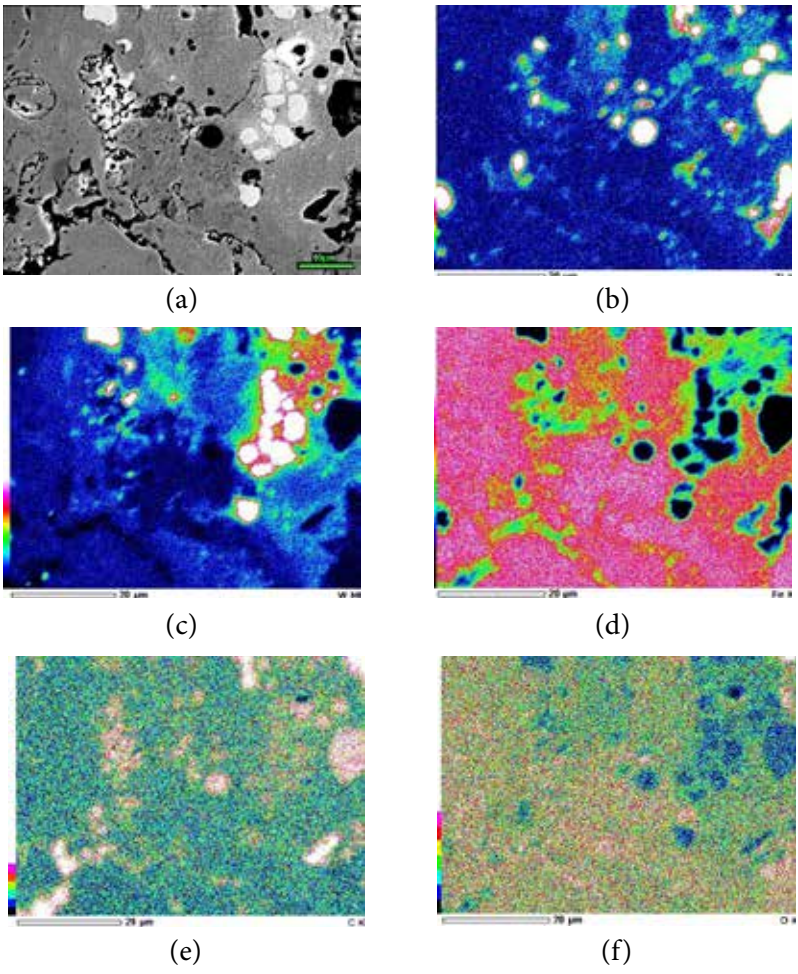

Figure 8.6 – Elemental EDX-mapping of the coating: (a) SEM (BSEI); distribution of (b) Ti, (c) W, (d) Fe, (e) C, (f) O

More detailed information on elemental distribution in the matrix was derived from (Figure 8.7, b). As seen, the line crosses the carbide-free ma-

trix (point 011) and the matrix with a carbide network (point 013). In the BSE image, the carbide network has bright coloration indicating its enrichment with the element of higher atomic number (tungsten). Tungsten profile through the "matrix/carbide network" area exhibited a higher level as compared to carbide-free matrix area proving its enrichment by tungsten. The same behaviour was noted for the titanium profile which follows the tungsten profile. The dotted particle crossed by line draws special attention: it is a titanium carbide (dark) surrounded by a W-rich matrix edge (bright). Therefore this particle attracts the spikes of W and Ti both.

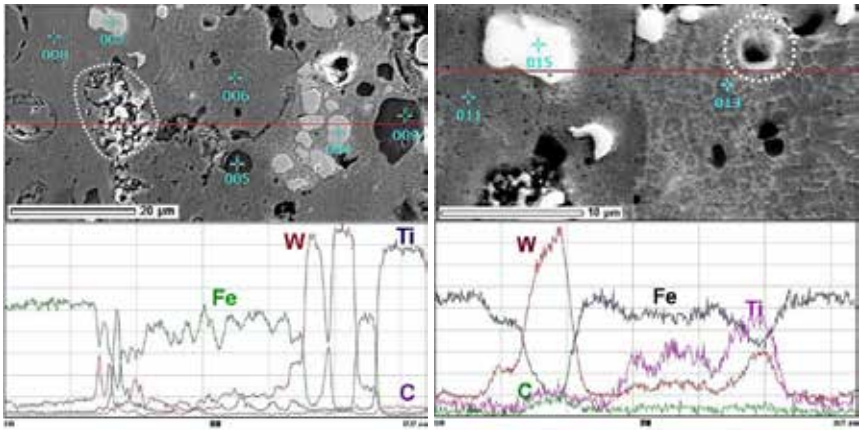

(a) (b)

Figure 8.7 – The EDX-profiles of C, W, Ti and Fe within the coating

The phase chemical composition of the coating has been clarified using a local EDX-analysis and summarized in Table 8.1 (the indicative analyzed points are designated in Fig. 8.7). The bright-contrast precipitates contained 89.5 wt.% W, 7.8 wt.% C and 2.7 wt.% Fe that is close to tungsten monocarbide WC stoichiometry (93.9 wt.% W, 6.1 wt.% C). The dark-contrast particles had a composition (77.6 wt.% Ti, 17.5 wt.% C, 4.3 wt.% Fe, 0.7 wt.% W) revealing them as titanium carbide TiC (stoichiometric composition is 80 wt.% Ti and 20 wt.% C). Impurity elements found in carbides (iron in WC and TiC; tungsten in TiC) were presumably absorbed due to plasma-chemical reactions in a plasma flow. The features of EDX-spectra for different carbides are shown in (Figures 8.8, a and 8.8, b).

Considering the spotty character of a matrix's structure, EDX point analyzing was performed on homogenous areas (the point 008 in Figure 8.7,

a and the point 011 in Figure 8.7, b) and on "carbide network" areas (the point 006 in Figure 8.7, a and the point 013 in Figure 8.7, b).

Table 8.1 – Phase chemical composition of the coating

Phase	Elements (wt.%)				
	C	Ti	W	Cu	Fe
WC	7.79±1.91	–	89.53±0.82	–	2.67±0.79
TiC	17.46±3.65	77.57±6.92	0.72±0.43	–	4.25±3.02
Carbide-free matrix	5.95±0.89	0.37±0.06	11.26±1.28	0.77±0.24	81.25±1.93
"Carbide network" matrix	8.76±0.70	3.32±1.07	16.98±2.02	1.06±0.05	74.72±2.86

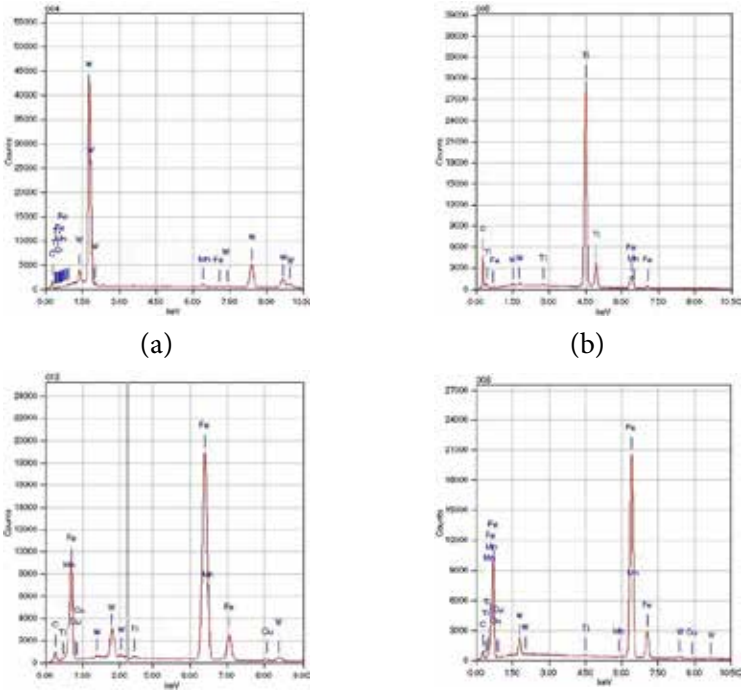

(a) (b) (c) (d)

Figure 8.8 – EDX-spectra for the indicative points shown in Figure 8.6: (a) WC carbide (point 004); (b) TiC carbide (point 005); (c) "carbide network"-matrix (point 013); (d) carbide-free matrix (point 008)

The major element in both cases was iron (about 80 wt.%); Ti, W and Cu were also detected in both areas as well. The "matrix/carbide network" responded higher amounts of C, W and Ti (Figure 8.8, c), which was affected by the carbide net. Since a spatial resolution of EDX beam was 2–3 μm, the analyzed spot included both matrix phase and carbide network, thus the latter contributed to EDS results. Carbide-free matrix had lower amount of C, W (by 1.5 times) and Ti (by 10 times) and slightly higher content of copper (Fig. 8.8, d). Carbon content measured in matrix (6–8.7 wt.%) is considered as excessive due to high sensitivity of EDX method to carbon contamination [160].

Tribological behaviour evaluation. The tribological properties of the coating were evaluated in comparison with the substrate (steel of AISI 4145H grade). Variation of CoF during the sliding test is shown in (Figure 8.9). When sliding against the steel ball the substrate performed the highest coefficient of friction: after a running-in period, the mean CoF value was 0.62 (Fig. 8.9, a). The coating responded with lower mean CoF value (0.52). The sliding against SiC ball was characterized by much lower friction force for both the substrate and the coating: the mean coefficient of friction for the substrate reached 0.43 while the coating exhibited CoF = 0.10 (Fig. 8.9, b).

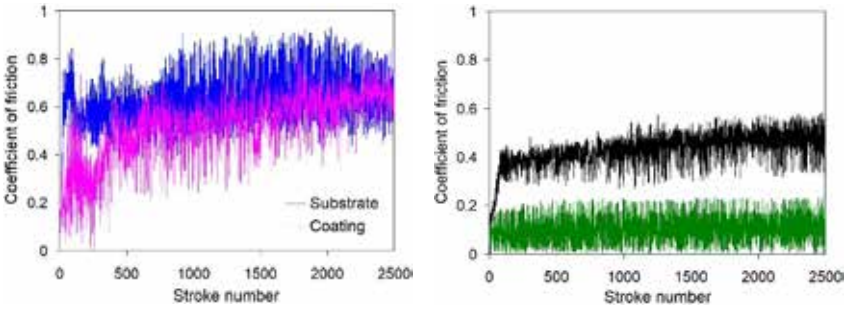

(a) (b)

Figure 8.9 – Variation of a mean CoF value during the wear test:
(a) sliding against 100Cr6 ball, (b) sliding against SiC ball

According to CoF variation, the wear tracks of different sliding couples significantly varied in their width and depth (as shown in Fig. 8.10). As follows from 3D images, the tracks on the substrate (Figs. 8.10, a, b) were much larger in width and depth than that of the coating (Figs. 8.10, c, d). The comparison of wear track profiles, presented in (Figure 8.10, e), allows to reveal that sliding against 100 Cr 6 counter-body resulted in wider and deeper wear

tracks than that of Si C. Especially large track (300 μm wide and 0.8 μm deep) was ploughed by the steel ball on the substrate (steel of AISI 4145H grade) surface; the wear track on the coating surface was twice as shallow. The sliding against silicon carbide ball produced more shallow tracks with a depth of 0.17 μm (on the substrate surface) and 0.05 μm – on the coating surface.

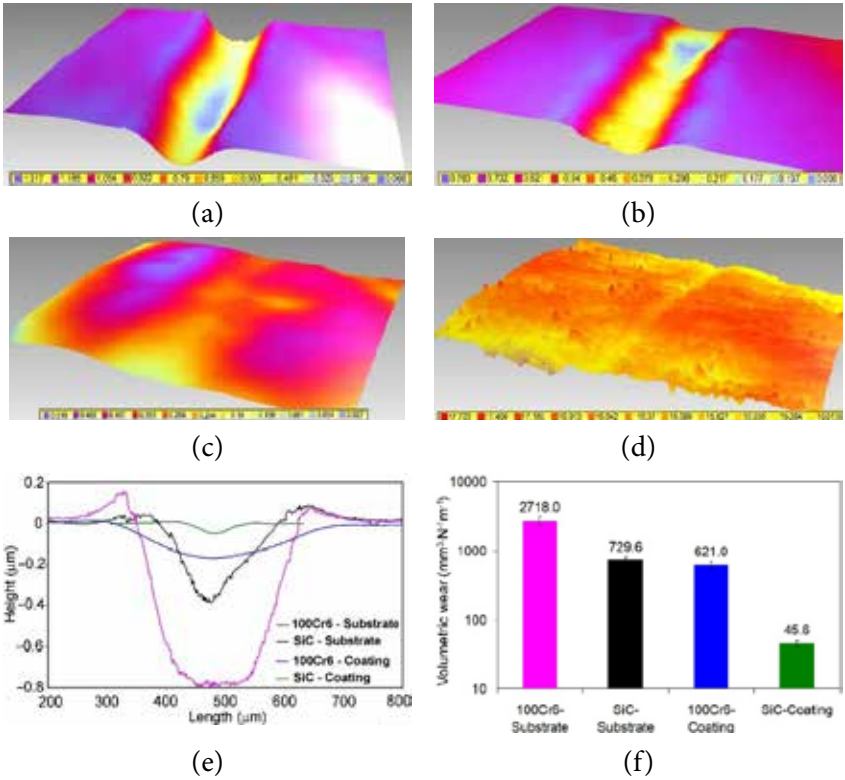

Figure 8.10–3D images of the wear tracks for different sliding couples and Dry-sliding wear characteristics of the specimens: (a) 100Cr6-substrate (steel of AISI 4145H grade); (b) SiC-substrate (steel of AISI 4145H grade); (c) 100Cr6-coating; (d) SiC-coating; (e) wear track profiles; (f) volumetric wear (The values of a profile height in Figs. (a)-(d) are given in μm)

The difference in friction behaviour resulted in wear responses presented in (Figure 8.10, f). As seen, the highest volumetric wear (2718 $\mu m^3 \cdot \cdot N^{-1} \cdot m^{-1}$) was demonstrated by the substrate after sliding against 100 Cr 6 counter-body. The substrate's volumetric wear was 3 times lower

(~ 730 μm^3 · N^{-1} · m^{-1}) in contact with a SiC ball. As compared with the substrate, the coating had better wear-resistance which manifested in decreasing ΔV value to 621 μm^3 · N^{-1} · m^{-1} (sliding against 100 Cr 6 ball) and to ~ 46 ·m^3 · · N^{-1} · m^{-1} (sliding against SiC ball).

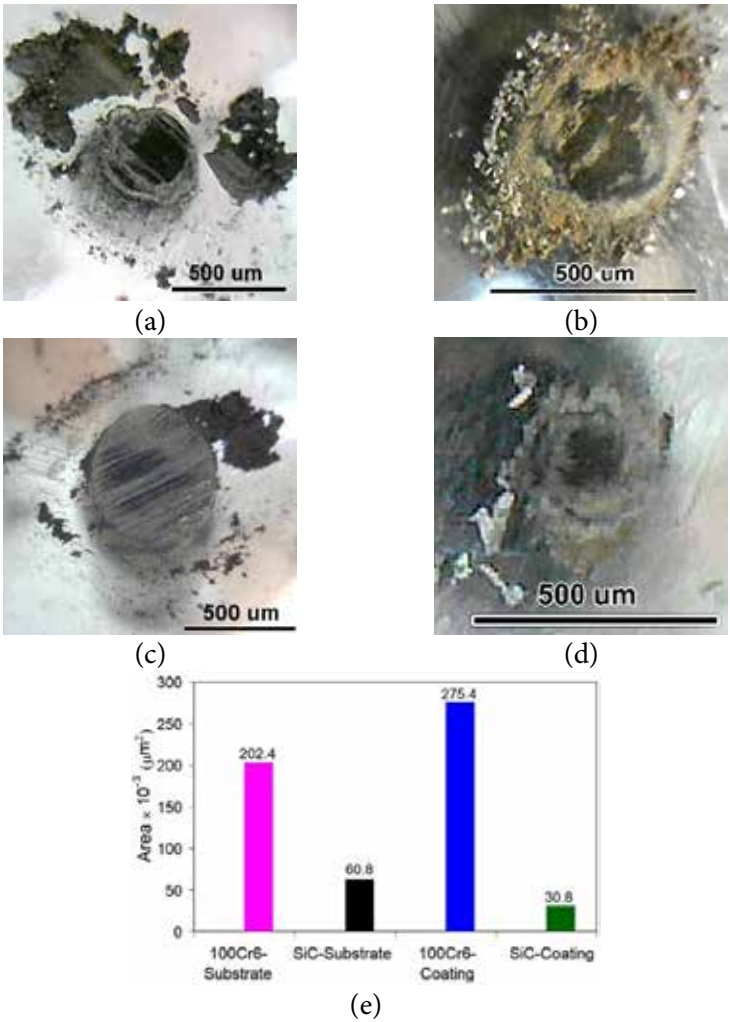

Figure 8.11 – Worn surface of the counter balls: (a) 100Cr6-substrate (steel of AISI 4145H grade); (b) SiC-substrate (steel of AISI 4145H grade); (c) 100Cr6-coating; (d) SiC- coating; (e) mean surface area of the wear spot on the ball after test

As follows from (Fig. 8.11), the wear testing affected a counter ball's surface. As seen, for each sliding couple the wear spot appeared on the ball surface surrounded by the wear debris. The largest spot area (275.4×10^{-3} μm^2) was attributed to the steel ball after sliding against the coating (Fig. 8.11, e). After testing against the substrate the spot area on the steel ball was also rather high – 202.4×10^{-3} μm^2. In contrast, the SiC ball featured a much lower spot area with a minimal value (30.8×10^{-3} μm^2) after sliding against the coating. After removing the debris from the ball surface it was found that the wear spots on 100 Cr 6 steel balls were flat with the parallel grooves appeared due to the ball wear-off (Figs. 8.11, a,c). The wear spots on SiC balls had a curvilinear shape; the wear spots were only noticeable owing to the traces of the adhered wear debris (Figs. 8.11, b, d).

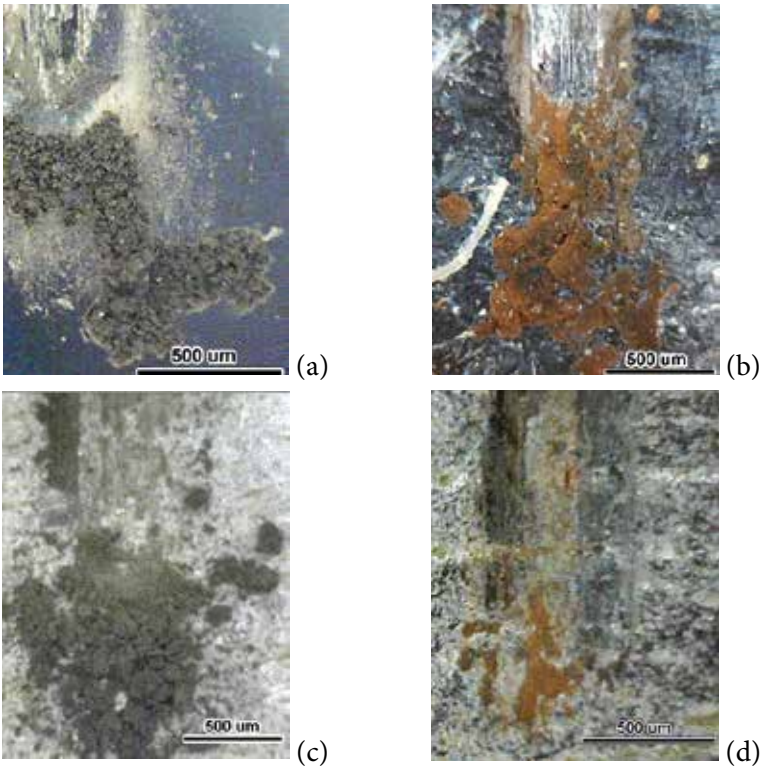

Figure 8.12 – Optical micrographs of the wear debris for different sliding couples: (a) 100Cr6-substrate (steel of AISI 4145H grade); (b) SiC-substrate (steel of AISI 4145H grade); (c) 100Cr6-coating; (d) SiC-coating

The wear debris was accumulated at the edges of the wear track (Fig. 8.12). Sliding against 100 Cr 6 ball resulted in powdered debris of dark-grey colour (Figs. 8.12, a, c). Unlike that, the debris formed after sliding against the SiC ball was of bright reddish colour having the petal-like shape. A difference in the nature of the wear products indicates the obvious dissimilarity in the mechanism of the specimen's wear depending on the material of a counter-body.

This assumption is supported by the appearance of wear tracks shown in (Figure 8.13). As follows from (Fig. 8.13, b), in sliding couple "SiC-substrate (steel of AISI 4145H grade)" the wear track was covered with a dense continuous oxide scale (with not numerous cracks within the scale). The dark colour of the scale indicated the high temperature that occurred in near-surface layers under the sliding. The same thick oxide scales were also characteristic for the wear tracks formed under sliding against a 100 Cr 6 steel ball, although in these cases the scales were discontinuous: they were interspersed with the dark-contrast areas of the scale spalling and the light-contrast areas of non-oxidized surface (Figs. 8.13, b, c). When SiC balls slid against the coating, the wear track was entirely covered with a thin continuous oxide scale; due to its low thickness the scale was transparent allowing the light beam interference manifestation (Fig. 8.13, d).

The performed studies have shown that using the proposed design of the cathode and the parameters of pulse-plasma deposition, it is possible to form a composite coating by direct deposition of carbides without their melting. This became possible due to the processes occurring inside the EAPA chamber during an electric discharge. The main in these processes is: (a) the burnout of the epoxy resin bond and the release of carbide particles (enabling their plasma-transfer to the surface) and (b) the formation of a high-carbon metal matrix due to the plasma-saturation of iron with carbon, which ensures the obtaining of high-carbon (hard) martensite in the matrix structure.

Comparison of the amount and size of carbides in the filler of the cathode and in the coating shows the closeness of their particle volume fraction and size distribution. This indicates that the carbides were delivered to the surface in their original state, i.e. in a non-molten state. This conclusion should be specified in a view of Ti and W presence on the matrix revealed by EDX-analyzing (Table 8.1, Figs. 8.8, c, d). The dissolution of some titanium and tungsten in the matrix is clearly seen in Figures 8 b and 8 c showing the halos surrounding the carbide particles that are the matrix areas enriched by Ti or W. One can speculate that partial melting of TiC/WC particles took

place under pulsed-plasma deposition with corresponding Ti/W enrichment of a melt around the particles.

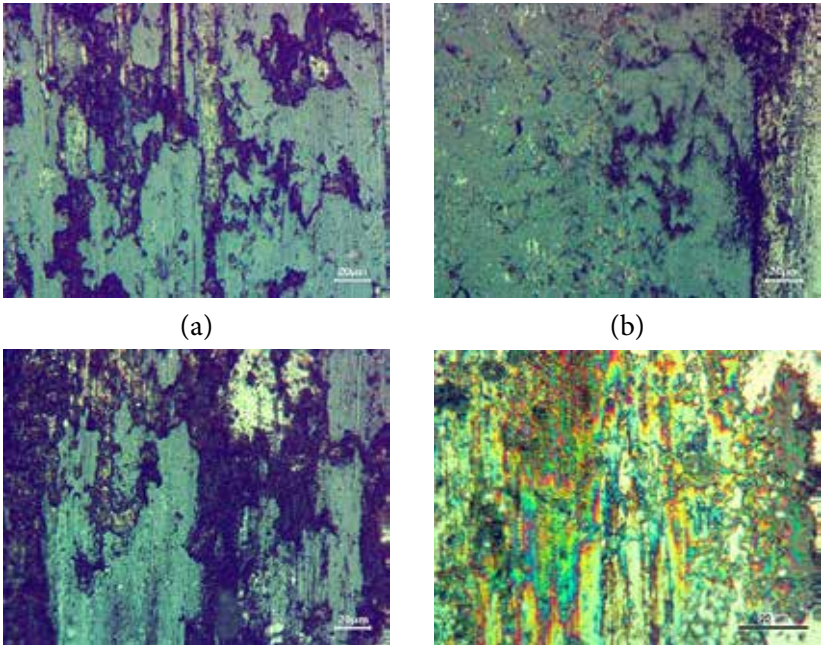

(a) (b)

(c) (d)

Figure 8.13 – Oxide films on the worn surface of the specimens: (a) 100Cr6-substrate (steel of AISI 4145H grade); (b) SiC-substrate (steel of AISI 4145H grade); (c) 100Cr6-coating; (d) SiC-coating

Another sources of Ti/W atoms could be the TiC/WC carbides evaporated (together with iron) in the cathode spot in direct contact with an electric arc. The released Ti, W, Fe atoms fell into the plasma flow and were transferred to the surface. Those atoms were presumably partially absorbed by the carbide particles in-flight that follows from the presence of W and Fe in TiC carbides and Fe – in WC carbides (Table 8.1). The presence of copper in the coating's matrix (0.8–1.0 wt.%) is also attributed to the plasma transfer of Cu atoms evaporated on the surface of the cathode copper mount. The matrix areas oversaturated with Ti and W enrichment crystallized through precipitation of $(Fe, W, Ti)_3C$ carbide network along the matrix grain boundaries. The areas with moderate Ti/W content remained non-decomposed being frozen under superfast coating crystallization (the

cooling velocity of pulsed-plasma coating was estimated as 10^6–10^7 K · · sec^{-1} in [120]).

The microstructural study allowed to conclude that PPT in the air atmosphere was accompanied by the oxidation of the products of the EAPA electrodes' erosion (carbides and liquid steel microdrops). The oxidation of the carbides was evidenced by the oxide inclusions present at the carbide/matrix boundaries. The oxidation of the molten steel microdrops was revealed by the extended oxide films not closely associated with the carbides. Similar phenomena (oxidation and decarburization) were described regarding the thermal spraying of WC carbides [258]. The presence of oxide film might negatively affect the mechanical properties of the coating and its resistance to abrasive wears, though in the case of dry-sliding application the oxide films can be useful serving as the solid lubricants. Carbide/steel oxidation was obviously caused by the interaction with atmospheric oxygen although it also could be enhanced by the gaseous combustion products of epoxy burning. According to [259] high-temperature combustion and pyrolysis of the epoxy polymer results in the emissions of different gases (CO_2, CO, H_2O, aliphatic hydrocarbons, etc.) some of which are oxidizing agents. This requires a further research to find a proper binder for the cathode's filler in order to avoid excessive oxide contamination of the coating.

High hardness and acicular pattern of the matrix revealed the presence of high-carbon plate martensite in the PMMC matrix. Most microhardness measurements fell to the interval of 700–800 HV being equivalent to 60–64 HRC typical for the cutting tool made of high-speed steel. A minor part of measurements was below 700 HV referring to the mixture of martensite and retained austenite (RA). As it was derived from the XRD pattern, the martensite was only about half of the matrix volume; the rest of the volume was occupied by austenite. The high volume fraction of RA was a result of the coating enrichment with carbon. Austenite was retained in matrix areas enriched with carbon up to 1.43 wt.% (as follows from XRD pattern). Austenite/martensite volume ratio depends on Ms temperature that can be calculated by Payson and Savage [260] equation:

$$\begin{aligned} Ms = 499–308 \cdot C – 32.4 \cdot Mn – 27 \cdot Cr – 16.2 \cdot Ni – \\ – 10.8 \cdot (Si + Mo + W) – –16.3 \cdot Cu + 10.8 \cdot Ti, \end{aligned} \quad (8.1)$$

where C, Mn, Cr, Ni, Si, Mo, W, Cu, Ti are contents of the elements (wt.%) in matrix.

The last two terms were added to Eq. (8.1) being adopted from Barbier equation [261] in order to use Eq. (8.1) for calculation of Ms for the coating's matrix. Carbon content was assumed as 1.43 wt.%, other elements (W, Cu, Ti) contents were taken from Table 1, for carbide-free matrix. Ms was calculated as –82.7 °C proving fully austenitic structure in carbon-enriched areas of the matrix. At the same time, the presence of martensite in the coating's matrix implies that the average Ms value was higher than room temperature.

The average Ms value for the coating can be derived from the Koistinen–Marburger equation assuming a quenching temperature of 20 °C and a fitting coefficient (a_m) of 0.008 (taken as for Fe-1.86 wt.% C alloy [65]). Assuming f_M = 0.43 for the coating's matrix (according to XRD pattern), the average Ms temperature was found as 90.8 °C which corresponds to the average carbon content of 0.865 wt.% C (by Eq. (8.1)). This means that carbon content in martensite should be 0.13 wt.% to balance with carbon content in RA (1.43 wt.%) (regarding the RA/martensite volume ratio). However, high microhardness measured in the matrix implies much higher carbon content in martensite. This means that actual carbon content in coating's matrix varies in very wide limits making heterogeneous matrix with a variation of structural state from "low-carbon lath martensite (soft)" to "high-carbon plate martensite (hard)" and to "high-carbon retained austenite (soft)". One can presume that exactly the "carbide network" matrix areas had mostly martensitic structure due to depletion by carbon and alloying elements that occurred through the carbide network formation. And conversely, the carbide-free matrix areas are supposedly austenite stabilized by dissolved carbon and other elements. According to [262, 263] the heterogeneous matrix is beneficial for wear-resistant materials due to better adaptability and redistribution of the stresses that occurred in contact with abrasive particles. Moreover, it can be assumed that RA in PMMC coating partially transforms to martensite under wear testing contributing to wear resistance via TRIP-effect [264].

The data presented in (Figs. 8.10–8.13) give insight to the mechanism of the specimens' wear. The sliding on the substrate surface caused intensive friction with a deep and wide groove formation. The sliding of the 100Cr6 steel ball resulted in protrusions on both sides of the wear track which is characteristic for abrasion of the soft materials. With the ball deepening the contact area increased and an abrasion transformed into intensive deformation of the near-surface layers of the substrate accompanied by their heating and dynamic oxidation with a thick oxide scale formation (Fig. 8.13). Oxide

scale protected the surface reducing the friction force and inhibiting the plasticity-dominated mechanisms; however, the repetitive sliding resulted in deterioration and delamination of the oxide scale with eventual debris formation as shown in (Figs. 8.11, 8.12). Thus, the main wear mechanism after a running-in period for all sliding couples was dry oxidative wear [265].

Noteworthy, that sliding of the steel ball produced a much higher surface deterioration of the substrate/coating surface as compared to the SiC ball (despite the increased hardness of the latter). This can be explained by the proximity of the crystal structure of the steel ball and the substrate which facilitates the interatomic interaction in a contact spot causing the adhesion with a galling manifestation [266, 267]. As seen in (Fig. 8.13, a), the oxide film on the substrate after sliding against the steel ball was discontinuous thus it could not fully protect the surface from the adhesion with the counter ball surface. This allowed to speculate, that after sliding against 100 Cr steel ball the debris consisted of the oxide chips and the products of galling. In contrast, SiC had a hexagonal crystal lattice that suppressed its adhesion with a cubic lattice of the substrate (BCC). Inhibiting an adhesion benefited the decrease in coefficient of friction (Fig. 8.9) and volumetric wear (Fig. 8.10, f). Therefore the sliding of SiC over steel surface responded only by deformation/oxidation behaviour where the oxidation presumably was more intensive than that of steel ball sliding. An intensive oxidation led to the formation of a more durable oxide scale with a higher protective potential. This assumption was supported by the micrograph of the wear track of the "SiC-substrate" couple (Fig. 8.13, b) showing the dense continuous oxide scale which tightly covered entire the surface of the wear track. The oxide films that emerged under the SiC ball sliding differed in structure/chemical composition from those of the sliding against 100 Cr steel ball. This follows from the different colour and the shape of the wear debris which were "dark-grey/powdered" for the steel ball and "reddish/petal-shaped" – for the SiC ball (Fig. 8.12). However, it is necessary to keep in mind that the colour of the debris might be affected by the products of the ball's wear.

Under the sliding, the protective oxide films acted as the abrasive agents abrading the counter ball surface. The steel balls were affected to more extent that manifested in the formation on their surface a flat worn spot covered by the parallel grooves (Figs. 8.11, a, c). The spot area was the highest for the "100Cr6-coating" couple. The increase in spot area in this case is explained by the contribution of WC/TiC carbides (present in the coating structure) into the abrading of the steel ball surface. The higher rate of

steel ball flattening resulted in wide and shallow wear track characteristic for the "100Cr6-coating" couple (Fig. 8.10, e). In contrast, the surface of SiC balls was negligibly affected by the sliding regardless of the counter surface material: only the slight adhering of wear debris was noted without the surface flattening. The high wear resistance of the SiC ball was due to its extremely high hardness (2600 HV). The maintaining of the spherical shape of the SiC ball during the testing led to lower width of the wear tracks as compared with the flattened steel ball. This also ensured the constancy of high stress in contact with the specimen promoting the higher rate of the "deformation-heating-oxidation" process with the dense protective oxide formation. Unlike this, fast flattening of steel ball decreased the contact stress that resulted in a less dense discontinuous oxide scale with lower protective ability.

The coating performed an undisputable advantage in the tribological properties as compared to the substrate (steel of AISI 4145H grade). An increased hardness (due to carbide particulates and hardened matrix) minimized the coating surface deformation when contacting with steel ball; therefore, the galling effect was suppressed resulting in a lower coefficient of friction. The decrease in CoF was additionally enabled by the oxide films (TiO_2, WO_2, WO_3) revealed in the coating's structure and confirmed by X-ray diffraction. Those oxides could act as a lubricant inhibiting adhesion between the contacting surfaces [268, 269]. However, the mean CoF for the "100 Cr 6-coating" was rather high (0.52) to be attributed to galling and abrasion of the ball surface by the carbide particles. Eventually, when testing with 100 Cr 6 counter ball, the volumetric wear of the coating was 4.4 times lower than that of the substrate.

The tribological advantage of the coating manifested to a greater extent when sliding against SiC ball. The coating's mean CoF decreased to a minimal value (0.10) while its volumetric wear lowered by 16 times relatively the substrate. The wear of the couple "SiC-coating" was accompanied by thin oxide films formation and minimal volume of the wear debris. This behavior reflects the high potential of "(TiC+WC)/Hardened steel" PMMC coating under the tribological contact with mineral particles (SiO_2, Al_2O_3, SiC, etc.) which is the most common case for abrasive wear. It is worth noting what the described behaviour of the studied PMMC coating refers only to the used testing parameters (normal load, sliding speed and distance, etc.). A more deep understanding of the coating's performance in other wear conditions requires an extended tribological study.

This study revealed that the PPD/EAPA technique with using the consumable cathode of a complex design enables the direct fabrication of a PMMC coating with a hard matrix without performing an additional post-deposition heat treatment. The wear testing proved the high wear resistance of the coating in contact with different counter-body materials. Pulsed-plasma fabrication of PMMC coating can be prospective for wear applications when the protective coating should be of several tens of microns of micron thickness. The optimization of phase/chemical composition and the ratio "carbide/binder" in the cathode filler regarding specific wear conditions is the topic of future research. Thus, the microstructure and sliding wear performance of a particle reinforced metal matrix composite (PMMC) manufactured by atmospheric pulsed-plasma deposition on AISI 4145H steel using an electro-thermal axial plasma accelerator (EAPA) were investigated.

The following conclusions can be drawn:

A composite coating "(TiC+WC)/Hardened matrix" of 24–31 μm thick was consolidated on the steel surface after 10 plasma pulsed with the discharge voltage of 4.0 kV and each discharge duration of 1 ms. Using the consumable cathode of a novel complex design (low-carbon plane steel tube filled with "TiC/WC + Epoxy resin" mixer) enables the direct formation of PMMC coating via plasma-transfer of carbides from the cathode to the substrate (steel of AISI 4145H grade) surface without their substantial melting. It is shown that the formation of the coating's matrix occurred due to melt enrichment with carbon released upon epoxy resin burnout and EAPA inner walls (bakelite) evaporation under high-current arc discharge. This resulted in the PMMC matrix consisting of 43 vol.% of plate martensite and 57 vol.% of retained austenite (RA) with high carbon content in the latter (1.43 wt.%). Also, partial melting/oxidation of TiC and WC particles occurred under the plasma transfer leading to oxide films (TiO_2, WO_2, WO_3) formation and matrix enrichment with Ti (up to 3.3 wt.%) and W (up to 17 wt.%). The latter caused the precipitation of $(Fe, W, Ti)_3C$ carbide network under the coating crystallization. The high hardness of the matrix (500–1044 HV) and its heterogeneous character supported by the protective oxide films presence enabled the improved wear behaviour of pulsed-plasma PMMC under dry-sliding conditions. It performed a lower coefficient of friction and increased wear characteristics compared with the substrate (steel of AISI 4145H grade): by 4.4 times lower volumetric wear under sliding against hardened 100 Cr 6 steel ball; by 16 times lower volumetric wear under sliding against SiO ball.

The wear mechanisms of pulsed-plasma PMMC coating depended on the counter-body material to be: (a) dry oxidative wear and galling when sliding against 100 Cr steel counter ball (proceeded through the formation/destruction of thick opaque discontinuous oxide scale on the coating surface), (b) dry oxidative wear when sliding against SiC ball (accompanied with the formation of thin transparent oxide scale entirely covering the wear track surface).

The content of the Chapter is adopted from Structural and tribological studies of "(TiC+WC)/Hardened steel" PMMC coating deposited by air pulsed plasma / Y. Chabak, V. Efremenko, V. Zurnadzhy, V. Puchý, I. Petryshynets, B. Efremenko, V. Fedun, K. Shimizu, I. Bogomol, V. Kulyk, D. Jakubéczyová // Metals.– 2022.– Vol. 12.– P. 218 https://doi.org/10.3390/met12020218

References

1. Kolyada Yu. E. Pulse electrothermal plasma accelerators and its application in scientific researches / Yu. E. Kolyada, V. I. Fedun // Problems of Atomic Science and Technology, Ser.: Plasma Physics. 2015. – Vol. 4. – P. 325–330.
2. Kolyada Yu. E. Pulse electrothermal plasma accelerators and its application in the technologies / Yu. E. Kolyada, A. A. Bizyukov, O. N. Bulanchuk [etc.] // Problems of Atomic Science and Technology. Series "Plasma Electronics and New Acceleration Methods". 2015. – Vol. 4. – P. 319–324.
3. Efremenko V. G. Pulsed plasma deposition of Fe-C-Cr-W coating on high-Cr-cast iron: Effect of layered morphology and heat treatment on the microstructure and hardness / V. G. Efremenko, Yu. G. Chabak, A. Lekatou [etc.] // Surface and Coatings Technology. 2016. – Vol. 304. – P. 293–305.
4. Vander Voort G. F. Metallography, Principles and Practice / G. F. Vander Voort. – Publisher: ASTM International, 1999.
5. Sun J. Microstructure development and mechanical properties of quenching and partitioning (Q&P) steel and an incorporation of hot-dipping galvanization during Q&P process / J. Sun, H. Yu // Materials Science and Engineering: A. 2013. – Vol. 586. – P. 100–107.
6. Kumar S. Microstructure-property relationship in the quenching and partitioning (Q&P) steel / S. Kumar, S. Brat Singh // Materials Characterization. 2023. – Vol. 196. – P. 112561.
7. Dijk N. H. Thermal stability of retained austenite in TRIP steels studied by synchrotron X-ray diffraction during cooling / N. H. Vandijk, A. M. Butt, L. Zhao [etc.] // Acta Materialia. 2005. – Vol. 53. – No. 20. – P. 5439–5447.
8. Berglund K. Novel reciprocating tribometer for friction and wear measurements with high contact pressure and large area contact configurations / K. Berglund, M. Rodiouchkina, J. Hardell [etc.] // *Lubricants.* 2021. – Vol. *9*. – P. 123.
9. Погребняк А. Д. Импульсно-плазменная модификация свойств поверхности и нанесение покрытий / А. Д. Погребняк, Ю. Н. Тюрин // Успехи физики металлов. 2003. – Т. 4. – С. 1–66.

10. Батраченко А. В. Влияние импульсно-плазменной обработки на микроструктуру и свойства стали 65Г / А. В. Батраченко // Проблеми трибології.2014. – №3.– С. 86–92.
11. Espallargas N. Dry wear and tribocorrosion mechanisms of pulse plasma nitrided Ni–Cr alloy / N. Espallargas, S. Mischler // Wear.2011.– Vol. 270, Iss. 7–8.– P. 464–471.
12. Samotugin S. S. The influence of plasma surface modification process on the structure and phase composition of cutting-tool hardmetals / S. S. Samotugin, V. I. Lavrinenko, E. V. Kudinova [etc.] // Journal of Superhard Materials.2011.– Vol. 33. – No. 3.– P. 200–207.
13. Romankov S. Pulsed plasma treatment of Ti–Al coatings produced by mechanical alloying method / S. Romankov, A. Mamaeva, S. D. Kaloshkin [etc.] // Materials Letters.2007.– Vol. 61.– P. 5288–5291.
14. Chabak Y. G. Phase-structural composition of coating obtained by pulsed plasma treatment using eroded cathode of T1 high speed steel / Yu. G. Chabak, V. I. Fedun, K. Shimizu [etc.] // Problems of Atomic Science and Technology. Series "Plasma Electronics and New Acceleration Methods".2016.– Vol. 104. – No. 4.– P. 100–106.
15. Чейлях А. П. Влияние параметров импульсно-плазменной обработки на структурообразование и свойства стали 40Х / А. П. Чейлях, Ю. Ю. Куцомеля, В. И. Федун [и др] // Строительство, материаловедение, машиностроение: Сб. науч. трудов.2014.– Вып. 73.– С. 235–239.
16. Савинков Н. А. Управление распределением микротвёрдости стали при импульсной плазменной обработке / Н. А. Савинков, Ю. Е. Коляда. // Вісник Приазовського державного технічного університету: Зб. наукових праць.2014.– Вип. 29.– С. 70–80.
17. Физические величины: Справочник / А. П. Бабичев, А. М. Братковский и др.; Под ред. И. С. Григорьева, Е. З. Мейлихова. – М.: "Энергоатомиздат", 1991.– 1232 с.
18. Андерсон Д., Таннехил Дж., Плетчер Р. Вычислительная гидромеханика и теплообмен. В 2-х томах. Т1: Пер. с англ. – М.: "Мир", 1990.– С. 384.
19. Дьяченко С. С. Образование аустенита в железоуглеродистых сплавах / С. С. Дьяченко.– Москва: "Металлургия", 1982.– 128 с.
20. Баландина Г. Ю. О причине смещения температуры инструментального начала аустенитного превращения в сталях при скоростном и лазерном нагреве / Г. Ю. Баландина, Б. И. Бертяев,

И. Н. Завестовская [и др] // Квантовая электроника.1986.– Т. 13. – № 11.– С. 2315–2319.
21. Ефременко В. Г. Кинетика превращения аустенита в рельсовых сталях марок М74 и 75ХГСМ при непрерывном охлаждении / В. Г. Ефременко, Ф. К. Ткаченко, С. О. Кузьмин [и др] // Вісник Дніпропетр. нац. унту залізн. трансп. ім. акад. В. Лазаряна: Зб. наукових праць.2009.– Вип. 29.– С. 198–201.
22. Smallman R. E. Modern Physical Metallurgy and Materials Engineering: Science, Process, Application / R. E. Smallman, R. J. Bishop.– Butterworth: "Heinemann", 1999.– 448 p.
23. Duriagina Z. A. The analysis of competitive methods of improvement of operational properties of functional layers of flat heating elements / Z. A. Duriagina, T. M. Kovbasyuk, S. A. Bespalov // Uspehi Fiziki Metallov.2016.– Vol. 17 (1).– P. 29–51.
24. Anders A. Fundamentals of pulsed plasmas for materials processing / A. Anders // Surface and Coatings Technology.2004.– Vol. 183 (2–3).– P. 301–311.
25. Zhukeshov A. M. Hardening of structural steel by pulsed plasma treatment / A. M. Zhukeshov, A. T. Gabdullina, A. U. Amrenova [etc.] // Journal of Nano- and Electronic Physics.2014. – Vol. 6 (3).– P. 03066–1–03066–3.
26. Bandura A. N. Alloying and modification of structural materials under pulsed plasma treatment / A. N. Bandura, O. V. Byrka, V. V. Chebotarev [etc.] // International Journal of Plasma Environmental Science & Technology.2011.– Vol. 5. – No.1.– P. 2–6.
27. Luo J. Effect of plasma-pulsed detonation treatment on microstructure and properties of the Ti-6Al-4V surface / Y. Luo, J. Chen, D. Xu // Surface and Coatings Technology.2019.– Vol. 366.– P. 164–169.
28. Chabak Yu. G. Modification of steel surface by pulsed plasma heating / Yu. G. Chabak, V. I. Fedun, T. V. Pastukhova [etc.] // Problems of Atomic Science and Technology.2017.– Vol. 110. – No 4.– P. 97–102.
29. Romankov S. Pulsed plasma treatment of Ti–Al coatings produced by mechanical alloying method / S. Romankov, A. Mamaeva, S. D. Kaloshkin [etc.] // Materials Letters.2007.– Vol. 61.– P. 5288–5291.
30. Nowakowska-Langer K. Synthesis of multicomponent metallic layers during impulse plasma deposition / K. Nowakowska-Langer, R. Chodun, K. Zdunek // Materials Science-Poland.2015.– Vol. 6133(4).– P. 841–846.

31. Kołek J. Practical design of a high-voltage pulsed power supply implementing SiC technology for atmospheric pressure plasma reactors / J. Kołek, M. Hołub // Applied Science.2019.– Vol. 9.– P. 1451.
32. Kovaleva M. G. Improving the wear resistance of thermally sprayed nanocomposite Cr_3C_2–25NiCr coatings by pulsed plasma treatment / M. G. Kovaleva, V. V. Sirota, V. M. Beresnev // Journal of Nano- and Electronic Physics.2018.– Vol. 10 (6).– P. 06035.
33. Kolyada Yu. E. Excitation of elastic pulses by powerful plasmoids in the acoustic waveguide / Yu. E. Kolyada, V. I. Fedun // Problems of Atomic Science and Technology, Ser.: Plasma Physics.2008.– Vol. 4.– P. 260–263.
34. Pogrebnyak O. D. Pulsed-plasma modification of surface properties and coating deposition / O. D. Pogrebnyak, Yu. M. Tyurin // Uspehi Fiziki Metallov.2003.– Vol. 4 (1).– P. 1–77.
35. Efremenko V. G. Abrasive wear resistance of spheroidal vanadium carbide cast irons / V. G. Efremenko, K. Shimizu, A. P. Cheiliakh [etc.] // Journal of Friction and Wear.2013.– Vol. 34. – No. 6.– P. 466–474.
36. Sukhovaya E. V. Structural approach to the development of wear-resistant composite materials / E. V. Sukhovaya // Journal of Superhard Materials.2013.– Vol. 35. – No. 5.– P. 277–283.
37. Efremenko V. G. Effect of bulk heat treatment and plasma surface hardening on the microstructure and erosion wear resistance of complex-alloyed cast irons with spheroidal vanadium carbides / V. G. Efremenko, K. Shimizu, T. V. Pastukhova [etc.] // Journal of Friction and Wear. 2017.– Vol. 38. – No. 1.– P. 58–64.
38. Fenech M. The post-deposition heat treatment of co-deposited Cr_3C_2 and AISI 410 stainless steel using the coaxial laser deposition technique / M. Fenech, B. Mallia, M. Grech [etc.] // Journal of Materials Science.– 2013.– Vol. 48.– P. 2224–2235.
39. Hemmati I. Microstructural characterization of AISI 431 martensitic stainless steel laser-deposited coatings / I. Hemmati, V. Ocelık, J. Th. M. De Hosson // Journal of Materials Science.2011.– Vol. 46.– P. 3405–3414.
40. Lanin S. N. The adsorption properties of titanium dioxide / S. N. Lanin, E. V. Vlasenko, N. V. Kovaleva [etc.] // Russian Journal of Physical Chemistry A, Focus on Chemistry.2008.– Vol. 82(12).– P. 2152–2155.
41. Глебов И. А. Мощные генераторы плазмы / И. А. Глебов, Ф. Г. Рутберг.– М.: Энергоатомиздат,1985.– 153 с.

42. Асланов С. К. К теории распада жидкой струи на капли / С. К. Асланов // Журнал технической физики.1999.– Т. 69, вып. 11.– С. 132–133.
43. Чиркин В. С. Теплофизические свойства материалов ядерной техники: справочник / В. С. Чиркин.– М.: Атомиздат, 1968.– 484 с.
44. Chabak Yu. G. Comparative analysis of the microstructural features of 28 wt.% Cr cast iron fabricated by pulsed plasma deposition and conventional casting / Yu. G. Chabak, V. G. Efremenko, K. Shimizu [etc.] // Journal of Materials Engineering and Performance.2018.– Vol. 27. – No. 2.– P. 379–388.
45. Vamsi Krishna B. Surface modification of AISI 410 stainless steel using laser engineered net shaping (LENS™) / B. Vamsi Krishna, A. Bandyopadhyay // Materials Design.2009.– Vol. 30.– P. 1490–1496.
46. Beresnev V. M. Influence of the high-temperature annealing on the structure and mechanical properties of vacuum–arc coatings from Mo/(Ti + 6 wt% Si)N / V. M. Beresnev, S. A. Klimenko, O. V. Sobol' [etc.] // Journal of Superhard Materials.2017.– Vol. 39 (3).– P. 172–177.
47. Chabak Yu. G. Change of secondary-carbides' nanostate in 14.5% Cr cast iron at high-temperature heating / Yu. G. Chabak, V. G. Efremenko // Metallofizika i Noveishie Tekhnologii.2012.– Vol. 34.– P. 1205–1220.
48. Imurai S. Microstructure And Erosion-Corrosion Behaviour of As-Cast High Chromium White Irons Containing Molybdenum in Aqueous Sulfuric-Acid Slurry / S. Imurai, Ch. Thanachayanont, J.T.H. Pearce [etc.] // Archives of Metallurgy and Materials.2015.– Vol. 60 (2).– P. 919–923.
49. Youping M. Effect of Ti-V-Nb-Mo Addition on Microstructure of High Chromium Cast Iron / M. Youping, L. Xiulan, L. Yugao [etc.] // China Foundry.2012.– Vol. 9 (2).– P. 148–153.
50. Efremenko V. G. Abrasive resistance of metastable V-Cr-Mn-Ni spheroidal carbide cast irons using the factorial design method / V. G. Efremenko, K. Shimizu, A. P. Cheiliakh [etc.] // International Journal of Minerals, Metallurgy, and Materials.2016.– Vol. 23. – No. 6.– P. 645–657.
51. Reda R. Investigation of Improving Wear Performance of Hypereutectic 15%Cr-2% Mo White Irons / R. Reda, A. Nofal, Kh. Ibrahim [etc.] // China Foundry.2010.– Vol. 7 (4).– P. 438–446.
52. Bedolla-Jacuinde A. Boron Effect on the Precipitation of Secondary Carbides During Destabilization of a High Chromium White Iron / A. Bedolla-Jacuinde, F. V. Guerra, I. Mejía [etc.] // International Journal of Cast Metals Research.2016.– Vol. 29 (1–2).– P. 55–61.

53. Chen H. Microstructure Refinement of Hypereutectic High Chromium Cast Iron with Electric Current Pulse / H. Chen, Z. Ling, W. Sheng Ming // Advanced Materials Research.2013.– Vol. 690–693.– P. 147–152.
54. Kasama A. H. Microstructure of Spray Formed 2.9%C-22% Cr High Chromium White Cast Iron / A. H. Kasama, R. D. Cava, A. Mourisco // Materials Science Forum.2003.– Vol. 416–418(1).– P. 419–424.
55. Janssen M. Effect of Spray-Forming on the Fracture Properties of High-Chromium White Iron. In F Nilsson (Ed.) / M. Janssen, D. N. Hanlon, I. C. Stone [etc.] // Proceedings of the 15th European Conference of Fracture Advanced Fracture Mechanics for Life and Safety Assessments (ECF15), Stockholm, Sweden. (pp. 1–8). – Stockholm, Sweden, 2004.
56. Matsuo T. T. Sliding Wear of Spray-Formed High-Chromium White Cast Iron Alloys / T. T. Matsuo, C. S. Kiminami, W. J. Botta Fo // Wear. 2005.– Vol. 259 (1–6).– P. 445–452.
57. Hanlon D. N. The Effect of Spray Forming on the Microstructure and P of a High Chromium White Cast Iron / D. N. Hanlon, W. M. Rainforth, C. M. Sellars // Journal of Materials Science.1999.– Vol. 34.– P. 2291–2301.
58. Hanlon D. N. The Rolling/Sliding Wear Response of Conventionally Processed and Spray Formed High Chromium Content Cast Iron at Ambient and Elevated Temperature / D. N. Hanlon, W. M. Rainforth, C. M. Sellars / Wear.1999.– Vol. 255–229.– P. 587–599.
59. Ted Guo M. L. Microstructure and Wear Behavior of Spray-Formed and Conventionally Cast Rolls of 18 Cr-2.5 Mo–Fe Alloy / M. L. Ted Guo, C.-H. Chiang, and C. Y. A. Tsao // Journal of Material Sciences & Engineering A.2002.– Vol. 326.– P. 1–10.
60. Özbek Y. Y. Wear Behavior of DIN1. 2210 Steel Modified by a Pulse Plasma Technique / Y. Y. Özbek, T. Gökkaya, C. V. Yavascan // Acta Physica Polonica.2016.– Vol. 129 (4).– P. 588–591.
61. Nowakowska-Langer K. Synthesis of multicomponent metallic layers during impulse plasma deposition / K. Nowakowska-Langer, R. Chodun, K. Zdunek // Materials Science-Poland.2015.– Vol. 33(4).– P. 841–846.
62. Kolyada Yu. E. The Use of a Magnetic Switch for Commutation of High-Current Pulse Circuits / Yu. E. Kolyada, V. I. Fedun, I. N. Onishchenko [etc.] // Instruments and Experimental Techniques.2001.– Vol. 44 (2).– P. 213–214.
63. Kolyada Y. E. Formation mechanism of the metallic nanostructures using pulsed axial electrothermal plasma accelerator / Y. E. Kolyada, V. I. Fedun,

V. I. Tyutyunnikov [etc.] // Problems of Atomic Science and Technology, Series Plasma Physics.2013. -Vol. 4.– P. 297–300.
64. Gelfi M. Effect of heat treatment on microstructure and erosion resistance of whitecast irons for slurry pumping applications / M. Gelfi, A. Pola, L. Girelli [etc.] // Wear.2019.– Vol. 428–429.– P. 438–448.
65. Wille G. Raman-in-SEM studies of inorganic materials / G. Wille, X. Bourrat, N. Maubec [etc.] // The Royal Society of Chemistry.– 2014.– P. 79–116.
66. Lekatou A. Mechanism of solid state reduction of chromite concentrate / A. Lekatou, R. D. Walker // Ironmak. Steelmak.1995.– Vol. 22.– P. 393–404.
67. Svensson L.-E. Fe-Cr-C Hardfacing Alloys for High-Temperature Applications / L.-E. Svensson, B. Gretoft, B. Ulander // Journal of Materials Science.1986.– Vol. 21.– P. 1015–1019.
68. Wiengmoon A. A Microstructural Study of Destabilised 30wt% Cr-2.3 wt% C High Chromium Cast Iron / A. Wiengmoon, T. Chairuangsri, J.T.H. Pearce // ISIJ International.2004.– Vol. 44.– P. 396–403.
69. Tang X. H. / Beneficial Effects of the Core–Shell Structure of Primary Carbides in High-Cr (45 wt%) White Cast Irons on Their Mechanical Behavior and Wear Resistance / X. H. Tang, Lei Li, B. Hinckley [etc.] // Tribology Letters.2015.– Vol. 58.– P. 44 (1–10).
70. Vasyukova E. S. Kinetic Description of $(Cr, Fe)_7C_3$ Carbide Precipitation from Austenite in High-Carbon Fe-Cr-C Ternary Alloys / E. S. Vasyukova, K. Yu. Okishev, A. S. Sozykina [etc.] // Solid State Phenomena. 2017.– Vol. 265.– P. 1005–1010.
71. Di X.-J. Effect of Post-weld Heat Treatment on the Microstructure and Corrosion Resistance of Deposited Metal of a High-Chromium Nickel-Based Alloy / X.-J.Di, X.-Q.Liu, C.-X. Chen [etc.] // Acta Metallurgica Sinica (English Letters).2016.– Vol. 29(12).– P. 1136.
72. Rafiei M. The effect of V addition on microstructure and tribological properties of Fe-Ti-C claddings produced by gas tungsten arc welding / M. Rafiei, H. Ghayour, H. Mostaan [etc.] // Journal of Materials Processing Technology.2019.– Vol. 266.– P. 569–578.
73. Zhao C. Microstructure and wear resistance of (Nb, Ti)C carbide reinforced Fe matrix coating with different Ti contents and interfacial properties of (Nb, Ti)C/α-Fe / C. Zhao, X. Xing, J. Guo [etc.] // Applied Surface Science.2019.– Vol. 494.– P. 600–609.

74. Efremenko V. G. Structure refinement of high-Cr cast iron by plasma surface melting and post-heat treatment / V. G. Efremenko, Yu. G. Chabak, K. Shimizu // Materials & Design.2017.– Vol. 126.– P. 278–290.
75. Efremenko V. G. High-Temperature Oxidation and Decarburization of 14.55 wt pct Cr-Cast Iron in Dry Air Atmosphere / V. G. Efremenko, Yu. G. Chabak, A. Lekatou [etc.] // Metallurgical and Materials Transactions A.2016.– Vol. 47 (4).– P. 1529–1543.
76. Guozhi X. Corrosion Characteristics of Plasma-Sprayed Ni-coated WC Coatings Comparison with Different Post-Treatment / X. Guozhi, L. Xiaoyan, W. Keyu [etc.] // Corrosion Science.2007.– Vol. 49.– P. 662–671.
77. Laird G. Abrasion-Resistant Cast Iron Handbook / G. Laird, R. Gundlach, K. Rohrig.– Des Plaines, Ill.: American Foundry Society, 2000.
78. Murakami T. Damping and tribological properties of Fe–Si–C cast iron prepared using various heat treatments / T. Murakami, T. Inoue, H. Shimura / Materials Science and Engineering: A.2006.– Vol. 432.– P. 113–119.
79. Abdou S. Wear behaviour of grey cast iron with the presence of copper addition / S. Abdou, A. Elkaseer, H. Kouta [etc.] // Advances in Mechanical Engineering A.2018.– Vol. 10.– P. 1–8.
80. Wang B. Effects of quench-tempering and laser hardening treatment on wear resistance of gray cast iron / B. Wang, Yu. Pan, Yu. Liu [etc.] // Journal of Materials Research and Technology.2020.– Vol. 09.– P. 8163–8171.
81. Pang Z. B. Effect of bionic coupling units' forms on wear resistance of grey cast iron under dry linear reciprocating sliding condition / Z. B. Pang, H. Zhou, G. Xie [etc.] // Optics & Laser Technology.2015.– Vol. 70.– P. 89–93.
82. Sui Q. Effect of alternate biomimetic coupling units on dry sliding wear resistance of grey cast iron / Q. Sui, H. Zhou, H. Zhang [etc.] // Journal of Materials Research.2017.– Vol. 32.– P. 343–353.
83. Sui Q. Lubricating property of cast iron combined with two-scale unit structure by biomimetic laser treatment / Q. Sui, H. Zhou, G. Liang [etc.] // Tribology International.2018.– Vol. 11.– P. 180–188.
84. Yang X. A bio-inspired concept to improve crack resistance of gray cast iron / X. Yang, L. Shi, S. Niu [etc.] // Materials Letters.2018.– Vol. 216.– P. 203–206.
85. Efremenko V. G. Application of the Q-n-P-treatment for increasing the wear resistance of low-alloy steel with 0.75% C / V. G. Efremenko,

V. I. Zurnadzhi, Y. G. Chabak [etc.] // Material Science.2017.– Vol. 53.– P. 67–75.
86. Fischer S. F. In-situ surface hardening of cast iron by surface layer metallurgy / S. F. Fischer, S. Muschna, A. Bührig-Polaczek [etc.] // Materials Science and Engineering: A.2014.– Vol. 615.– P. 61–69.
87. Chen Z.-K. Improved fatigue wear resistance of grey cast iron by localized laser carburizing / Z.-K. Chen, T. Zhou, R.-Y. Zhao [etc.] // Materials Science and Engineering: A.2015.– Vol. 644.– P. 1–9.
88. Zhou H. Wear properties of compact graphite cast iron with bionic units processed by deep laser cladding WC / H. Zhou, P. Zhang, N. Sun [etc.] // Applied Surface Science.2010.– Vol. 256.– P. 6413–6419.
89. Jeyaprakash N. Microstructure and tribological evolution during laser alloying WC-12% Co and Cr_3C_2–25% NiCr powders on nodular iron surface / N. Jeyaprakash, C.-H. Yang, M. Duraiselvam [etc.] // Results Physics.2019.– Vol. 12.– P. 1610–1620.
90. Zhong M. Corrosion and wear resistance characteristics of NiCr coating by laser alloying with powder feeding on grey iron liner / M. Zhong, W. J. Liu, H. J. Zhang // Wear.2006.– Vol. 260.– P. 1349–1355.
91. Tong X. Thermal fatigue characteristics of grey cast iron with non-smooth surface treated by laser alloying of Cr powder / X. Tong, H. Zhou, L.-Q.Ren [etc.] // Surface and Coatings Technology.2008.– Vol. 202(12).– P. 2527–2534.
92. Weng Z. Diode laser cladding of Fe-based alloy on ductile cast iron and related interfacial behavior / Z. Weng, A. Wang, Y. Wang [etc.] // Surface and Coatings Technology.2016.– Vol. 286.– P. 64–71.
93. Li Y. Elimination of voids by laser remelting during laser cladding Ni based alloy on grey cast iron / Y. Li, S. Dong, S. Yan // Optics & Laser Technology.2019.– Vol. 112.– P. 30–38.
94. Womersley D. Thermal spraying and powder spray welding processes for the hardfacing of grey cast iron / D. Womersley // Materials & Design.1990.– Vol. 11.– P. 153–155.
95. Lan D. Y. Interfacial microstructure and characterization of double-layer coatings on cast iron by arc spraying and sintering / D. Y. Lan, Q. Wang, Z. Z. Xuan // Materials Science and Engineering: A.2008.– Vol. 473.–P. 312–316.
96. Ryabtsev S. I. Effect of scandium on the structure and corrosion properties of vapor-deposited nanostructural quasicrystalline Al-Cu-Fe

films / S. I. Ryabtsev, V. A. Polonskyy, O. V. Sukhova // Powder Metallurgy and Metal Ceramics.2020.– Vol. 58.– P. 567–575.
97. Oleshkevych A. I. Enhanced Diffusion caused by Surface Reactions in Thin Films of Sn-Cu-Mn / A. I. Oleshkevych, S. M. Voloshko, S. I. Sidorenko [etc.] // Thin Solid Films.2014.– Vol. 550.– P. 723–731.
98. Singh S. K. Tribological properties of chromium nitride on the cylinder liner under the influence of high temperature / S. K Singh, S. Chattopadhyaya, A. Pramanik [etc.] // Materials.2020.– Vol. 13(20).– P. 4497.
99. Li Y. Microstructure evolution during laser cladding Fe-Cr alloy coatings on ductile cast iron / Y. Li, S. Dong, S. Yan // Optics & Laser Technology.2018.– Vol. 108.– P. 255–264.
100. Liu Y. TiC Reinforcement composite coating produced using graphite of the cast iron by laser cladding / Y. Liu, W. Qu, Y. Su // Materials. 2016.– Vol. 9(10).– P. 815.
101. Shi K. Y. Microstructure and fatigue properties of plasma transferred arc alloying TiC-W-Cr on grey cast iron / K. Y. Shi, S. B. Hu, H. F. Zheng // Surface and Coatings Technology.2011.– Vol. 206.– P. 1211–1217.
102. Fernandes F. Effect of arc current on microstructure and wear characteristics of a Ni-based coating deposited by PTA on grey cast iron / F. Fernandes, B. Lopes, A. Cavaleiro [etc.] // Surface and Coatings Technology.2011.– Vol. 205.– P. 4094–4106.
103. Perepl'otchikov E. F. Elevation of the wear resistance of low-alloy structural steel by Plasma-Powder surfacing with alloys based on iron, chromium, and nickel / E. F. Perepl'otchikov, K. B. Vasyliv, V. A. Vynar [etc.] // Materials Science.2018.– Vol. 54.– P. 378–386.
104. Halim Z. A. A. Rapid surface treatment of grey cast iron for reduction of friction and wear by alumina coating using gas tunnel plasma spray / Z. A. A. Halim, N. Ahmad, M. F. Hanapi [etc.] // Materials Chemistry and Physics.2021.– Vol. 260.– P. 124134.
105. Morks M. F. Microstructure and friction properties of plasma sprayed Al–Si alloyed cast iron coatings / M. F. Morks, Y. Tsunekawa, N. F. Fahim [etc.] // Materials Chemistry and Physics.2006.– Vol. 96.– P. 170–175.
106. Qi X. B. Effect of CeO_2 addition on thermal shock resistance of WC-12%Co coating deposited on ductile iron by electric contact surface strengthening / X. B. Qi, S. G. Zhu // Applied Surface Science. 2015.– Vol. 349.– P. 792–797.

107. Sokolov O. D. Enhancement of the corrosion resistance of grey cast iron by ion nitriding / O. D. Sokolov, O. V. Mannapova, A. I. Kostrzhyts'kyi [etc.] // Materials Science.2006.– Vol. 42.– P. 849–852.
108. Park I.-C. Microstructure and cavitation damage characteristics of surface treated grey cast iron by plasma ion nitriding / I.-C. Park, H.-K. Lee, S.-J. Kim // Applied Surface Science.2019.– Vol. 47731.– P. 147–153.
109. Agarwal K. DC pulsed plasma deposition of nanocomposite coatings for improved tribology of grey cast iron stamping dies / K. Agarwal, R. Shivpuri, J. Vincent [etc.] // Journal of Materials Processing Technology.2013.– Vol. 213.– P. 864–876.
110. Duryagina Z. A. Examination of the dielectric layers on the structural materials formed by hybrid ion-plasma discharge system / Z. A. Duryagina, S. A. Bespalov, V. Ya. Pidkova [etc.] // Metallofizika i Noveishie Tekhnologii.2011.– Vol. 33.– P. 393–400.
111. Posuvailo V. M. The effect of electrolyte composition on the plasma electrolyte oxidation and phase composition of oxide ceramic coatings formed on 2024 aluminium alloy / V. M. Posuvailo, V. V. Kulyk, Z. A. Duriagina [etc.] // Archives of Materials Science and Engineering.2020.– Vol. 105.– P. 49–55.
112. Cheng X. A comparative study on grey and nodular cast irons surface melted by plasma beam / X. Cheng, S. Hu, W. Song // Vacuum.– 2014.– Vol. 101.– P. 177–183.
113. Tyurin Y. N. Plasma for modification of a surface / Y. N. Tyurin, O. V. Kolisnichenko, B. V. Baskaran [etc.].– Square Energy Equipments Pvt Ltd, Tamilnadu, 2018.
114. Kovaleva M. Properties of Detonation Nanostructured Titanium-Based Coatings / M. Kovaleva, Y. Tyurin, O. Kolisnichenko [etc.] // Journal of Thermal Spray Technology.2013.– Vol. 22.– P. 518–524.
115. Ayday A. Reciprocating wear behavior of ductile cast iron modified by pulse plasma technology / A. Ayday, M. Durman // Acta Physica Polonica A.2014.– Vol. 125.– P. 189–191.
116. Cherenda N. N. The influence of the coating thickness on the phase and element composition of a Ti coating/steel system surface layer treated by a compression plasma flow / N. N. Cherenda, V. Uglov, M. G. Poluyanova [etc.] // Plasma Processes and Polymers.2009.– Vol. 6.– P. 178–182.

117. Chabak Yu. G. Surface modification of grey cast iron by pulsed-plasma deposition and subsequent laser beam melting / Yu. G. Chabak, V. G. Efremenko, V. I. Fedun [etc.] // Journal of Nano- and Electronic Physics. 2021. – Vol. 13(2). – P. 02030 (7 p).
118. Chabak Yu. G. Plasma coating formation by the deposition of cathode material eroded through high-current pulsed discharge / Yu. G. Chabak, V. I. Fedun, V. G. Efremenko [etc.] // Problems of Atomic Science and Technology: Series Plasma Physics. 2019. – Vol. 123. – P. 167–174.
119. Efremenko V. Three-body abrasive wear behaviour of metastable spheroidal carbide cast irons with different chromium contents / V. Efremenko, K. Shimizu, T. Pastukhova [etc.] // International Journal of Materials Research. 2018. – Vol. 109. – P. 147–156.
120. Efremenko V. G. Formation mechanism, microstructural features and dry-sliding behaviour of "Bronze/WC carbide" composite synthesised by atmospheric pulsed-plasma deposition / V. G. Efremenko, Yu. G. Chabak, V. I. Fedun [etc.] // Vacuum. 2021. – Vol. 185. – P. 110031.
121. Kazantsev E. I. Industrial Furnaces / E. I. Kazantsev. – Metallurgia: – Moscow, 1975.
122. Loboda P. I. Effect of the crystallization kinetic parameters on the structure and properties of a eutectic alloy of the LaB_6–TiB_2 system / P. I. Loboda, T. O. Soloviova, Y. I. Bogomol [etc.] // Journal of Superhard Materials. 2015. – Vol. 37(6). – P. 394–401.
123. Gonzalez-Pociño A. Erosive wear resistance regarding different destabilization heat treatments of austenite in high chromium white cast iron, alloyed with Mo / A. Gonzalez-Pociño, F. Alvarez-Antolin, J. Asensio-Lozano // Metals. 2019. – Vol. 9(5). – P. 522.
124. Efremenko V. G. refinement of high-Cr cast iron by plasma surface melting and post-heat treatment / V. G. Efremenko, Yu. G. Chabak, K. Shimizu [etc.] // Materials & Design. 2017. – Vol. 126. – P. 278–290.
125. Malinov L. S. Impact of metastable austenite on the wear resistance of tool steel / L. S. Malinov, V. L. Malinov, D. V. Burova // Journal of Friction and Wear. 2018. – Vol. 39. – P. 349–353.
126. Sugishita J. The effect of cast iron graphites on friction and wear performance I: graphite film formation on grey cast iron surfaces / J. Sugishita, S. Fujiyoshi // Wear. 1981. –Vol. 66 (2). – P. 209–221.
127. Tysoe W. On stress-induced tribochemical reaction rates / W. Tysoe // Tribology Letters. 2017. – Vol. 65. – P. 1–16.

128. Zhou D. Development of YSZ thermal barrier coatings using axial suspension plasma spraying / D. Zhou, O. Guillon, R. Vaßen // Coatings.2017.– Vol. 7(8).– P. 120.
129. Mendiratta M. G. The development of martensitic microstructure and microcracking in an Fe-1.86 C alloy / M. G. Mendiratta, G. Krauss // Metallurgical and Materials Transactions B.1972.– Vol. 3.– P. 1755–1760.
130. Kukhar V. V. Shape indexes for dieless forming of elongated forgings with sharpened end by tensile drawing with rupture / V. V. Kukhar, A. V. Grushko, I. V. Vishtak // Solid State Phenomena.2018.– Vol. 284.– P. 408–415.
131. Pereira A. Estimating the effective elastic parameters of nodular cast iron from micro-tomographic imaging and multiscale finite elements: Comparison between numerical and experimental results / A. Pereira, M. Costa, C. Anflor [etc.] // Metals.2018.– Vol. 8(9).– P. 695.
132. Elmer J. W. The thermal expansion characteristics of stainless steel weld metal / J. W. Elmer, D. Olson, K. Matlock // Welding Research Supplement.1982.– P. 293–301.
133. Shmykov A. A. Thermist's Handbook / A. A. Shmykov.– Mashgis: – Moscow, 1961.
134. Chabak Yu. G. Effect of cathode material on microstructure status of the coating fabricated using an electro-thermal axial plasma accelerator / Yu. G. Chabak, V. I. Fedun, V. G. Efremenko [etc.] // Romanian Journal of Physics.– 2021.– Vol. 66(3–4).– P. 501 (11 p.)
135. Pavlina E. J. Correlation of yield strength and tensile strength with hardness for steels / E. J. Pavlina, C. J. Vantyne // Journal of Materials Engineering and Performance.2008.– Vol. 7(6).– P. 888–893.
136. Sapronov O. O. Menou, A. Research of crack initiation and propagation under loading for providing impact resilience of protective coating / O. O. Sapronov, A. V. Buketov, P. O. Marushchak [etc.] // Functional Materials.2019.– Vol. 26.– P. 114–120.
137. Xiang Y. Effects of thermal plasma jet heat flux characteristics on surface hardening / Y. Xiang, D. Yu, Q. Li [etc.] // Journal of Materials Processing Technology.2015.– Vol. 226.– P. 238–246.
138. Semboshi S. Surface hardening of age-hardenable Cu–Ti alloy by plasma carburization / S. Semboshi, A. Iwase, T. Takasugi // Surface and Coatings Technology.2015.– Vol. 283.– P. 262–267.
139. Özbek Y. Y. Surface properties of M2 steel treated by pulse plasma technique / Y. Y. Özbek, H. Akbulut, M. Durman // Vacuum.2015.– Vol. 122, Part A.– P. 90–95.

140. Kovaleva M. Deposition and characterization of Al_2O_3 coatings by multi-chamber gas-dynamic accelerator / M. Kovaleva, Yu. Tyurin, N. Vasilik [etc.] // Surface and Coatings Technology.2013.– Vol. 232.– P. 719–725.
141. Bratushka S. N. Structure and tribological characteristics of steel under melting by plasma flow and simultaneous Mo and W alloying / S. N. Bratushka, Yu. N. Tyurin, O. V. Kolisnichenko [etc.] // Journal of Friction and Wear.2012.– Vol. 33.– P. 22–33.
142. Zhao N. Fabrication, microstructure and abrasive wear characteristics of an in situ tantalum carbide ceramic gradient composite / N. Zhao, Y. Xu, L. Zhong [etc.] // Ceramics International.2015.– Vol. 41, Part A.– P. 12950–12957.
143. León-Patiño C. A. Dry sliding wear of gradient Al-Ni/SiC composites / C. A. León-Patiño, E. A. Aguilar-Reyes, E. Bedolla-Becerril [etc.] // Wear.2013.– Vol. 301.– P. 688–694.
144. Ye F. $(Fe, Cr)_7C_3$/Fe surface gradient composite: Microstructure, microhardness, and wear resistance / F. Ye, M. Hojamberdiev, Y. Xu [etc.] // Materials Chemistry and Physics.2014.– Vol. 147.– P. 823–830.
145. Xie Z. Improving anti-wear and anti-corrosion properties of AM60 magnesium alloy by ion implantation and Al/AlN/CrAlN/CrN/MoS_2 gradient duplex coating / Z. Xie, Z. Luo, Q. Yang [etc.] // Vacuum. 2014.– Vol. 101.– P. 171–176.
146. Cadenas P. Effect of post-deposition heat treatment on the sliding wear resistance of a nickel-based coating deposited using high velocity oxy-fuel / P. Cadenas, M. Rodriguez, M. H. Staia // Welding International. 2009.– Vol. 23.– P. 763–772.
147. Karantzalis A. E. High chromium white irons, microstructure, carbide precipitation, sub-critical heat treatment, austenite destabilization / A. E. Karantzalis, A. Lekatou, H. Mavros // International Journal of Cast Metals Research.2009.– Vol. 6.– P. 448–456.
148. Efremenko V. G. Effect of vanadium and chromium on the microstructural features of V-Cr-Mn-Ni spheroidal carbide cast irons / V. G. Efremenko, K. Shimizu, A. P. Cheiliakh [etc.] // International Journal of Minerals, Metallurgy and Materials.2014.– Vol. 21.– P. 1096–1108.
149. Karantzalis A. E. Phase transformations and microstructural observations during subcritical heat treatments of a high-chromium cast iron / A. E. Karantzalis, A. Lekatou, A. Kapoglou [etc.] // Journal of Materials Engineering and Performance.2012.– Vol. 21.– P. 1030–1039.

150. Efremenko V. G. Kinetic parameters of secondary carbide precipitation in high-Cr white iron alloyed by Mn-Ni-Mo-V complex / V. G. Efremenko, Yu. G. Chabak, M. N. Brykov // Journal of Materials Engineering and Performance. 2013. – Vol. 22. – P. 1378–1385.
151. Cheng X. A comparative study on gray and nodular cast irons surface melted by plasma beam / X. Cheng, S. Hu, W. Song [etc.] // Vacuum. 2014. – Vol. 101. – P. 177–183.
152. Jeong B.-Y. Thermal fatigue characteristics of plasma duplex treated nodular cast irons / B.-Y. Jeong, J.-H. Chang, M.-H. Kim // Surface and Coatings Technology. 2010. – Vol. 205. – P. 896–901.
153. Efremenko V. Effect of destabilizing heat treatment on solid-state phase transformation in high-chromium cast irons / V. Efremenko, K. Shimizu, Yu. Chabak // Metallurgical and Materials Transactions A. 2013. – Vol. 44. – P. 5434–5446.
154. Halfa H. Thermodynamic calculation for silicon modified AISI M2 high speed tool steel / H. Halfa // Journal of Minerals and Materials Characterization. 2013. – Vol. 1. – P. 257–270.
155. Halfa H. Three main solidification reactions of vanadium modified T1–tungsten high speed tool steel / H. Halfa // Conference: 24th International Conference on Metallurgy and Materials At: Voronez I, Brno, Czech Republic, EU Metal. 2015. Jun 3rd – 5th, 2015. – 8 p.
156. Roberts G. A. Tool Steels, fifth ed. / G. A. Roberts, R. Kennedy, G. Krauss. – ASTM International, 1998. – 364 p.
157. Totten G. E. Microstructural characterization of layers produced by plasma nitriding on austenitic and superaustenitic stainless steel grades / G. E. Totten, L. C. Casteletti, F. A. P. Fernandes // Journal of ASTM International. 2011. – Vol. 9. – P. 1–11.
158. Qian L. Deformed microstructure and hardness of Hadfield high manganese steel / L. Qian, X. Feng, F. Zhang // Materials Transactions. 2011. – Vol. 52. – P. 1623–1628.
159. Shatynski S. R. The Thermochemistry of Transition Metal Carbides / S. R. Shatynski // Oxidation of Metals. 1979. – Vol. 13. – P. 105–118.
160. Rolland P. Improved Carbon Analysis with Evactron Plasma Cleaning / P. Rolland, V. L. Carlino, R. Vane // Microscopy and Microanalysis. 2004. – Vol. 10. – P. 964–965.
161. Pierson H. O. Handbook of Refractory Carbides & Nitrides: Properties, Characteristics, Processing and Applications / H. O. Pierson. – Noyes Publications, 1996. – 340 p.

162. Michaiski A. Layers of high speed steel with microstructures characteristic of heat-treated materials / A. Michaiski, A. Olszyna // Surface and Coatings Technology.1993.– Vol. 59.– P. 287–289.
163. Buchely M. F. The effect of microstructure on abrasive wear of hardfacing alloys / M. F. Buchely, J. C. Gutierrez, L. M. Leon [etc.] // Wear. 2005.– Vol. 259.– P. 52–61.
164. Karantzalis A. E. Effect of destabilization heat treatments on the microstructure of high-chromium casti: A microscopy examination approach / A. E. Karantzalis, A. Lekatou, E. Diavati // Journal of Materials Engineering and Performance.2009.– Vol. 8.– P. 1078–1085.
165. Rajan T. V. Heat Treatment: Principles and Techniques, 2nd ed. / V. Rajan, C. P. Sharma, A. Sharma // PHI Learning Pvt.– P. 241–242.
166. Laird II G. Microstructures of Ni-hard I, Ni-hard IV and high-Cr white cast irons / G. Laird II // Transactions of AFS.1991.– Vol. 99.– P. 339–357.
167. Filipovic M. Chemical composition and morphology of M7C3 eutectic carbide in high chromium white cast iron alloyed with vanadium / M. Filipovic, E. Romhanji, Z. Kamberovic // ISIJ International. 2012.– Vol. 52.– P. 2200–2204.
168. Chaus A. S. Microstructural and properties evaluation of M2 high speed steel after inoculating addition of powder W and WC / A. S. Chaus // Materials Science and Technology.2014.– Vol. 30.– P. 1105–1115.
169. Cheiliakh A. P. The structure and properties of steel 40Kh after pulsed plasma processing using titanium electrodes / A. P. Cheiliakh, Yu. Yu. Kutsomelya, V. I. Fedun [etc.] // Science and Education a New Dimension Natural and Technical Science.2013.– Vol. 8.– P. 79–84.
170. Savinkov N. O. The allocation of the micro-hardness of steel under pulsed plasma treatment / N. O. Savinkov, Yu. E. Kolyada // Reporter of the Priazovskyi State Technical University.2014.– Vol. 29.– P. 70–80.
171. Cheiliakh A. P. The influence of parameters of pulse-plasma treatment on structure and properties of steel 40 Cr / A. P. Cheiliakh, Yu. Yu Kutsomelya, V. I. Fedun [etc.] // Building, Materials Science, Mechanical Engineering.2014.– Vol. 73.– P. 235–239.
172. Lu W. Effect of different levels of free water in oil on the fretting wear of nickel-aluminum bronze-based composites / W. Lu, W. Zhai, P. Zhang [etc.] // Wear.2017.– Vol. 390–391.– P. 376–384.
173. Niu Y. Comparison of W–Cu composite coatings fabricated by atmospheric and vacuum plasma spray processes / Y. Niu, D. Lu, L. Huang [etc.] // Vacuum.2015.– Vol. 117.– P. 98–103.

174. Lungu M. V. Tungsten-copper composites for arcing contact applications in high voltage circuit breakers / M. V. Lungu, D. Pătroi, V. Marinescu // Material Science Research India.2020.– Vol. 17(3).
175. Ju W. Microstructure and electric contact properties of spark plasma sintered Ta-Cu composite / W. Ju, Y.-D. Kim, J. J. Sim [etc.] // Journal of Korean Powder Metallurgy Institute.2017.– Vol. 24(5).– P. 377–383.
176. Girish B. M. Electrical resistivity and mechanical properties of tungsten carbide reinforced copper alloy composites / B. M. Girish, B. R. Basawaraj, B. M. Satish // International Journal of Composite Materials. 2012.– Vol. 2(3).– P. 37–42.
177. Zhang Q. Microstructure and properties of W-25 wt% Cu composites reinforced with tungsten carbide produced by an in situ reaction / Q. Zhang, Y. Cheng, B. Chen [etc.] // Vacuum.2020.– Vol. 177.– P. 109423.
178. Silvain J.-F. Copper-carbon and aluminum-carbon composites fabricated by powder metallurgy processes / J.-F. Silvain, A. Veillère, Y. Lu // Journal of Physics: Conference Series.2014.– Vol. 525.– P. 012015.
179. Dias M. WC–Cu thermal barriers for fusion applications / M. Dias, F. Guerreiro, E. Tejado [etc.] // Surface and Coatings Technology. 2018.– Vol. 355.– P. 222–226.
180. Li S. Arc erosion behavior of TiB2/Cu composites with single-scale and dual-scale TiB_2 particles / S. Li, X. Guo, S. Zhang [etc.] // Nanotechnology Reviews.2019.– Vol. 8(1).– P. 619–627.
181. Banthia S. Reciprocating sliding wear of Cu, Cu-SiC functionally graded coating on electrical contact / S. Banthia, M. Amid, S. Sengupta [etc.] // Journal of Materials Engineering and Performance.2020.– Vol. 29.– P. 3930–3940.
182. Cui L. Carbon fiber reinforced Carbon-Al-Cu composite for friction material / L. Cui, R. Luo, D. Ma // Materials.2018.– Vol. 11(4).– P. 538.
183. Mechnik V. A. Physico-mechanical and tribological properties of Fe-Cu-Ni-Sn and Fe-Cu-Ni-Sn-VN nanocomposites obtained by powder metallurgy methods / V. A. Mechnik, N. A. Bondarenko, V. M. Kolodnitskyi [etc.] // Tribology in Industry.2019.– Vol. 41 (2).– P. 188–198.
184. Lentzaris K. Effects of in-situ intermetallics on the microstructural array and saline corrosion performance of cast Al/WCp composites / K. Lentzaris A. G. Lekatou, N. Gkikas [etc.] // Journal of Materials Engineering and Performance.2018.– Vol. 27.– P. 5164–5176.

185. Buketov A. Investigation of tribological properties of two-component bidisperse epoxy-polyester composite materials for its use in the friction units of means of sea transport / A. Buketov, M. Brailo, S. Yakushchenko [etc.] // Periodica Polytechnica Mechanical Engineering. 2019.– Vol. 63(3).– P. 171–182.
186. Kopeliovich D. Effect of interface modified by Graphene on the mechanical and frictional properties of carbon/grapheme/carbon composites / D. Kopeliovich // Advances in Ceramic Matrix Composites, Publishing Series in Composites Science and Engineering.2018.– P. 93–119.
187. Mashovets N. S. Aspects of the practical application of titanium alloys after low temperature nitriding glow discharge in hydrogen–free–gas media / N. S. Mashovets, I. M. Pastukh, S. M. Voloshko [etc.] // Applied Surface Science.2017.– Vol. 392.– P. 356–361.
188. Tigrinho J. J. Plasma transferred arc surface modification of a low carbon steel / J. J. Tigrinho, A. S. d'Oliveira // Journal of Materials Science.2007.– Vol. 42.– P. 7554–7557.
189. Özbek Y. Y. Effect of heat treatment and pulse plasma process on surface properties of steels / Y. Y. Özbek // Acta Physica Polonica A. 2017.– Vol. 31.– P. 182–185.
190. Zhukeshov A. The pulse plasma flows application in material science and nanotechnology / A. Zhukeshov, V. Nikulin, A. Gabdullina [etc.] // AIP Conference Proceedings.2019.– Vol. 2179 (1).– P. 020029.
191. Özbek Y. Y. The effect of plasma detonation parameters on residual stresses developed in the plasma modified layer / Y. Y. Özbek, C. Sarıoğlu, M. Durman // Vacuum.2014.–Vol. 106.– P. 11–15.
192. Özbek Y. Y. Surface properties of AISI 4140 steel modified by pulse plasma technique / Y. Y. Özbek // Journal of Materials Research and Technology.2020.– Vol. 9.– P. 2176–2185.
193. Yu J. Effect of pulse detonation-plasma technology treatment on T8 steel microstructures / J. Yu, L. Zhang, K. Liu [etc.] // Journal of Materials Engineering and Performance.2017.– Vol. 26.– P. 6198–6206.
194. Fujii K. Fabrication of diamond-like-carbon thin films by pulsed plasma deposition technique / K. Fujii, E. Fujiwara, T. Namazu [etc.] // Proceedings of JSPE Semestrial Meeting.– 2010.
195. Sartowska B. Phase changes in steels irradiated with intense pulsed plasma beams / B. Sartowska, J. Piekoszewski, L. Walisa [etc.] // Vacuum.2023.– Vol. 70.– P. 285–291.

196. Tyurin Yu. N. Properties and peculiarities of WCCoCr coatings formed by multi-chamber detonation sprayer / Yu. N. Tyurin, M. G. Kovaleva, N. J. Vasilik [etc.] // Applied Mechanics and Materials.2015.– Vol. 752–753.– P. 17–21.
197. Kovaleva M. G. Dense ZrB_2-$MoSi_2$ composite coating fabricated by a new multi-chamber detonation accelerator on Carbon/Carbon composites / M. G. Kovaleva, I. Yu. Goncharov, V. Yu. Novikov [etc.] // Materials Science Forum.2020.– Vol. 987.– P. 53–58.
198. Rosinski M. S. W/Cu composites produced by low temperature pulse plasma sintering (PPS) / M. S. Rosinski, E. Fortuna, A. J. Michalski // 24th Symposium on Fusion Technology.2013.– P4-I-405.
199. Chabak Yu. G. Features of formation of microstructure, elemental and phase compositions, and properties of the 1.7%C-14%Cr-3%Mn-3%Si-1%Ni-0.6%V-1.2%B steel under casting and pulsed plasma deposition / Yu. G. Chabak, T. V. Pastukhova, V. G. Efremenko [etc.] // Metallofizika i Noveishie Tekhnologii.2017.– Vol. 39.– P. 491–505.
200. Efremenko V. G. Structural and phase elemental distribution in pulsed plasma coating deposited with cemented carbide cathode / V. G. Efremenko, Yu. G. Chabak, K. Shimizu [etc.] // Journal of Nano- and Electronic Physics.2020.– Vol. 12 (3).– P. 03039.
201. Garcia J. Cemented carbide microstructures: a review / J. Garcia, V. C. Ciprés, A. Blomqvist [etc.] // International Journal of Refractory Metals and Hard Materials.2019.– Vol. 80.– P. 40–68.
202. Kurlov A. S. Tungsten Carbides: Structure, Properties and Application in Hardmetal / A. S. Kurlov, A. I. Gusev.– Springer Science & Business Media, 2013.
203. Scimeca M. Energy Dispersive X-ray (EDX) microanalysis: A powerful tool in biomedical research and diagnosis / M. Scimeca, S. Bischetti, H. K. Lamsira [etc.] // European Journal of Histochemistry.2018.– Vol. 62 (1).– P. 2841.
204. Gashkov M. A. The mechanism of liquid metal jet formation in the cathode spot of vacuum arc discharge / M. A. Gashkov, N. M. Zubarev, G. A. Mesyats [etc.] // Technical Physics Letters.2016.– Vol. 42(8).– P. 852–855.
205. Gashkov M. A. Model of liquid-metal splashing in the cathode spot of a vacuum arc discharge / M. A. Gashkov, N. M. Zubarev, O. V. Zubareva [etc.] // Journal of Experimental and Theoretical Physics.2016.– Vol. 122.– P. 776–786.

206. Utsumi T. Study of electrode products emitted by vacuum arcs in form of molten metal particles / T. Utsumi, J. H. English // Journal of Applied Physics.1975.– Vol. 46 (1).– P. 126–131.
207. Shalev S. Velocities and emission rates of cathode produced molybdenum macroparticles in a vacuum arc / S. Shalev, R. L. Boxman, S. Goldsmith // Journal of Applied Physics.1985.– Vol. 58 (7).– P. 2503–2507.
208. Shalev S. In situ determination of macroparticle velocities in a copper vacuum arc / S. Shalev; S. Goldsmith, R. L. Boxman // IEEE Transactions on Plasma Science.1983.– Vol. 11 (3).– P. 146–151.
209. Aslanov S. Theory of breakup of a liquid jet into droplets / S. Aslanov // Technical Physics.1999.– Vol. 4 (11).– P. 132–133.
210. Pabst O. Measurement of Young's modulus and residual stress of thin SiC layers for MEMS high temperature applications / O. Pabst, M. Schiffer, E. Obermeier [etc.] // Microsystem Technologies.2012.– Vol. 18.– P. 945–953.
211. Rendtel A. Hardness and hardness determination in silicon carbide materials / A. Rendtel, B. Moessner, K. A. Schwetz // Advances in Ceramic Armor.2005.
212. Ghasemi A. R. The relationship between flake graphite orientation, smearing effect, and closing tendency under abrasive wear conditions / A. R. Ghasemi, L. Elmquist // Wear.2014.– Vol. 317 (1–2).– P. 153–162.
213. Wang P. Wear and friction behaviours of copper mesh and flaky graphite- modified carbon/carbon composite for sliding contact material under electric current / P. Wang, H. Zhang, J. Yin [etc.] // Wear.2017.– Vol. 380–381.– P. 59–65.
214. Bauri R. Metal Matrix Composites by Friction Stir Processing / R. Bauri, D. Yadav.– Elsevier: Amsterdam, Netherlands, 2018.– 1–119 p.
215. Samal P. Recent progress in aluminum metal matrix composites: A review on processing, mechanical and wear properties / P. Samal, P. R. Vundavilli, A. J. Meher [etc.] // Journal of Manufacturing Processes.2020.– Vol. 59.– P. 131–152.
216. Mechnik V. A. Effect of vacuum hot pressing temperature on the mechanical and tribological properties of the Fe-Cu-Ni-Sn-Vn composites / V. A. Mechnik, N. A. Bondarenko, V. M. Kolodnitskyi [etc.] // Powder Metallurgy and Metal Ceramics.2020.– Vol. 58 (11–12).– P. 679–691.
217. Kandeva M. Influence of chromium concentration on the abrasive wear of Ni-Cr-B-Si coatings applied by supersonic flame jet (HVOF)

/ M. Kandeva, Z. Kalitchin, Y. Stoyanova // Metals.2021.– Vol. 11.– P. 915.
218. Alpas A. T. Wear of particulate metal matrix composites / A. T. Alpas, S. Bhattacharya, I. M. Hutchings // In Comprehensive Composite Materials II.2018.– Vol. 4.– P. 137–172.
219. Bakkar A. Microstructure, wear, and corrosion characterization of high TiC content Inconel 625 matrix composites / A. Bakkar, M. M. Z. Ahmed, N. A. J. Alsaleh // Journal of Materials Research and Technology.2019.– Vol. 8(1).– P. 1102–1110.
220. Sukhova O. V. New metallic materials and synthetic metals / O. V. Sukhova, Yu. V. Syrovatko // Metallofizika i Noveishie Tekhnologii. 2019.– Vol. 41(9).– P. 1171–1185.
221. Pramanik S. Coating Technologies for Metal Matrix Composites / S. Pramanik, K. K. Kar // Encyclopedia of Materials: Composites. 2021.– Vol. 1.– P. 454–473.
222. Kılıç F. Effect of CTAB concentration in the electrolyte on the tribological properties of nanoparticle SiC reinforced Ni metal matrix composite (MMC) coatings produced by electrodeposition / F. Kılıç, H. Gül, S. Aslan [etc.] // Colloids and Surfaces A.2013.– Vol. 419.– P. 53–60.
223. Lee Y. T. R. Effect of type of reinforcing particles on the deposition efficiency and wear resistance of low-pressure cold-sprayed metal matrix composite coatings / Y.T.R. Lee, H. Ashrafizadeh, G. Fisher [etc.] // Surface and Coatings Technology.2017.– Vol. 324.– P. 190–200.
224. Winnicki M. Field electron emission experiments with cold-sprayed Cu-SiC composite coatings / M. Winnicki, W. Łapa, Z. Znamirowski // Coatings.2021.– Vol. 11(2).– P. 134.
225. Xie X. Effect of annealing treatment on microstructure and mechanical properties of cold sprayed TiB2/AlSi10Mg composites / X. Xie, C. Chen, Z. Chen [etc.] // Surfaces and Interfaces.2021.– Vol. 26.– P. 101341.
226. Wang W. Fabrication, microstructure, and wear performance of WC-Fe composite/metal coating fabricated by resistance seam welding / W. Wang, X. Zeng, Y. Li [etc.] // Materials Characterization.2017.– Vol. 134.– P. 182–193.
227. Farías I. Wear modes in open porosity titanium matrix composites with TiC addition processed by spark plasma sintering / I. Farías, L. Olmos, O. Jiménez [etc.] // Transactions of Nonferrous Metals Society of China.2019.– Vol. 29(8).– P. 1653–1664.

228. Cabezas-Villa J. L. Constrained sintering and wear properties of Cu-WC composite coatings / J. L. Cabezas-Villa, L. Olmos, H. J. Vergara-Hernández [etc.] // Transactions of Nonferrous Metals Society of China.2017.– Vol. 27(10).– P. 2214–2224.
229. Ziejewska C. Influence of size and volume share of WC particles on the properties of sintered metal matrix composites / C. Ziejewska, J. Marczyk, A. Szewczyk-Nykiel [etc.] // Advanced Powder Technology.2019.– Vol. 30(4).– P. 835–842.
230. Xu J. Fabrication and properties of ZrC-ZrB_2/Ni cermet coatings on a magnesium alloy by atmospheric plasma spraying of SHS powders / J. Xu, B. Zou, S. Zhao [etc.] // Ceramics International.2014.– Vol. 40(10).– P. 15537–15544.
231. Xu L. Microstructure and corrosion resistance of WC-based cermet/Fe-based amorphous alloy composite coatings / L. Xu, J. Song, X. Zhang [etc.] // Coatings.2018.–Vol. 8(11).– P. 393.
232. Mordyuk B. N. Enhanced resistance of Ti 6Al 4V alloy to high-temperature oxidation and corrosion by forming alumina composite coating / B. N. Mordyuk, S. M. Voloshko, V. I. Zakiev [etc.] // Journal of Materials Engineering and Performance.2021.– Vol. 30.– P. 1780–1795.
233. Ostolaza M. Study of the reinforcement phase dilution into the metal matrix in functionally graded Stellite 6 and WC metal matrix composite by laser metal deposition / M. Ostolaza, J. I. Arrizubieta, M. Cortina // Procedia CIRP.2020.– Vol. 94.– P. 330–335.
234. Duryagina Z. A. Magnetometric analysis of surface layers of 12X18H10T steel after ion-beam nitriding / Z. A. Duryagina, S. A. Bespalov, A. K. Borysyuk [etc.] // Metallofizika i Noveishie Tekhnologii. 2011.– Vol. 33(5).– P. 615–622.
235. Tang B. Effects of TiB2 particles content on microstructure, mechanical properties and tribological properties of Ni-based composite coatings reinforced with TiB_2 particles by laser cladding / B. Tang, Y. Tan, T. Xu [etc.] // Coatings.2020.– Vol. 10(9).– P. 813.
236. Kotarska A. Characterization of the structure, mechanical properties and erosive resistance of the laser cladded Inconel 625-based coatings reinforced by TiC particles / A. Kotarska, T. Poloczek, D. Janicki // Materials.2021.– Vol. 14(9).– P. 2225.
237. Li Z. Improving surface resistance to wear and corrosion of nickel-aluminum bronze by laser-clad TaC/Co-based alloy composite coat-

ings / Z. Li, H. Yan, P. Zhang [etc.] // Surface and Coatings Technology. 2021.– Vol. 405.– P. 126592.
238. Tan H. Effect of strengthening particles on the dry sliding wear behavior of Al_2O_3–M_7C_3/Fe metal matrix composite coatings produced by laser cladding / H. Tan, Z. Luo, Y. Li [etc.] // Wear.2015.– Vol. 324–325.– P. 36–44.
239. Peng Y. Effect of WC content on microstructures and mechanical properties of FeCoCrNi high-entropy alloy/WC composite coatings by plasma cladding / Y. Peng, W. Zhang, Li T. [etc.] // Surface and Coatings Technology.2020.– Vol. 385.– P. 125326.
240. Oukach S. Physical and chemical phenomena occurring between solid ceramics and liquid metals and alloys at laser and plasma composite coatings formation: A review / S. Oukach, B. Pateyron, Pawłowski L. [etc.] // Surface Science Reports.2019.– Vol. 74(3).– P. 213–241.
241. Czupryński A. Microstructure and abrasive wear resistance of metal matrix composite coatings deposited on steel grade AISI 4715 by powder plasma transferred arc welding part 1. Mechanical and structural properties of a cobalt-based alloy surface layer reinforced with particles of titanium carbide and synthetic metal–diamond composite / A. Czupryński // Materials.2021.– Vol. 14(9).– P. 2382.
242. Zhang X. Effects of TiB_2+TiC content on microstructure and wear resistance of Ni55-based composite coatings produced by plasma cladding / X. Zhang, H. Z. Cui, J. F. Wang [etc.] // Transactions of Nonferrous Metals Society of China.2019.– Vol. 29(1).– P. 132–142.
243. Rokanopoulou A. Improvement of the tribological properties of Al_2O_3 reinforced duplex stainless steel MMC coating by the addition of TiS_2 powder / A. Rokanopoulou, P. Skarvelis, G. D. Papadimitriou // Surface and Coatings Technology.2016.– Vol. 289.– P. 144–149.
244. Huang Z. Microstructure and properties of Cr_3C_2-modified nickel-based alloy coating deposited by plasma transferred arc process / Z. Huang, Q. Hou, P. Wang [etc.] // Surface and Coatings Technology.2008.– Vol. 202(13).– P. 2993–2999.
245. Sivkov A. Deposition of a TiC/Ti coating with a strong substrate adhesion using a high-speed plasma jet / A. Sivkov, I. Shanenkov, A. Pak [etc.] // Surface and Coatings Technology.2016.– Vol. 291.– P. 1–6.
246. Kovaleva M. Effect of processing parameters on the microstructure and properties of WC-10Co-4Cr coatings formed by a new multi-

chamber gas-dynamic accelerator / M. Kovaleva, Y. Tyurin, N. Vasilik [etc.] // Ceramics International.2015.– Vol. 41(10).– P. 15067–15074.
247. Kovaleva M. G. Dense ZrB_2-$MoSi_2$ composite coating fabricated by a new multi-chamber detonation accelerator on carbon/carbon composites / M. G. Kovaleva, I. Y. Goncharov, V. Y. Novikov [etc.] // Materials Science Forum.2020.– Vol. 987.– P. 53–58.
248. Rosinski M. W/Cu composites produced by pulse plasma sintering technique (PPS) / M. Rosinski, E. Fortuna, A. Michalski [etc.] // Fusion Engineering and Design.2007.– Vol. 82.– P. 2621–2626.
249. Darabara M. Production of Fe–B–TiB_2 metal matrix composites on steel surface / M. Darabara, G. D. Papadimitriou, L. Bourithis [etc.] // Surface and Coatings Technology.2006.– Vol. 201(6).– P. 3518–3523.
250. Efremenko B. Simulation of structure formation in the Fe-C-Cr-Ni-Si surfacing materials / B. Efremenko, A. Belik, Y. Chabak [etc.] // Eastern-European Journal of Enterprise Technologies.2018.– Vol. 2(12).– P. 33–38.
251. Salloom R. Laser surface engineering of B_4C/Fe nano composite coating on low carbon steel: Experimental coupled with computational approach / R. Salloom, S. S. Joshi, N. B. Dahotre [etc.] // Materials & Design.2020.– Vol. 190.– P. 108576.
252. Zhang Z. Laser cladding of iron-based erosion resistant metal matrix composites / Z. Zhang, R. Kovacevic // Journal of Manufacturing Processesю 2019. – Vol. 38.– P. 63–75.
253. Chen H. Coarse TiC particles reinforced H13 steel matrix composites produced by laser cladding / H. Chen, Y. Lu, Y. Sun [etc.] / Surface and Coatings Technology.2020.– Vol. 395.– P. 125867.
254. Jiang W. H. Laser deposited TiC/H13 tool steel composite coatings and their erosion resistance / W. H. Jiang, R. Kovacevic [etc.] // Journal of Materials Processing Technology.2007.– Vol. 186.– P. 331–338.
255. Gordo E. Wear mechanisms in high speed steel reinforced with (NbC)p and (TaC)p MMCs / E. Gordo, F. Velasco [etc.] // Wear.2000.– Vol. 239(2).– P. 251–259.
256. Buketov A. Development of epoxy-polyester composite with improved thermophysical properties for restoration of details of sea and river transport / A. Buketov, M. Brailo, S. Yakushchenko [etc.] // Advanced Material Science.2018.– P. 6378782.

257. Atta A. M. Hybrid ZrO_2/Cr_2O_3 epoxy nanocomposites as organic coatings for steel / A. M. Atta, M. A. Ahmed, A. M. El-Saeed [etc.] // Coatings.2020.– Vol. 10(10).– P. 997.
258. Yuan J. Decarburization mechanisms of WC–Co during thermal spraying: Insights from controlled carbon loss and microstructure characterization / J. Yuan, Q. Zhan, J. Huang // Materials Chemistry and Physics.2013.– Vol. 142.– P. 165–171.
259. Tansir A. Thermal degradation and evolved gas analysis of epoxy (DGEBA)/novolac resin blends (ENB) during pyrolysis and combustion / A. Tansir, S. Alshehri // Journal of Thermal Analysis and Calorimetry.2012.– Vol. 111.– P. 445–451.
260. Payson P. Martensite reactions in alloy steels / P. Payson, C. H. Savage // Trans. ASM.1944.– Vol. 33.– P. 261–280.
261. Barbier D. Extension of the martensite transformation temperature relation to larger alloying elements and contents / D. Barbier // Advanced Engineering Materials.2014.– Vol. 1.– P. 122–127.
262. Malinov L. S. Effect of particular combinations of quenching, tempering and carburization on abrasive wear of low-carbon manganese steels with metastable austenite / L. S. Malinov, I. E. Malysheva, E. S. Klimov [etc.] // Materials Science Forum.2019.– Vol. 945.– P. 574–578.
263. Golyshev A. A. The formation of heterogeneous wear-resistant coatings by the additive technology method / A. A. Golyshev, A. G. Malikov, A. M. Orishich // Journal of Physics: Conference Series.2019.– Vol. 1404.– P. 012019.
264. Efremenko V. G. Abrasive resistance of metastable V–Cr–Mn–Ni spheroidal carbide cast irons using the factorial design method / V. G. Efremenko, K. Shimizu, A. P. Cheiliakh [etc.] // International Journal of Minerals, Metallurgy and Materials.2016.– Vol. 23(6).– P. 645–657.
265. Hutchings I. Tribology: Friction and Wear of Engineering Materials, Second Edition / I. Hutchings, P. Shipway.– Butterworth-Heinemann, 2017.
266. Dohda K. Galling phenomena in metal forming / K. Dohda, M. Yamamoto, C. Hu // Friction.2021.– Vol. 9.– P. 665–685.
267. Ostash O. P. Fatigue crack growth resistance of welded joints simulating the weld-repaired railway wheels metal / O. P. Ostash, V. V. Kulyk, V. D. Poznyakov [etc.] // Archives of Materials Science and Engineering.2017.– Vol. 86(2).– P. 49–55.

268. Ilie F. Tribological properties of the lubricant containing titanium dioxide nanoparticles as an additive / F. Ilie, C. Covaliu // Lubricants. 2016.– Vol. 4.– P. 12.
269. Cura M. E. Mechanical and tribological properties of $WO_{2.9}$ and ZrO_2 + $WO_{2.9}$ composites studied by nanoindentation and reciprocating wear tests / M. E. Cura, M. Trebala, Y. Ge [etc.] // Wear.2021.– Vol. 478–479.– P. 203920.